

**USE SOLID-STATE NMR TO STUDY THE MOLECULAR STRUCTURES OF
DISEASE-ASSOCIATED PEPTIDE AGGREGATES**

A Dissertation
Presented to
The Academic Faculty

By

Yuan Gao

In Partial Fulfillment
of the Requirements for the Degree
Doctor of Philosophy in the
School of Chemical and Biomolecular Engineering

Georgia Institute of Technology

August 2022

Copyright © Yuan Gao 2022

**USE SOLID-STATE NMR TO STUDY THE MOLECULAR STRUCTURES OF
DISEASE-ASSOCIATED PEPTIDE AGGREGATES**

Approved by:

Dr. Anant K. Paravastu, Advisor
School of Chemical and Biomolec-
ular Engineering
Georgia Institute of Technology

Dr. Julie A. Champion
School of Chemical and Biomolec-
ular Engineering
Georgia Institute of Technology

Dr. Yuhang Hu
School of Chemical and Biomolec-
ular Engineering
Georgia Institute of Technology

Dr. Mark P. Styczynski
School of Chemical and Biomolec-
ular Engineering
Georgia Institute of Technology

Dr. Raquel L. Lieberman
School of Chemistry and Biochem-
istry
Georgia Institute of Technology

Date Approved: July 11th, 2022

I'm smart enough to know that I'm dumb.

Richard P. Feynman

I dedicate this achievement to my wife Lin, who with love and effort have accompanied me along the path, without hesitating at any moment of seeing our dreams come true.

ACKNOWLEDGEMENTS

First and foremost, I would like to thank my adviser, Dr. Anant Paravastu. He has served as a valuable mentor, sounding board, supporter, and friend who has taught me about the joys and challenges of researches. While I will miss doing research with him, I look forward to his mentorship and continued interest in my career development.

I would also like to thank my thesis committee, Dr. Raquel Lieberman, Dr. Julie Champion, Dr. Yuhang Hu, and Dr. Mark Styczynski. They have provided thoughtful and helpful feedback on my presentations and research throughout the past 3 years. Also, I would like to especially thank Dr. Lieberman for all the help in our collaboration.

Research has become increasingly collaborative, and I have been the lucky enough to benefit from the advice and support of many wonderfully talented PIs, Dr. Carol Hall, Dr. Terrone Rosenberry, Dr. Huan-Xiang Zhou, Dr. Scott Stagg, Dr. Michael Blaber, and Dr. Raquel Lieberman.

As an NMR researcher, access to well-maintained magnets is very important. Luckily, I have Dr. Anil Mehta, Dr. Johannes Leisen, and Dr. Les Gelbaum as resources in this arena. They provided great training on these magnets.

During my study and work in Georgia Tech, I have been fortunate to meet a wide range of people from different universities, departments, and backgrounds.

First and foremost, I would like to thank past and present Paravastu Lab members, Danting Huang, Ben Hudson, Evan Roberts, Gan Wang, Elizabeth Lee, and Alicia Robang. They helped me in lab work, data analyses, and writing.

Much of the insights from my thesis would not be possible without the contributions from a wonderful group of collaborators. Dr. Liam Longo guided me for my first project. Dr. Shannon Hill, Dr. Dustin Huard, and Emily Saccuzzo produced good samples of protein or peptide amyloid. Dr. Yiming Wang and Dr. Cong Guo is very professional at MD simulations. Dr. Jens Watzlawik can produce the perfect oligomer samples as we expected.

Graduate school has its challenging moments, but with a crew of friends like Yao Ma, Fengyi Zhang, and Yi Sun, there is always a shoulder to lean on. I also want to thank Tingzhen Shi, my childhood friend, who just decided to pursue a graduate degree in medical school from zero. His determination encouraged me to face up to the challenges in my research.

Special thanks to my wife, Lin Yuan. In this long long journey, she gives me courage, faces all the challenges along with me, and take good care of me. I love you as always! BTW, thanks for bring happy Fitz into my life.

Finally, I would like to thank my parents who always care about me and support me. I would not have been able to participate in the countless educational opportunities afforded to me without their support.

TABLE OF CONTENTS

| | |
|---|-------|
| Acknowledgments | v |
| List of Tables | xiii |
| List of Figures | xv |
| List of Abbreviations | xx |
| Summary | xxiii |
| Chapter 1: Introduction and Background | 1 |
| 1.1 Amyloid Diseases and Protein Aggregation | 1 |
| 1.1.1 Alzheimer's Disease and Amyloid- β Oligomers (A β Os) | 3 |
| 1.1.2 Primary Open Angle Glaucoma and Myocilin | 11 |
| 1.2 Solid-State NMR and Its Application in Structural Studies | 12 |
| 1.2.1 History of Solid-State NMR | 12 |
| 1.2.2 Applications of Solid-State NMR in Biomolecular Structural Studies | 14 |
| 1.3 The Motivation to Study The Structures of Protein Aggregates | 16 |
| Chapter 2: Materials and Methods | 18 |
| 2.1 The Strategy of Solid-State NMR Structural Study | 18 |
| 2.2 NMR Sample Preparation | 20 |

| | | |
|---|--|--------|
| 2.2.1 | Solid-Phase Peptide Synthesis and Protein Expression | 20 |
| 2.2.2 | Preparing Aggregates of Peptides | 22 |
| 2.2.3 | Packing Samples into NMR Rotors | 23 |
| 2.3 | Solid-State NMR Techniques and Experiments | 24 |
| 2.3.1 | Overview of Solid-State NMR Techniques | 24 |
| 2.3.2 | The NMR Experiments and Simulations in Our Structural Studies . | 27 |
| 2.4 | Molecular Dynamics (MD) Modeling | 38 |
| 2.4.1 | NMR-Constrained MD Simulation | 39 |
| 2.4.2 | Compare The Experimental Constraints and The Model-Predicted Atomic Proximity: DARR Contact Chart | 39 |
| Chapter 3: Solid-State NMR Characterization of Residual Structure in Aggre- gated Form of Fibroblast Growth Factor-1 | | 42 |
| 3.1 | Project Overview | 42 |
| 3.2 | Introduction | 43 |
| 3.3 | Materials and Methods | 45 |
| 3.3.1 | FGF-1 Expression and Purification | 45 |
| 3.3.2 | Sample Preparation for Solid-State NMR | 45 |
| 3.3.3 | Solid-State NMR Characterization of Aggregated FGF-1 | 46 |
| 3.3.4 | Quantification and Statistical Analysis | 46 |
| 3.4 | Experimental Results | 47 |
| 3.4.1 | FGF-1 Aggregated State Is Inconsistent with Amyloid Structure . . | 47 |
| 3.4.2 | 2D NMR Spectra Characterize Residual Structure in The FGF-1 Aggregate | 47 |

| | | |
|-------|---|----|
| 3.4.3 | Inter-Residue Crosspeaks Are Located in The Region of The FGF-1 Folding Nucleus | 50 |
| 3.4.4 | Prediction of FGF-1 Thermodynamic Parameters in The Absence of Aggregation | 53 |
| 3.4.5 | Protein Concentration and Scan-Rate Dependence of The T_m of FGF-1 | 55 |
| 3.5 | Discussion | 56 |
| 3.5.1 | NMR Data Reveals The Region of Residual Structure | 56 |
| 3.5.2 | The Causes of Aggregate Propensity | 57 |
| 3.5.3 | Protein Functions and Folding Stability | 59 |
| 3.5.4 | A Peek at The Aggregation Pathway of Well-Folded Proteins | 60 |

Chapter 4: Comprehensive Analyses of Molecular Structure of 150-kDa Oligomers Formed by The Alzheimer’s Amyloid- β (1–42) Peptide 61

| | | |
|-------|--|----|
| 4.1 | Project Overview | 61 |
| 4.2 | Introduction | 62 |
| 4.3 | Materials and Methods | 67 |
| 4.3.1 | A β (1–42) Peptide Synthesis | 67 |
| 4.3.2 | A β (1–42) 150kDa Oligomer Preparations for Solid-State NMR . . | 68 |
| 4.3.3 | Solid-State NMR Experiments | 69 |
| 4.3.4 | TEM and cryo-EM | 70 |
| 4.3.5 | Molecular Modeling | 70 |
| 4.3.6 | NMR-Related Spin Simulation | 71 |
| 4.4 | Experimental Results | 72 |
| 4.4.1 | 2D ^{13}C NMR Spectra Reveal Two β -Strands and Evidence for Multi-site Occupancy | 72 |

| | | |
|-------|---|----|
| 4.4.2 | 2D DARR and PITHIRDS-CT Results Support Out-of-Register Parallel β -Sheet Models for The N-Strand | 75 |
| 4.4.3 | NMR Spectra with Higher Resolution Yielded New Structural Constraints | 77 |
| 4.4.4 | DPC-stabilized oligomers have the same structure as SDS-stabilized oligomers | 82 |
| 4.4.5 | TEM Revealed Primarily Globular Species but Anisotropic Self-Association | 87 |
| 4.4.6 | Cryo-EM Revealed a Four-Fold Symmetry | 89 |
| 4.4.7 | Structural Modeling Shows How EM and NMR Constraints Can Be Harmonized | 89 |
| 4.5 | Discussion | 93 |
| 4.5.1 | Features of The Oligomer Structural Model | 93 |
| 4.5.2 | The Size Limitation of The 150 kDa Oligomers | 96 |
| 4.5.3 | The Assembly Pathways of Oligomers | 97 |

Chapter 5: NMR-Constrained Molecular Modeling of Amyloid Fibril Formed by P1 Peptide Derived from The Glaucoma-Associated Myocilin 98

| | | |
|-------|--|-----|
| 5.1 | Project Overview | 98 |
| 5.2 | Introduction | 99 |
| 5.3 | Materials and Methods | 103 |
| 5.3.1 | Peptide Fibrillization Experiments | 103 |
| 5.3.2 | Solid-State NMR | 103 |
| 5.3.3 | NMR-Related Spin Simulations | 105 |
| 5.3.4 | Molecular Dynamics Modeling | 105 |
| 5.4 | Experimental Results | 106 |

| | | |
|--|---|------------|
| 5.4.1 | Isotope Labeling Strategy | 106 |
| 5.4.2 | 2D fpRFDR Experiments:Single Uniform Structure | 108 |
| 5.4.3 | 2D DARR Experiments:Inter-residue Contacts Exclude the S-Shaped Model | 110 |
| 5.4.4 | Dipolar Recoupling NMR and 2D CHHC Experiments:Antiparallel β -Sheets | 112 |
| 5.4.5 | Structural Modeling and Isotope-Dilution Effect:U-Shaped Antiparallel Model | 117 |
| 5.5 | Discussion | 121 |
| 5.5.1 | Stability of U-Shaped Antiparallel Amyloid Model | 124 |
| 5.5.2 | Comparison of P1 Model with Other Amyloid Structures | 125 |
| Chapter 6: Conclusions and Future Work | | 129 |
| 6.1 | Conclusions and Next Steps | 129 |
| 6.2 | Emerging Techniques and New Challenges | 131 |
| 6.2.1 | New Solid-State NMR Techniques | 131 |
| 6.2.2 | Help from Other Techniques | 133 |
| 6.2.3 | New Challenges | 135 |
| Appendix A: Reprint License Agreement | | 137 |
| A.1 | Reprint License Agreement for Chapter 3 | 137 |
| A.2 | Reprint License Agreement for Chapter 4 | 139 |
| A.3 | Reprint License Agreement for Chapter 5 | 140 |
| Appendix B: Supplementary Materials for Chapter 2 | | 141 |
| B.1 | Pulse Program Code of R ² W Experiment | 141 |

| | |
|--|------------|
| B.2 An example of SPINEVOLUTION input and output | 143 |
| Appendix C: Supplementary Materials for Chapter 3 | 146 |
| Appendix D: Supplementary Materials for Chapter 4 | 154 |
| Appendix E: Supplementary Materials for Chapter 5 | 168 |
| References | 205 |
| Vita | 206 |

LIST OF TABLES

| | | |
|-----|---|-----|
| 1.1 | Some amyloid diseases and their amyloidogenic proteins | 2 |
| 2.1 | A list of commonly used dipolar recoupling experiments. | 25 |
| 2.2 | A list of commonly used multidimensional experiments in ssNMR for biological samples. | 26 |
| 4.1 | Isotope labeling employed for the 150-kDa oligomer samples. | 73 |
| 5.1 | Isotope-labeling scheme for P1 amyloid samples. | 107 |
| 5.2 | Chemical shifts/linewidths for ^{13}C crosspeaks in the 2D fpRFDR spectrum of P1 amyloid fibril | 110 |
| 5.3 | Crosspeaks detected in the 2D DARR spectrum of Sample 5.A. | 112 |
| 5.4 | Dilution ratios of well-distinguished crosspeaks in the 2D DARR spectra. . | 123 |
| C.1 | Chemical shifts/linewidths for distinguishable ^{13}C -NMR peaks in the 2D fpRFDR spectrum of hydrated FGF-1 aggregated sample | 146 |
| C.2 | Chemical shifts/linewidths for distinguishable ^{13}C -labeled sites in the 2D fpRFDR spectrum of dehydrated FGF-1 aggregated sample | 149 |
| D.1 | Chemical shifts/linewidths for ^{13}C crosspeaks in the 2D fpRFDR spectrum of A β (1-42) 150 kDa oligomers. | 156 |
| D.2 | Chemical shifts/linewidths of ^{13}C -labeled sites in the ultracentrifuged A β 150kDa oligomer sampels. | 163 |

| | | |
|-----|---|-----|
| E.1 | Measured relative intensities of 2D DARR crosspeaks on isotope-diluted and non-diluted spectra. | 170 |
|-----|---|-----|

LIST OF FIGURES

| | | |
|------|--|----|
| 1.1 | Schematic representation of the biogenesis and the aggregation of A β | 6 |
| 1.2 | Structural studies of different A β Os. | 9 |
| 2.1 | The strategy of ssNMR structural studies. | 19 |
| 2.2 | General procedure of SPPS. | 21 |
| 2.3 | Use the ultracentrifugal packing widget to put samples into an NMR rotor. . | 24 |
| 2.4 | The pulse sequence of ^1H - ^{13}C CP-MAS experiment. | 27 |
| 2.5 | The ^{13}C CPMAS spectrum of P1 amyloid. | 28 |
| 2.6 | The pulse sequence of ^{13}C PITHIRDS-CT. | 30 |
| 2.7 | An example of ^{13}C PITHIRDS-CT data set and spin simulation. | 31 |
| 2.8 | The pulse sequence of ^{13}C - ^{13}C R 2 W. | 32 |
| 2.9 | An example of using R 2 W to measure the distance between two ^{13}C atoms. . | 32 |
| 2.10 | The pulse sequence of 2D ^{13}C - ^{13}C fpRFDR experiment. | 33 |
| 2.11 | An example of 2D ^{13}C - ^{13}C fpRFDR spectrum of P1 amyloid sample. | 35 |
| 2.12 | The pulse sequence of 2D ^{13}C - ^{13}C DARR experiment. | 35 |
| 2.13 | An example of 2D ^{13}C - ^{13}C DARR spectrum with 500 ms mixing time. . . . | 36 |
| 2.14 | The pulse sequence of 2D CHHC experiment. | 37 |
| 2.15 | An example of 2D CHHC spectrum of P1 amyloid sample. | 38 |

| | | |
|------|---|----|
| 2.16 | Use DARR contact chart to check the consistency between the structural model and the NMR experimental data. | 40 |
| 3.1 | Crystal structure and primary structure of FGF-1 | 44 |
| 3.2 | TEM images of thermally-aggregated FGF-1. | 48 |
| 3.3 | 2D fpRFDR spectrum of hydrated aggregated FGF-1. | 49 |
| 3.4 | Comparison of 2D fpRFDR spectra of the hydrated and the dehydrated aggregate FGF-1. | 51 |
| 3.5 | 2D CHHC spectra of fully-labeled and 50% isotopically-diluted aggregated FGF-1. | 52 |
| 3.6 | 2D DARR spectra with 50 ms and 100 ms mixing times of aggregated FGF-1. | 53 |
| 3.7 | Slices of 2D DARR spectra with 50 ms and 100 ms mixing times of aggregated FGF-1. | 54 |
| 3.8 | Primary structure of FGF-1 and Phifoil with highlighted unstructured and well-structured residues. | 55 |
| 4.1 | The fibrillar and non-fibrillar pathway of A β (1-42) assemblies. | 64 |
| 4.2 | The conformation of N-strand and C-strand regions in 150kDa A β (1-42) oligomers. | 65 |
| 4.3 | Comparison of some A β aggregate structures with our experimental NMR constraints in DARR contact chart. | 66 |
| 4.4 | Use secondary chemical shift values to predict the secondary structure regions in the 150 kDa A β (1-42) oligomer. | 74 |
| 4.5 | A parallel N-strand β -sheet shifted three residues out of register is consistent with the NMR constraints. | 76 |
| 4.6 | Doubly ^{13}C O-labeled PITHIRDS-CT data indicate out-of-register alignments of the N-strands. | 78 |
| 4.7 | Simulated PITHIRDS-CT curves and measured data for samples 4.F, 4.G, and 4.H according to ^{13}C O atom coordinates in parallel β -sheet with registry shift ± 3 and ± 4 | 79 |

| | | |
|------|---|-----|
| 4.8 | The 2D 50ms DARR spectra of ultracentrifuged sample have sharp cross-peaks revealing multiple molecular conformations. | 80 |
| 4.9 | Comparing 2D DARR slices from lyophilized and ultracentrifuged A β (1-42) 150 kDa oligomer samples. | 82 |
| 4.10 | The full contact chart summarizing all the experimental NMR constraints. . | 83 |
| 4.11 | Comparison between the 2D DARR spectra from the SDS-induced and the DPC-induced oligomer samples. | 84 |
| 4.12 | The pre- and post-SDS isotope-dilution strategy for verifying the 2-4mer residual structure in 150 kDa oligomers. | 85 |
| 4.13 | Three different C-strand alignments in antiparallel β -sheets. | 86 |
| 4.14 | NMR data reflects a center shift existing in the antiparallel C-sheet. | 87 |
| 4.15 | The TEM image and the cryoEM class average of A β 150 kDa oligomers. . | 88 |
| 4.16 | The β -sheet stacking, domain-swapping, and peptide conformation in the A β 150 kDa oligomer structure. | 90 |
| 4.17 | Introducing heterogeneous conformations into the 150 kDa oligomer model to make it more consistent with experimental NMR constraints. | 92 |
| 4.18 | The optimized model of A β (1-42) 150 kDa oligomers that can harmonize both NMR data and cryo-EM dimensions. | 94 |
| 5.1 | Crystal structure of mOLF and fibrils formed by P1 peptide. | 100 |
| 5.2 | CPMAS ^{13}C spectrum of P1 and P3 aggregates with no ^{13}C enrichment. . . | 101 |
| 5.3 | Hypothesized structures for P1 peptide amyloids. | 102 |
| 5.4 | Predicted patterns of inter-residue proximity that would be detectable by 2D solid-state NMR measurements. | 108 |
| 5.5 | 2D fpRFDR spectrum of Sample 5.A. | 109 |
| 5.6 | 2D DARR spectrum of Sample 5.A and the summary of detected contacts. . | 111 |
| 5.7 | PITHIRDS-CT data indicates not an in-register parallel β -sheet. | 113 |

| | | |
|------|--|-----|
| 5.8 | R ² W and 2D CHHC measurements indicating an antiparallel β -sheet. . . . | 115 |
| 5.9 | All-atom models of P1 native β -hairpin in different alignments. | 116 |
| 5.10 | Isotope-dilution effect on the crosspeak between V3 C α and F11 C α in 2D CHHC spectra. | 117 |
| 5.11 | Two candidate models inspired by experimental constraints and their expected patterns of 2D DARR contacts. | 119 |
| 5.12 | All-atom models of P1 peptide in non-native β -hairpin. | 120 |
| 5.13 | Effects of isotopic dilution on the 2D DARR spectrum. | 122 |
| 5.14 | Comparison of measured dilution ratios with the expected values from the U-shaped antiparallel and the non-native β -hairpin models. | 124 |
| 5.15 | U-Shaped antiparallel model of the P1 amyloid fibril, which agrees best with the data. | 125 |
| 5.16 | Representations of the U-shaped antiparallel structural model showing hydrogen bonds and hydrophobic core. | 126 |
| C.1 | Comparison of DARR spectra slices with different mixing times for Arg in FGF-1. | 150 |
| C.2 | Isothermal extrapolation of FGF-1 DSC data. | 151 |
| C.3 | Predicted non-aggregating FGF-1 DSC endotherm. | 152 |
| C.4 | Concentration and scan rate dependence of FGF-1 apparent T _m | 153 |
| D.1 | The fpRFDR spectra of the isotope-labeled A β (1-42) 150kDa oligomers from Samples 4.2 to 4.7 in Table 4.1. | 154 |
| D.2 | The fpRFDR spectra of the isotope-labeled A β (1-42) 150kDa oligomers from Samples 4.8 to 4.13 in Table 4.1. | 155 |
| D.3 | 2D 500ms DARR spectra from sample 4.1, 4.2, and 4.3. | 158 |
| D.4 | 2D 500ms DARR spectra from sample 4.4, 4.5, and 4.6. | 159 |
| D.5 | 2D 500ms DARR spectra from sample 4.7, 4.8, and 4.9. | 160 |

| | | |
|-----|---|-----|
| D.6 | 2D 500ms DARR spectra from sample 4.10, 4.11, and 4.13. | 161 |
| D.7 | 2D 50ms DARR spectra from ultracentrifuged oligomer samples 4.15, 4.16, and 4.17. | 162 |
| D.8 | Comparing intra-residue crosspeaks between lyophilized and ultracentrifuged A β (1-42) oligomer samples. | 166 |
| D.9 | 2D 1000 ms DARR spectra from ultracentrifuged oligomer samples 4.15, 4.16, and 4.17. | 167 |
| E.1 | The PITHIRDS-CT experimental data of Sample 5.C and different spin sim- ulation curves. | 168 |
| E.2 | Comparison between the slices from 500ms 2D DARR spectra of Sample 5.A and Sample 5.B. | 169 |

LIST OF ABBREVIATIONS

| | |
|----------------|--|
| A β | Amyloid- β |
| A β Os | Amyloid- β Oligomers |
| AD | Alzheimer's Disease |
| AFM | Atomic Force Microscopy |
| ANS | 1-Anilino-8-naphthalnesulfonate |
| APP | Amyloid Precursor Protein |
| β PFOs | β -sheet Pore-Forming A β (1-42) Oligomers |
| BSH-CP | Band-Selective Homonuclear Cross Polarization |
| cgMD | coarse-grained Molecular Dynamic |
| CP | Cross Polarization |
| CPMAS | Cross Polarization Magic Angle Spinning |
| cryo-EM | cryogenic Electron Microscopy |
| DARR | Dipolar-Assisted Rotational Resonance |
| DPC | DodecylPhosphoCholine |
| DSC | Differential Scanning Calorimetry |
| DMD | Discontinuous Molecular Dynamics |
| DQ-DRAWS | Double-Quantum Dipolar Recoupling with A Windowless Sequence |
| <i>E. coli</i> | <i>Escherichia coli</i> |
| FGF-1 | Fibroblast Growth Factor-1 |

| | |
|---------|---|
| FNSE | Folding Nucleus Symmetric Expansion |
| fpRFDR | finite pulse RadioFrequency Driven Recoupling |
| fsREDOR | frequency-selective Rotational-Echo DDouble-Resonance |
| HB plot | Hydrogen Bonding plot |
| IAPP | Islet Amyloid Polypeptide |
| IDP | Intrinsically Disordered Protein |
| MALS | Multi-Angle Light Scattering |
| MAS | Magic-Angle Spinning |
| MD | Molecular Dynamics |
| mOLF | myocilin Olfactomedin domain |
| MPL | Mass Per unit Length |
| MRI | Magnetic Resonance Imaging |
| NFT | Neurofibrillary Tangles |
| NMR | Nuclear Magnetic Resonance |
| PAIN-CP | Proton Assisted Insensitive Nuclei Cross Polarization |
| PAR | Proton Assisted Recoupling |
| PBS | Phosphate-Buffered Saline |
| PIR | Parallel-In-Register (β -sheet) |
| POAG | Primary Open Angle Glaucoma |
| PrP | Prion Protein |
| R^2 | Rotational Resonance |

| | |
|------------------|--|
| R ² W | Rotational Resonance Width |
| REDOR | Rotational-Echo DOuble-Resonance |
| RMSD | Root-Mean-Square Deviation |
| SDS | Sodium Dodecyl Sulfate |
| SEC | Size Exclusion Chromatography |
| SPPS | Solid-Phase Peptide Synthesis |
| STEM | Scanning Tunneling Electron Microscopy |
| ssNMR | solid-state Nuclear Magnetic Resonance |
| TABFOs | Toxic A β (1-42) Fibrillar Oligomers |
| TEM | Transmission Electron Microscopy |
| ThT | Thioflavin-T |

SUMMARY

In this thesis, we use solid-state nuclear magnetic resonance (ssNMR) to characterize the molecular structures of different types of aggregates formed by disease-associated proteins or peptides. ssNMR is widely used in the structural studies of protein assemblies because it can reveal the atomic-level information in the solid samples with short-range structure order. ssNMR is typically used along with electron microscopy techniques and molecular modeling to generate a comprehensive structural model.

Our lab collaborated with Dr. Blaber's lab to characterize the thermal aggregate of Fibroblast Growth Factor-1 (FGF-1). We performed 2D NMR experiments on the uniformly ^{13}C , ^{15}N -labeled FGF-1 aggregate, and the data indicates the well-structured region in aggregate comprised the folding nucleus of FGF-1. The folding nucleus is the region triggering FGF-1 folding process and keeping the native-like structure in the folding intermediate. The result is consistent with the hypothetical aggregation mechanism.

Another structural study in our lab is to collaborate with Dr. Rosenberry to investigate the 150 kDa Amyloid- β (1-42) ($\text{A}\beta$) oligomers associated with Alzheimer's disease. After measuring many 150 kDa oligomer samples with different isotope-labeled residues, we located two β -strand regions in $\text{A}\beta$ —the N-strand (residue 11-24) and the C-strand (residue 30-42). Surprisingly, the N-strands of $\text{A}\beta$ peptide aligned as out-of-register parallel β -sheets, while the C-strands assembled into antiparallel β -sheets. Dr. Stagg helped us generate a cryo-EM class average of a single oligomer particle, showing the oligomer has four-fold symmetry with a central pore. Furthermore, we improved the resolution of 2D NMR spectra by applying ultracentrifuge in NMR sample packing, and the improvement led to more NMR structural constraints. To rationalize the NMR constraints and the cryo-EM-resolved dimensions, we propose a domain-swapped four-subunit structural model.

We also collaborated with Dr. Lieberman's lab to investigate an amyloid sample—the P1 amyloid fibril. The P1 peptide sequence was derived from the glaucoma-associated my-

ocilin. The NMR data indicates a U-shaped fibril arrangement and an antiparallel backbone alignment. Finally, we proposed a structural model with stacked U-shaped antiparallel β -sheets for the P1 amyloid, which is further verified by the isotope-dilution effects in ssNMR experiments.

With these structural studies, we demonstrated the power of ssNMR in the structural characterizations of protein aggregates. The techniques and strategies of ssNMR are still under rapid development. First, the resolution and the signal-to-noise ratio of ssNMR can be further enhanced using novel instruments. Second, there are more methods to use to access the structures of aggregating intermediates. In addition, the development of other analytical tools provides a different angle for revealing the full structures of protein aggregates. We hope that the analyses of protein aggregates can become more efficient and automatic.

CHAPTER 1

INTRODUCTION AND BACKGROUND

This chapter will introduce the protein aggregation phenomenon in amyloid diseases and the structural studies of some aggregates, especially the oligomeric assembly of amyloid- β (A β) peptides in Alzheimer's disease. Although the underlying mechanisms of these diseases are currently under debate, structural studies of the aggregated proteins have shed light on the pathological pathways. In addition, with four decades of development, solid-state Nuclear Magnetic Resonance (ssNMR) has become a powerful tool for characterizing protein structures. The development and the application of ssNMR greatly expand the understanding of protein aggregation phenomenon.

1.1 Amyloid Diseases and Protein Aggregation

Amyloid diseases are human diseases caused by extracellular or intracellular oligomers and amyloid fibrils formed by the abnormal self-assembly of peptides or proteins. Table 1.1 lists several amyloid diseases and the affiliated amyloidogenic proteins. These diseases affect millions of people worldwide and have been studied in depth for several decades [1, 2]. Alzheimer's disease (AD), for example, was first identified more than 100 years ago [3, 4], and it affects more than 35 million people globally [5]. Meanwhile, more diseases, such as primary open-angle glaucoma, are added to the list when their pathological mechanisms are revealed.

Protein aggregation is generally a phenomenon observed for practically all protein species under a wide variety of conditions. For instance, recombinant overexpression of proteins in bacterial cells often aggregates into so-called inclusion bodies, in which the proteins mostly adopt undefined insoluble conformations [15]. Additionally, changing the condi-

Table 1.1 Some amyloid diseases and their amyloidogenic proteins.

| Disease | Amyloidogenic proteins (or peptides) | Reviews |
|-----------------------------|--|----------|
| Alzheimer's disease | Amyloid- β peptide (A β , usually 40-42 residues) | [5–7] |
| Parkinson's disease | α -synuclein (140 residues) | [8, 9] |
| Type-II diabetes | human islet amyloid polypeptide (IAPP or amylin, 37 residues) | [10, 11] |
| Creutzfeldt–Jakob disease | scrapie isoform of the human prion protein (PrP ^{Sc} , 253 residues) | [12] |
| Primary open-angle glaucoma | mutant myocilin olfactomedin-domain (mOLF, \sim 257 residues) | [13, 14] |

tions of protein solutions, *e.g.*, pH, temperature, or salt concentration, may easily lead to the aggregation of well-folded proteins. The structural study of a thermal-induced aggregate sample is presented in Chapter 3.

The disease-associated protein aggregates mainly refer to amyloids, which are the physiologic assembly of proteins into amyloid fibrils. The amyloid fibrils are defined based on several common features. First, their core structures are extremely stable and strongly resistant to degradation once formed [16]. It has been postulated that the generic amyloid conformation may be a universal, energetic minimum for aggregated proteins [17], and thus it is the likely endpoint of most aggregations. Second, the amyloid is specifically recognized by some fluorescent dyes, *e.g.*, Thioflavin T (ThT) [18] and Congo Red [19]. The dye binding provides an efficient way to detect the amyloid fibrils and measure the fibril growth (ThT assay) [20]. Third, in the amyloid core structure, the peptide backbones adopt β -strand conformations running perpendicular to the fibril axis, which results in cross- β architecture with versatility and remarkable stability [21]. The cross- β structures were first interpreted from X-ray fiber diffraction patterns in the 1960s [22], but the determination of atom-level amyloid structure takes half a century.

However, the amyloid formation processes of distinct amyloid diseases are completely

different. The amyloid-forming polypeptides (Table 1.1) range from short intrinsically disordered peptides (*e.g.*, A β) to large well-folded proteins (*e.g.*, mOLF). Additionally, the insoluble amyloid fibrils can be deposited intracellularly (*e.g.*, Lewy bodies formed by α -synuclein) or extracellularly (*e.g.*, amyloid plaques formed by A β).

It is important to note that the accumulation of oligomers of key proteins may be the culprit in some amyloid diseases, but the amyloid form is less harmful. The oligomers, which refer to small, soluble, and freely diffusible protein aggregates, are believed to initiate a series of events leading to neuronal or tissue death [23, 24].

1.1.1 Alzheimer's Disease and Amyloid- β Oligomers (A β Os)

AD and A β are undoubtedly the best-known and the most widely-studied amyloid disease and the affiliated amyloid protein. Therefore, the story between AD and A β is an excellent example showing the complexity, the challenges, and even the controversies in the research about amyloid diseases.

1.1.1.1 Alzheimer's Disease and the Possible Causes

Alzheimer's disease is an irreversible, progressive brain disorder that slowly destroys memory, thinking skills, and, eventually, the ability to carry out the simplest tasks [25]. The first case of Alzheimer's disease was reported in 1906 [3], and the efforts to understand it have never ceased in the past 100 years [26]. However, we still do not know the culprit that initiates the damage to neurons. There are some hypotheses of the molecular pathological pathways, but they are still under intense debate.

The most famous hypothesis is that the amyloid fibrils of A β launch the degeneration of neurons, namely the amyloid cascade hypothesis first expounded in 1992 [27–29]. There are two hallmarks in the brains of patients with Alzheimer's disease: one is the extracellularly amyloid plaques that mainly consist of A β amyloid, and the other one is the neurofibrillary tangles (NFT) made of aggregates of the hyperphosphorylated tau protein in the neurons

[3, 30]. The deposition of A β fibrils was reported to trigger the NFT formation and the following neurodegeneration [27, 31–33], hence the hypothesis of amyloid plaques as the culprit initiating AD pathologies. Many reports showed that highly aggregated A β fibrils, but not A β monomers, induce AD pathologies *in vitro* and *in vivo* [34–37]. Furthermore, recent preparations and structural studies of A β amyloid fibrils illuminate their capabilities of self-recognition, replication, and propagation [38–40], which are common features of pathogenic species like prions [41, 42]. Hence A β amyloid may behavior like prions to cause AD.

However, many concerns of the amyloid hypothesis cannot be neglected. First, the severity of cognitive deficits was found to correlate better with the soluble A β species rather than with the amount of amyloid plaque in the patient's brain [43, 44]. Second, abundant amyloid plaques were detected in healthy brains [45], and more importantly, this type of plaques is reported to link with much lower levels of oligomeric forms of A β [46]. Third, some previous clinical trials showed that removing the amyloid plaques in the brain will not stop or reverse the symptoms [47]. Last but not least, the A β O-selective antibodies were shown to protect cell models against the damage caused by exogenous A β O [48, 49], and to prevent AD-like pathology when administered to various Tg AD mice [50, 51].

With these concerns, the amyloid cascade hypothesis has been modified to include and emphasize the toxicity of smaller, soluble A β aggregates, which were collectively known as A β oligomers. The molecular weights of A β oligomers are ranging from 9 to above 200 kDa, which correspond to the assemblies from dimer to more than 50mer. The effects of oligomers have also been widely studied in mice models, for example, A β O may trigger a harmful cascade to damage neurons and synapses [52, 53], and the fibril-free A β O solutions are essential for memory loss [54]. In addition, many possible mechanisms of the cytotoxicity of A β O had been proposed. The A β O-related neuron death could be initiated by outer and mitochondrial membrane permeabilization [55–59], disruption of Na⁺ or Ca²⁺ regulation [60–62], and receptor-mediated apoptosis [63, 64]. Zott *et al.* [65] recently reported

that the circuit dysfunction in the early stage of AD started from A β dimers suppressing the glutamate reuptake of neurons. Because dimers are the earliest assemblies during aggregation, their effect may underlie the proposed pathological mechanisms. Currently, there is still no general consensus to explain the neurotoxicity of A β O_s. In our research (Chapter 4), we will focus on characterizing the structure of a specific A β O sample, and try to explain the cytotoxicity based on a novel oligomer structure.

For the treatment of AD, we got an encouraging news recently. On July 7th, 2021, U.S. Food and Drug Administration (FDA) granted accelerated approval for ADUHELM™ (aducanumab-avwa) as the first and only Alzheimer’s disease treatment to address the accumulation of amyloid plaques in the brain. Aducanumab, the active pharmaceutical ingredient (API) of ADUHELM™, is a human monoclonal antibody that targets aggregated A β , and it was shown to reduce the brain A β burden and slow the development of Dementia [66, 67]. Nevertheless, Aducanumab targets both amyloid plaques and oligomeric A β aggregates, and we still do not know whose clearance is more effective and more significant during the treatment. A point of view is that the engagement with senile plaques is likely off-target and useless, leading to the high dosage-requirement found in clinical trials [7].

Although some research reports showed the oligomeric A β aggregates are the toxic species that initiate AD, we cannot neglect that almost all potential drugs targeting A β have failed in clinical studies [68]. For the pathological mechanism, we only have a very limited understanding of the correlation between A β oligomers and distinct prion-like structures or strains implicated in the phenotypic diversity of AD. Moreover, the latest report, published on July 22nd, 2022, showed that scientific misconduct was found in some studies of an A β oligomer sample impairing the memory of mice [69]. This upsetting fabrication does not invalidate the whole oligomer hypothesis of AD, but it may cause a slump in the confidence of further oligomer studies. The fabricated results also imply the difficulties in extracting, purifying, and analyzing the brain-generated A β oligomer samples due to their transient and heterogeneous nature [68].

Furthermore, there are many other hypotheses about the onset of Alzheimer's disease [70, 71]. For example, some researches showed that phosphorylated tau protein can increase A β production [72, 73], and thus the abnormal tau protein could be the origin of Alzheimer's disease. Another latest study presented the evidence linking the activity of specific viruses (*i.e.*, human herpesvirus 6A and human herpesvirus 7) with AD [74].

1.1.1.2 A β Biogenesis and Aggregation

The assembly processes of A β peptides, which are widely studied but remain unclear, are briefly illustrated here to show the diversity and complexity of the aggregate species in patients' brains [75, 76]. It represents typical aggregation mechanisms of intrinsically disordered proteins (IDP) [77]. In general, the A β peptide is derived from the proteolytic cleavage of the transmembrane amyloid precursor protein (APP) by secretases, and then self-assembles into oligomeric aggregates or amyloid fibrils (Figure 1.1).

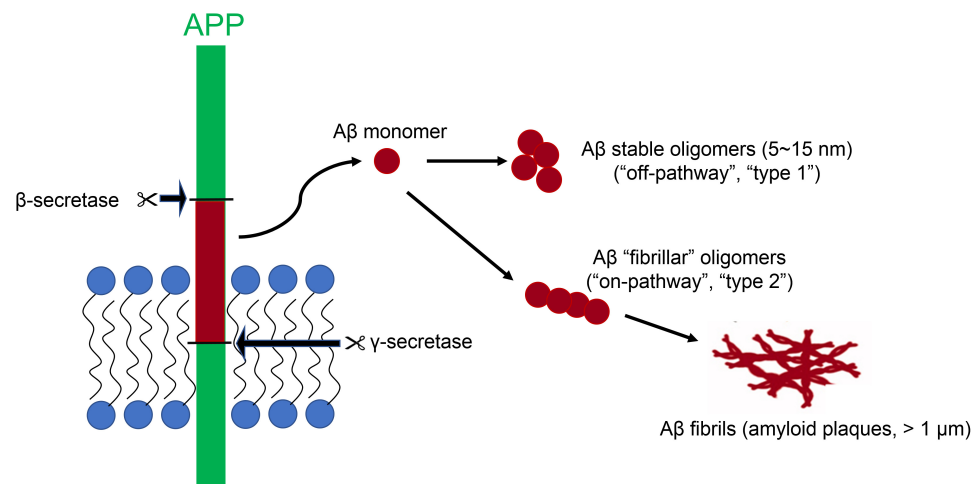


Figure 1.1 Schematic representation of the biogenesis and the aggregation of A β . APP: the transmembrane amyloid precursor protein.

APP is an integral membrane protein expressed in many tissues, especially in the synapses of neurons, which plays a central role in Alzheimer's disease (AD) pathogenesis. APP con-

sists of a single membrane-spanning domain, a large extracellular glycosylated N-terminus, and a shorter cytoplasmic C-terminus [78]. The rapid metabolization of APP leads to the A β peptides, with 38 to 43 amino acid residues, and other nonamyloidogenic peptides [79]. The A β generation (or the amyloidogenic pathway) involves initial cleavage of APP by β -secretase, right between residue M671 and D672, and following cleavage by γ -secretase, which lacks fidelity and results in a variety of A β peptide length [80]. It is worth noting that the A β peptides are created by γ -secretase cleavage in cholesterol-rich lipid raft domains, indicating the membrane environment plays a critical role in the assembly process [81, 82]. Also, β -secretase and γ -secretase inhibition have been the focus of AD drug discovery for slowing the amyloidogenic pathway [83].

A β monomer, referring to a single peptide molecule, is the building block of any A β oligomers or amyloid. The A β peptides have a number of amino acid sequences with various C-terminal ends. The two most abundant A β isoforms are the 40-residue peptide, namely A β (1-40), and the 42-residue form—A β (1-42). The amino acid sequence of A β (1-42) is DAEFR₅ HDSGY₁₀ EVHHQ₁₅ KLVFF₂₀ AEDVG₂₅ SNKGA₃₀ IIGLM₃₅ VGGVV₄₀ IA₄₂, while A β (1-40) does not have the last two residues. Their primary sequences share a common pattern: two hydrophobic patches, L17 A21 and A30 A42 (or V40), separated by a hydrophilic patch E22 G29. Despite the nearly identical primary structure except the two residues at the C-terminus, A β (1-40) and A β (1-42) self-assemble through totally distinct mechanisms with contrasting kinetics [84–87], form different amyloid structures [88, 89], and contribute to amyloid plaques at various phases [90, 91]. Regardless of the difference, the A β isoforms still share many aggregate and amyloid features (*e.g.*, cross- β architecture) and can co-assemble with each other under pathological conditions [92, 93]. Thus, we use A β to represent both A β (1-40) and A β (1-42) in our general discussions unless otherwise specified. An interesting fact is that A β monomers do not have a well-folded 3D structure in aqueous solution [94, 95], but they tend to form helical domains and reside on the micelle/membrane surface in micelle-water complex environment [96, 97]. That is why A β

peptides are classified as IDPs.

The next stage of assembly is A β oligomers, an ill-defined term in protein aggregate studies. An oligomer is an assembly composed of 50 A β peptides or fewer (masses ranges from 9 to 200 kDa), spanning the oligomeric aggregates in brain-detected and lab-synthesized samples [75, 98, 99]. They are the smallest assemblies (10 nm or less), appearing as roughly spherical nanoparticles when imaged by electron microscopy (EM) or atomic force microscopy (AFM) [57, 100, 101]. Although the oligomers extracted from AD patient brains are very heterogeneous, they can be roughly divided into two main classes, toxic and non-toxic A β O, based on simple aspects of their quaternary structure, molecular weight, and antibody reactivity, as well as their relationship to amyloid plaques. On the one hand, the toxic A β O species appear to be greater than 50 kDa [102–104], reactive with the anti-amyloid oligomer antibody A11, and unrelated to amyloid plaques [104]. On the other hand, the non-toxic A β O species appear to be less than 50 kDa [102–104], reactive with the anti-fibril antibody OC, and related to amyloid plaques temporally, spatially, and structurally [104]. These populations have also been referred to in the literature as “type 1” and “type 2”, respectively [7]. As the name suggested, lots of evidence supports a toxic role for the larger type 1 A β O but not for type 2 [105, 106]. A preponderance of data now supports the hypothesis that some A β O species are “on-pathway” to fibril formation, while others are “off-pathway”, which cannot directly grow into fibrils and may be the most toxic [107]. This on/off-pathway classification appears to correlate with the type 1 or 2 A β O classifications: data shows that toxic type 1 A β O are off-pathway, while non-toxic type 2 are on-pathway [108, 109]. It is very important to investigate the differences in the aggregation pathways of these two A β O structures, potentially leading to therapies that block the toxic aggregation mechanisms. Interestingly, the simulations indicate the differences in the pathways occur as early as the dimer stage [110].

Subsequent aggregation of on-pathway oligomers results in protofibrils and finally amyloid fibrils. Protofibrils are elongated assemblies with widths of 10 nm or less and lengths

on the order of 100 nm, corresponding to the assembly of hundreds of molecules [111]. They are usually regarded as metastable intermediates for the formation of mature fibrils [112]. Mature fibrils can be microns long, with dimensions consistent with organization of millions of A β monomers [113]. The amyloid fibrils are the final state of protein aggregation and the most abundant assembly form in AD patient brains: it could be the thermodynamically most stable structure of proteins [114, 115]. Furthermore, the kinetics models of the growth of A β amyloid have been established, involving both on- and off-pathway oligomer species, but little structural information was revealed [86, 87, 116, 117].

1.1.1.3 Structural Studies of A β Oligomers

Structural studies of A β oligomers did shed some light on the peptide conformation. In summary, the studies went well with synthesized small oligomers (up to hexamer, < 30 kDa), and be able to characterize the corresponding atomic structures (Figure 1.2). However, for large oligomers (> 50 kDa), no detailed structure has been experimentally determined to the best of my knowledge.

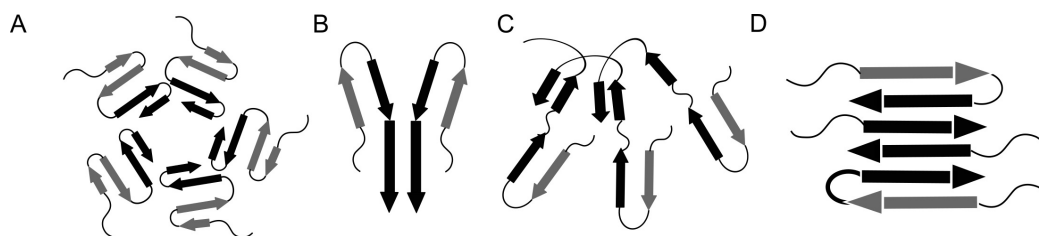


Figure 1.2 Structural studies of different A β O. (A) A β (1-42) disc shaped pentamers [101]. (B) Dimer conformation in preglobulomers [118]. (C) Protomer conformation in the hexamer barrel [119]. (D) Tetramer formed in a membrane mimicking environment [120].

Ahmed *et al.* [101] prepared homogeneous A β (1-42) oligomers under low-temperature and low-salt conditions. The study reports disc-shaped A β assemblies with average width of 10-15 nm and height of 1.5-2.5 nm. By combining the AFM and ssNMR data the authors introduced a molecular model (Figure 1.2A) with multiple β -strands separated by turns.

The pentamer model is a strange assembly structure because there are no intermolecular H-bonds, which usually play an important role in stabilizing the assembled particle.

Yu *et al.* [118] studied A β aggregates, called preglobulomers and globulomers [121], composed of both antiparallel and parallel β -sheets (Figure 1.2B). The globulomers are found to be off-pathway intermediate aggregates, and they exhibit high neurotoxicity [122, 123]. The researchers generated the oligomers from A β (M01-42) (an A β alloform containing an extra methionine in the N-terminus) with the help of sodium dodecyl sulfate (SDS) micelles. The globulomers appear as spherical particles with a mass of 64 kDa (diameter 4-5 nm) and incorporate 12 to 16 peptide units, while preglobulomer are tetramers with molecular mass of 16 kDa (diameter 1-2 nm). The authors determined the preglobulomer molecular structure by solution NMR and propose that it consists of a repeating peptide dimer unit. The dimer comprises a β -hairpin with antiparallel β -sheets and intermolecular in-register parallel β -sheet (Figure 1.2B).

Lendel *et al.* [119] performed structural analyses on the intermediate oligomers formed by A β (1-42)cc, an A β (1-42) double cysteine mutant in which the β -hairpin is stabilized by an intramolecular C21/C30 disulfide bond. The A β peptides adopt a β -hairpin conformation as expected. Furthermore, a third β -strand near the C-terminus contributes to intermolecular assemblies (Figure 1.2C). The quaternary structure of the oligomers was modeled with intermolecular ssNMR restraints. A hexamer barrel with a six-fold cylindrical symmetry was found to be consistent with the experimental data.

More recently, Ciudad and coworkers [120] prepared β -sheet pore-forming A β (1-42) oligomers (β PFOs) in a membrane mimicking environment and characterized the atomic structures. The β PFOs are stabilized in dodecylphosphocholine (DPC) micelles at pH 9.0. The minimum structural unit of the pore-forming oligomers are determined to be a tetramer comprising a six stranded β -sheet core (Figure 1.2D). By increasing the concentration of A β (1-42) in the sample, A β (1-42) octamers are also formed, made by two A β (1-42) tetramers facing each other forming a β -sandwich structure. We will discuss the tetramer structure in

detail in Section 4.4.

Parthasarathy *et al.* [124] characterized another highly toxic A β (1-42) oligomer entitled amylospheroid (ASPD, 128 kDa) [100, 107]. The amyloid intermediate represents a class of pathologically relevant spherical intermediates with diameter of 10-15 nm, which are derived from AD patients [125]. Their findings established that ASPD structure encompasses β -strand regions at L17-E22, A36-V36 and V39-I41, but no further alignment was revealed.

There is a special oligomer structure with non- β -strand conformation being reported. Shea *et al.* [126] found the peptide molecules in lag phase oligomer might adopt α -sheet secondary structure [127]. However, the structure was mainly characterized by comparing the microfluidic modulation spectroscopy data from the mixed A β aggregates and a model α -sheet peptide. They did not produce stable and purified oligomer samples.

1.1.2 Primary Open Angle Glaucoma and Myocilin

Glaucoma is a group of ocular diseases that cause irreversible damage of the optic nerve and eventually lead to blindness. Although it has already become the second leading cause of blindness in the world, the understanding of glaucoma is still deficient [128]. Consequently, the current management of glaucoma is mainly intraocular pressure-lowering eye drops, β -blockers, and trabeculectomy [129], none of which directly targets the underlying cause of the disease.

Primary open-angle glaucoma (POAG) is a subset of glaucoma and is the second leading cause of blindness in the United States [13]. The main clinical features of POAG are an open iridocorneal angle and cupping of the optic-nerve head, with corresponding loss of visual field. Research found that about 4% of cases of adult-onset POAG are associated with mutations in MYOC, which encodes the protein myocilin [130, 131]. Thus, it was established that myocilin was closely related to the cause of POAG [13, 132].

The initiation of POAG is hypothesized to be related to the amyloid formation of myocilin. The proposed basic pathogenic mechanism is initiated from the coaggregation of

mutant myocilin and the molecular chaperone Grp94 [133–135]. The cell debris caused by the cytotoxic aggregated myocilin will subsequently affect aqueous humor fluid outflow and homeostatic control of intraocular pressure, and eventually lead to glaucoma symptoms. The POAG-causing mutants of myocilin are primarily found in the olfactomedin domain (mOLF) [132], and the toxic aggregates of mOLF were characterized as amyloid [136, 137]. Thus, the POAG caused by mutant myocilin aggregation can hopefully be added to the family of amyloid diseases. Dr. Lieberman’s lab has made significant progress in the purification, structural characterization, and amyloid preparation of wild-type or mutant mOLF [136, 138–140]. They collaborate with Dr. Hall and our lab to continue the effort to illustrate the role of the mOLF amyloid in the pathological pathway.

In addition, the oligomeric aggregates of full-length myocilin have been observed recently [141]. TEM data showed the evidence of dimer, tetramer, and octamer states. Further tests on the pathological effects and the assembly structures are required to reveal the correlation between the oligomers and glaucoma.

1.2 Solid-State NMR and Its Application in Structural Studies

This section briefly introduces the evolution of NMR with an emphasis on several milestone techniques, which are the fundamentals of today’s NMR measuring and processing. One of the most important applications of NMR, especially solid-state NMR, is to study biomolecular structures (nucleic acids and proteins). The instruments and methods of ssNMR kept being developed and optimized to reveal higher structural resolution in the biomolecular samples. State-of-art ssNMR techniques are the main weapon in our lab to access the atomic structures in different forms of protein aggregates.

1.2.1 History of Solid-State NMR

Nuclear magnetic resonance (NMR) has now been flourishing for two-thirds of a century but is a field that has come from centuries of scientific development. In the 1920s signifi-

cant progress was made toward the discovery of NMR. Otto Stern (Nobel Prize, 1943) and Walter Gerlach found quantised angular momentum of molecular beams and measured the electron magnetic moment. Isidor Rabi (Nobel Prize, 1944) is credited with being the first person to observe nuclear magnetic resonance. He added a loop of wire to Stern’s technique, hence the generation of an radiofrequency field over the atomic beam. When tuned to the Larmor frequency of the nuclei, Rabi registered an absorption on his atomic-beam detector indicating the spins were flipping [142]. In 1946, Felix Bloch and Edward Purcell (shared Nobel Prize, 1952) expanded the technique for use on liquids and solids [143].

In the late 1940s and 1950s, when the techniques were unified under the moniker of NMR, much of the theoretical groundwork was prepared; interactions were discovered, NMR experiments for chemical characterization were developed and commercial companies were incorporated. For example, spin echo technique was developed by Erwin Hahn in 1950 [144] and is still widely used in magnetic resonance imaging (MRI) [145]. The stage was set for the revolutionary discoveries that made NMR spectroscopy the technique that we know today.

Andrew and Lowe took the first steps into the modern era, around 1958, by introducing magic angle spinning (MAS) [146]. Rotating the sample at a certain angle (54.74°) to the static magnetic field removed the dipolar broadening and enhanced resolution. This paved the way for solids to be as accessible to NMR as liquids. The basic idea of suspending and spinning a rotor using compressed air is central to solid-state NMR today.

Around this time, Lowe and Norberg were the first to Fourier transform the resulting NMR signal after an RF pulse [147]. However, it was Ernst (Nobel Prize, 1991) and Anderson that provided a full treatment of the Fourier transform method and realized the dramatic implications for sensitivity enhancement [148].

Homonuclear correlation experiments can arguably trace their beginnings back to one of the first 2D NMR experiments invented—a three-pulse sequence by Jeener *et al.* that is popularly known in the solution-state NMR as NOESY [149]. The sequence marked the

birth of exchange spectroscopy. At first, two-dimensional experiments of the time had a complex problem regarding the shape of crosspeaks, which reduced the resolution of the spectrum. The pioneering work of States, Haberkorn and Ruben [150] targeted this issue in the early 1980s. Shortly, pure-absorption-mode exchange spectra was developed, heralding the new age of quantitative exchange spectroscopy [151].

A milestone in ssNMR development is the Cross Polarization with Magic Angle Spinning technique (CP-MAS). Pines *et al.* [152] and Schaefer *et al.* [153] observed highly resolved ^{13}C NMR spectra obtained from solid specimens using magic angle spinning in combination with cross polarization double-resonance methods. It became the basis of modern ssNMR techniques. In addition, many important pulse sequences were invented in 1980s and are still frequently used in today's NMR labs, such as Rotational-Echo Double-Resonance (REDOR) [154] and Rotational Resonance (R^2) [155].

1.2.2 Applications of Solid-State NMR in Biomolecular Structural Studies

Structural information always constitutes fundamental knowledge in molecular biology. Researchers have developed many different tools to investigate the atom-level details in proteins, nucleic acids, and their complexes. NMR is handy in revealing the inter-nuclear spatial distances, hence a widely used tool for protein structural determination. In 1984, the first *de novo* structure of a protein was solved by solution NMR by the group of Kurt Wüthrich [156].

It is necessary to develop similar techniques in ssNMR because it allows access to samples not approachable by other techniques, *e.g.*, amyloids and membrane protein. However, for ssNMR, the complexity caused by the additional anisotropic interactions made its development for solving protein structures slower than that of solution NMR.

The entry of ssNMR analyses in protein structural studies is the application of dipolar recoupling experiments to reveal the intermolecular alignments of amyloid samples. In 1998, Benzinger, Gregory, and coworkers [157, 158] used the double-quantum dipolar recoupling

with a windowless sequence (DQ-DRAWS) technique to demonstrate the in-register parallel β -sheet structure in A β amyloid. It ended the debate on the β -strand alignment in the cross- β structure of amyloid samples [159, 160] and provided the basis for future amyloid structural determination.

Assignable high-resolution spectra of proteins were only obtained around the year 2000 [161], following progress in magnetic-field strength, decoupling and recoupling pulse sequences, and sample preparation techniques to solve, in 2002, the first high-resolution structures of a peptide [162] and a protein [163] by ssNMR. In 2005, short ^1H - ^1H distances were measured (via ^{13}C - ^{13}C 2D spectra) for a 38-residue U- ^{13}C , ^{15}N -labeled protein, kalitoxin, and by combining these restraints with dihedral angles predicted from the chemical shifts, its 3D structure was solved [164]. In the same year, the structure of human microcrystalline ubiquitin was also solved by using unambiguous distance restraints from ^{13}C - ^{13}C 2D spectra with DARR mixing on uniformly ^{13}C -labeled samples [165]. These structures were based on the determination of unambiguous distance restraints, resulting from the reintroduction of the dipolar couplings through rotor-synchronized radio frequency pulses, and on the use of simulated annealing programs for the structure calculations [166]. From 2002 to 2008, Robert Tycko's lab applied these ssNMR techniques and molecular dynamic simulations into the characterization of A β (1-40) amyloid fibrils [88, 167–169], and they successfully identified the structural basis for amyloid polymorphism [38]. Dr. Paravastu established our methodology based on his work in Tycko's lab.

Currently, thanks to the development of new pulsed experiments with stronger NMR signal and higher resolution, NMR researchers are able to determine the atomic structures of many different protein amyloids, such as HET-s(218-289) [170], human α -synuclein [171], and A β (1-42) [89, 172]. More recently, with the advances in electron detectors and image analyzing software, cryo-EM gradually becomes a mainstream technique for determining amyloid structures [173–175]. Although cryo-EM is usually more efficient and reveals higher structural resolution than ssNMR, ssNMR experiments can help verify the derived

structures [176] and determine the unclear structural segments [177].

1.3 The Motivation to Study The Structures of Protein Aggregates

First of all, we hope the structural information of protein aggregates can shed light on possible biomolecular interactions and cytotoxic mechanisms. A consensus among structural biologists is that the protein's folding structure is always related to its biological functions, and we assume a similar relationship applies to the aggregated species. Thus, obtaining the structural features in specific disease-associated protein assemblies may explain the proposed "gain-of-toxicity" effects of the protein aggregates [178]. For instance, in the structural study of A β (1-42) 150kDa oligomers, we built a structural model of the oligomer with a central pore (Chapter 4). When the pore-forming oligomers insert into the neuron membrane, they can cause the formation of ion channel pores that disrupt intracellular Ca²⁺ homeostasis [59]. Moreover, the stability and the size limitation of toxic oligomers help the species accumulate in the patient's brain. Our oligomer structural model can also explain the stability of these oligomer family.

Second, the characterization of different forms of aggregates may lead to a thorough understanding of the molecular mechanism in protein assemblies. The aggregation processes of proteins are extremely complicated, like the aggregation of A β (Figure 1.1). The processes usually involve many species of aggregates with different sizes and conformations, and many aggregating intermediates are transient and unstable [179]. Thus, it is challenging to directly observe the transformation during the assembly. We developed two strategies to access the molecular conformation of the aggregating intermediates. One method is to link the protein aggregating intermediate to the folding intermediate, which can be studied by many other techniques (*e.g.*, solution-state NMR). In our characterization of FGF-1 aggregates, we successfully connected the folding and the aggregating intermediates by identifying the well-structured regions in both the partially folded state and the aggregated state (Chapter 3). The other method is to stabilize the intermediate structures. For example,

Ciudad *et al.* produced a stable tetramer of A β [120], and we showed the tetramer is very similar to an intermediate oligomer (namely 2-4mer) in our preparation. We were able to deduce the oligomeric assembly pathway using the structural information of the tetramer (Chapter 4).

Third, we want to develop an efficient and automated strategy of ssNMR structural study that can be applied to different forms of protein aggregates, including oligomers and amyloids. To achieve this goal, we first needed a workflow that can be automated. Then, we build a database containing diverse peptide or proteins capable of forming aggregates and their structural arrangements. The database can serve as a source of hypothetical structures. In Chapter 2, I introduce the workflow of structural studies in our lab. Our research strategy involves many iterations of ssNMR measurements and molecular modeling. I tried to automate the procedure by introducing a visualized consistency check between the structural modeling and the NMR constraints (Section 2.4.2). The entire workflow is validated and optimized in specific structural studies. As for the structural data collection, our lab continues to characterize the different molecular arrangements in short peptide assemblies. In the study of P1 peptide amyloid—a short peptide derived from glaucoma-associated myocilin protein, a special U-shaped antiparallel amyloid structure was determined (Chapter 5), which expands our understanding of amyloid structures of small peptide.

Ultimately, the revelations of aggregate structures, the knowledge of assembly pathways, and the development of quick structural analyses help us develop new therapies for amyloid diseases. With the structural information, structure-based drug discovery [180] can be performed to find candidate molecules to clean up specific aggregate forms or even block certain assembly pathways (Section 4.5.3). Moreover, the automatic NMR methods can be used to design early-diagnostic tools, which are essential for the treatment of amyloid diseases [181].

CHAPTER 2

MATERIALS AND METHODS

In this chapter, I will introduce the general strategy used in our lab to study protein aggregate structure, which includes the work of building atomic structural models, preparing samples in correct forms for ssNMR, performing designed ssNMR experiments, and analyzing NMR data to generate structural constraints.

2.1 The Strategy of Solid-State NMR Structural Study

Figure 2.1 shows the basic steps to resolve an unknown protein aggregate structure using ssNMR techniques. Although the diagram looks simple, a comprehensive structural study usually requires many rounds of the “modeling-synthesizing-measuring-analyzing” loops. In addition, some other analytical methods, providing complementary information to NMR structural constraints, are necessary for full-structure characterization. For example, Transmission electron microscopy (TEM) helps to reveal the dimensions of fibrils [182, 183], scanning tunneling electron microscopy (STEM) measures the mass per unit length of assemblies [89], and small-angle X-ray scattering (SAXS) characterizes the sizes and shapes of oligomeric aggregates [184]. Some new techniques from our collaborators greatly facilitate our structural studies, *e.g.*, the low-resolution cryogenic electron microscopy (cryo-EM) data disclosed the symmetry of subunits in the structure of 150kDa A β (1-42) oligomer (see Section 4.4).

The first step is to build one or more hypothetical structural models to guide the design of isotope labeling schemes and the choices of ssNMR techniques. The initial hypothesized model does not have to be a detailed full-structure model, which is very difficult to establish without experimental data. Our lab usually starts with some possible arrangements of short

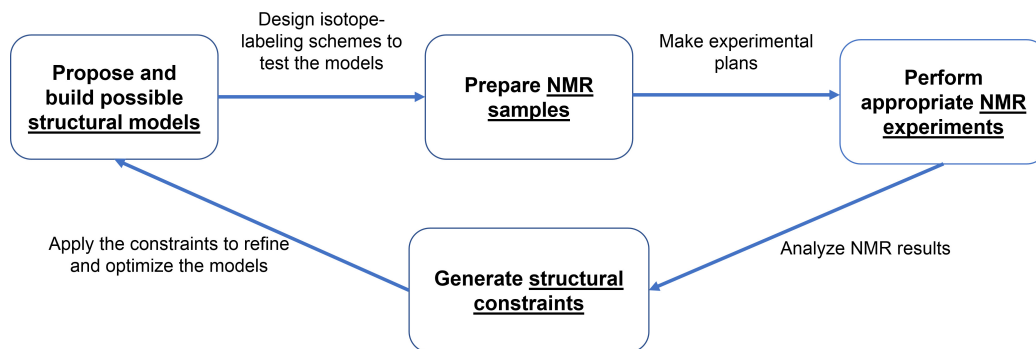


Figure 2.1 The strategy of ssNMR structural studies.

segments or regions, predicted by software, molecular dynamic modeling, preliminary tests, and similar samples that have been studied. The hypotheses always play a crucial role in the process because they determine whether the following NMR experiments could effectively generate useful information, usually called NMR structural constraints. When the initial hypothesis is very close to the correct structure, it can be verified by one or two simple spectra [185, 186]; but when the hypothesis is misleading, it takes so much effort to be corrected (see Section 4.4).

Second, we synthesize the isotope-labeled peptides or proteins according to our experiment plan. The isotope labeling scheme we usually use is called selectively labeling—the ^{13}C or ^{15}N nuclei are placed at specific residues on the peptide. Another widely used labeling method in bio-synthesis is uniformly labeling, which literally means all the C or N atoms are replaced by NMR active isotopes. Then, the soluble peptides or proteins assemble into the right form of aggregates under special treatment, and the aggregate samples will be packed into rotors ready for the ssNMR test.

Third, perform all the necessary ssNMR experiments on the samples. As sample preparation can be expensive and time consuming, it is desirable to obtain maximal structural information from each isotopically labeled sample. Thus, the data collection require days or even weeks to overcome the weak-signal-to-noise nature of ssNMR. Moreover, the quality of NMR data also depends on the strength of magnetic field, the amount and the structural

features of samples, and the specific pulse sequence used in each measurement.

Finally, we need to analyze the experimental results, *i.e.*, NMR spectra, to extract structural constraints to guide molecular modeling. The modeling processes relying on NMR data were well developed in solution-state NMR [187, 188] but were still under improvement in ssNMR studies [189] because the structural information provided by ssNMR experiments is relatively limited. When an optimized structural model is generated based on the latest NMR constraints, it will serve as a new hypothesis for the next round of characterization.

2.2 NMR Sample Preparation

Our research samples included thermally-aggregated FGF-1, Amyloid- β (1-42) 150kDa oligomers, P1 amyloid fibrils, and disordered P3 amyloids. The typical procedure for preparing these samples are: First, isotope-labeled peptides are purchased or synthesized; Second, our collaborators help us to produce the right aggregate forms we want to study; Finally, we pack the aggregates into NMR rotors and make them ready for solid-state NMR experiments.

2.2.1 Solid-Phase Peptide Synthesis and Protein Expression

Solid-phase peptide synthesis (SPPS) is the ideal method to produce short peptides (usually less than 50 amino acids) [190–192] with isotope labels at specific sites. The first step in SPPS is to couple the C-terminal amino acid of a peptide with a solid phase (resin). What follows is a series of coupling reactions to elongate the solid-attached peptide sequence from C-terminus to N-terminus. The coupling reactions in solid-phase synthesis are usually rapid and close to completion because of using excess activated amino acid derivatives. The extra reactants can be removed by washing the solid-phase after every coupling reaction. When we finally get the desired amino acid sequence, the peptide is cleaved from the solid phase and then purified (Figure 2.2). Because the whole process is automated in peptide

synthesizer and the synthesizing sequences can be easily controlled by computer, SPPS is able to prepare a large amount of peptides with different isotope-labeled sites, which meets the requirement of solid-state NMR samples.

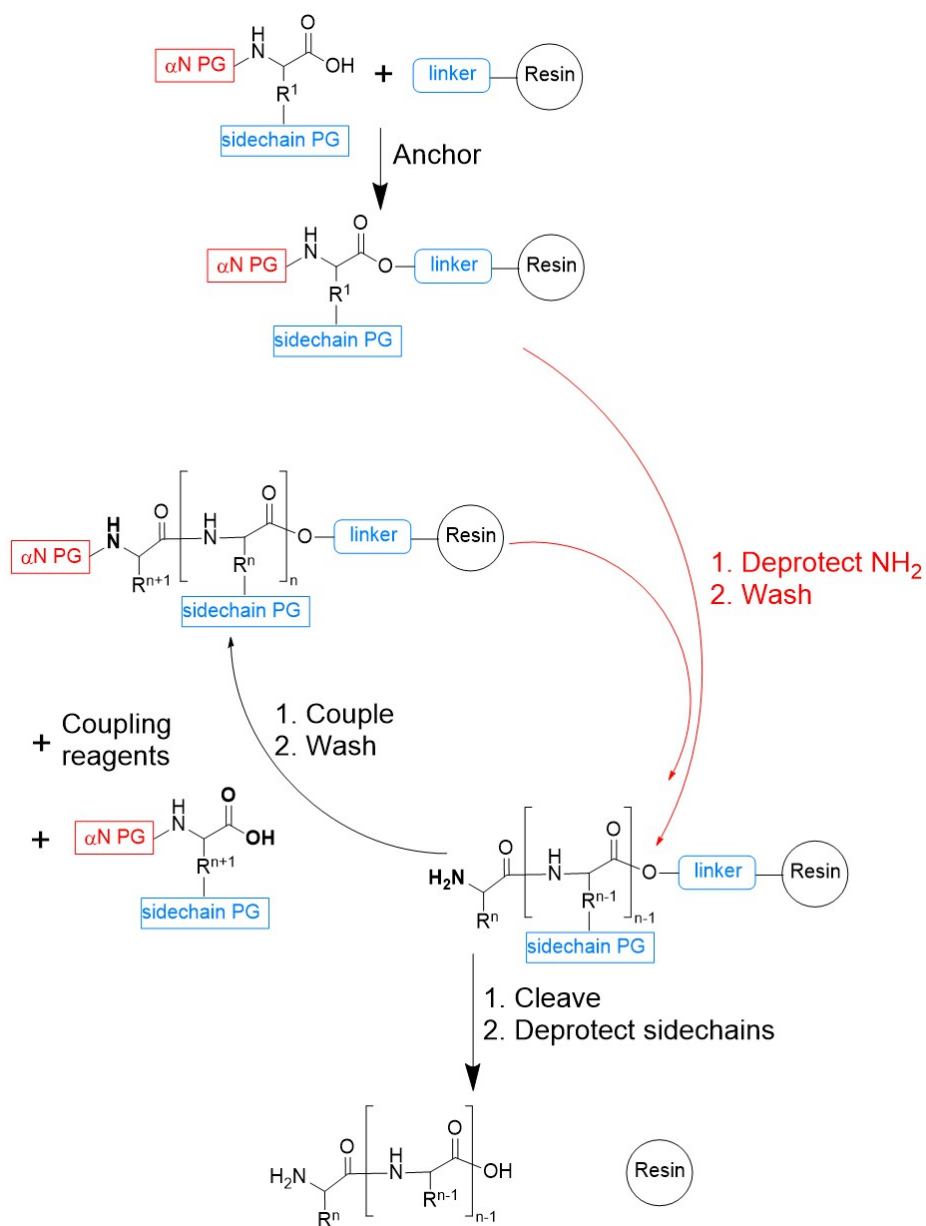


Figure 2.2 General procedure of SPPS. PG: protecting group.

Our lab used to purchase synthesized short peptides from commercial peptide synthe-

sizing companies. All the P1 and P3 short peptides, with or without isotope labels, were synthesized by CPC Scientific (Sunnyvale, CA). Our lab had also purchased labeled and unlabeled A β (1-42) peptides from New England Peptide (Gardner, MA) and by the Proteomics Core at the Mayo Clinic (Rochester, MN).

Our lab bought a Liberty Blue peptide synthesizer to synthesize A β (1-42) peptide, which is the same type of synthesizer as those in New England Peptide and Mayo Clinic. Although many research groups use synthetic A β peptides, solid-phase syntheses of the 42-residue sequence are still challenging due to the peptide's high propensity to aggregate both on resin and in solution [193]. Moreover, SPPS may generate peptides with wrong chiral centers on the backbone due to epimerization side reactions, which can lead to inhomogeneous molecular conformations in amyloid samples [89]. Liberty Blue peptide synthesizer applied microwave-assisted reactions to avoid aggregation on resins and to minimize many side reactions [194]. With the recommended protocol from CEM Corporation [195], the manufacturer of the peptide synthesizer, our lab can produce non-aggregated A β (1-42) peptide with good yield and purity.

For aggregates of large proteins, we used recombinant proteins produced by *Escherichia coli* (*E. coli*) expression system. To prepare NMR samples with uniform ^{13}C and ^{15}N isotopic labeling, the expression media was made from ^{13}C -labeled glucose as a carbon source and ^{15}N -labeled ammonium chloride as a nitrogen source. The expression and purification of recombinant proteins were all completed by our collaborators—Liam Longo, Connie Tenorio, and Emily Saccuzzo.

2.2.2 Preparing Aggregates of Peptides

Preparing the correct aggregated forms of peptides is the crucial step in our structural study. The aggregation of different peptides or proteins requires distinct conditions. For instance, the formation of A β globulomers requires 18-hour incubation at 37°C in phosphate-buffered saline (PBS) (pH 7.4) with 0.2% sodium dodecyl sulfate (SDS) [121]; while the amyloid

assembly of HET-s(218-289) prion is happening immediately at 25°C in pH 7.5 [196]. More importantly, a single sequence of peptide could produce a variety of aggregate structures under different incubating conditions, like peptide concentration [168], pH [197, 198], ionic strength [137, 199], and seeding effect [200].

The following research chapters describe specific procedures for preparing different aggregate samples.

2.2.3 Packing Samples into NMR Rotors

The classic rotor packing is very straightforward. The peptide aggregates are first converted into states that are easy to handle: insoluble aggregates such as amyloid fibrils are centrifuged to pellets, while soluble aggregates are lyophilized to powders. The pellets or powders are then moved into an NMR rotor manually. However, these steps may introduce undesired heterogeneous structures into samples. For the aggregate powders, freeze and lyophilization may give rise to the change of molecular conformations due to low temperature, freeze-concentration, and ice formation [201]. For the pellets, the final packing step may cause inhomogeneous hydration in the sample, which strongly affects the linewidths of NMR signals [169]. In addition, manually packing samples into the small rotors with 2.5–3.2 mm outer diameter is time-consuming, so it is not compatible with samples that are unstable at room temperature.

To prepare homogeneous samples for structural studies, many labs tried to avoid lyophilizing and developed ultracentrifugal packing tools for solid-state NMR rotors [202]. In these tools, peptide aggregates are quickly centrifuged into NMR rotors from solutions, resulting in a sample with uniform hydration. Evan Roberts had designed a small widget for ultracentrifugal rotor packing in our lab (Figure 2.3). We saw a significant improvement in spectra quality when using the new packing method [203]. Besides, because ultracentrifugation is typically conducted at low temperatures, some unstable samples, such as A β oligomers, can also be packed in this way for better spectra resolution (see Section 4.4).

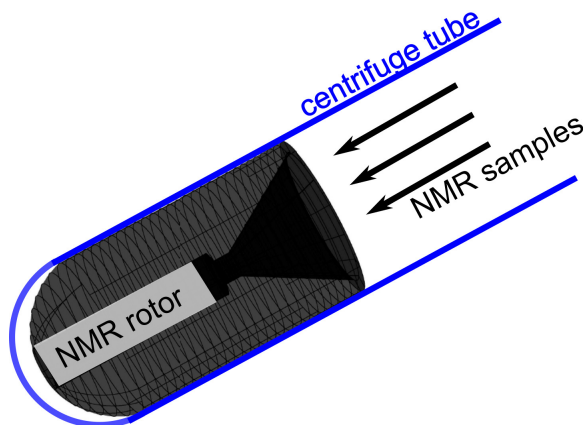


Figure 2.3 Use the ultracentrifugal packing widget to put samples into an NMR rotor. The widget (black) is placed at the bottom of a centrifuge tube, and the tube is filled by the solution or suspension of peptide aggregates.

2.3 Solid-State NMR Techniques and Experiments

2.3.1 Overview of Solid-State NMR Techniques

In general, we apply two types of ssNMR techniques on the samples. One of them is dipolar recoupling experiment, measuring NMR signal evolution under dipolar coupling of labeled nuclei; the other one is multidimensional NMR spectra experiments, revealing the spectrum-dependent correlations between labeled atoms. They can provide different aspects and scales of structural information.

The dipolar recoupling measurements are developed based on the fundamental differences between solid samples and solution samples: dipolar coupling is the dominant means of magnetization transfer in the solid state, but is averaged out by the reorientation of the molecules in solution. By elaborate pulse sequences, specific dipolar couplings are reintroduced to lead to time-dependent NMR signal evolution, which is sensitive to the types, properties, and relative positions of the coupled nuclei. We can use simulations to predict the NMR signal for isotope nuclei in specific coordinates under certain pulse sequences, namely spin simulations [204, 205]. The simulation results can be directly compared to the experimental data to see whether the simulated nuclei system is consistent with the atom

coordinates in the structure. A list of commonly used dipolar recoupling techniques and their measuring objects is in Table 2.1. Some example data and simulations are shown in Section 2.3.2.2 and 2.3.2.3 to illustrate the determination of 3D geometry of nuclei.

Table 2.1 A list of commonly used dipolar recoupling experiments.

| NMR Experiment | NMR Observables | Structural Constraints | Ref. |
|--|---|---|-------|
| PITHIRDS-CT | ^{13}C - ^{13}C dipolar couplings (identical chemical shift) <0.7 nm | inter-molecular backbone distance; backbone torsion angles | [206] |
| Rotational-Echo Double-Resonance (REDOR) | ^{15}N - ^{13}C dipolar couplings <0.7 nm (or other heteronuclear dipolar couplings) | the distance between ^{15}N and ^{13}C | [154] |
| Frequency-selective REDOR (fsREDOR) | ^{15}N - ^{13}C dipolar couplings <0.5 nm | the distance between sidechain ^{15}N and ^{13}C ; salt bridge | [207] |
| Rotational Resonance (R^2) | ^{13}C - ^{13}C dipolar couplings (distinct chemical shifts) <0.7 nm | the distance between two different ^{13}C s (<i>e.g.</i> ^{13}CO and $^{13}\text{C}\alpha$) | [155] |

The multidimensional experiments (Table 2.2) in ssNMR look very similar to the classical solution-state NMR methods: both of them generate a correlation map with detected signals, called crosspeaks, indicating the pulse-dependent correlation between the nuclei corresponding to different dimensions. However, the commercially available ssNMR instruments, unlike solution NMR, do not support well-resolved ^1H detection. Thus, the ssNMR samples must have ^{13}C or ^{15}N isotope labels for multidimensional detection, and the final spectra have much sparser crosspeaks than proton spectra, leading to limited structural information from one experiment. In addition, fully resolving signals in ^{15}N dimension requires strong magnetic field (> 600 MHz ^1H Larmor frequency), which we cannot use very often, so our lab focused on ^{13}C - ^{13}C 2D experiments.

Different types of multidimensional experiments aim for diverse parts of structural constraints (Table 2.2). The start point in NMR spectra analysis is always to assign the chemical

Table 2.2 A list of commonly used multidimensional experiments in ssNMR for biological samples.

| NMR Experiment | Detectable Correlation | Purpose | Ref. |
|--|---|--|-------|
| Finite Pulse Radiofrequency Driven Recoupling (2D-fpRFDR) | ^{13}C - ^{13}C one bond correlation | Chemical shifts assignment for ^{13}C -labeled residues | [208] |
| Dipolar-assisted Rotational Resonance (2D-DARR) | ^{13}C - ^{13}C spatial correlation (mixing-time dependent, up to 0.6 nm) | Provide inter-residue, inter-strand and intermolecular distance constraints | [209] |
| Proton Assisted Recoupling (2D-PAR) Proton Assisted Insensitive Nuclei Cross Polarization (2D-PAIN-CP) | ^{13}C - ^{13}C long distance correlations ^{15}N - ^{13}C long distance correlations (mixing-time dependent, up to 0.9 nm) | Provide inter-residue, inter-strand and intermolecular distance constraints | [210] |
| 2D-CHHC | $^1\text{H}\alpha$ - $^1\text{H}\alpha$ spatial correlation (< 0.3 nm) | Specifically detecting the $\text{H}\alpha$ - $\text{H}\alpha$ correlations in antiparallel β -sheet | [211] |
| 2D-NCA 3D-NCACX | ^{15}N - $^{13}\text{C}\alpha$ one bond correlation $^{13}\text{C}(\text{sidechain})$ - $^{13}\text{C}\alpha$ intra-residue correlation | Fingerprint spectrum; Chemical shifts assignment for uniformly ^{13}C , ^{15}N - labeled samples | [212] |
| 2D-NCO 3D-NCOCX | $^{15}\text{N}(\text{i})$ - $^{13}\text{CO}(\text{i}-1)$ one bond correlation $^{13}\text{C}(\text{sidechain})$ - $^{13}\text{CO}(\text{i}-1)$ intra-residue correlation | Chemical shifts assignment for uniformly ^{13}C , ^{15}N - labeled samples | [212] |

shifts of observable nuclei, *i.e.*, labeled ^{13}C and ^{15}N . We often use 2D fpRFDR and short mixing 2D DARR to assign the crosspeaks to the pairs of ^{13}C atoms, which work perfectly in selectively labeled samples (examples in Section 2.3.2.4). While some “backbone walking” methods, *e.g.*, 3D NCACX and 3D NCOCX, are often applied in uniformly labeled samples. The chemical shift values and the crosspeak linewidths, extracted from the assignment, not only help identifying atoms on different residues, but also facilitate predicting the secondary structure regions in the full peptide or protein. The further step of structural ana-

lyzing is to generate distance constraints between atoms (or residues) based on the detected crosspeaks on spatial-correlated multidimensional spectra. More details about the distance constraints and the application of constraints in modeling work are included in Section 2.3.2.5 and 2.4.1.

2.3.2 The NMR Experiments and Simulations in Our Structural Studies

I will briefly introduce each technique and explain how the data is interpreted. For detailed instructions on setting up and running the experiments, check out the book chapter summarizing our experimental methods [213]. The method sections in the following chapters list the experimental-specific power level of decoupling, length of mixing time, and other important parameters.

2.3.2.1 Cross Polarization Magic-angle Spinning (CP-MAS)

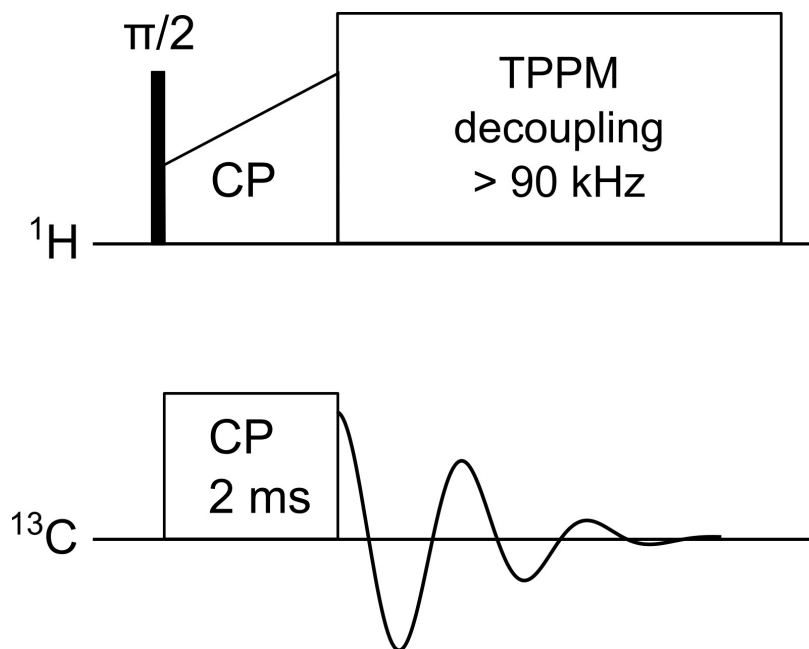


Figure 2.4 The pulse sequence of ^1H - ^{13}C CP-MAS experiment. Black block: $\pi/2$ pulse. Two pulse phase modulation (TPPM) is used in the decoupling pulses [214].

Cross Polarization Magic-angle Spinning (CP-MAS) experiment [215, 216] implements the two milestone techniques for ssNMR: magic-angle spinning (MAS) and cross polarization (CP). MAS refers to sample rotation about an angle $\theta = \cos^{-1} \frac{1}{\sqrt{3}} \approx 54.7^\circ$ relative to the static magnetic field \vec{B}_0 [146]. Typical MAS spin rate range from 5 to 67 kHz, depending on the rotor dimensions, rotor materials, and NMR probe capability. MAS technique was invented to partially eliminate nuclear dipolar interactions and chemical shift anisotropy (CSA) in solid-state samples so that they generate narrow and distinguishable NMR signals. In regard of CP, it is a technique in which the polarization of one type of nucleus is transferred to another type of nucleus by applying simultaneous pulses on the corresponding NMR channels [152]. The most commonly used CP is the ^1H -X CP (Figure 2.4), transferring polarized magnetic momentum from proton to other nuclei (*e.g.*, ^{13}C or ^{15}N) [217]. It is implemented in many ssNMR pulse sequences to enhance the signal from insensitive nuclei and avoid long relaxation time. The CP between nuclei is also used to detect the correlations in multidimensional spectra, such as 2D-NCA [218].

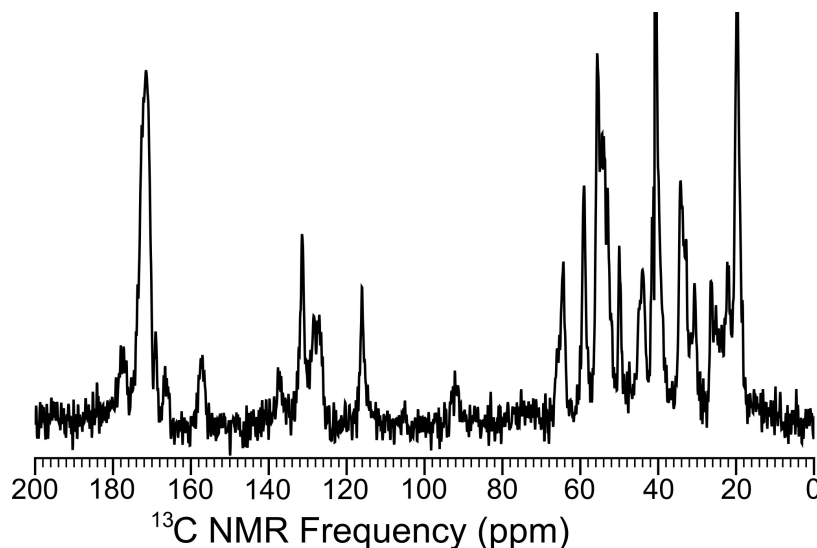


Figure 2.5 The ^{13}C CPMAS spectrum of P1 amyloid (see Chapter 5). The 1D ^{13}C CPMAS spectrum of P1 amyloid shows sharp linewidths. It indicates a well-ordered structure that can be characterized by ssNMR.

Thus, CP-MAS experiments usually generate signal-enhanced and peak-narrowed 1D spectra of the chosen nucleus, like ^{13}C . We can use ^{13}C CPMAS spectra to estimate the order of structures in peptide aggregate samples (Figure 2.5, which is further explained in Section 5.2) and check the stability of samples. Because CPMAS measurement can acquire enough signal on the samples without isotope labels, it is our choice for preliminary test of new aggregate samples. However, although it is a cheap and efficient test, CPMAS provides very limited information about the sample. The 1D CPMAS does not contain any correlated signal between atoms, and the peaks on it are too crowded to be identified (for most peptide samples). Moreover, the original CPMAS is not a quantitative NMR method, denoting that the peak integration in the spectrum is not proportional to the numbers of nuclei in the respective chemical sites. Some quantitative CPMAS methods were designed to overcome this disadvantage [219–221].

2.3.2.2 *PITHIRDS-CT*

PITHIRDS-CT [206] is a constant-time homonuclear dipolar recoupling technique that has been used to probe 3D arrangements of ^{13}C or ^{15}N atoms in selectively labeled samples. The name PITHIRDS is not an acronym and it represents the π (PI) pulse that lasts one THIRD of rotor period during the dipolar recoupling time (Figure 2.6). Additionally, the pulse program applied a constant-time (CT) combination of predefined rotor-synchronized pulse patterns to ensure a constant measuring time (illustrated in Figure 2.6). The PITHIRDS-CT technique, in particular, only measures signals from the nuclei with similar or identical chemical shifts. For the experiments on ^{13}C , samples are usually labeled selectively at carbonyl (CO) or methyl sites because of their special chemical shifts. It is worth noting that natural abundance ^{13}C signals always contribute to the experimental PITHIRDS-CT data. Thus, the original PITHIRDS-CT data must be corrected before comparing to the simulated curves, namely natural abundance correction [222].

Just like other dipolar recoupling techniques, the PITHIRDS-CT data should be overlaid

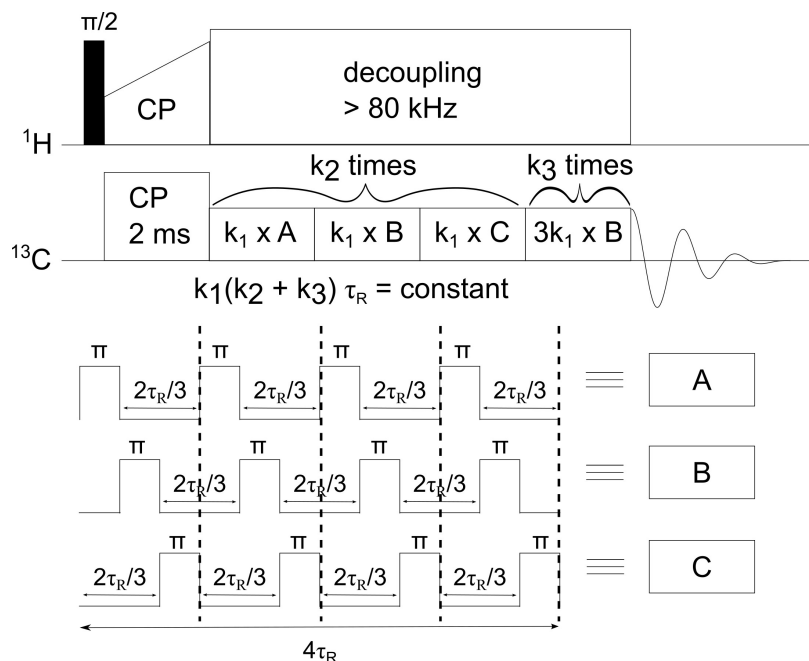


Figure 2.6 The pulse sequence of ^{13}C PITHIRDS-CT. A, B, and C are three different rotor-synchronized pulse patterns. Black block: $\pi/2$ pulse. τ_R : rotor period. k_1 , k_2 , and k_3 are positive integers. Specific combinations of k_1 , k_2 , and k_3 are used to ensure a constant experimental time.

with simulated NMR signals to reveal structural information (Figure 2.7A). As an example, the PITHIRDS-CT experiment is particularly useful for identifying in-register parallel β -sheets. In such a molecular configuration, equivalent backbone sites on adjacent molecules are arranged within 0.5 nm of one another (Figure 2.7B). Hence, a linear array of eight ^{13}C spins separated by constant distance is used to generate the simulated curves (Figure 2.7C). Apparently, the simulated curves of 0.5 nm inter-nucleus distance fit best with the CO and the methyl data, verifying the in-register parallel β -sheet structure. PITHIRDS-CT technique can also be used to measure backbone torsion angles, if the two adjacent $\text{C}\alpha$ are both labeled with ^{13}C [223].

2.3.2.3 Rotational Resonance Width (R^2W)

R^2W [224, 225] is a variant method of classic rotational resonance (R^2) [155, 226], which reintroduces the homonuclear dipolar couplings between the two selectively-labeled nuclei

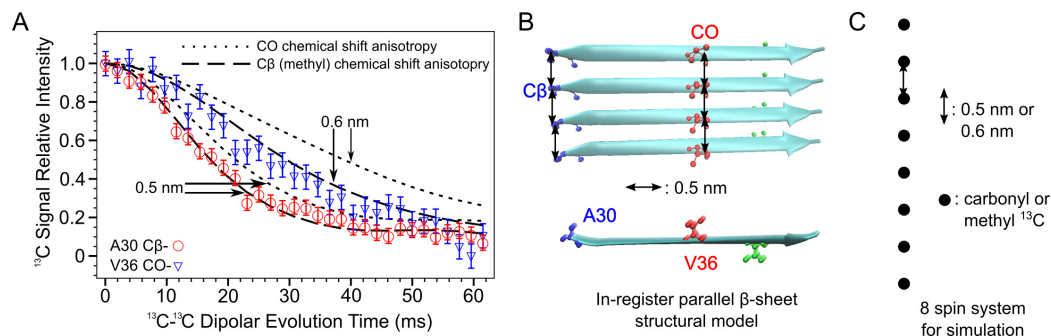


Figure 2.7 An example of ^{13}C PITHIRDS-CT data set and spin simulation. (A) PITHIRDS-CT measures the loss of NMR peak intensity as a function of dipolar recoupling time to reveal the geometry of spin system. Symbols represent the experimental data points, and the lines are simulated curves based on linear spin system in panel C. (B) In-register parallel β -sheet structure in A β amyloid. The double-head arrows label the inter-strand distances between the ^{13}C sites. (C) The linear eight-spin system represents the ^{13}C -labeled sites in parallel β -sheet. The simulations of this system generate the signal evolution curves in panel A.

when the MAS rotational frequency matches a R^2 condition, $\Delta\omega_{nuc} = n \times \omega_{MAS}$, where $\Delta\omega_{nuc}$ denotes the resonance frequency difference between the two spins. The total signal evolution is determined by the distance between the two spins, the CSA parameters of each spin and the zero-quantum relaxation time ($T_{2,zq}$) of the system [226]—the three necessary inputs for R^2 simulation. Unfortunately, although the CSA parameters are easy to measure for each nucleus, the $T_{2,zq}$ is very hard to calculate or estimate in practical samples. Even worse, the broad NMR peaks (linewidth > 100 Hz) from protein aggregate samples make it difficult to find the exact R^2 condition.

To overcome these limitations, Costa *et al.* designed the R^2W strategy [224] (Figure 2.8), in which they assessed the dephasing of ^{13}C NMR signal intensity when the MAS rate (ω_{MAS}) is varying near the difference of NMR peak frequency between the two labeled sites ($\omega_{MAS} = \Delta\omega_{nuc} \pm 0.5\text{kHz}$). The benefit of measuring spinning-rate dependent NMR signal is that: i) distance and zero-quantum relaxation parameters can be extracted independently, and ii) the exact R^2 condition is not required. Therefore, we can perform a two-parameter optimization to find the best fitted distance between the labeled sites (Figure 2.9A). Through

this method, we can easily measure the distances between selectively labeled ^{13}C as long as their chemical shifts have appropriate separation (*e.g.*, $\text{C}\alpha$ and CO , Figure 2.9B).

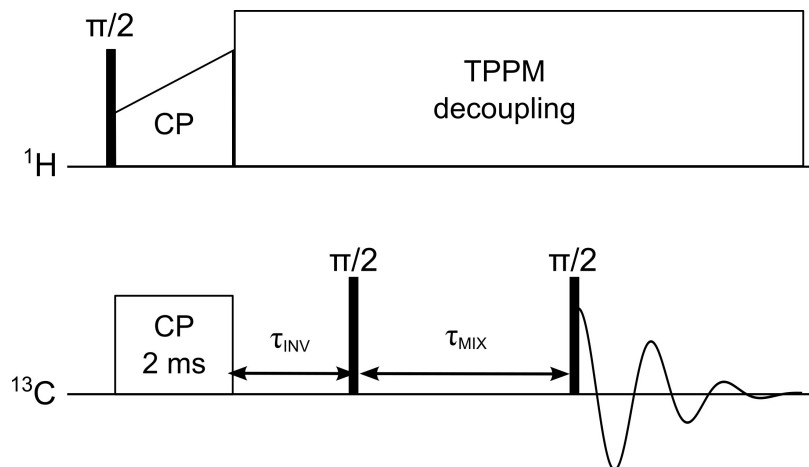


Figure 2.8 The pulse sequence of ^{13}C - ^{13}C R^2W . Black block: $\pi/2$ pulse. τ_{INV} : inverse delay. τ_{MIX} : mixing time. The definition and calculation of inverse delay is included in Appendix B.1

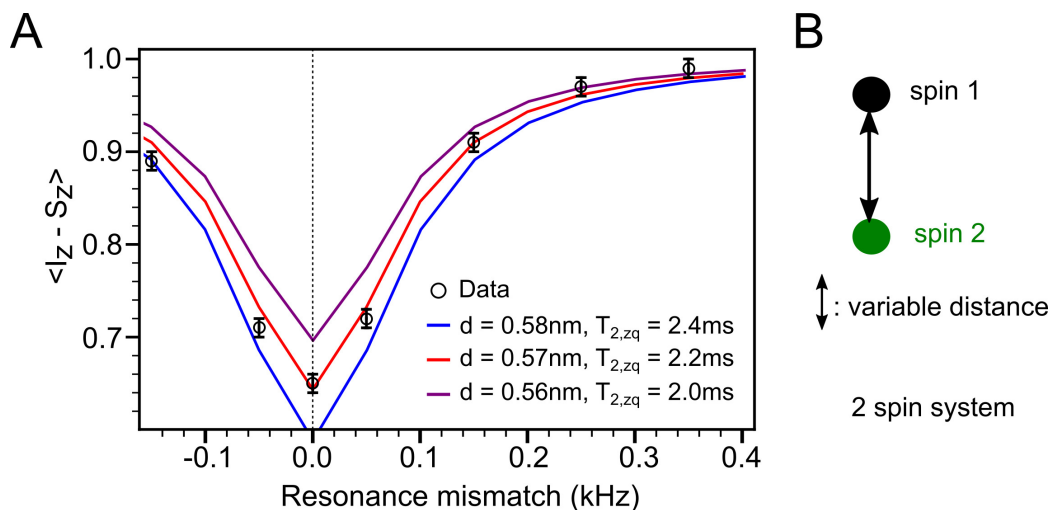


Figure 2.9 An example of using R^2W to measure the distance between two ^{13}C atoms. (A) Comparison of R^2W data and spin simulation results. (B) Two spin system used in R^2W spin simulation.

Since the pulse sequence of R^2W is not available in the Bruker TopSpin software, I

manually programmed it, debugged the phase cycle and ran the experiments. The code of R²W pulse program and more discussion of the experiment are in Appendix B.1.

2.3.2.4 2D Finite Pulse Radio Frequency Driven Recoupling (2D fpRFDR)

2D fpRFDR experiment [208] (Figure 2.10) applies a rotor-synchronized pulse pattern, akin to the PITHIRDS-CT technique, to produce ¹³C-¹³C 2D exchange spectra with signals on the diagonal and crosspeaks that are approximately symmetric about the diagonal (Figure 2.11). The symmetry of spectra occurs because polarization transfers can occur in both directions between coupled pairs of spins: for example, polarization transfers from a CO to the adjacent C α occur at the same rate as transfers from the C α to CO during the fpRFDR mixing period. At mixing times near 1.3 ms, crosspeaks are observed primarily between directly bonded ¹³C atoms (*e.g.*, between ¹³C-labeled C α and C β in the same residue). Weak crosspeaks might be observed between ¹³C atoms separated by two covalent bonds (*e.g.*, between C α and C γ sites of Valine).

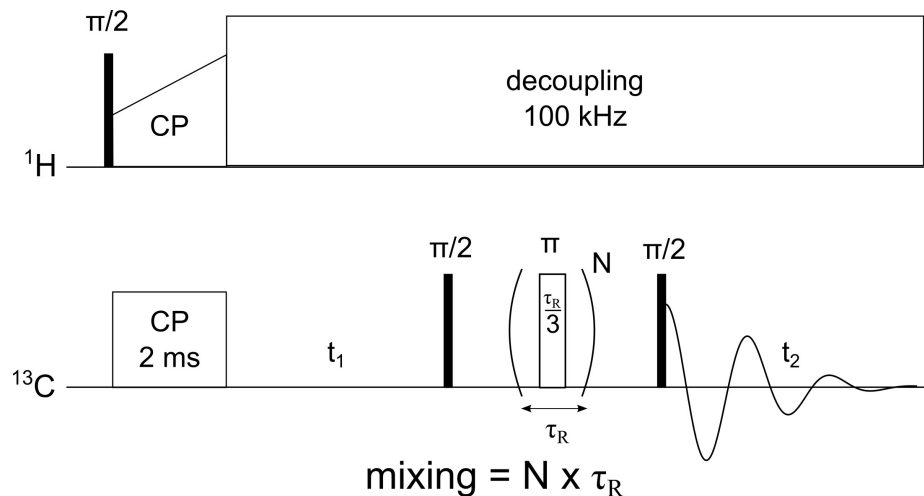


Figure 2.10 The pulse sequence of 2D ¹³C-¹³C fpRFDR experiment. Black block: $\pi/2$ pulse. τ_R : rotor period. N is a positive integer.

The 2D-fpRFDR technique has been used to obtain ¹³C spectral assignments and pre-

cise NMR peak positions for each labeled site (Figure 2.11) in the selectively ^{13}C -labeled sample. Through non-linear fitting of each crosspeak to a 2D Gaussian function [227], we can determine the chemical shifts and linewidths of labeled nuclei. Analysis of secondary chemical shifts (values relative to the same atoms on the same amino acids within random coil peptides [228]) for ^{13}C atoms near the peptide backbone (CO, $\text{C}\alpha$, and $\text{C}\beta$) has been used to predict secondary structures [229]. The secondary chemical shift analysis performed in TALOS-N [230, 231] helped us to reveal the β -strand regions in A β oligomer sample (see Section 4.4). Analysis of linewidths is a basis for evaluating structural order, and this method has been used to identify unstructured regions of peptide assemblies [167]. In addition, comparisons of 2D fpRFDR crosspeak positions and line shapes, from different aggregate samples of the same labeled peptide, have been used as a basis for evaluating structural variation [88, 168].

2.3.2.5 2D Dipolar Assisted Rotational Resonance (2D DARR)

The 2D DARR technique [232, 233] produces ^{13}C - ^{13}C 2D exchange spectra through the dipolar coupling reintroduced by rotational resonance (Figure 2.12), as the name suggests. 2D DARR pulse sequence is very similar to the one of R^2 (Figure 2.8) except the low power ^1H irradiation during mixing period, *i.e.*, the DARR irradiation. This low-power but long-lasting irradiation, with pulse power (in the unit of frequency) equal to MAS rate ($\omega_{1H} = \omega_{MAS}$), gives a larger dipolar broadening, and leads to broadband recoupling and polarization transfer among all ^{13}C . Therefore, it does not have the limitation that polarization transfer occurs only between a specific pair of ^{13}C with a fixed chemical shift difference, hence more flexibility than the conventional R^2 . Furthermore, 2D DARR does not need high-power ^1H decoupling during the mixing period, unlike 2D fpRFDR, so it can be performed under a wider range of possible mixing time, usually varying from 10 ms to 1000 ms.

At mixing times of 50 ms or less, 2D DARR spectra exhibit crosspeaks that correspond

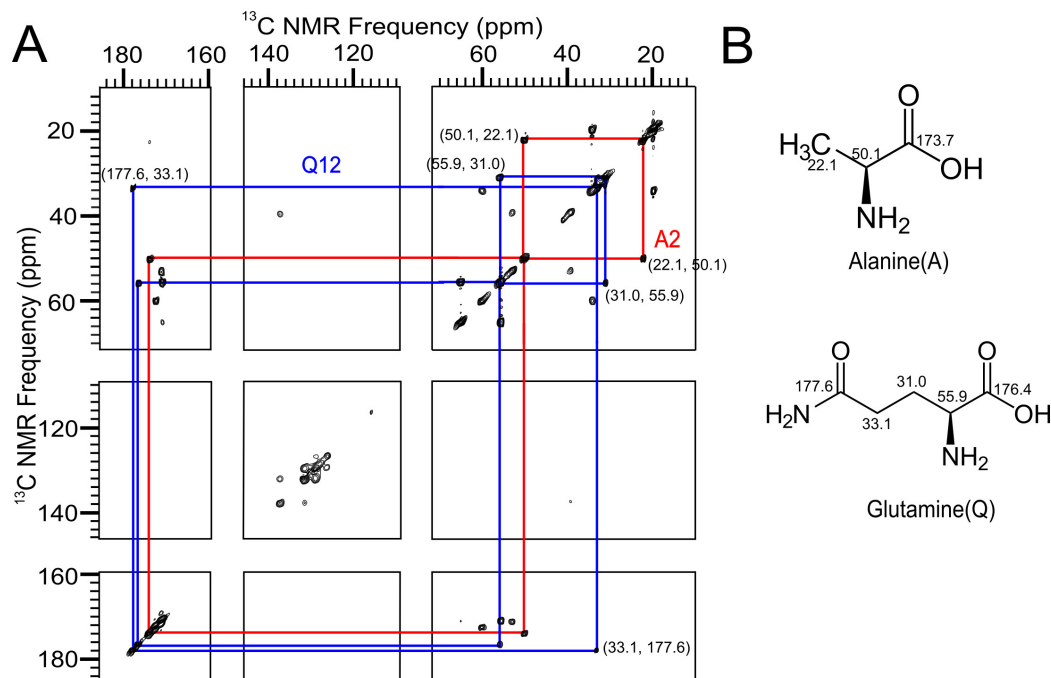


Figure 2.11 An example of 2D fpRFDR spectrum of P1 amyloid sample. (A) 2D fpRFDR spectrum with the correlation pathways of A2 and Q12 residue in P1 peptide. The symmetric pathways mark the crosspeak positions for the two residues. The unlabeled crosspeaks are from other residues. (B) The molecular structure of Alanine and Glutamine with the chemical shifts of ^{13}C nuclei measured in 2D fpRFDR.

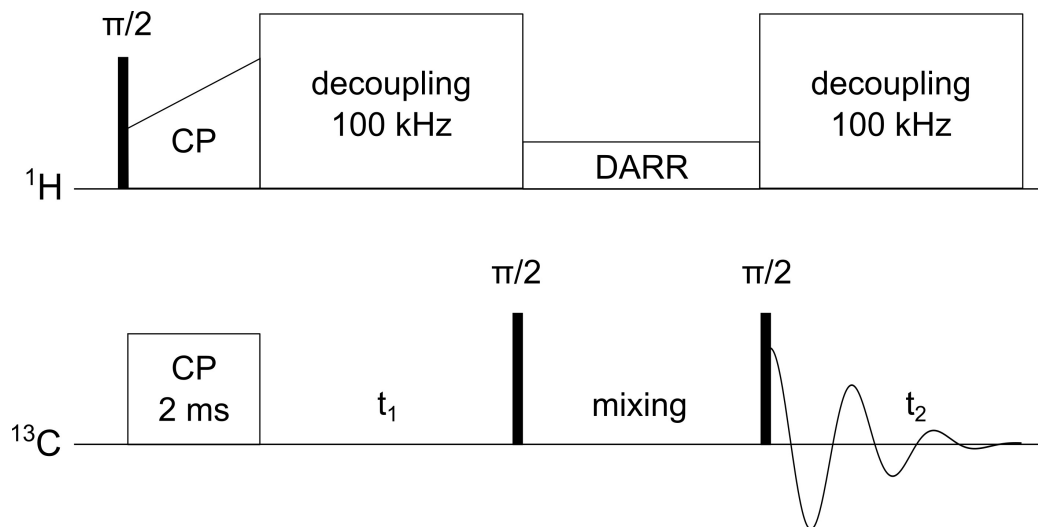


Figure 2.12 The pulse sequence of 2D ^{13}C - ^{13}C DARR experiment. Black block: $\pi/2$ pulse. DARR: the low-power irradiation during mixing.

mostly to ^{13}C atoms within a single amino acid. As mixing times are increased to 100 ms, additional crosspeaks can be observed that correspond to adjacent amino acids within the primary structure [234]. With mixing times at 500 ms or above, the crosspeaks that report on amino acids brought into close proximity by molecular folding show up on 2D DARR spectra. Thus, the long mixing time DARR becomes our most frequently used method for probing long-distance ^{13}C - ^{13}C structural constraints. According to our tests and some literatures [209, 235], the 2D DARR with 500 ms mixing time can detect crosspeaks between two ^{13}C atoms separated by a distance of 0.6 nm or less. For ease of expression, we describe the correlation of two ^{13}C atoms that produce crosspeak on 500 ms mixing DARR as they have a **DARR contact**, indicating the distance between them is less than 0.6 nm (Figure 2.13, Section 2.4.2). However, one flaw of long mixing time DARR is not working well in fast MAS conditions—crosspeaks corresponding to longer distances (above 0.5 nm) are difficult to detect when MAS speeds are too fast (above 20 kHz).

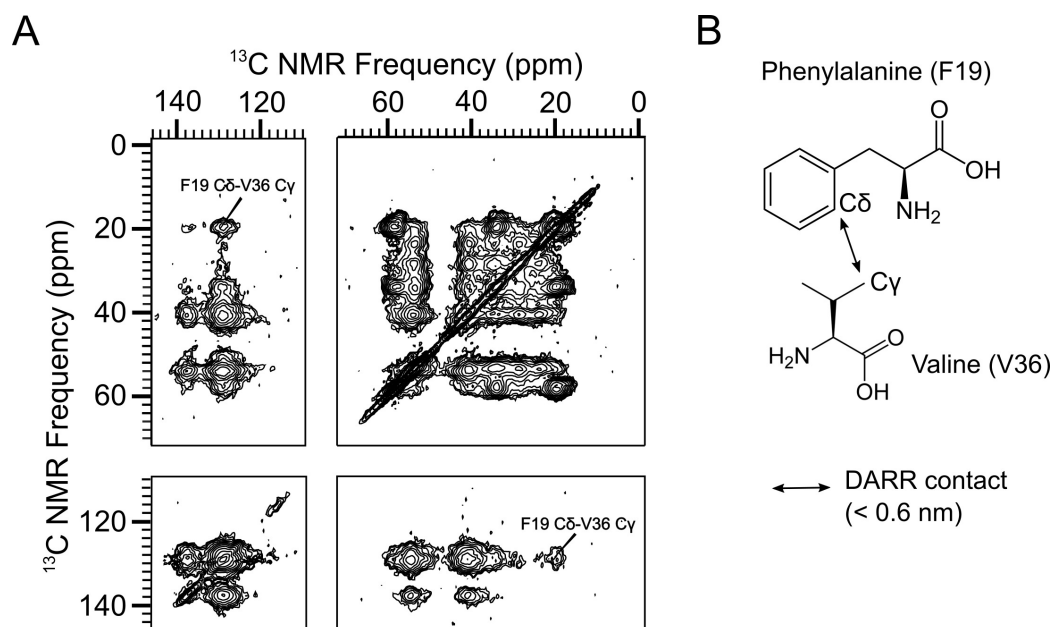


Figure 2.13 An example of 2D ^{13}C - ^{13}C DARR spectrum with 500 ms mixing time. (A) The symmetric crosspeaks between F C δ and V C γ on the 2D DARR spectrum of A β (1-42) oligomer sample. The mixing time is 500 ms. (B) The crosspeaks indicate a DARR contact between Phenylalanine and Valine sidechains.

2.3.2.6 2D CHHC

2D CHHC experiment [211, 236], as the name indicates, involves one-bond CP from ^{13}C to ^1H , mixing-dependent ^1H - ^1H transfer, and then one-bond CP from ^1H back to ^{13}C for detection (Figure 2.14). In other word, 2D CHHC measures ^{13}C - ^{13}C exchange spectrum to interrogate ^1H - ^1H proximity.

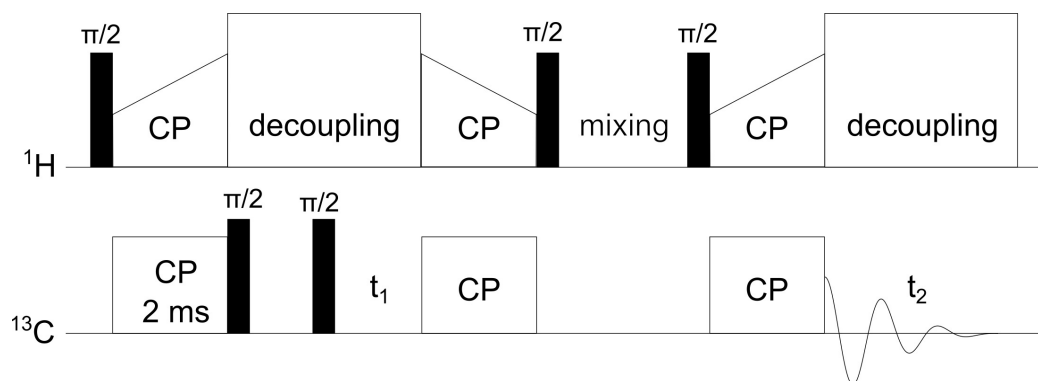


Figure 2.14 The pulse sequence of 2D CHHC experiment. Black block: $\pi/2$ pulse.

One great application of 2D CHHC is to characterize antiparallel β -sheet (Figure 2.15). An antiparallel β -sheet structure will place $\text{H}\alpha$ atoms in super close proximity (<0.3 nm) for specific pairs of amino acids [237], *i.e.*, the closest residues on neighboring β -strands. This configuration predicts a extremely strong ^1H - ^1H dipolar coupling between these $\text{H}\alpha$ atoms, which can be detected by 2D CHHC with $200\ \mu\text{s}$ mixing. Some long mixing time ($> 400\ \mu\text{s}$) 2D CHHC experiments were applied to analyze amyloid structure [172], but, to our knowledge, it required extremely long experimental time to collect enough crosspeak signals.

2.3.2.7 Spin Simulation

We used SPINEVOLUTION [204] to simulate the PITHIRDS-CT and R^2W signals. It is a very powerful and efficient NMR simulation software developed by Mikhail Veshtort.

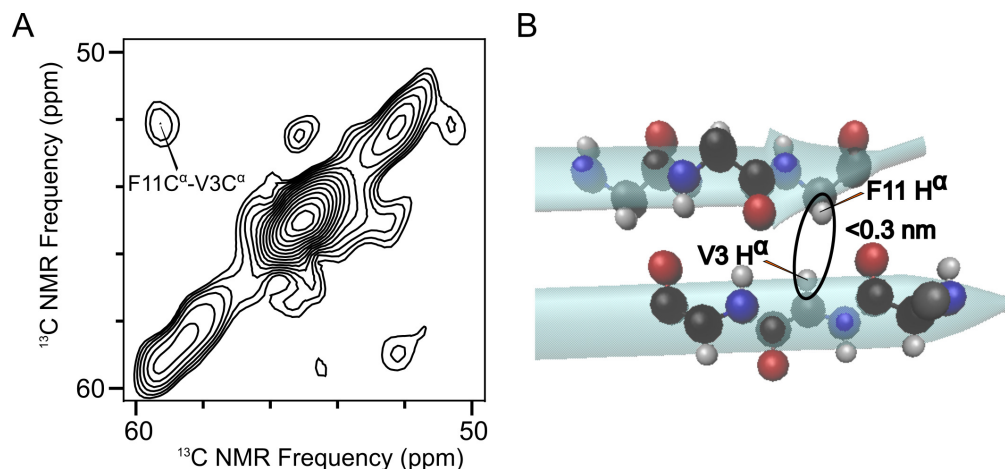


Figure 2.15 An example of 2D CHHC spectrum of P1 amyloid sample. (A) The 2D CHHC spectrum with symmetric crosspeaks between F11 C α and V3 C α . (B) The crosspeaks indicate a close proximity between F11 H α and V3 H α in antiparallel β -sheet.

In general, we take the coordinates of NMR-related atoms, the chemical shift anisotropies (CSA) of all nuclei, the pulse sequence and the experimental-specific parameters as input to initiate a simulation, and finally get the desired output dataset. SPINEVOLUTION is smart enough to transform or integrate the simulated result so that it can be directly overlaid with the experimental data. As an example, the input and output files for simulation in Figure 2.7 is included in Section B.2. Some details of the spin simulations (*e.g.*, CSA parameters) will be present in the method sections of the following chapters.

2.4 Molecular Dynamics (MD) Modeling

Molecular modeling plays an important role in ssNMR structural studies to summarize the NMR data and provide insights into the atomic-level conformation. Given the limited structural information from ssNMR results, we rely on the structural models to design new experiments for verifying, optimizing, and refining the proposed structures. Although a wrong model may mislead us into a dead end, the new experimental strategies and the novel structures in our research were all inspired by modeling works, serving as a source of innovation.

Our collaborator helped us to build many hypothesized structures. Cong Guo built the

N-sheet models and the full four-fold symmetric model of A β oligomer (see Section 4.4). Yiming Wang produced the initial structural model of P1 amyloid by discontinuous molecular dynamics (DMD) simulations (see Section 5.2).

2.4.1 NMR-Constrained MD Simulation

Our lab used VMD (Visual Molecular Dynamics) scripts [238] to generate the initial conformation of peptide sequence and the basic arrangement of strands. Then, we applied NAMD [239, 240] to run MD simulation with constraints, including both secondary structural constraints and NMR result constraints. More specifically, i) a single peptide was generated using standard β -strand backbone torsion angles [241], the common secondary structure in most amyloid and aggregate samples. ii) The torsion angles of non- β -strand residues are manually adjusted to form the desired turns or disordered regions. iii) Repetitive peptide molecules are created in parallel or antiparallel alignment to assemble into a β -sheet. iv) The structural features are defined in a list of secondary structural constraints (backbone torsion angles, hydrogen bonds, and hydrogen bond angles) and NMR experimental constraints (the distances between ^{13}C atoms). v) A reasonable structural model is generated by running MD simulation with all the constraints inputted. vi) The initial structural model is optimized for better consistency with other experimental data (*e.g.*, cryo-EM class average). The optimization includes modifying peptide arrangements and adjusting sidechain orientations.

The processes of building complicated structural models are further explained in the method sections of different projects.

2.4.2 Compare The Experimental Constraints and The Model-Predicted Atomic Proximity: DARR Contact Chart

With a freshly built structural model, we developed a correlation map of the peptide residues to check whether the structural model is consistent with the NMR constraints provided by

500 ms mixing DARR experiments, namely DARR contact chart (Figure 2.16). The idea of the correlation map was inspired by the hydrogen bonding plot (HB plot) and protein contact map, which are both used to analyze protein secondary and tertiary structures [242, 243]. The predicted DARR contact chart captures some basic structural features of the model and visualizes the comparison between the structural model and NMR data.

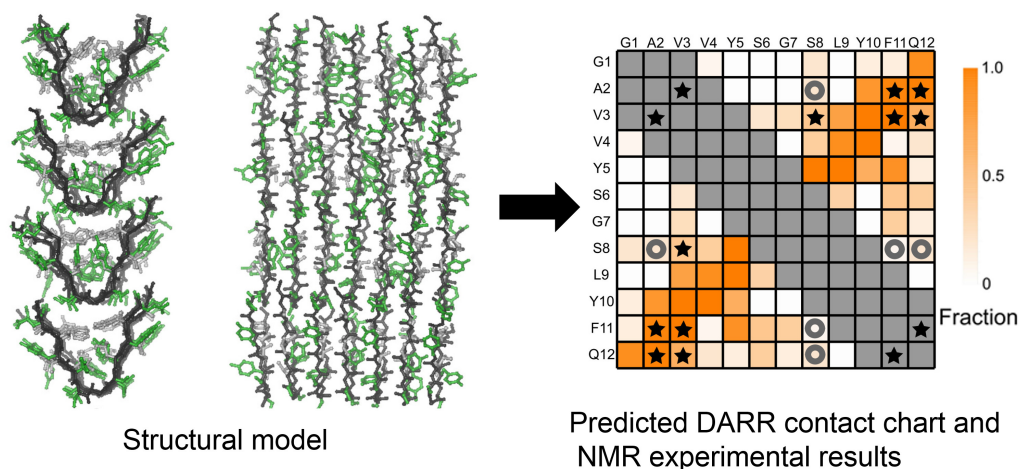


Figure 2.16 Use DARR contact chart to check the consistency between the structural model and the NMR experimental data. The gray squares near the diagonal cover the combinations of residues that do not provide any useful structural information. The detected inter-residue DARR contacts are denoted as stars, while the negative results are labeled as circles. The darkness of orange color indicate the fraction of peptide molecules that contribute to observable 2D DARR crosspeaks, which is predicted based on the structural model.

As shown in Figure 2.16, the residues in the peptide are listed in the rows and columns, and thus each cell in the chart represents a pair of residues. The colored cells (orange) indicate nearest-neighbor residues separated by a distance of 0.6 nm or less, *i.e.*, the minimum distance between one C atom on one residue and one C atom on the other is 0.6 nm or less, as would be necessary for detection of inter-residue ^{13}C - ^{13}C crosspeaks in 2D DARR experiment (with 500 ms mixing time). Hence the colored cell predicts that at least one inter-residue ^{13}C - ^{13}C crosspeak between the pair of residues, as long as they have appropriate isotope labels, would be detected in 2D DARR, namely a predicted DARR contact.

Sometimes, we use different colors in the cells (Figure 2.16) to indicate the fraction of peptide molecules that contribute to observable 2D DARR crosspeaks: a predicted contact with a low fraction of molecules usually has weak NMR signals. This feature works well when we analyze minor structures in the assemblies containing many molecules (Section 4.4). In addition, by visualizing the predicted DARR contacts, the patterns of different secondary structures can be easily identified (Section 4.4). The gray squares near the diagonal cover the combinations of residues that do not provide any useful structural information. This is because that contacts between residues that are 2 residues apart or less in the primary structure would always have crosspeaks on 2D DARR (if they are ^{13}C -labeled) and would not report on molecular conformation.

The 500 ms mixing 2D DARR results can be directly recorded in the DARR contact chart. If one or more crosspeaks between a pair of residues are observed on the spectra, we denote the detected inter-residue DARR contact as a star in the cell corresponding to the pair of residues. Conversely, if no crosspeak between a pair of ^{13}C -labeled residues shows up, we use circles to mark the cell as undetected contacts. Finally, we simply look at the chart and compare the structural model to the NMR data: the stars are expected only in colored cells, while the circles are expected in nearly-white and white cells. With the visualized tool, we can quickly locate the flawed region in the current model and try to fix it.

CHAPTER 3

SOLID-STATE NMR CHARACTERIZATION OF RESIDUAL STRUCTURE IN AGGREGATED FORM OF FIBROBLAST GROWTH FACTOR-1

Portions of this chapter have been adapted and reproduced from L. M. Longo, Y. Gao, C. A. Tenorio, G. Wang, A. K. Paravastu, and M. Blaber, “The Folding Nucleus Structure Persists in Thermally-Aggregated FGF-1,” *Protein Sci.*, vol. 27, no. 2, pp. 431–440, 2017 [234]. Copyright 2017 Wiley (See Appendix A for the reprint license agreement). Additional supporting materials is included in Appendix C.

3.1 Project Overview

For *de novo* design of protein, we usually wish to have an efficient folding pathway leading to target structure without unexpected aggregation. However, design details to achieve efficient folding and avoid aggregation are still poorly understood. Fibroblast growth factor-1 (FGF-1) is a small globular protein with high aggregation propensity, and its folding pathway has been revealed [244, 245]. Dr. Blaber’s lab had designed a well-folded protein that shares the same FGF-1 folding nucleus, but has a different amino acid sequence outside the folding nucleus, and does not thermally aggregate [246]. Subsequently, we postulate that these regions outside the folding nucleus unfold early in the unfolding pathway and that the partially folded intermediate structure is more prone to intermolecular aggregation.

In this study, we use solid-state NMR (ssNMR) and other methods to characterize the thermally aggregate of FGF-1. The NMR spectra are consistent with residual structure in the aggregate and provide evidence of a structured region that corresponds to the folding nucleus region. NMR data also indicate the presence of unstructured regions that exhibit hydration-dependent dynamics and suggest that unstructured regions of aggregated FGF-

1 are outside the folding nucleus. The span of the structured and unstructured regions in FGF-1's primary sequence is consistent with the aggregate mechanism in our hypothesis.

The results suggest that the design of an efficient folding nucleus, and the avoidance of aggregation in the folding pathway, are potentially separable design criteria – the latter of which could principally focus upon the physicochemical properties of primary structural outside the folding nucleus.

3.2 Introduction

Aggregate mechanism is a poorly-understood aspect of protein biophysics and *de novo* protein design. Aggregation processes involve properties of the primary structure that influence the cooperative folding process [247], unstructured potential [248], and intermolecular interactions [249]. The understanding of amino acid sequence that promote aggregation in protein design can benefit from experimental studies that elucidate fundamental principles that drive the aggregation processes. For example, while general protein design heuristics have identified a “stability/function trade-off” [250, 251] and a “foldability/function trade-off” [245, 252], first principles underlying such heuristics remain to be fully elucidated, and our understanding is especially limited as regards protein aggregation.

Dr. Blaber's lab had studied the structure and the folding pathway of FGF-1 in detail, and they revealed FGF-1 is a single-domain globular protein belonging to the common β -trefoil fold [253, 254]. FGF-1 is well-known to be highly aggregation-prone and have some intermediate structures during thermal denaturation [244, 255]. One interesting fact they noticed is that the tertiary structure of FGF-1 has three-fold symmetry, but the amino acid sequence does not (Figure 3.1A and 3.1B). To better understand the relationship between sequence symmetry and structural symmetry, Liam Longo in Blaber's lab had designed Phifoil by folding nucleus symmetric expansion (FNSE) [246]. He first located the folding nucleus region (Figure 3.1B) [245], which triggers the overall folding process, in the primary sequence of FGF-1 using Φ (Phi)-value analysis [256], then built Phifoil sequence as

three repeating instances of amino acid sequence extracted from the FGF-1 folding nucleus. Phifoil has similar thermodynamic properties to FGF-1, but critically, does not thermally aggregate – exhibiting instead two-state reversible thermal denaturation [246]. Therefore, the basis of thermal aggregation of FGF-1 may be assigned to regions outside the folding nucleus. Because those regions are believed to unfold early in the thermally-induced unfolding pathway and thus become unstructured, the folding nucleus of FGF-1 must contribute to the residual structure in the partially folded intermediates and the final aggregates.

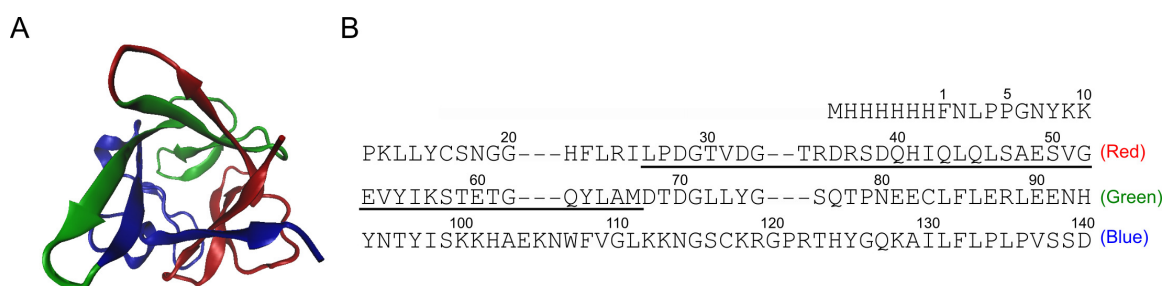


Figure 3.1 Crystal structure and amino acid sequence of FGF-1. A) Ribbon diagram of the FGF-1 crystal structure. B) The primary structures of FGF-1 (single-letter code) are arranged according to the three repeating trefoil-fold structural subdomains, which are labeled by different colors in panel A. The underlined region of contiguous amino acid positions 23–64 identifies the folding nucleus of FGF-1.

To shed more light on the residual structure in aggregates, we performed direct structural measurements on the heat-induced aggregated state of FGF-1 by MAS-ssNMR analysis. The data are most consistent with the aggregated state of FGF-1 containing a partially folded intermediate, and the structure of this intermediate is consistent with the region comprising the FGF-1 folding nucleus. The comparison between FGF-1 and Phifoil as well as the structural information extracted from FGF-1 aggregates supports that the regions outside the folding nucleus are more likely to cause thermal aggregation. These regions in FGF-1 are also associated with specific functionality [257, 258]. The results therefore support a function/aggregation tradeoff hypothesis of protein evolution and design, as well as provide further evidence that evolutionary processes of gene duplication and fusion that produce

symmetric primary structure (within symmetric protein architecture) can be compatible with efficient folding pathways that avoid aggregation.

3.3 Materials and Methods

3.3.1 FGF-1 Expression and Purification

FGF-1 with an N-terminal 6xHis tag was used for all experiments, and is the same expression construct utilized for Phifoil. Expression and purification were performed as previously published [255]. To produce samples with uniform ^{13}C and ^{15}N isotopic labeling, expression media was prepared with ^{13}C -labeled glucose as a carbon source and ^{15}N -labeled ammonium chloride as a nitrogen source (Cambridge Isotope Laboratories, Cambridge MA). Purified protein was exchanged into 20 mM N-(2-Acetamido)iminodiacetic acid (ADA), 100mM sodium chloride, pH 6.6 (ADA buffer). Liam Longo and Connie Tenorio produced FGF-1 protein for all the studies.

3.3.2 Sample Preparation for Solid-State NMR

Aqueous solutions of 40 μM FGF-1 in ADA buffer were incubated at 95 $^{\circ}\text{C}$ for 1 hr, yielding visibly cloudy suspensions of aggregated protein. This aggregate was collected as pellets by centrifugation at 17,000 x g for 10 min, and it was washed with water to remove the buffer salt. The final pellets were partially dried in air at room temperature for about 2 hrs, yielding a paste-like aggregate that exhibited a large bulk water peak in the ^1H NMR spectrum (referred to as the “hydrated” sample). Further drying of aggregated FGF-1 in air for 5 days produced a sample with only a weak water signal in the ^1H NMR spectrum (referred to as the “dehydrated” sample). The uniformly ^{13}C -labeled aggregate samples were analyzed by 2D-fpRFDR, 2D-CHHC, and 2D-DARR NMR spectroscopy. A 50% isotopically-diluted sample (aggregate from solutions of equal parts labeled and unlabeled FGF-1) was analyzed by 2D-CHHC NMR spectroscopy.

3.3.3 Solid-State NMR Characterization of Aggregated FGF-1

The 2D ^{13}C - ^{13}C fpRFDR spectra (Section 2.3.2.4) were measured on a Bruker 11.75 Tesla (500-MHz ^1H NMR frequency) solid-state NMR system with an Avance III console and a 2.5 mm magic angle spinning (MAS) NMR probe. The 2D-DARR (Section 2.3.2.5) and 2D-CHHC (Section 2.3.2.6) experiments were performed on a Bruker narrow-bore 11.75 Tesla magnet, equipped with a 3.2 mm HCN MAS probe. Decoupling of ^1H , which applied two pulse-phase modulation (TPPM) [214] with ^1H radiofrequency field of 110 kHz (for a 2.5 mm probe) or 100kHz (for a 3.2 mm probe), was employed during all free evolution and fpRFDR recoupling periods. The π pulses (180 °pulse) on ^{13}C channel for recoupling in fpRFDR had 37.5 kHz radiofrequency fields so that the pulse durations (13.3 μs) were one-third of the rotor period at 25 kHz MAS for 2.5 mm rotors. The total recoupling period in 2D fpRFDR is set to 1.28 ms. In 2D DARR experiments, continuous irradiation for 50 or 100 ms with ^1H field was applied in the exchange periods with powers corresponding to 11 kHz (same frequency as the MAS spinning rate). 2D CHHC spectra were acquired at 11 kHz MAS with 3.2 mm rotors with 150 μs ^{13}C - ^1H and ^1H - ^{13}C cross-polarization periods and a 182 μs ^1H - ^1H spin diffusion period between t_1 and t_2 . The 2D-fpRFDR spectra, the 2D DARR spectra, and the 2D CHHC spectrum of the uniformly labeled FGF-1 aggregates were each the result of 48 hrs of signal averaging, while the 2D CHHC spectrum of the isotope-diluted sample had an increasing signal averaging for 72 hrs.

3.3.4 Quantification and Statistical Analysis

ssNMR data were collected and Fourier transformed using TopSpin software (Bruker BioSpin Corp., Billerica, MA). Visualization of NMR spectra and line shape analysis via nonlinear fitting was performed using custom Mathematica scripts (Wolfram Research, Champaign, IL).

Linear fits and determination of coefficient of correlation utilized the Origin software (Origin Lab Corp., Northampton MA). Nonlinear least-squares fitting of all thermodynamic

models, and associated standard error determinations, were performed using the DataFit software package (Oakdale Engineering, Oakdale PA). The fit and associated error analysis for determination of ΔC_p from a direct fit of a two-state model to the extrapolated stability curve data were performed using the SciPy software package [259]. Fitting of differential scanning calorimetry (DSC) endotherm data and error determination utilized the DSCFit software package [260]. The analyses of the folding thermodynamics of FGF-1 were all completed by Liam Longo.

3.4 Experimental Results

3.4.1 FGF-1 Aggregated State Is Inconsistent with Amyloid Structure

Freshly aggregated samples of FGF-1 were analyzed by negative stain transmission electron microscopy (TEM) to probe for the presence of amyloid fibrils. Samples were bath sonicated for between 0–30 s to break up samples prior to deposition on a carbon grid. Under no condition were fibrils observed (Figure 3.2). Freshly aggregated samples of FGF-1 were also incubated with thioflavin T (ThT) to detect amyloid formation; however, no significant fluorescence signal was detected. Thus, we believe that FGF-1 does not form amyloid fibrils in thermally-aggregated conditions.

3.4.2 2D NMR Spectra Characterize Residual Structure in The FGF-1 Aggregate

An aggregated FGF-1 sample with uniform ^{13}C and ^{15}N isotopic labeling was analyzed by MAS solid-state NMR. Preliminary measurements showed that sample hydration had a significant effect on peak sharpness, which is common in the ssNMR studies of other protein samples [169, 261]. To observe the highest peak resolution, aggregated FGF-1 was kept moist (with a paste-like consistency), and MAS rotors were sealed with Teflon plugs to minimize drying during data acquisition (unless otherwise noted, all spectra were collected on hydrated samples).

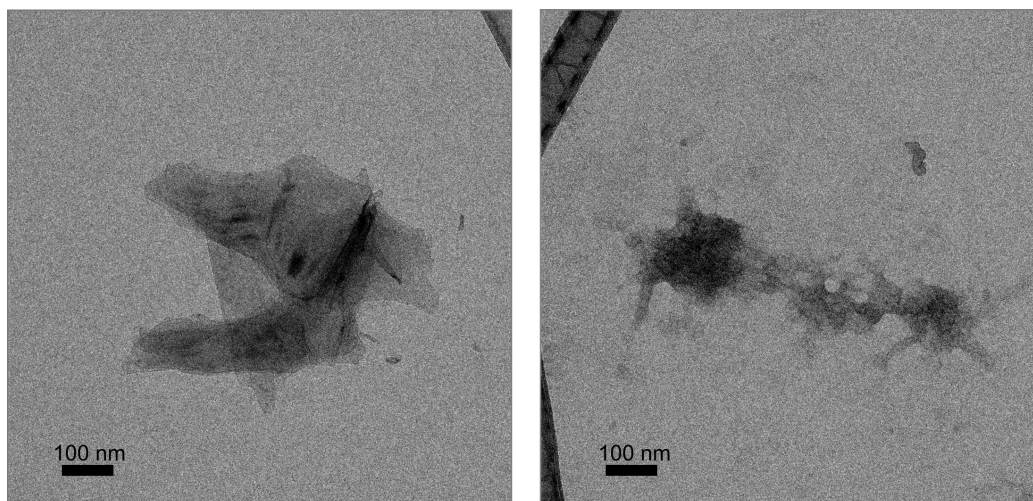


Figure 3.2 TEM images of thermally-aggregated FGF-1.

In the 2D fpRFDR spectrum (Figure 3.3), signals from amino acids that occur more than once in the primary structure (*e.g.*, Ile) are not resolved due to insufficient spectrum resolution. For example, we can observe a broad peak for Ile C β /C γ 2 correlation (marked in Figure 3.3) consisting of signals from different Ile in FGF-1 sequence, but the separate crosspeaks cannot be identified. For this reason, as well as the lack of resolution in the ^{15}N signals preventing 3D NMR, NMR signals were assignable to residue type only. The spectral assignment (described in Section 2.3.2.4) for each distinguishable amino acid type is indicated by the colored lines and single-letter abbreviations in Figure 3.3. The chemical shifts and linewidths of the off-diagonal peaks were calculated using nonlinear peak fitting to Gaussian functions (Table C.1). The observed ^{13}C linewidths are within the range of 2–3 ppm and indicate that FGF-1 aggregation is associated with a degree of structural order comparable to those previously observed for amyloid fibrils [38, 167]. The secondary NMR chemical shifts for labeled CO, C α , and C β sites of most residues are consistent with β -strand secondary structure [229]. Pro and Gly chemical shifts do not report on secondary structure, and the majority of these residues lie within turn/coil regions in FGF-1 [254].

To test for possible dynamic disorder (backbone motion) in the aggregated FGF-1 sample, a 2D fpRFDR spectrum was collected on a dehydrated FGF-1 aggregate sample. Figure

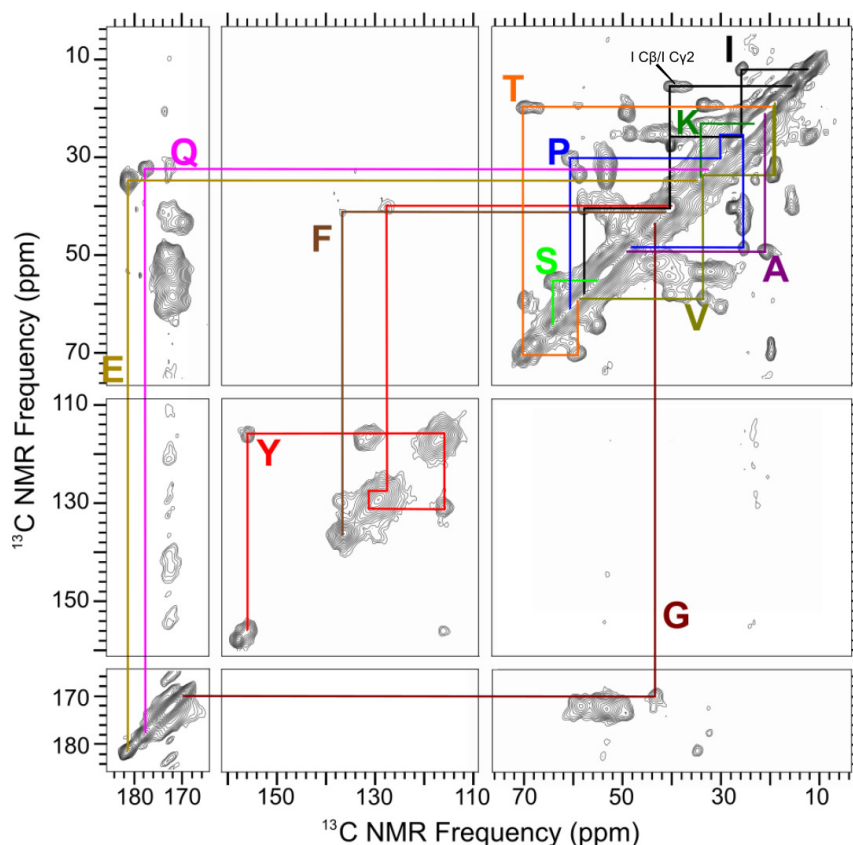


Figure 3.3 The 2D fpRFDR spectrum of ^{13}C , ^{15}N uniformly labeled aggregated FGF-1. The off-diagonal crosspeaks correspond to correlations between covalently bonded ^{13}C atoms. Colored horizontal and vertical lines indicate assignment of crosspeaks based on amino acid type, indicated by single-letter abbreviations.

3.4A shows the overlaid 2D fpRFDR spectra of hydrated and dehydrated aggregated FGF-1 samples. The main effect of dehydration on the 2D fpRFDR spectrum was to increase the intensity of broad (above 3 ppm) ^{13}C NMR signals in the spectrum. This effect is likely the result of reduced mobility for regions of FGF-1 that are not in the structured core of the aggregate as mobility attenuates ^1H - ^{13}C cross-polarization. Consistent with this interpretation, dehydration did not affect the positions of crosspeaks detected in the 2D fpRFDR spectrum of the hydrated sample but broadened most peaks (Table C.2), suggesting that loss of water did not change the structure but did affect the structural order of the core. We identified three notable amino acids with crosspeaks expected in positions corresponding to weak (on the order of the noise) NMR signals in the spectrum of the hydrated aggregate

sample but remarkably enhanced in the spectrum of the dehydrated sample: these crosspeaks are the C α (56.5 ppm)-C β (26.3 ppm) of Cys, the C β (39.4 ppm)-C γ (175.5 ppm) of Asn and the C ζ 2 (115.5 ppm)-C ϵ 2 (136.2 ppm) of Trp (Figure 3.4B), and the chemical shifts of these residues match the corresponding values measured in random-coil structure [228]. Based on the strong hydration-dependence of NMR intensities, we suggest that Cys, Asn, and Trp exhibit weak NMR signals in the hydrated sample due to dynamic disorder and broad signals in the dehydrated sample due to static disorder arising from relative large conformational variation. In other words, we suggest that Cys, Asn, and Trp residues reside primarily within flexible, unstructured regions of the aggregate structure. These three residue types are all located outside the folding nucleus of FGF-1 (Figure 3.1).

The 2D CHHC spectra were collected to test for the existence of antiparallel β -strands in the structured region of aggregated FGF-1, which would be consistent with the native FGF-1 structure. As shown in Figure 3.5, crosspeaks were observed between α -carbons, indicating native-like antiparallel β -sheets. Furthermore, the relative intensity to the diagonal signals of C α -C α crosspeaks was not affected by 50% isotopic-dilution. Lack of an isotopic dilution effect on C α -C α crosspeaks indicates that adjacent antiparallel β -strands are within the same molecules and that β -sheets in aggregated FGF-1 are not produced by “domain swapped” structure between neighboring molecules. The restoration of native-like intramolecular antiparallel β -sheets in aggregates was also reported for other proteins [262]. It should be noted, however, that a positive identification of antiparallel β -sheet structure by the CHHC pulse sequence does not rule out the existence of additional non-native parallel β -sheets, which cannot be tested by this method.

3.4.3 Inter-Residue Crosspeaks Are Located in The Region of The FGF-1 Folding Nucleus

2D DARR spectra of aggregated FGF-1 were collected in order to approximately identify which region of FGF-1 retains structure in the aggregated state. Figures 3.6 show 2D DARR data collected at 50 and 100 ms mixing times for ^{13}C - ^{13}C dipolar recoupling. For the 2D

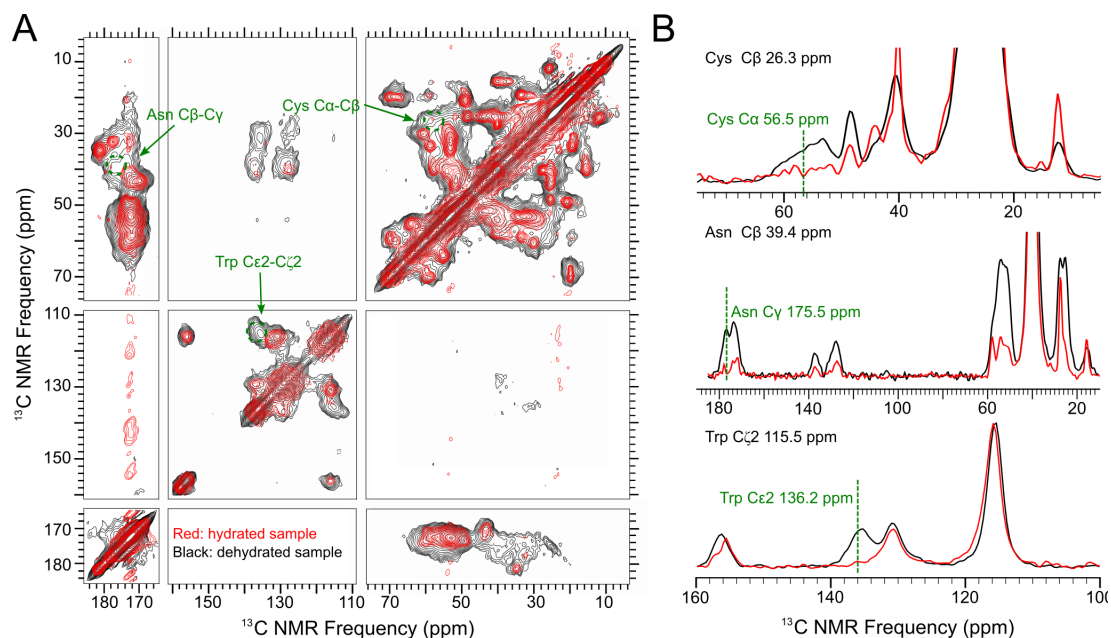


Figure 3.4 Comparison of 2D-fpRFDR spectra of the hydrated and the dehydrated aggregate FGF-1. A) Overlay of 2D fpRFDR spectra collected on hydrated (red) and dehydrated (black) samples of aggregated FGF-1. The arrows and dashed circles mark the expected locations of Cys, Asn and Trp crosspeaks, which are significantly enhanced in the dehydrated sample. B) Horizontal slices of the 2D-fpRFDR spectrum, taken at frequencies expected for Cys signal (26.3 ppm), Asn signal (39.4 ppm), and Trp signal (115.5 ppm). The red slices are from the spectrum of hydrated sample, while the black ones are from the dehydrated sample. The slice spectra are normalized to the diagonal signal intensity. The green vertical dashed lines indicate expected positions of the crosspeaks (random-coil values). Comparison of NMR intensities for hydrated and dehydrated samples indicates enhanced crosspeak intensities likely to correspond to Cys, Asn, and Trp.

DARR spectrum collected with 50 ms mixing, the crosspeaks correspond to correlations between ^{13}C atoms within the same residues. At the longer mixing time of 100 ms, additional crosspeaks were observed between adjacent residues (marked in Figures 3.6). Longer mixing times may lead to 2D spectra that are too crowded to be reliably analyzed. The effect of 2D DARR mixing time is illustrated in Figure C.1. The spectrally resolved $\text{C}\zeta$ slice of Arg is separated from the other ^{13}C atoms in Arg by an N atom. Crosspeaks between $\text{C}\zeta$ and all the other Arg signals are observed with 100 ms mixing but not with 50 ms mixing. The distance between the Arg $\text{C}\zeta$ and $\text{C}\delta$ atoms is similar to the distance between CO and C α atoms on adjacent residues in the primary structure. Thus, the data in Figure C.1 indi-

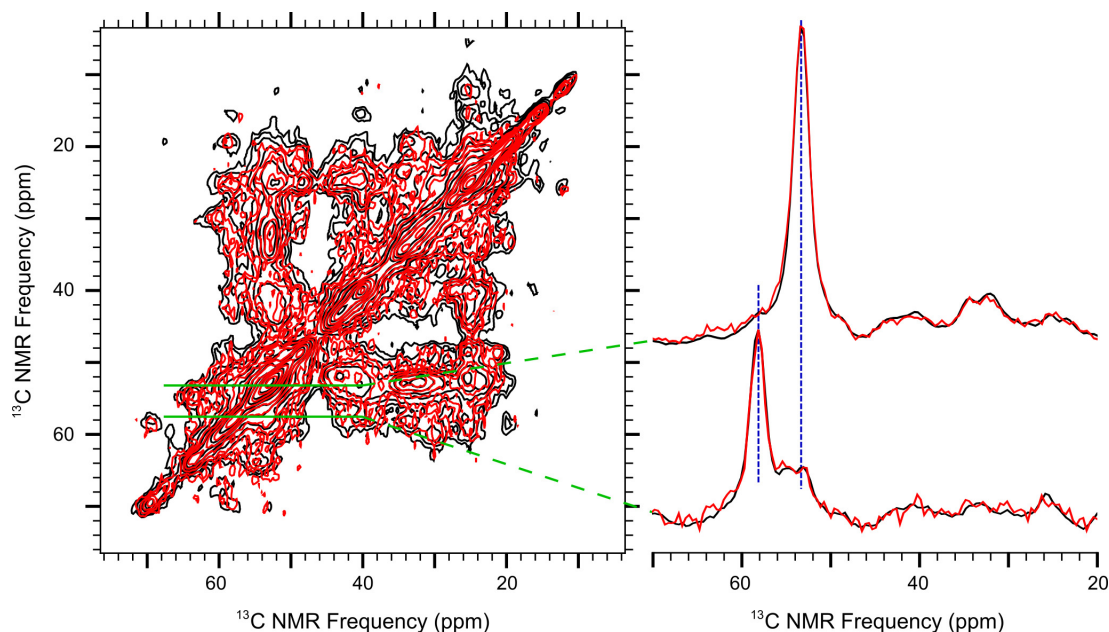


Figure 3.5 2D CHHC spectra of fully-labeled and 50% isotopically-diluted aggregated FGF-1. The fully-labeled aggregated FGF-1 spectra (black) is overlaid with the 50% isotopically-diluted spectra (red). The corresponding horizontal slices (53.3 ppm and 58.0 ppm) indicate $\text{C}\alpha$ - $\text{C}\alpha$ crosspeaks with no intensity loss in isotope-diluted experiments.

cate that 100 ms DARR mixing should yield crosspeaks between adjacent residues, which provide us the information of NMR-detectable residue sequences.

By comparing 2D DARR spectra with 50 ms and 100 ms mixing times, candidate inter-residue interactions can be determined by the peaks of intensity enhancement in longer mixing time. In addition, the $\text{C}\alpha$ - $\text{C}\alpha$ or $\text{C}\alpha$ - $\text{C}\beta$ interactions of adjacent residues are most likely to be detected because of their spatial proximity, and the $\text{C}\alpha$ - $\text{C}\alpha$ crosspeaks should have stronger signals. Based on analyses of the slices from 50 ms and 100 ms DARR spectra, five unique sets of inter-residue crosspeaks were observed: Ser-Thr, Ser-Ala, Leu-Pro-Asp, and Gly-Glu (as further illustrated by slices of the 2D DARR spectra shown in Figure 3.7). All of these NMR contacts can be explained as interactions between pairs of neighboring residues localized specifically to the region previously identified as the FGF-1 folding nucleus (Figure 3.8).

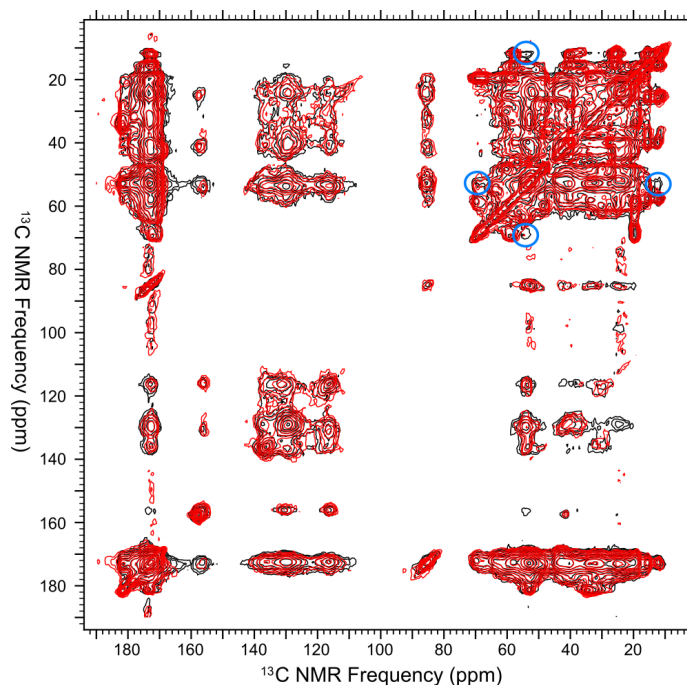


Figure 3.6 2D DARR spectrum of aggregated FGF-1. 2D DARR spectra are shown with 50 ms (red) and 100 ms (black) mixing times. Some inter-residue crosspeaks (blue circle) emerge in the spectrum with longer mixing time.

3.4.4 Prediction of FGF-1 Thermodynamic Parameters in The Absence of Aggregation

The analyses about folding thermodynamics of FGF-1 were done by Liam Longo, and the results are briefly summarized here. DSC data collected in the presence of 0.7–1.1 M GuHCl yielded $\Delta H_{\text{vH}}/\Delta H_{\text{cal}}$ values near unity, no hysteresis when comparing heating and cooling scans, and significant recovery of enthalpy upon subsequent up-scan; thus, two-state reversible thermal denaturation under these buffer conditions is comprehensively supported [255]. In the present report a detailed re-analysis of these DSC data were performed to predict the FGF-1 endotherm in the absence of aggregation. Orthogonal isotherms extracted from the FGF-1 0.7–1.1 M GuHCl DSC data were used to generate an extrapolated $\Delta G_{\text{unf}}(T)$ function at 0 M GuHCl and calculate some thermodynamic parameters for the predicted thermal denaturation of FGF-1 under non-aggregating conditions (Figure C.2). A complete predicted unfolding endotherm ($C_p(T)$) for FGF-1 in the absence of aggregation,

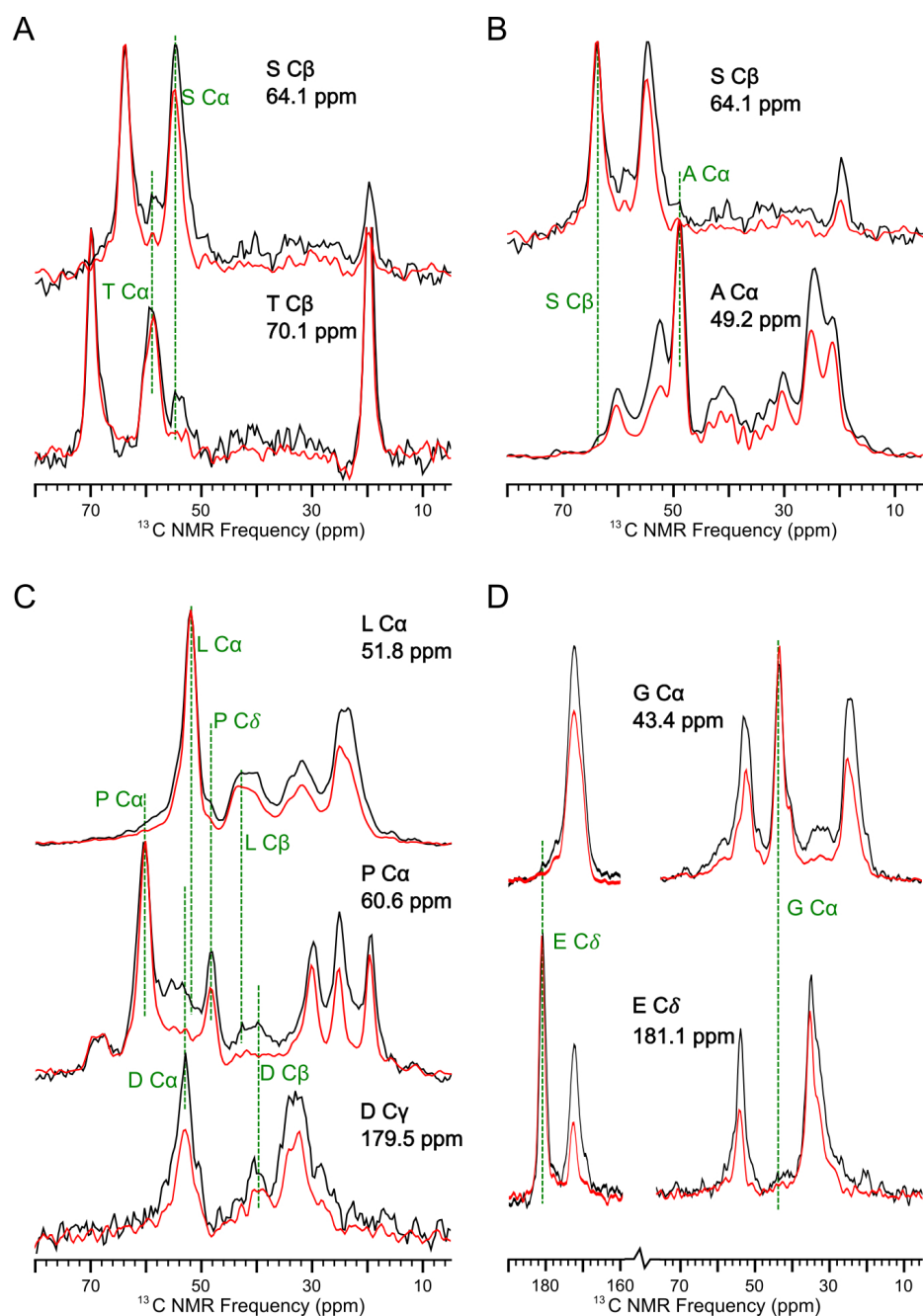


Figure 3.7 Slices of 2D DARR spectra of aggregated FGF-1. DARR spectra slices (red for 50 ms mixing time, black for 100 ms mixing time) showing unambiguous consecutive residue interactions. A) Ser58 and Thr59; B) Ser47 and Ala48; C) Leu68, Pro69 and Asp70; D) Gly52 and Glu53.

along with the experimentally derived endotherm for FGF-1 in 0 M GuHCl (with aggregation) and Phifoil in 0 M GuHCl (no aggregation) is shown in Figure C.3.



Figure 3.8 Primary structure of FGF-1 and Phifoil. The primary structure of FGF-1 is shown using the single letter amino acid code, and the alignment is the same as Figure 3.1. The primary structure of Phifoil is shown below FGF-1 and positions of identity are indicated by a black dot. Residues of FGF-1 which are unstructured/dynamic are indicated by a gray background; residues for which there are unambiguous consecutive interactions in 2D DARR spectra are indicated by inverse lettering. The region of the FGF-1 folding nucleus utilized in the exact threefold symmetric design of Phifoil is marked in the box.

3.4.5 Protein Concentration and Scan-Rate Dependence of The T_m of FGF-1

The analyses about measured T_m of FGF-1 under different conditions were designed and completed by Liam Longo, and the results are briefly summarized here. The apparent T_m of FGF-1 determined by fluorescence under aggregating conditions (0 M GuHCl) varies log-linearly with protein concentration (Figure C.4A). Extrapolation of this relationship suggests that a protein concentration of 0.22 μM would result in a T_m equivalent to the theoretically determined T_m (325.4K) for reversible denaturation under non-aggregating conditions; thus, the thermal aggregation of FGF-1 in aqueous solution is a concentration-dependent intermolecular process with a critical concentration for aggregation of 0.22 μM . DSC studies of FGF-1 thermal unfolding under non-aggregating and reversible conditions (*i.e.*, in the presence of ≥ 0.7 M GuHCl) demonstrate a process that is in thermal equilibrium only with scan rates ≤ 0.25 K \cdot min $^{-1}$ [255]; at faster scan rates the T_m increases monotonically, while below this scan rate the T_m assumes a constant value. The scan rate dependence of FGF-1 (5 μM) under aggregating conditions in ADA buffer is shown in Figure C.4B. These data suggest that FGF-1 thermal aggregation is coupled to the overall unfolding process and cannot be described as a simple Native to Aggregation model and is a hallmark of

three-state (or higher) unfolding events [263].

3.5 Discussion

3.5.1 NMR Data Reveals The Region of Residual Structure

The ssNMR measurements of aggregated FGF-1 strongly indicate the presence of residual structure in the aggregated state. More specifically: 2D fpRFDR spectra indicate the presence of ordered regions, 2D CHHC spectra exhibit Ca-Ca cross-peaks corresponding to intramolecular antiparallel β -sheets, and 2D DARR crosspeaks uniquely identify structural interaction between particular residues. These data implicate a partially folded, aggregation-prone intermediate along the unfolding trajectory – a common theme for proteins exhibiting aggregation [264]. The solid-state NMR data identify ten different residue positions (marked with gray background in Figure 3.8), *i.e.* Asn, Cys, and Trp residues, that may correspond to unstructured regions within the FGF-1 aggregate. These ten residue positions are distributed throughout the FGF-1 primary structure, although none lie within the folding nucleus (a contiguous region comprising 50% of the entire amino acid sequence) [245]. Notably, the observation that Cys is disordered in the aggregated state suggests that the Cys containing regions of FGF-1 are unstructured in the partially folded intermediate. Indeed, the functional half-life of FGF-1 is known to be dramatically reduced by thiol-mediated chemistries [265], which would be greatly accelerated upon exposure of Cys to solvent since all Cys residues are buried in the FGF-1 native structure [254]. Because the Cys residues neatly delineate the folding nucleus (Figure 3.8), the absence of strong Cys crosspeaks from the hydrated solid-state NMR spectra suggests the folding nucleus remains structured in the thermally aggregated state. In addition, the NMR data also identify a total of nine residue positions having structural features consistent with folded conformation; all of these positions lie within the folding nucleus (highlighted with inverse lettering in Figure 3.8). Thus, these data for the aggregate form of FGF-1 are consistent with a partially structured aggregate with persistent folding nucleus structure and are inconsistent with either a

domain-swapped oligomeric structure (*e.g.* TABFOs [266]) or an amyloid aggregate composed of fully-unfolded protein (*e.g.* A β amyloid [176], α -synuclein amyloid fibril [267]).

3.5.2 The Causes of Aggregate Propensity

Phifoil is a designed protein that is constructed from a triplet repeat of the FGF-1 folding nucleus primary structure [246]. Phifoil and FGF-1 exhibit a number of similar biophysical properties, such as overall thermostability ($\Delta G_{\text{unf}} = 21.9 \text{ kJ}\cdot\text{mol}^{-1}$ for FGF-1 and $20.7 \text{ kJ}\cdot\text{mol}^{-1}$ for Phifoil) and folding cooperativity ($19.4 \text{ kJ}\cdot\text{mol}^{-1}\cdot\text{M}^{-1}$ for FGF-1 and $17.5 \text{ kJ}\cdot\text{mol}^{-1}\cdot\text{M}^{-1}$ for Phifoil) – prompting the conclusion that these general folding properties of FGF-1 are dictated by the folding nucleus region [246]. However, while FGF-1 exhibits pronounced thermal aggregation, Phifoil exhibits reversible thermal denaturation; thus, the primary structure outside the folding nucleus region appears to be a prime contributor of thermal aggregation. The possible basis for such aggregation prone amino acid sequence could include: (i) a difference in net charge and isoelectric point; (ii) a difference in unstructured potential; (iii) different physicochemical properties (*e.g.*, hydrophobicity); or (iv) promotion of a kinetically-trapped intermediate in the folding pathway.

Proteins are known to be least soluble at their isoelectric point (pI) [268]; furthermore, increasing the net charge on a protein by mutation has been shown to increase the solubility and aggregation resistance of proteins [269]. Thus, the difference in aggregation properties between FGF-1 and Phifoil might be based upon differences in electrostatic properties. However, the predicted molecular charge as a function of pH indicates that FGF-1 and Phifoil have an identical net charge (although opposite in sign) of +5.9 and -5.9, respectively, at pH 6.6 (the pH at which the biophysical and thermal aggregation studies were performed). Thus, the tendency of FGF-1 to aggregate compared to Phifoil does not appear to be due to a difference in general charge magnitude.

The FGF-1 aggregate is consistent with amorphous structure in N- and C-terminal regions outside the folding nucleus. Thus, a difference in the unstructured potential of these

regions, or a difference in overall thermostability or folding cooperativity between FGF-1 and Phifoil, may contribute to FGF-1's propensity to aggregate. A comparison of the intrinsically unstructured potential (calculated using *IUPred* [270]) of the primary structure of FGF-1 and Phifoil suggests that the N- and C-terminal β -strands of FGF-1 actually have greater propensity for structure than Phifoil, and the general stability properties and unstructured potential of regions outside the folding nucleus for FGF-1 and Phifoil do not identify an obvious contributor to the thermally-induced aggregation of FGF-1.

Substantial data also identify the formation of intermolecular interactions between hydrophobic surfaces of partially folded intermediates as a driving force in protein aggregation [271]. With the exception of residue positions 129-137 in FGF-1, the N- and C-terminal regions outside the folding nucleus of both FGF-1 and Phifoil are broadly hydrophilic. Residue positions 129-137 comprise the C-terminal β -strand in the overall β -trefoil architecture. The primary structure of positions 129-137 in FGF-1 is a nine-residue stretch of exclusively hydrophobic amino acids (AILFLPLPV), whereas in Phifoil this region contains a majority of hydrophilic amino acids (HIQLQLSAE, Figure 3.8). The hydrophobic side chains in this C-terminal β -strand are largely buried in the native FGF-1 structure [254] and would thus transition to solvent exposure upon unfolding. Previously reported X-ray and solution NMR data indicate that the N- and C-terminal β -strands comprise a region of high relative structural mobility and are a likely region of initial unfolding [244]; furthermore, the thermal denaturation of FGF-1 is associated with ANS binding over pH 5.0–8.0, while Phifoil does not exhibit ANS binding over this pH range [246]. Thus, initial unfolding of FGF-1 is associated with exposure of hydrophobic groups while Phifoil is not.

A metastable unfolding intermediate involved in the aggregation process is also indicated by some properties of FGF-1. Previous studies of FGF-1 thermal denaturation reported that aggregation initiates near the apparent T_m and is concomitant with the formation of a species that strongly binds 1-Anilino-8-naphthalnesulfonate (ANS) [272], a reagent to detect molten globule-like states. Similarly, while DSC studies of FGF-1 performed in the

presence of 0.6 M GuHCl enabled reversible thermal denaturation, an analysis of the endotherm was consistent with non-two-state denaturation and the presence of an unfolding intermediate [255].

Taken together, the data are consistent with an unfolding process for FGF-1 that involves: (i) initial unfolding of regions outside the folding nucleus; (ii) concomitant exposure of a C-terminal region rich in hydrophobic residues; (iii) intermolecular aggregation promoted by hydrophobic interactions. Aggregations triggered by partially-folded structures have also been reported for other proteins, such as Het-s prion [273].

3.5.3 Protein Functions and Folding Stability

In the view of protein functions, the folding nucleus region of FGF-1 largely excludes functional residues; correspondingly, Phifoil, consisting of only amino acid sequences from FGF-1 folding nucleus, is devoid of known functionality. Constraints upon the FGF-1 folding nucleus region appear to be principally limited to providing for an efficient folding pathway, and not functionality. Thus, as a region, the folding nucleus is unlikely to contain regions of extreme charge or hydrophobicity, or to have general properties of insolubility or intrinsic disorder – properties that might arise under a functional constraint. The folding nucleus symmetric expansion (FNSE) methodology [246] used to “fill in” the missing primary structure of Phifoil outside the folding nucleus produced a protein that, while devoid of functional sequences, was consequently also devoid of regions having extremes of physicochemical properties that could promote aggregation. If the key heritable element for foldability acted on by gene duplication and fusion evolutionary events [274], which lead to the common symmetric protein architectures, includes the folding nucleus then the natural consequence may be folding cooperativity that avoids aggregation.

3.5.4 A Peek at The Aggregation Pathway of Well-Folded Proteins

In the study of the cause of FGF-1 aggregation, we combined the ssNMR measurements of the aggregated state and the phi-value analyses of the FGF-1 folded state to reveal the connection between the aggregating and the folding intermediate. Previous phi-value analysis and thermodynamic measurements indicated that FGF-1 has a partially folded intermediate during the normal folding/unfolding process, and the folded region in the intermediate is defined as the folding nucleus. With the help of Hydrogen-Deuterium exchange technique, we knew that the folding intermediate largely reserves the native folding conformation in the folded regions [244]. Meanwhile, our ssNMR data showed that the folding nucleus native structure persists in the aggregated state, which implies that the aggregating intermediate also has a native-like folding nucleus region. Thus, the native-like folded folding nucleus not only triggers the native folding, but also initiates the thermally aggregation of FGF-1. In other words, the functional protein folding and the dysfunctional aggregating may have an identical intermediate. A slight change in solution condition alters the paths of structural transformation.

Because FGF-1 is a well-folded functional protein with a common β -propeller architecture, the aggregating mechanism involving a native-like folding nucleus may be generalized to the proteins with symmetric architectures (*e.g.*, myocilin olfactomedin domain with five-blade β -propeller). The determination of the folding nucleus region could also be critical to find the aggregation-triggering primary sequence.

CHAPTER 4

COMPREHENSIVE ANALYSES OF MOLECULAR STRUCTURE OF 150-KDA OLIGOMERS FORMED BY THE ALZHEIMER'S AMYLOID- β (1–42) PEPTIDE

Portions of this chapter have been adapted and reproduced from Y. Gao, C. Guo, J. O. Watzlawik, P. S. Randolph, E. J. Lee, D. Huang, S. M. Stagg, H.-X. Zhou, T. L. Rosenberry, and A. K. Paravastu, “Out-of-register parallel β -sheets and antiparallel β -sheets coexist in 150-kDa oligomers formed by amyloid- β (1–42),” *J. Mol. Biol.*, vol. 432, no. 16, pp. 4388–4407, 2020 [275]. Copyright 2020 Elsevier (See Appendix A for the reprint license agreement). Additional supporting materials is included in Appendix D.

4.1 Project Overview

Dr. Rosenberry's lab found that sodium dodecyl sulfate (SDS) near its critical micelle concentration can drive the assembly of A β (1-42) along a pathway that produces 150 kDa peptide oligomers (around 32 peptides) but does not produce amyloid fibrils. We utilized multiple 2D NMR and ^{13}C - ^{13}C dipolar recoupling experiments to reveal the molecular structural features of these oligomer samples and try to shed some light on the oligomeric assembly pathway.

Our previous report indicated a β -strand spanned by residues 30–42, namely C-strand, arranges into an antiparallel β -sheet. New results presented here indicate that there is a second β -strand formed by residues 11–24, namely N-strand. Contrary to expectations, NMR data indicate that N-strands are organized into a parallel β -sheet despite the co-existence of an antiparallel β -sheet in the same structure. For the N-strand parallel β -sheet, we also found evidence for an inter-strand registry shift of three residues that likely alternate in direction between adjacent N-strands.

We also obtained new atomic-level constraints via improved-resolution ssNMR spectroscopy on samples concentrated by ultracentrifugation. More importantly, 2D cryo-EM reconstruction reveals a previously unknown 4-fold symmetric structure with a central pore in the oligomer particles. To rationalize the NMR constraints and the cryo-EM-resolved dimensions, we propose a domain-swapped structural model. Our model predicts alternating domain-swapped and non-swapped peptide conformations along each β -sheet, and also demonstrates how parallel and antiparallel β -sheets can coexist in a single aggregate structure. The proposed structural model motivates the hypothesis that a recently published tetramer structure may be a precursor in the pathway forming 150 kDa oligomers. The structural model and the pathway-based interpretation may explain why 150 kDa oligomers do not undergo further assembly into amyloid fibrils.

4.2 Introduction

An unmet challenge in Alzheimer's disease research is the determination of structures of oligomeric assemblies of the amyloid- β peptide (A β). Oligomers may represent the most pathological species in patient brains [106, 276–278]. In this context, an oligomer is an assembly composed of 50 A β peptides or fewer (mass range: 9 to 200 kDa). This range spans oligomers in brain-detected and lab-synthesized samples [75, 98, 99]. Compared to insoluble amyloid fibrils with lengths up to several micrometers, oligomers can diffuse further or interact with more cells due to their small size [279]. It has been proposed that oligomers could originate in the neuronal membrane following enzymatic cleavage of the amyloid precursor protein, where oligomers could be pathological without being readily detectable [280]. Understanding oligomeric structures, underlying assembly mechanisms, and oligomer-membrane interactions could help explain proposed mechanisms of oligomer toxicity. Proposed oligomer toxicity mechanisms include outer and mitochondrial membrane permeabilization [55, 58], disruption of Na⁺ or Ca²⁺ regulation [60, 61], and receptor-mediated apoptosis [63, 64].

Studying oligomeric structures with solid-state NMR techniques is challenging because it is difficult to produce samples with homogeneous and stable structures. Structural heterogeneity occurs because A β can self-assemble along a variety of pathways. Most A β aggregates have β -strand secondary structures and are broadly classified in terms of their nanoscale dimensions [75]. Oligomers are the smallest assemblies (10 nm or less), appearing as roughly spherical nanoparticles when imaged by electron microscopy (EM) or atomic force microscopy (AFM) [57, 100, 185]. Protofibrils are elongated assemblies with widths of 10 nm or less and lengths on the order of 100 nm, corresponding to the assembly of hundreds of molecules [111]. Fibrils can be microns long, with dimensions consistent with organization of millions of molecules [113]. The aggregation pathways possible for A β have not been characterized comprehensively or in full atomic detail, but it is known that the peptide can form multiple fibril structures [38, 168]. Assembly pathways and concomitant aggregate structures are susceptible to the solution environment [199] and interactions with interfaces during assembly [281]. Distinct fibril structures have also been observed for different A β isoforms (e.g., A β (1-40) vs. A β (1-42)) or mutants (e.g., Iowa, Dutch) of A β [282, 283]. Atomic-level structural knowledge has been obtained for some stable homogeneous A β fibril samples [88, 89, 176, 177, 284], but considerably less structural information is known for protofibrils and oligomers. Nevertheless, some reports suggest a variety of possible oligomer structures (Section 1.1.1.3).

Dr. Rosenberry's lab produced a stable A β (1-42) oligomer sample with around 150 kDa mass, comprising about 32 A β peptides. The assembly of this large oligomer is driven by interaction with the anionic detergent SDS near its critical micelle concentration [285]. Initially, 2–4mer species are formed by A β monomers. Dialysis to remove SDS results in an increase in aggregate size to 150 kDa, as determined by multi-angle light scattering [286] (Figure 4.1). Significantly, the formation of 150 kDa oligomers goes through an assembly pathway that is not relevant to amyloid fibril formation [285] (Figure 4.1). The 150 kDa oligomers are assumed to have similar neurotoxicity to the globulomers [60,

61] because they are both produced under membrane mimicking environments [121] and both classified as “off-pathway” oligomers (Section 1.1.1.2). We are interested in the structure of the 150 kDa oligomers because they are not only potentially pathogenetic but also pathway-dependent. Thus, the structural study of this oligomer sample may reveal the detailed mechanism in the oligomeric assembly pathway.

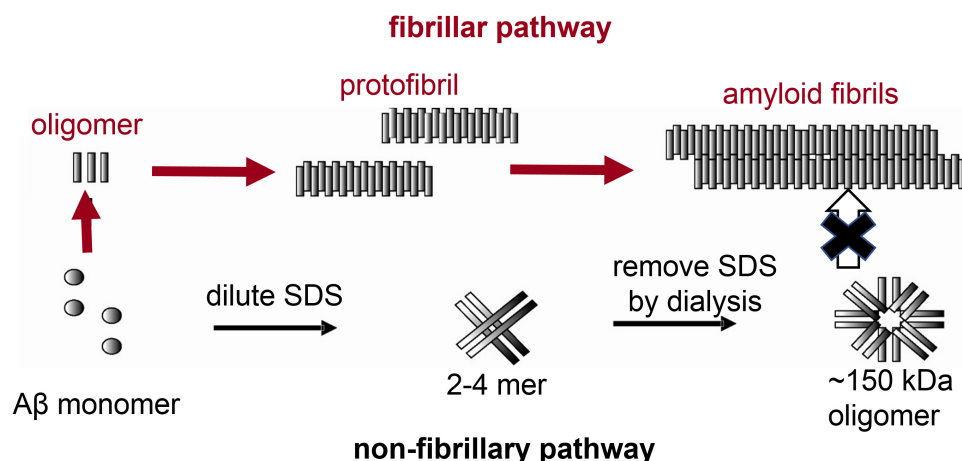


Figure 4.1 The fibrillar and non-fibrillar pathway of Aβ(1-42) assemblies. The fibrillar pathway produces mature amyloid fibrils. The non-fibrillar pathway generates 150 kDa Aβ(1-42) oligomers, which cannot quickly converted into amyloid fibrils [285].

In this chapter, we show how the NMR data reveals a unique arrangement of β-strands in this oligomer sample. In the unique arrangement, Aβ(1-42) peptide has two β-strand regions – N-strand (E11 to V24) and C-strand (A30 to A42) (Figure 4.2). The C-strands were found to assemble into antiparallel β-sheets [186]. However, our NMR data also indicated that the N-strands form out-of-register parallel β-sheets, and the inter-strand registry shifts are likely to alternate between +3 and -3 [275] (Figure 4.2). Parallel arrangement of N-strands appears to contradict the antiparallel arrangement of C-strands, which cannot be rationalized by any known amyloid structures. The only known Aβ aggregate with both parallel and antiparallel β-strands was from Yu *et al.*, which is a dimer structure with an intermolecular pair of parallel β-strands and two intramolecular antiparallel β-hairpins [118] (Figure 1.2B).

However, it is not clear how such a structure could be extended to a larger oligomer.

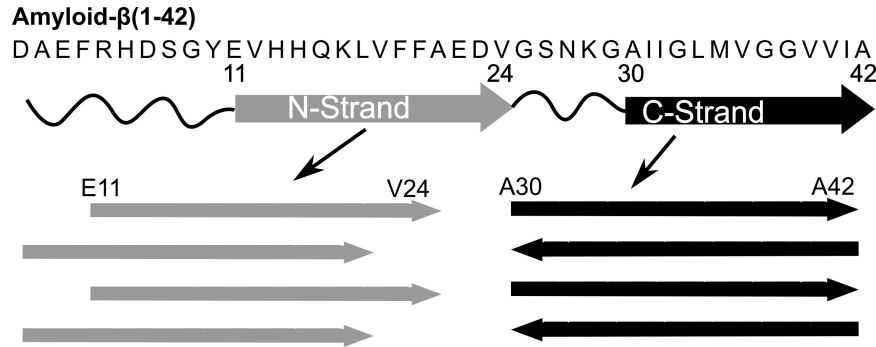


Figure 4.2 The conformation of N-strand and C-strand regions in 150kDa A β (1-42) oligomers.

As illustrated in Figure 4.3, we are not aware of any measured or modeling A β aggregate structure that is consistent with our data on the 150 kDa oligomer. Structural features unique to the 150 kDa oligomer include 1) a registry-shifted parallel N-strands, 2) antiparallel C-strands, and 3) multi-site occupancy. The complex pattern of β -strand alignments were established primarily by ^{13}C - ^{13}C dipolar recoupling measurements, which we will describe in Section 4.4. Figure 4.3 employs DARR contact charts to illustrate why the pattern of experimentally measured inter-residue proximities differs between the 150 kDa oligomers and the previous experimentally-based structures (see Section 2.4.2).

In addition to not explaining the intermolecular arrangement, existing structural knowledge cannot elucidate the size of the 150 kDa oligomer. A foundational aspect of the special toxicity of A β oligomers is their existence for an appreciable time with a structure that is distinct from amyloid fibrils. Reports indicate that non-fibrillar aggregates are not necessarily intermediates that undergo further aggregation to form amyloid fibrils [107, 285]. Instead, dissociation such “off-pathway” aggregates into monomers must likely occur first [87]. Analysis of 150 kDa oligomers by size exclusion chromatography (SEC) and multi-angle light scattering (MALS) indicates that these particles do not grow to fibrillar dimensions. Furthermore, measurements based on thioflavin-T fluorescence indicate that 150 kDa

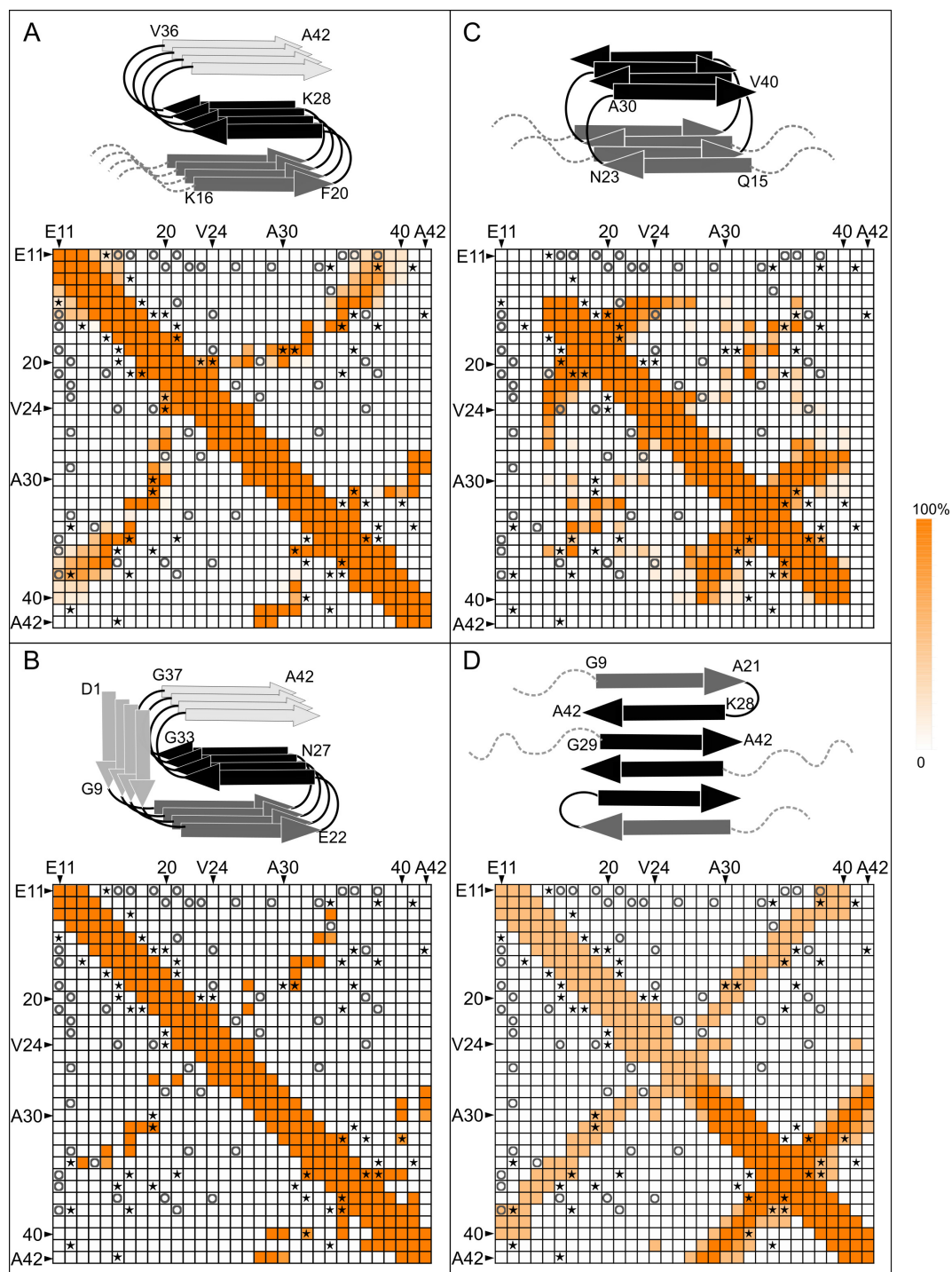


Figure 4.3 Comparison of some A β aggregate structures with our experimental NMR constraints in DARR contact chart (Section 2.4.2). (A) A β (1-42) fibril structure determined by Colvin *et al.* [89]. (B) A β (1-42) fibril structure from cryo-EM measurement [176]. (C) Iowa mutant A β (1-40) fibril [284]. (D) A tetramer A β (1-42) oligomer [120].

oligomers do not seed assembly of monomeric A β (1-42) to amyloid fibrils [285]. These observations appear inconsistent with the β -sheet structure since the β -sheet is an approximately planar structure with hydrogen bond donors and acceptors at the ends (that could recruit additional β -strands) regardless of size. Present knowledge establishes that β -sheet oligomers exist but do not explain why such a structure would not undergo further aggregation to produce amyloid fibrils. Previously proposed theories for oligomer size limitation include: 1) geometries for oligomer structure, such as the barrel shape [287], characterized by increasing strain with increasing size or complete incompatibility with growth beyond a limit, and 2) kinetic size limitation via a dissociation rate that balances the growth rate [288]. It has also been suggested that oligomer structures may be more disordered when compared with fibrils, and such disorder may be caused by competition between conformations, leading to a kinetic size limitation [86].

In the result section, we first present how the β -strand regions are identified and the arrangement of N-strands are determined. Then, the ssNMR spectra from ultracentrifuged samples and the cryogenic EM (cryo-EM) images of oligomer particles are analyzed. The resolution of observed NMR spectra was improved by employing ultracentrifuge to pellet oligomers into solid-state NMR rotors (Section 2.2.3). New cryo-EM constraints on oligomer nanoscale shape and size provide critical information analogous to scanning transmission EM-derived mass per unit length measurements used in the previous modeling of fibril structure [89, 177]. Our analysis culminates in a proposed structural model that rationalizes numerous NMR and EM constraints. In addition, we proposed the possible explanations for the limited size and the cytotoxicity of the oligomers.

4.3 Materials and Methods

4.3.1 A β (1-42) Peptide Synthesis

A β (1-42) peptides with or without ^{13}C and ^{15}N labels were synthesized by New England Peptide, by the Proteomics Core at the Mayo Clinic, and by our lab, which all equipped

Liberty Blue solid-phase peptide synthesizers from CEM. The isotope-labeled compounds used in syntheses were all purchased from Cambridge Isotope Laboratories.

4.3.2 A β (1–42) 150kDa Oligomer Preparations for Solid-State NMR

The crude product of A β (1–42) peptide synthesis was dried from hexafluoroisopropanol (HFIP), dissolved with 0.1 M NaOH, and subjected to SEC on a Superdex 75HR 10/30 column equilibrated with 20 mM sodium phosphate (pH 7.5; at a flow rate of 0.5 ml/min) to isolate A β (1–42) monomers as previously described [185, 186]. Aliquots of SEC-purified A β monomer were incubated overnight at room temperature with 50 mM sodium chloride and 4 mM SDS to give initial small oligomers called 2–4mers. The solution of 2–4mers was then dialyzed against 20 mM NaP for 48–72 h with at least five buffer changes and then against 10 mM NaP for 3–4 h to remove SDS and reduce the concentration of salt. The quality of oligomer samples was tested by circular dichroism and ThT fluorescence at each step of preparation. Finally, residual or unassembled monomers were removed by filtering with an Amicon Ultra 4 centrifugal concentration/filtration device, which has a molecular mass cutoff of 50 kDa.

For solid-state NMR experiments, at least five preparations were performed for each sample to provide sufficient amounts of oligomers (5–9 mg). The preparations for one sample were combined, flash-frozen, and immediately lyophilized. The lyophilized oligomer samples were stored at -80 °C until use. The isotope-diluted samples were prepared from isotope-labeled and unlabeled A β (1–42) monomers mixed in the desired ratio.

For the ultracentrifugation of ssNMR samples, the oligomer solution was first combined and concentrated to 1mg/mL. Then, the solution was loaded onto the rotor packing widget (Figure 2.3) and perform overnight ultracentrifuge (280,000 x g, 24 h at 4 °C) to ensure all the oligomers were packed in to the bottom of rotor.

4.3.3 Solid-State NMR Experiments

All the ssNMR experiments were performed on a Bruker narrow-bore 11.7 Tesla magnet (^1H frequency of 500 MHz), equipped with a 3.2-mm HCN MAS probe. The 2D fpRFDR and 2D DARR spectra are 2D ^{13}C - ^{13}C exchange experiments with different mechanisms to reintroduce dipolar coupling between ^{13}C and thus providing cross-peaks. Proton decoupling with a ^1H radiofrequency field of 100 kHz was used in fpRFDR recoupling periods and acquisitions, and two-pulsephase modulation [74] was selected to be the decoupling method. In 2D DARR experiments, continuous irradiation with power corresponding to 11 kHz nutation frequencies (same as the MAS spinning rate) in the ^1H channel was applied during the exchange periods. The lengths of exchange periods were set to 50 or 500 ms for verifying intraresidue contacts or detecting inter-residue longdistance contacts, respectively. For 2D fpRFDR experiment, the power of the π pulse on ^{13}C channel was adjusted to 33 kHz to match the duration (15.2 μs) of one-third of rotor period at 22 kHz MAS. The signal averaging of 2D fpRFDR and 2D DARR required 36 to 48 h. For isotope-diluted samples, the signal averaging was increased to 72 h due to less ^{13}C in the sample. To determine the positions and the linewidths of crosspeaks on 2D fpRFDR spectra, non-linear fitting with a 3D Gaussian function was performed for each crosspeak. We treated board crosspeaks as single 3D Gaussian peak, although it might consist of several overlapping peaks from the same residue in different conformations.

PITHIRDS-CT experiments were performed with a MAS spinning rate of 12.5 kHz. The dipolar recoupling time was adjusted by number of blocks of pulses (k_1 , k_2 , and k_3 defined by Tycko [206]), and it was fixed to be between 0 and 61.4 ms in our measurements. Proton decoupling of 100 kHz was conducted by continuous wave decoupling during PIRHIRDS recoupling and acquisition. PITHIRDS data were generated from signal averaging of about 24 h. All the peak intensities in PITHIRDS data sets were corrected by subtracting signals contributed by natural abundance ^{13}C in A β (1–42) molecule. We estimate natural abundance signal by multiplying the number of similar ^{13}C sites with the isotopic abundance of

^{13}C , and we assume the correction intensity is constant for all evolution time. For backbone ^{13}CO labels in A β (1–42), there are 35 similar CO sites per molecule (excluding all glycines and the C terminus). For alanine $^{13}\text{C}\beta$ labels, there are 22 similar methyl sites per molecule.

4.3.4 TEM and cryo-EM

Imaging by TEM was performed on 150kDa oligomers prepared with the same protocol we use for ssNMR, but without the lyophilization step. The samples were imaged through negative stain TEM (2% uranyl acetate) on a CM120 BioTwin. Dilution series were conducted to determine optimal concentration for particle dispersion. Grids were prepared within 72 h of sample preparation, as aggregation would become an issue after this window.

4.3.5 Molecular Modeling

Anti-parallel and parallel β -sheets were built by assembling β -strands with VMD (Visual Molecular Dynamics) scripts [238]. A single β -strand was generated by Ambertools using standard backbone torsion angles (anti-parallel β -sheets: $\phi = -139^\circ$, $\psi = 135^\circ$; parallel β -sheets: $\phi = -119^\circ$, $\psi = 113^\circ$). Anti-parallel β -sheets were built by replicating a two-stranded sheet, in which two replicate β -strands ran in opposite directions and were at an inter-strand distance of 0.48 nm. In-register parallel β -sheets were built by replicating a single β -strand with an inter-strand distance of 0.48 nm. Out-ofregister parallel β -sheets were built upon in-register ones in two steps. First, an in-register parallel β -sheet consisting of alanine residues was built in the above-mentioned way. Second, an out-ofregister β -sheet in A β sequence was constructed by replacing alanine residues with the corresponding A β residues. For parallel β -sheets with n A β residues per strand and a registry shift of i , residues 1 to n in the first strand were replaced, residues i to $i+n$ in the second strand were replaced, and so on. Residue replacements were carried out with the Mutagenesis Wizard in PyMOL.

4.3.6 NMR-Related Spin Simulation

Simulated PITHIRDS-CT curves were generated using SPINEVOLUTION [204] with the use of parameters that matched the experimental conditions. Briefly, all ^{13}C atoms were treated as identical spins and their positions were fixed by atomic coordinates. All the initial spin vectors were in + x direction, and they evolved according to the pulse sequence of PITHIRDS. The intensities of detected signal at different time points were stored and were used to plot the simulation curves. The REPULSION powder averaging scheme (376 pairs of α and β Euler angles and 36 γ angles) was used for the simulations [289].

Simulations for singly labeled samples were based on a linear eight-spin system, which is a linear array of eight ^{13}C spins separated by identical constant distances. For doubly labeled samples, the simulated curves were generated from a 16-spin system, which used the coordinates of sixteen ^{13}CO sites from eight strands in the idealized models of out-of-register β -sheets. The 16-spin system was divided into three eight-spin simulations to reduce computing time. The eight-spin simulations included ^{13}C spins on the first four strands, the third to the sixth strand, or the fifth to the eighth strand. The NMR signal for the 16-spin system was computed using the simulated spin polarizations of non-overlapping portions of the three eight-spin simulations. For the four-spin simulation, only four ^{13}CO sites from two neighboring strands were involved. In addition, two sets of parameters of chemical shift anisotropy were used for spins in each simulation. One set is isotropic chemical shift ($\delta_{aniso} = 0$ ppm, $\eta_{\Omega} = 0$, $\alpha_{\Omega} = 0^{\circ}$, $\beta_{\Omega} = 0^{\circ}$, $\gamma_{\Omega} = 0^{\circ}$), and the other is the anisotropic parameters measured from L17 CO ($\delta_{aniso} = -75$ ppm, $\eta_{\Omega} = 0.75$, $\alpha_{\Omega} = 0^{\circ}$, $\beta_{\Omega} = 0^{\circ}$, $\gamma_{\Omega} = 0^{\circ}$). These parameters are required input for SPINEVOLUTION.

4.4 Experimental Results

4.4.1 2D ^{13}C NMR Spectra Reveal Two β -Strands and Evidence for Multi-site Occupancy

Spectral assignments, correspondences between ^{13}C NMR peaks and isotopically labeled sites, were determined by collecting 2D ^{13}C - ^{13}C fpRFDR and short-mixing DARR spectra (Section 2.3.2.4 and 2.3.2.5) on samples that were uniformly ^{13}C -labeled within selected amino acids. Table 4.1 reports the isotopic labeling employed for the full series of 150-kDa oligomer samples examined in the study. Figure D.1 and D.2 show the 2D-fpRFDR spectra for samples 4.1 to 4.14, with labels chosen so that structure could be assessed for the whole A β (1-42) peptide. Table D.1 tabulates all ^{13}C NMR peak positions (chemical shifts) and peak widths we have measured from the spectra of samples 4.1-4.14 (Figure D.1 and D.2).

We can assess the peptide secondary structure through analysis of ^{13}C chemical shifts for backbone carbon sites. Figure 4.4A reports secondary ^{13}C chemical shifts of all CO, C α , and C β for 34 sequential residues and indicates the presence of two β -strand regions. Secondary structure is known to correlate with ^{13}C chemical shift when CO, C α , and C β chemical shifts deviate in systematic ways from corresponding random-coil values for contiguous sequences of amino acids within the primary structure [229]. To be more precise, we fed the assigned chemical shifts and peptide sequence into a computer program called TALOS-N [231] to predict the backbone torsion angles (ϕ/ψ). For the 150 kDa oligomer, TALOS-N predicts the presence of two β -strands as shown in Figure 4.4C. The β -strands span residues 11–24 and 30–42; we refer to them as the N-strand and C-strand, respectively. The regions spanned by residues 1–10 and 25–29 are predicted to be an unstructured segment and a turn, respectively.

An interesting observation is that the linewidths were larger for N-strand ^{13}C signals than the C-strand counterparts, especially for the residues near the ends of the N-strand (Figure 4.4B). On average, the CO, C α , and C β linewidths were 3.3 ± 0.5 , 3.2 ± 0.5 , and 4.0 ± 1.1 ppm (95% confidence region for full width half maximum), respectively, for the N-

Table 4.1 Isotope labeling employed for the 150-kDa oligomer samples. The samples that are ultracentrifuged into NMR rotors are indicated by “*”.

| Sample | Isotope labeling |
|--------|---|
| | Uniform ^{13}C , ^{15}N labeling at the indicated residues: |
| 4.1 | K16, F20, V24, G37 |
| 4.2 | D7, G9, E11, L17, F19, A21 |
| 4.3 | E11, F19, I31, V36 |
| 4.4 | E11, L17, A21, M35, G38 |
| 4.5 | I32, M35, G37, V40 |
| 4.6 | Q15, V18, A21 |
| 4.7 | S8, Y10, V12, L34, G38, I41 |
| 4.8 | V12, E22, S26, N27, G33 |
| 4.9 | V12, F20, D23, K28, G29 |
| 4.10 | E11, H13, Q15, L17 |
| 4.11 | E11, K16, F19, V36 |
| 4.12 | A2, E3, F4, G9, V39 |
| 4.13 | H14, K16, L34, A42 |
| 4.14 | F19, V24, G25, A30, I31, L34, M35 [185] |
| 4.15* | V12, D23, K28, M35, G38 |
| 4.16* | K16, F19, G25, V36 |
| 4.17* | F19, E22, V24, S26 |
| | Selective ^{13}C labeling at the indicated sites: |
| 4.A | L17 CO |
| 4.B | V18 CO |
| 4.C | F19 CO |
| 4.D | F20 CO |
| 4.E | A21 CO |
| 4.F | L17 CO and F19 CO |
| 4.G | V18 CO and A21 CO |
| 4.H | L17 CO and A21 CO |
| 4.I | A30 C β and V36 CO |

strand residues. The corresponding average linewidths for the C-strand were 2.5 ± 0.4 , 2.7 ± 0.2 , and 3.0 ± 0.7 ppm. It suggests that N-strand residues occupy multiple magnetically inequivalent sites while C-strand residues do not. We will see more obvious multi-site occupancy when we analyze the higher resolution NMR spectra from the ultracentrifuged samples.

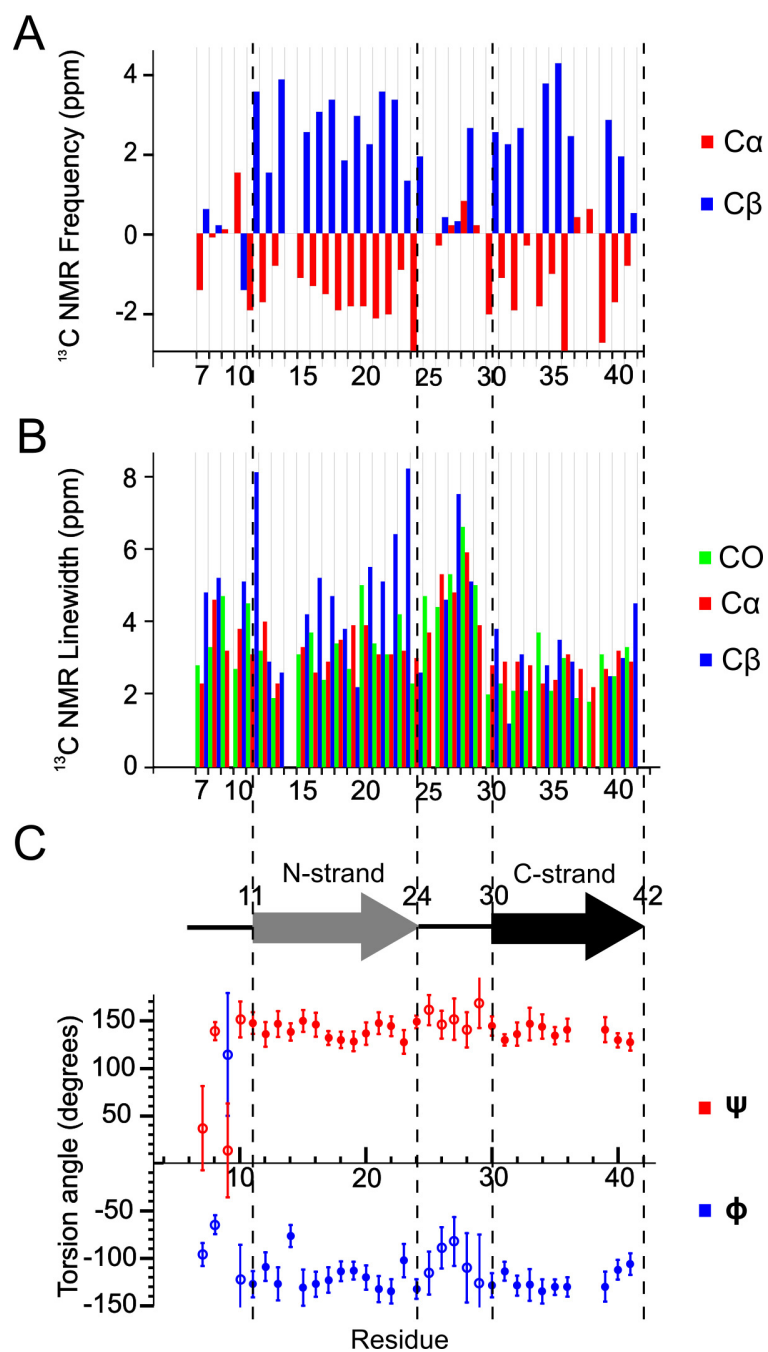


Figure 4.4 Use secondary chemical shift values to predict the secondary structure regions in the 150-kDa Aβ(1–42) oligomer. (A) The measured secondary ^{13}C NMR backbone chemical shifts. (B) The NMR linewidths of CO (green), $\text{C}\alpha$ (red), and $\text{C}\beta$ (blue). (C) The secondary structure regions and the torsion angles predicted by TALOS-N.

4.4.2 2D DARR and PITHIRDS-CT Results Support Out-of-Register Parallel β -Sheet Models for The N-Strand

The antiparallel arrangement of C-strands was characterized in our previous report [186], and we want to look further into the inter-strand correlation of N-strands. To obtain NMR structural constraints, we collected 2D DARR spectra with 500 ms mixing time for the sample 4.1 to 4.14. Figure 4.5A shows the 2D-DARR spectrum of Sample 4.1 (K16, F20, V24, and G37). With this spectrum, we observed inter-residue contacts between K16 and F20 and between F20 and V24. Since these contacts each correspond to a pair of residues that are four residues apart within the N-strand, they must arise from intermolecular ^{13}C - ^{13}C dipolar couplings because the N and the N+4 residue are too faraway on a β -strand. Additional 2D-DARR spectra showing detected inter-residue crosspeaks are presented in Figure D.3 to D.6. Finally, a total of nine inter-residue DARR contacts, for N-strand residue pairs that are separated by three or four residues in sequence, were observed and shown as stars in Figure 4.5B. The detected contacts, as well as the undetectable contact (anticipated but not observed) are mostly consistent with the predicted contacts from parallel β -strands with +3 or ± 3 registry shift (Figure 4.5C and D).

We performed PITHIRDS-CT experiments on singly labeled samples (4.A to 4.E) and doubly labeled samples (4.F to 4.H in Table 4.1) to further test the backbone interactions between N-strands. First, the measured PITHIRDS decays from sample 4.A to 4.E are all considerably weaker than the simulated 0.5 nm distance curve (Figure 4.6A), indicating that we did not detect the influence of intermolecular dipolar couplings for these singly ^{13}C -labeled samples. The results—site-independent weak PITHIRDS decays—tell a completely different story from C-strands [185] and rule out an in-register parallel β -sheet or an antiparallel β -sheet for N-strands. Second, in comparison to the decay observed with ^{13}C labeling of the oligomer at only one site (sample 4.A), samples with pairs of ^{13}C -labeled CO sites exhibited measurably stronger PITHIRDS-CT decays (Figure 4.6B). For samples 4.F, 4.G, and 4.H, the ^{13}C -labeled sites were either two residues apart (sample 4.F: L17

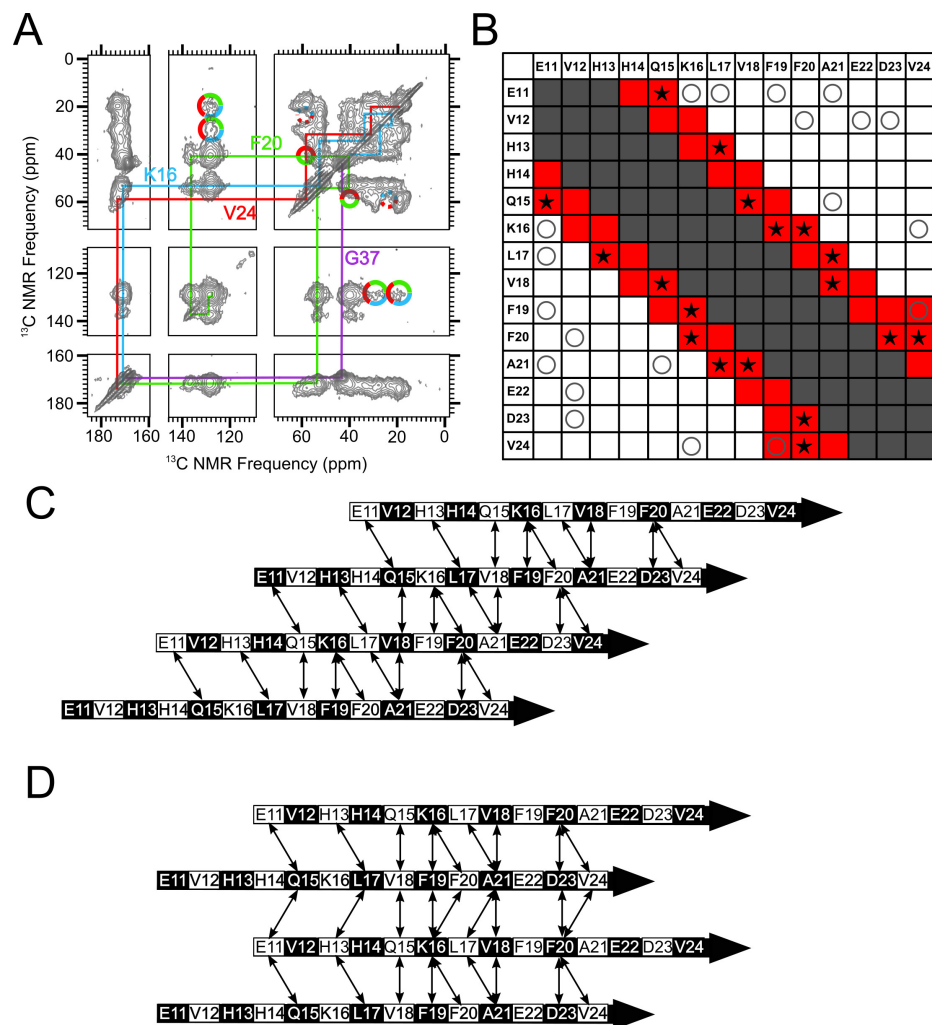


Figure 4.5 A parallel N-strand β -sheet shifted three residues out of register is consistent with the NMR constraints. (A) 500 ms 2D-DARR spectrum of sample 4.1, which was uniformly ^{13}C -labeled at residues K16, F20, V24, and G37. The colored lines indicate intra-residue cross-peaks, and the multi-colored solid circles indicate observed inter-residue crosspeaks. (B) A DARR contact chart comparing the observed NMR constraints and the contacts predicted from the arrangement in panel C and D. (C) +3 registry-shifted parallel β -sheet. Black and white shading on the β -strand schematics indicates whether an amino acid side-chain is above or below the plane of the diagram, respectively. (d) ± 3 registry-shifted parallel β -sheet. The double-headed arrows in panel C and D convey the observed contacts in panel B.

and F19), three residues apart (sample 4.G: V18 and A21), or four residues apart (sample 4.H: L17 and A21). Stronger PITHIRDS-CT decay for doubly labeled samples relative to sample 4.A supports the presence of an out-of-register parallel N-strand β -sheet because the

enhancement of decays indicates backbone proximity of N-strands.

The PITHIRDS-CT decays in Figure 4.6B can be rationalized in terms of relative atomic positions predicted by molecular models of out-of-register parallel β -sheets. Figure 4.6C illustrates the relative positions of the ^{13}C -labeled sites for samples 4.F, 4.G, and 4.H within candidate models with registry-shifted parallel N-strand β -sheets. The PITHIRDS-CT technique was originally designed to characterize “fully coupled” spin system, in which every ^{13}C -labeled site experiences a dipolar coupling with at least one other ^{13}C -labeled site within 0.5 nm, such as ^{13}CO labels in an in-register parallel β -sheet. However, in an out-of-register parallel β -sheet, the single ^{13}CO label becomes “fully uncoupled” and thus provides site-independent weak decays. By introducing the second ^{13}C -labeled site on N-strand, we deliberately create a “half coupled” spin system that modified the results of signal decay (Figure 4.6C). If we perform spin simulations according to the nuclei positions in these doubly labeled system, we can find the best consistency with data is from the model with ± 3 registry shift (Figure 4.7).

4.4.3 NMR Spectra with Higher Resolution Yielded New Structural Constraints

We used lyophilization to dry oligomer samples to minimize the possibility of further aggregation during NMR measurements, although lyophilization is also known to broaden NMR lines in amyloids [169]. To improve NMR spectral resolution, we employed ultracentrifugation to load oligomer samples into NMR rotors (Section 2.2.3) and performed NMR measurements on the wet ultracentrifuged pellets. During the ultracentrifugation and the NMR test, the 150 kDa oligomers sample is kept at 4 °C to ensure its stability. Three A β (1-42) 150 kDa oligomer samples with isotope labeling were packed and tested in this way (Sample 4.15 to 4.17 in Table 4.1).

We first performed 2D DARR experiment on the ultracentrifuged samples with 50 ms mixing time. The spectra shows all the intra-residue crosspeaks for the ^{13}C -labeled residues. The positions of the crosspeaks are consistent with those from previous lyophilized samples

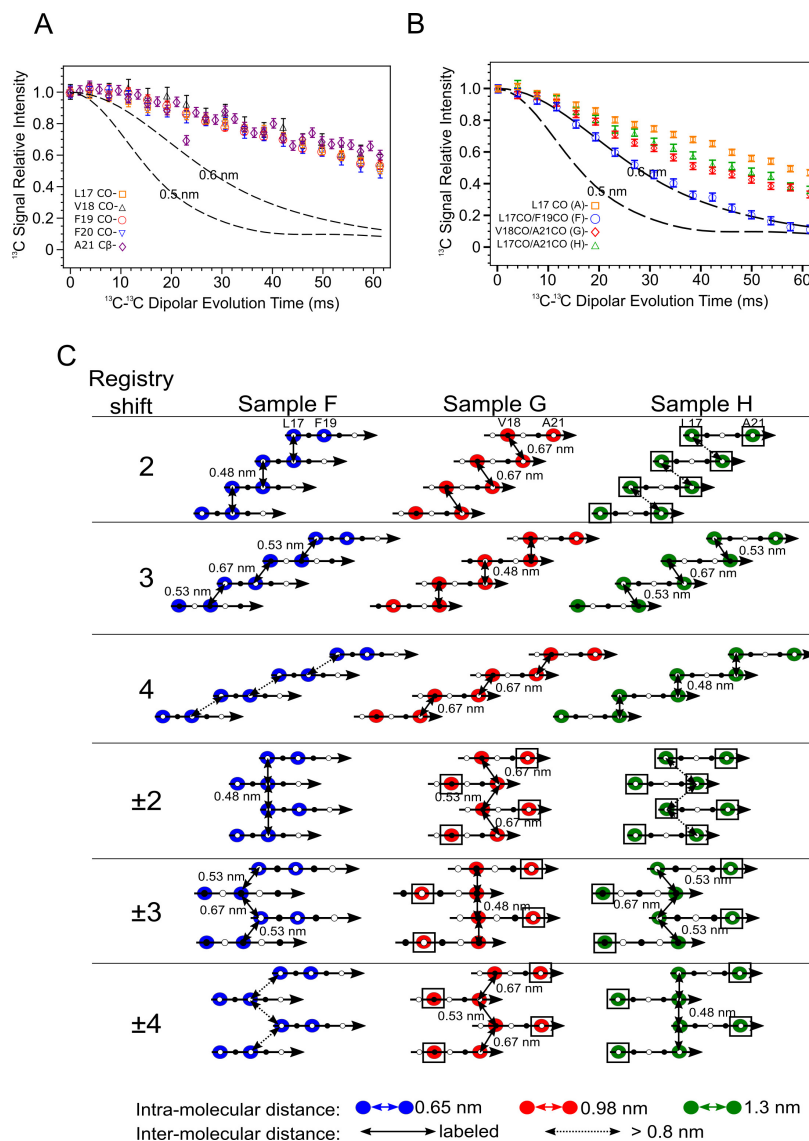


Figure 4.6 Doubly ^{13}C CO-labeled PITHIRDS-CT data indicate out-of-register alignments of the N-strands. (A) PITHIRDS-CT data measured for 150 kDa A β (1–42) oligomer samples with ^{13}C -label at one backbone CO position per molecule within the N-strand (samples 4.A–4.E). Dashed lines in PITHIRDS-CT panels indicate simulated ^{13}C interatomic distances that were calculated for a linear array of eight ^{13}C spins separated by the indicated identical constant distances (Section 2.3.2.2). (B) PITHIRDS-CT data for 150 kDa oligomers ^{13}C -labeled at two backbone CO positions within the N-strand (samples 4.F, 4.G, and 4.H). For comparison, the PITHIRDS-CT curves for sample 4.A (^{13}C at L17 CO) are also plotted. (C) Diagrams illustrating the relative positions of ^{13}C -labeled CO sites for samples 4.F, 4.G, and 4.H, predicted by different registry shifts. Colored circles indicate residues in which CO sites are ^{13}C -labeled. Doubled headed arrows indicate ^{13}C - ^{13}C distances between the labeled sites. Boxes around circles indicate positions of uncoupled spins.

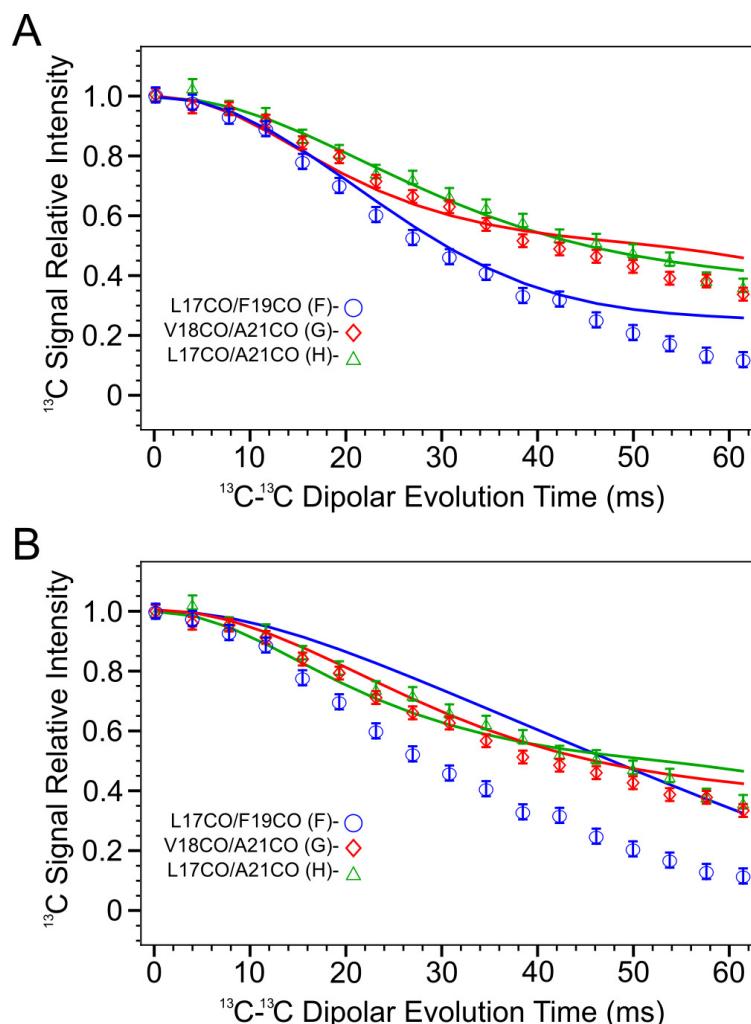


Figure 4.7 Simulated PITHIRDS-CT curves and measured data for samples 4.F, 4.G, and 4.H according to ^{13}C atom coordinates in parallel β -sheet with registry shift ± 3 (A) and ± 4 (B). Each simulated curve has the same color as the corresponding data series (blue: sample 4.F, red: sample 4.G, and green: sample 4.H).

with the same isotope-labeled residues, but the linewidths are sharper (Figure 4.8A). We were able to make assignment for each crosspeak and get the chemical shift and linewidth values from non-linear peak fitting (Figure D.7 and Table D.2). It was worth noting that some intra-residue crosspeaks are found to split into two or more distinct peaks (Figure 4.8B and D.8) with sharp linewidths. It verifies the multi-site occupancy we proposed for the alternating registry shift in N-strand arrangement (Figure 4.8C).

To learn more about residue conformations, the secondary chemical shifts for CO, $\text{C}\alpha$,

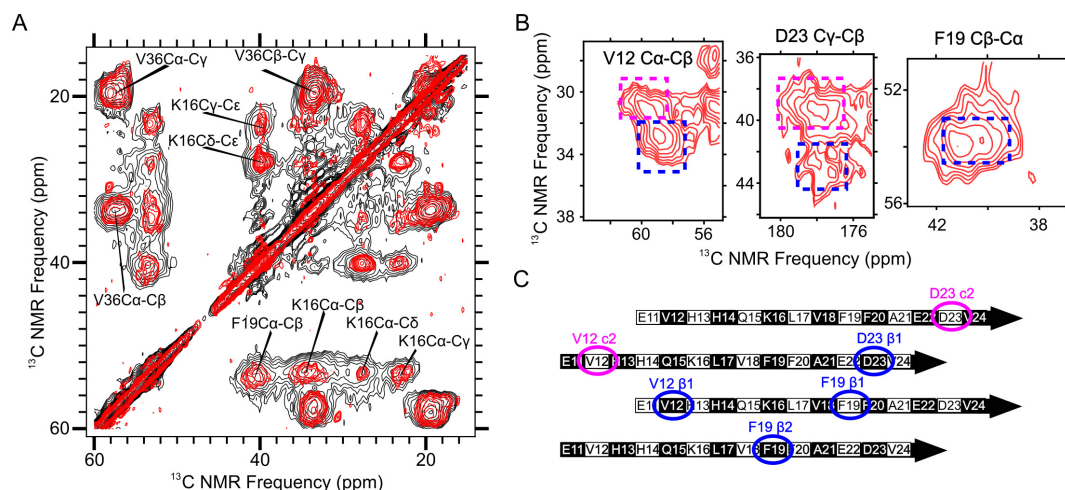


Figure 4.8 The 2D 50ms DARR spectra of ultracentrifuged sample have sharp crosspeaks revealing multiple molecular conformations. (A) Comparison of the 2D 50 ms DARR spectra of an ultracentrifuged sample and a lyophilized sample. Red contours: Sample 4.16 (K16, F19, G25, V36); black contours: Sample 4.11 (E11, K16, F19, V36) (B) Comparison of intra-residue crosspeaks of V12 C α -C β , D23 C β -C γ , and F19 C α -C β . Red contours: ultracentrifuge samples; black contours: lyophilized samples; Dashed blue boxes: the region which matches secondary chemical shifts of β -strand. (C) Out-of-register parallel β -sheet formed by N-strands. The colored circles mark the ^{13}C -labeled residues with multiple conformations. The names of conformations are listed in Table D.2.

and C β sites were calculated for the ultracentrifuged samples (Table D.2). A quick way to classify the secondary structure is by calculating $\Delta\delta\text{C}\alpha$ - $\Delta\delta\text{C}\beta$: if the value is less than -2, it is β -strand-like structure; if the value is between -2 and +2, it is random-coil. We labeled the ^{13}C -labeled residues by the estimated conformations in Table D.2, in which “ β ” represents β -strand-like conformation and “c” represents random-coil. The conformations of labeled glycines (G25 and G38) are from the TALOS-N prediction (Figure 4.4C).

The secondary structures of the labeled residues are consistent with our previous proposed β -strand distribution. First, as the residues close to the edges of N-strand, V12 and D23 show distinct crosspeaks for two different conformations—one is β -strand, the other is random-coil (Figure 4.8B). The result supports the proposed alternating registry shifts for the N-strand β -sheet (Figure 4.8C). V12 and D23 were reported to have broadening crosspeaks in the lyophilized sample, but we cannot separate the NMR signals from distinct

secondary structures due to limited resolution and low signal-to-noise level. Second, F19 and V36, the residues at the central region of N-strand and C-strand, are also found to have two conformations, but both conformations match β -strand-like secondary chemical shifts (Figure 4.8B). This is also what we expected for F19 because of the backbone flip caused by an odd number registry shift (Figure 4.8C). However, the multi-site occupancy of V36 seems to contradict our previous conclusion that the C-strand forms an antiparallel β -sheet centered right at V36 [186]. As the only center of an antiparallel β -sheet, V36 should only have one single conformation. We will deal with this conflict later.

In addition, G25 and K28, the residues that are proposed to be in a disordered turn region, have crosspeaks that look like a cluster of peaks (Figure D.8D and F). It suggests that more than two conformations are existing in the oligomer structure for these residues, and most of them belong to random-coil, which is consistent with the prediction of disordered turn region. Interestingly, we also found β -strand-like secondary chemical shifts in one of the K28 crosspeaks (K28(β 2) in Table D.2). These values may just arise from a small portion of K28 with some particular torsion angles in the turn regions. A real β -strand secondary structure usually requires consecutive residues with β -strand-like secondary chemical shifts, but we do not have well-resolved crosspeaks for N27 or G29 yet.

2D DARR spectra with long mixing time were also collected to verify and detect NMR structural constraints (Figure D.9). In addition, because we switched onto a higher magnetic field and a higher MAS spin rate in these experiments, 1000 ms DARR mixing time was used instead of the previous 500 ms mixing to provide similar intensities of inter-residue crosspeaks. It appears that all the expected cross-peaks are detected with similar intensities comparing to the previous lyophilized sample (Figure 4.9). Thus, we believe that the new experimental conditions can reveal the same DARR contacts as the previous measurements.

Finally, all the newly detected contact constraints are summarized in the contact chart (red symbols in Figure 4.10) with all the previous NMR constraints (from the spectra in Figure D.3 to D.6). It is worth noting that we detected D23 and K28 contacts in sample

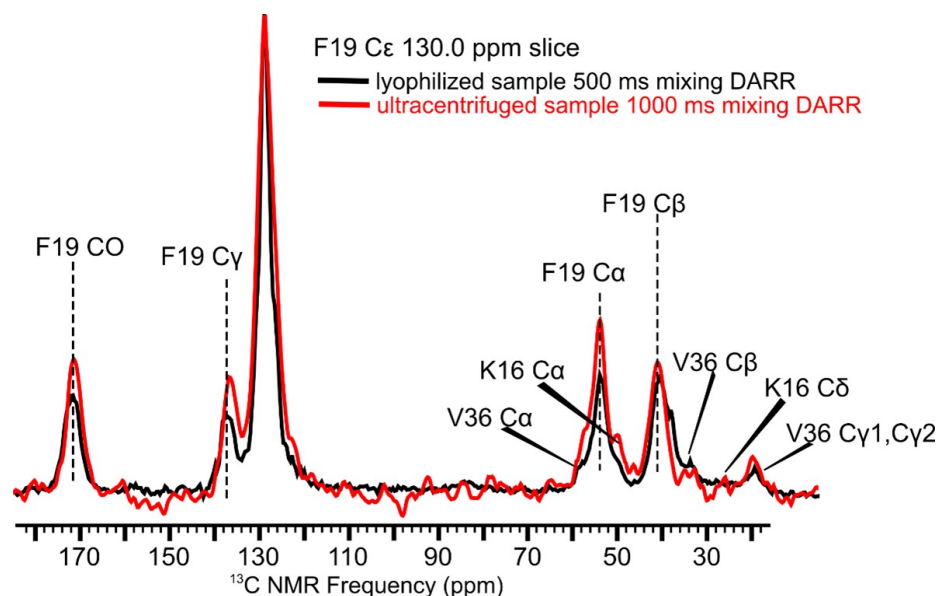


Figure 4.9 Comparing 2D DARR slices from lyophilized and ultracentrifuged A β (1-42) 150 kDa oligomer samples. Red: 1000 ms mixing DARR from Sample 4.16. Black: 500 ms mixing DARR from Sample 4.11.

4.15, but we did not detect them in the previous lyophilized sample 4.9. The non-detection of crosspeak might be caused by the broadening of crosspeaks from lyophilized oligomers. The full contact chart in Figure 4.10 will guide us in the following modeling efforts.

4.4.4 DPC-stabilized oligomers have the same structure as SDS-stabilized oligomers

Ciudad and co-workers [120] had prepared and characterized A β (1-42) tetramer in a membrane mimicking environment (Figure 4.3D). They used dodecylphosphocholine (DPC) solution to stabilize an A β tetramer species and applied solution-state NMR to determine the 3D structure, which features a six-stranded β -sheet core (Figure 4.3D). Their preparation is very similar to our initial step of producing the small oligomers (2-4mer in Figure 4.1) that are formed in 4mM sodium dodecylsulfate (SDS) and will finally assemble into 150kDa species [285]. However, we found the 2-4mers are in quick equilibrium with A β monomers in the SDS solution, hindering further characterization of their structures.

If we could show the connections between the DPC-stabilized tetramer and the SDS-

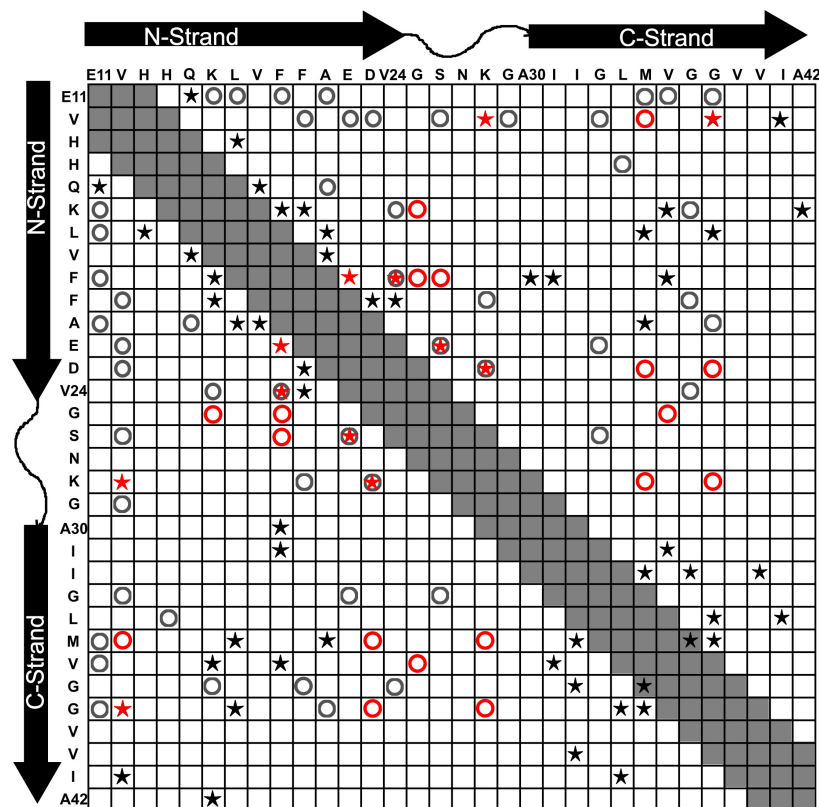


Figure 4.10 The full contact chart summarizing all the experimental NMR constraints. The red symbols are the results from the three ultracentrifuged samples. The red stars over circles represent newly detected contacts in ultracentrifuged oligomers, which were not observed in the lyophilized samples.

stabilized 2-4mer, it would be a good starting point for understanding the mechanism in the 150 kDa oligomer pathway. To show the possible connections, Dr. Rosenberry's lab modified their procedure to initiate A β assembly in DPC solution and finally generate a new oligomer sample with approximate 150 kDa particle weight, namely DPC-induced oligomer sample. We found the DPC-induced oligomers can remain stable during ssNMR test. Thus, we planned to compare the DPC- and SDS-induced oligomer samples in NMR experiments.

To directly compare the molecular structures of the two oligomers, we performed 2D DARR experiments on freshly produced oligomers, with identical isotope-labels at E11, K16, F19, and V36. Both NMR samples were prepared by lyophilization, as we did for most of the previous samples, to ensure the robustness of the measurements. The 500 ms

mixing DARR spectra from the two oligomer samples showed surprisingly high similarity (Figure 4.11). We used a numerical method to calculate the root-mean-square deviation (RMSD) value between two 2D spectra [40], which straightforwardly reveals the structural variation. The RMSD value between the two spectra is at the same level as the sample variation between different rounds of preparations for the SDS-labeled oligomers (Figure 4.11A). In addition, we compared slices from both spectra to get a closer look at some structure features. The contours and the peaks in the slices are nearly identical (Figure 4.11B), suggesting we got the same 150kDa oligomer sample in the DPC-induced and the SDS-induced preparation.

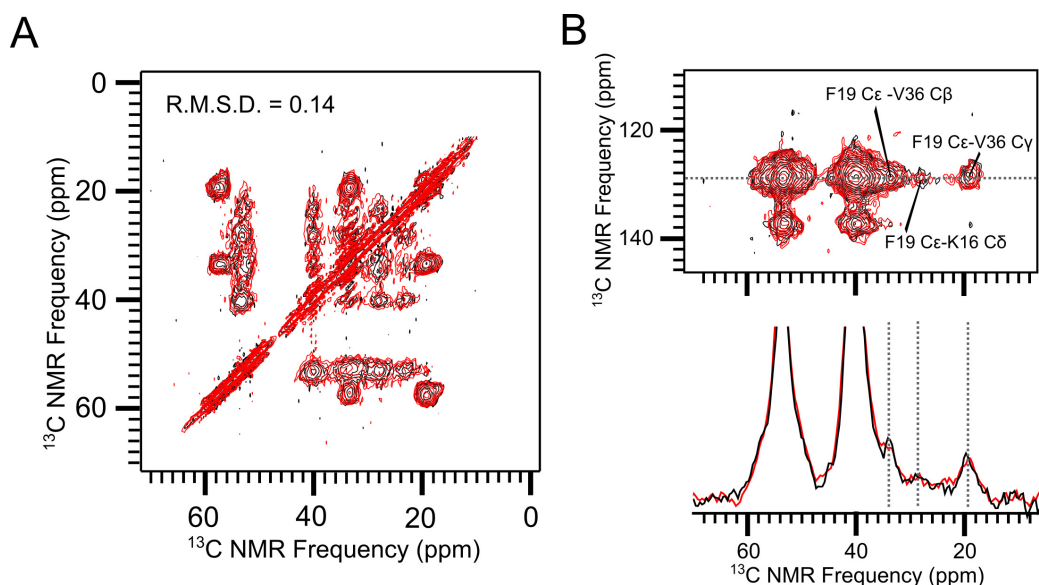


Figure 4.11 Comparison between the 2D DARR spectra from the SDS-induced (Black) and the DPC-induced (Red) oligomer samples (E11, K16, F19, and V36). (A) Calculate RMSD for the aliphatic region of the two spectra. (B) Compare the aromatic crosspeaks in contour and in slices.

With the assumption that the two procedures, the SDS-induced and the DPC-induced one, are similar, we want to shed some light on the 2-4mer structure based on the structural knowledge from the tetramer. If the C-strand antiparallel β -sheet formed in the 2-4mer and the 2-4mer continues to assemble into large oligomers, we expect to see some evidence

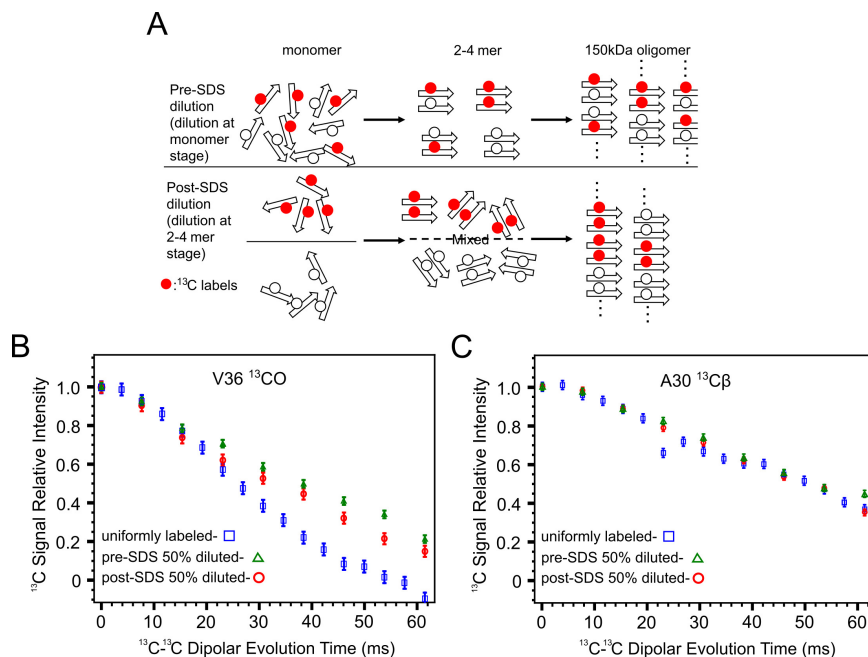


Figure 4.12 The pre- and post-SDS isotope-dilution strategy for verifying the 2-4mer residual structure in 150 kDa oligomers. (A) The diagram illustrating the pre- and post-SDS dilution strategy. (B) The PITHIRDS-CT decay of V36 CO in non-diluted, pre- and post-diluted oligomer samples. (C) The PITHIRDS-CT decay of A30 C β in non-diluted, pre- and post-diluted oligomer samples.

of residual structure in the final 150 kDa oligomer structure. A special isotope-dilution strategy (Figure 4.12A) was employed on sample 4.I (A30 $^{13}\text{C}\beta$ and V36 ^{13}CO). The pre-SDS dilution is just mixed 50% labeled and 50% unlabeled A β peptides in the monomer solution, while the post-SDS dilution is happening after the formation of 2-4 mers. If the final 150 kDa oligomer contains some residual structure from 2-4mers, different dilution effects of NMR signal are expected. If the assumption were correct, we would see stronger dilution effect in the pre-SDS experiments.

The results partially match our anticipation (Figure 4.12B). We observed different dilution effects in the PITHIRDS-CT decay, but the difference is very small. Repeated tests may be necessary to further validate the data. In addition, we see no explicit difference of dilution effect for the controlled label–A30 $^{13}\text{C}\beta$ (Figure 4.12C), verifying that the PITHIRDS-CT decay of A30 C β are mainly caused by natural abundance ^{13}Cs .

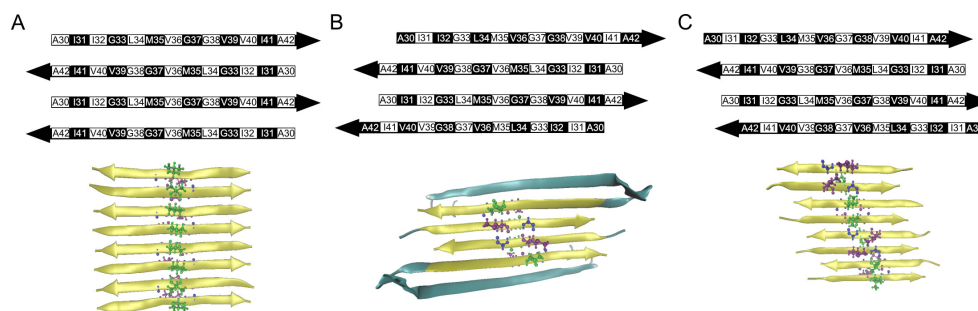


Figure 4.13 Three different C-strand alignments in antiparallel β -sheets. (A) An antiparallel β -sheet with the center at V36. (B) The antiparallel β -sheet from the reported tetramer structure [120]. (C) An antiparallel β -sheet with the center shifted between V36 and G37.

Some key features of the six-stranded β -sheet in the tetramer may help us to resolve the multi-site occupancy of V36. First, the four strands in the center assemble into an antiparallel β -sheet similar to the C-strand arrangement (Figure 4.13A). The difference is that there is a center shift in the tetramer β -sheet (Figure 4.13B), which can be regarded as introducing a registry shift in the uniform antiparallel C-sheet. It inspires us to test whether a center shift exists in the β -sheet formed by the C-strands. A 2D CHHC experiment was performed on sample 4.15 to verify the center shift. The $\text{C}\alpha$ - $\text{C}\alpha$ crosspeaks between M35 and G38 were observed (Figure 4.14A), indicating a special spatial proximation (<0.3 nm) of the α Hs from the two residues, which characterizes an antiparallel β -sheet centering at V36 and G37 (Figure 4.13C and 4.14B). Because we had observed the same contact between M35 and G37 in previous studies [186], which requires the C-strand antiparallel β -sheet centers at V36, it is necessary to introduce center shifts to meet both constraints (Figure 4.13C). Moreover, the slight center shift in the antiparallel β -sheet also agrees with the previously published PITHIRDS-CT data (Figure 4.14C). Thus, we believe the C-sheet comprise center shifted C-strands, but the overall alignments are still antiparallel. A possible design of the β -sheet is in Figure 4.13C, and we will use this arrangement in later molecular modeling.

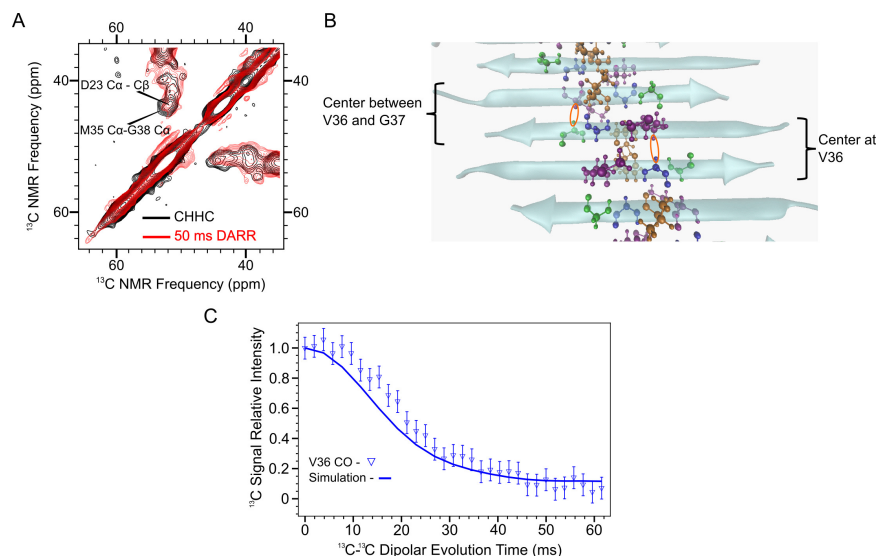


Figure 4.14 NMR data reflects a center shift existing in the antiparallel C-sheet. (A) 2D CHHC spectrum from sample 4.15 shows crosspeaks between M35 Ca and G38 Ca. (B) The antiparallel C-sheet with a center shift, which can explain the crosspeaks in panel A. (C) The simulated PITHIRDS-CT curve based on the coordinates in panel B is consistent with the experimental data.

4.4.5 TEM Revealed Primarily Globular Species but Anisotropic Self-Association

Figure 4.15A shows our oligomeric samples were separated from monomers using size-exclusion chromatography (SEC), and then the SEC peak of oligomer was fractionated into several fractions which were then imaged by negative-stain transmission electron microscope (TEM) (Figure 4.15B). The early-eluting fractions appeared to be primarily composed of string-like assemblies with morphologies consistent with association of globular particles. With subsequent fractions, there was a decrease in the string-like morphologies and the appearance of globular particles with approximately spherical shapes and a diameter under 10 nm. The strings appear to be self-limiting in terms of size and do not appear to follow any helical rule other than stacking in one dimension. The apparent association of globular species into strings suggests that globular particles have anisotropic structures that promote particle-particle association in a preferential direction.

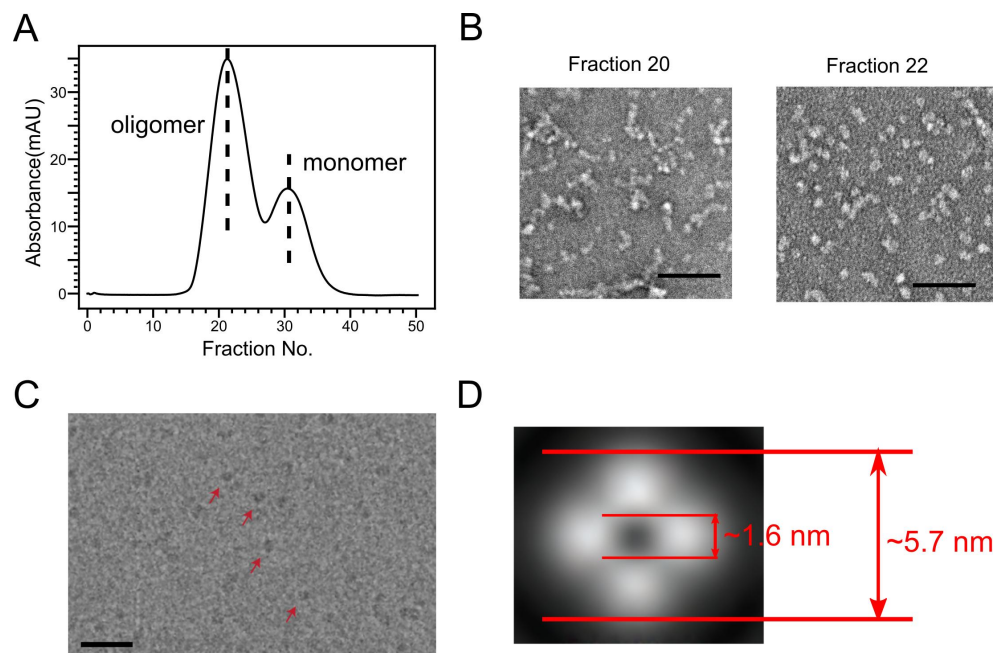


Figure 4.15 The TEM image and the cryoEM class average of A β 150 kDa oligomers. (A) SEC trace for 150 kDa oligomer sample, marked to indicate the peaks corresponding to oligomers and monomers. Milli-absorbance units (mAU) were recorded at 280 nm. Fractions 18 to 24, corresponding to molecules predominantly in oligomeric states, were selected for EM analysis. (B) Negative-stain TEM images taken from SEC fractions 20 and 22. The scale bars correspond to 50 nm. (C) A cryo-EM image. The scale bar corresponds to 50 nm. The red arrows indicate globular particles with a hole in the middle, which were selected for 2D reconstruction. (D) The class average of 150 kDa oligomer particles calculated with cryoSPARC [290].

4.4.6 Cryo-EM Revealed a Four-Fold Symmetry

Given the relative homogeneity of the globular particles, Dr. Stagg performed cryo-EM single particle analysis on this species. Aliquots were frozen on C-Flat holey carbon grids and imaged with their Titan Krios equipped with a DE64 in electron counting mode. They collected a dataset with Legion to assess the quality of the sample, the distribution of particles in the ice, and the particle alignment. Embedded globular particles were clearly visible in the ice (Figure 4.15C), and a pore was clearly visible in many of them. Contrast transfer function (CTF) estimates for selected globular particles were made, and 2D class averages were produced using cryoSPARC [290] (Figure 4.15D). This analysis revealed a class average with four-fold symmetry and a clear pore in the center.

4.4.7 Structural Modeling Shows How EM and NMR Constraints Can Be Harmonized

The EM data inspires us to design a novel structural model explaining all the solid-state NMR structural constraints on the 150 kDa oligomers. Prior to introducing the structural model, we summarize previous NMR results: 1) the peptide secondary structure includes four regions, an unstructured tail composed of residues 1-10, a β -strand (the N-strand) composed of residues 10-24, a turn region formed by residues 25-29, and a second β -strand spanning residues 30-42 (the C-strand); 2) the C-strands are arranged into antiparallel β -sheet; 3) the N-strands arrange in parallel alignment but with a registry shift with N-strands on adjacent molecules; 4) numerous inter-residue 2D NMR correlations indicate close association between residues in the C-strand and residues in the N-strand. While individual β -sheet models could explain aspects of our data on inter-strand arrangements, none of the models we previously considered could simultaneously rationalize structural constraints on N-strand arrangement, C-strand arrangement, and interaction between the N- and C-strands. We consider the coexistence of parallel and antiparallel β -sheets to be the most challenging structural requirement.

Inspired by the multiple subunits observed in the class average of the oligomer particles,

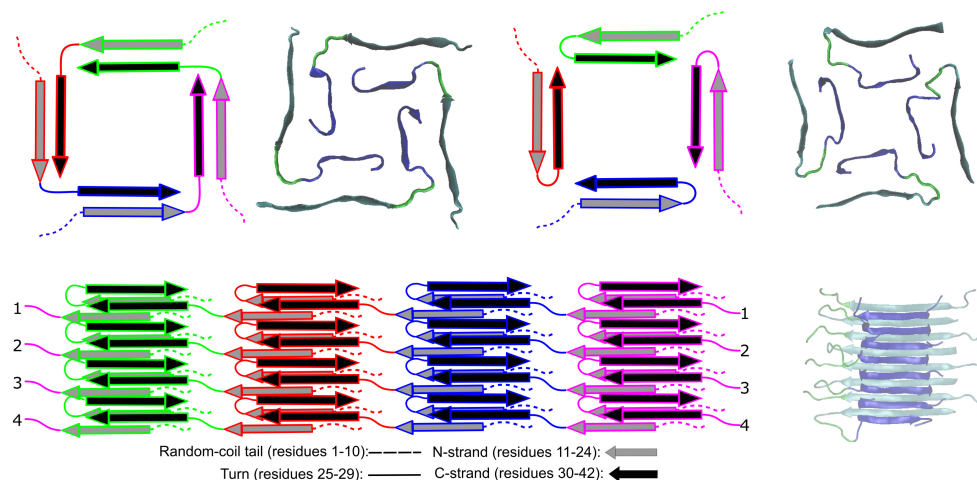


Figure 4.16 The β -sheet stacking, domain-swapping, and peptide conformation in the A β 150 kDa oligomer structure. Top panel: top view of the central pore in the oligomer structure. Bottom panel: side view of the stacking β -sheets.

we designed a domain-swapping structure to distribute the two different β -sheets formed by N-strands and by C-strands (Figure 4.16). First, an N-strand β -sheet and a C-strand β -sheet are stacked with each other to form one subunit. Because of the alternating nature in both the antiparallel β -sheet and the out-of-register parallel β -sheet, we were able to connect half of the N-strands in one subunit to half of the C-strands in the adjacent subunit (highlights in Figure 4.16). Thus, half of the A β peptides in this structure span two adjacent subunits—adopting domain-swapping conformation. The other half of A β peptides have their N-strand and C-strand stacked in one subunit. The two distinct conformations of A β peptide are easy to identify from the top view. In one conformation (U-shaped), the peptide molecule contributes an N-strand and a C-strand to β -sheets in the same subunit. The other conformation (L-shaped) is a domain-swapped conformation in which the N-strand and C-strand from one peptide contributes to adjacent subunits.

We arrived at a final structural model when 2D cryo-EM reconstruction revealed four-fold symmetry for the full 150 kDa oligomer. To match the four-fold symmetry and the molecular weight, we create four subunits of the stacked β -sheets, and each β -sheet contains eight strands. Hence, the model has 32 A β (1-42) peptides with a total molecular weight

of 144 kDa. The model predicts the N-strands arranged into a parallel β -sheet with an alternating registry shift of ± 3 residues on the outside of the structure. The C-strands form antiparallel β -sheets within the layers of N-strand β -sheets and surround a central pore (Figure 4.17A). Moreover, the observed I31/V36, F19/I31 and K16/A42 contacts indicate the edges of C-strands are close to the central region of stacking, and thus the NMR constraints lead to a bending C-strand β -sheet. We introduced two turns into C-strand to ensure two edge residues (I31 and A42) come close to the central region of N-strand, and we found the sidechain of K16 and the carboxyl acid of A42 could form salt bridges in this conformation. Although we did not successfully perform fs-REDOR to test the salt bridge, the K16 C ϵ /A42 CO crosspeaks (Figure D.6) support this structural feature.

Figure 4.17A illustrates the attempt to bring the bending C-strand β -sheets into the four-fold symmetric structure. The four-fold symmetry includes four subunits with stacked interfaces between N-strand and C-strand β -sheet, and the four subunits are placed in a way to best match the detected inter-subunit contacts—I32/M35 and I32/G37. To simplify the first structural model, we used a C-strand antiparallel β -sheet centering at V36 to produce the bending C-strands. Thus, in this structural model, all the V36 sidechains are pointing towards the N-strand β -sheets (green sidechains in Figure 4.17A), leading to clear predicted contacts of K16/V36 and F19/V36 (Figure 4.17B). However, the adjacent M35 sidechains are all extended into the pore (purple sidechains in Figure 4.17A), which is not consistent with the detected L17/M35 and A21/M35 contacts (Figure 4.17B).

In the second round of modeling, we introduced the center shifts into the bending C-strand β -sheet (Figure 4.17C). To not interfere most of the predicted contacts, we consider the center shifts as defect in the structure, and only introduced eight shifted C-strands (two in each subunit). Because the backbone is flipped when we move V36 to form hydrogen bonds with G37 in the center shifts (Figure 4.14B), the sidechains near the center of C-strands are placed in the opposite direction. Thus, we can see some M35 sidechains pointing to the N-strand β -sheet when the C-strand backbones are flipped (purple sidechains in Figure

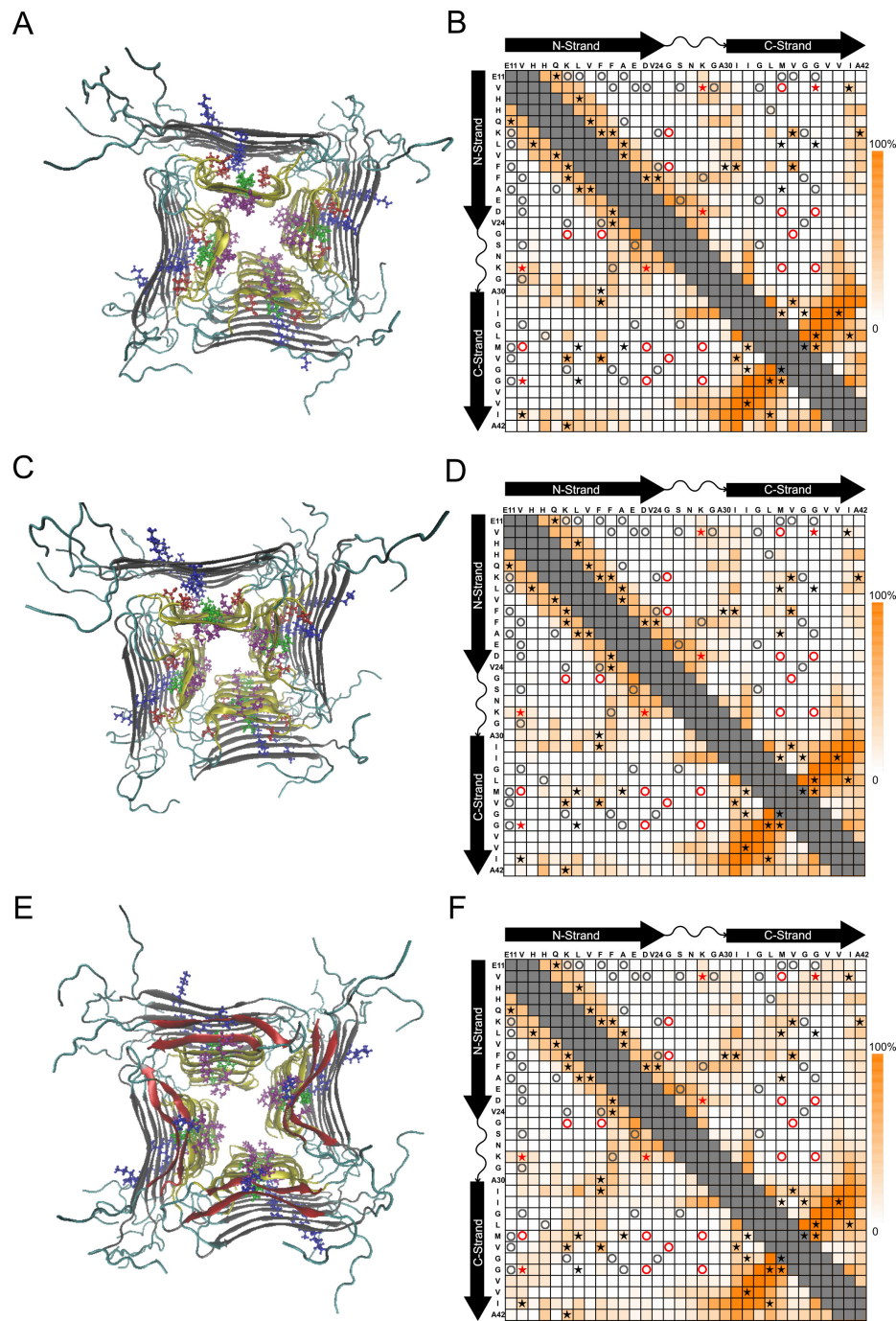


Figure 4.17 Introducing heterogeneous conformations into the 150 kDa oligomer model to make it more consistent with experimental NMR constraints. (A, B) The first structural model based on the peptide conformation in Figure 4.16. (C, D) Introducing center shifts into C-strand β -sheets to produce the second model. (E, F) Introducing β -hairpins at the edge of C-strand β -sheets to generate the third model, which is more consistent with the NMR constraints. The DARR contact charts in panel B, D, and F directly compare the model-predicted contacts with the experimental constraints.

4.17C). These changes provide L17/M35 and A21/M35 contacts in the stacking interface (Figure 4.17D), hence more consistent with the observed NMR constraints. There are still two detected residue contacts, V12/G38 and L17/G38, cannot be explained by this model.

If we recall the tetramer structure (Figure 4.13B), the N-strand and the C-strand form β -hairpins at the edge of the oligomer. Interestingly, the β -hairpin structure provides a contact between V12 and G38 (Figure 4.3D). Therefore, we decide to introduce β -hairpins at the ends of the oligomer structure (Figure 4.17E), which could be a residual structure of A β tetramers when they assemble into large oligomers. The β -hairpins not only have the right conformation to bring V12 and G38 close to each other, but they also cap the end of the oligomer to prevent further assembly. For the third model, most of the detected and the undetected DARR contacts can be rationalized. The predicted but not detected contacts (F19/V24, E22/S26, F20/K28) might be caused by the weak NMR signals from random-coil residues in lyophilized samples. The only not predicted but detected contact, L17/G38, might indicate more defects in the structure.

Finally, we want to generate a structural model that can explain as many NMR constraints as possible and can also match the particle dimensions determined by cryo-EM. With the help from Dr. Zhou's lab, we were able to get an optimized structural model that explains all the detected DARR contact and has similar dimensions to the cryo-EM class average (Figure 4.18A and B). The color scheme of the predicted contacts is modified to emphasize the minor structures in the model.

4.5 Discussion

4.5.1 Features of The Oligomer Structural Model

For the proposed structural model, it has some interesting features as a stable A β oligomer. First, the out-of-register parallel β -sheet structure, with alternating registry shifts of +3 and -3 in the N-strand region that we deduce for 150 kDa oligomers, is a very unusual arrangement. Although there are few examples of structures with such shifts, one is the out-of-

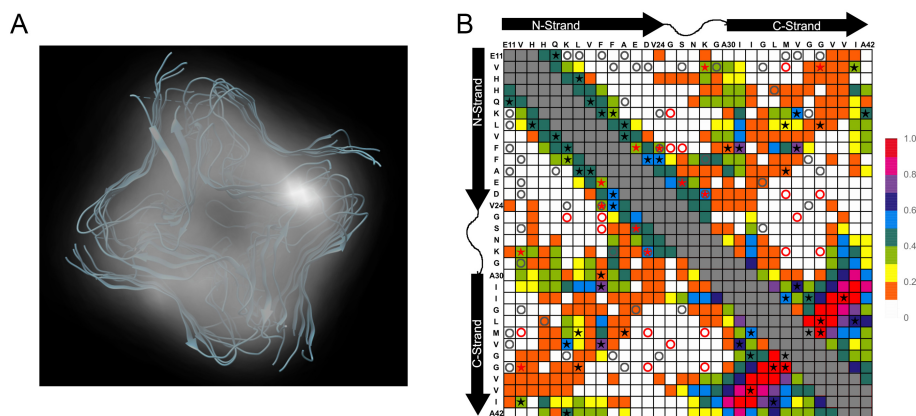


Figure 4.18 The optimized model of Aβ(1-42) 150 kDa oligomers that can harmonize both NMR data and cryo-EM dimensions. (A) The cryo-EM class average overlaps the top view of the optimized model. (B) The DARR contact chart of the optimized model.

register anti-parallel β -sheets formed by Aβ(11–25) fibrils formed at pH 2.4 [197]. The β -strands in these fibrils correspond to the N-strand region in 150-kDa oligomers but are antiparallel rather than parallel. A second example is the model peptide ccβ-p, which has pH-dependent registry shift numbers in anti-parallel β -sheets that form fibrils [291]. One registry shift is +3, and this odd number registry shift would create a flip-over between neighboring β -strands. The flip-over would require that side-chains from the same residue on adjacent molecules alternately point up and down within one β -sheet. The N-strand region of Aβ(1–42) and the ccβ-p model peptide (Ac-SIREL EARIR ELELR IG-NH₂) both contain several charged side-chains, and thus, the pH dependence indicates that side-chain charges may motivate the registry shifts.

Second, the secondary structure features involving antiparallel and out-of-register parallel β -sheets have been reported in other oligomers. Raussens and co-workers [292] observed a conversion of antiparallel β -sheets in Aβ(1–42) oligomers to parallel β -sheets in Aβ(1–42) fibrils by Fourier transform infrared spectroscopy. Eisenberg and co-workers crystallized oligomers produced from peptide fragments of several disease-related amyloid proteins including Aβ and found out-of-register anti-parallel β -sheets in oligomers and fibrils [293]. A recent solid-state NMR study by Ishii and co-workers [125] of an Aβ(1–42) oligomer

called SPA revealed a structure with some similarities to our 150-kDa oligomer, including aggregate dimensions, predicted β -strand regions, and ^{13}C linewidths (3-4 ppm) on NMR spectra. However, fpRFDR-CT NMR measurements of SPA selectively labeled at ^{13}C of A30, L34, or V39 indicated out-of-register parallel β -sheets, in contrast to the C-strand structure in our 150-kDa oligomers.

Third, the oligomer particle has a central pore. Many pore forming structures are visualized in protein aggregates, including protofibrils [294] and A β oligomers [57]. Furthermore, the pore-forming feature was found to be closely related to the cytotoxicity of oligomers because they have the potential to insert into cell membrane and create ion-conductive pores or destabilizes the membrane organization [287, 295]. The amyloid pore hypothesis had been proposed for nearly three decades [296]. The tetramers, which might have similar structure as the 2-4mer intermediate, can further assemble into octamers and then insert into membrane bilayer [120]. Thus, pore-forming may be a common feature for large A β oligomers, and it causes general neurotoxicity.

Forth, we introduced domain-swapping peptide conformation to combine the antiparallel and the parallel β -sheet in one structure. In fact, domain-swapping was also proposed in the structural model of toxic A β 42 fibrillar oligomers to build a pore-forming large oligomer [266]. For large oligomers, domain-swapping might be inevitable and necessary to connect the nearly identical subunits. Meanwhile, the domain-swapping may lock the connections of subunits, leading to aggregates with fixed size [297].

Fifth, we also introduced β -hairpins at the edge of oligomers. The β -hairpin is a common structure in many forms of aggregates, such as preglobulomers [118], protofibrils [119, 298], and even amyloid fibrils [177]. Under most circumstances, the β -hairpin motif can be easily converted into stacking β -strand, *e.g.* the conversion from protofibrils to mature amyloid. When using an engineered disulfidecontaining A β (1–42) that locks into a peptide β -hairpin (A β cc) [299, 300], the peptides can form elongated protofibrils, but they cannot proceed to fibrils [119]. Hence, normal β -hairpins cannot block the end of β -sheets and

limit the growth of oligomers.

Last but most importantly, we introduce defects into the 150 kDa oligomer structure to meet the NMR constraints. This is not an acceptable method for most structural studies, but it may be the right way treating large A β oligomers considering the transient and heterogeneous nature of oligomer samples. The A β oligomer samples cannot archive the structural order of amyloid, and the amyloid seeding techniques cannot be used for oligomers. It might be the reason why no atomic level structural study succeed on large oligomers. Many studies of peptide oligomers only reported the secondary structure regions and the backbone alignment [124, 125]. We need to figure out a new way to describe the oligomer structure. For example, we can report the scaffold of structure including the subunits and the backbone arrangement, and then provide the possible variation in specific positions.

4.5.2 The Size Limitation of The 150 kDa Oligomers

The size limitation of the “off-pathway” oligomers is important for their structural stability, and hence the continuous effects of neurotoxicity. In addition, the stable oligomer species can accumulate in patient’s brain. If the auto-clearance mechanism slows down, the accumulation of the oligomers may lead to the initiation of AD. Conversely, the fast conversion to amyloid makes the “on-pathway” oligomers hard to accumulate. Thus, the structural stability and the size limitation plays a critical role in the pathological mechanism.

The structural model we proposed can explain the size limitation of the 150 kDa oligomers. Monomer addition is usually the most efficient way of amyloid assembly [301]. However, to get the domain swapping structure, the A β peptide molecule needs to adopt the appropriate conformation (U-shaped or L-shaped in Figure 4.16) when it was recruited to the opening end of the oligomer particles. If the coming peptide molecule adopts the wrong conformation, it will temporarily block the growing end and inhibit the expand of cross- β architecture. Hence the monomer addition mechanism is not efficient for the oligomer growth. The slow monomer addition results in an equilibrium between the assembly and

the disassociation, and hence the size limitation.

4.5.3 The Assembly Pathways of Oligomers

It is still hard to investigate the assembly mechanism when we only have the structural information of the final assembly product. The key to reveal the molecular mechanism is the characterization of 2-4mer structures (Figure 4.1). Although we performed some tests to compare the DPC-induced and the SDS-induced small oligomers, there is still no solid evidence to show they have similar structures. To fully understand the oligomeric assembly pathway, we still need to characterize the 2-4mer structures.

If we assume the 2-4mer has the same structure as the DPC-induced tetramer, an aggregation pathway can be proposed for the 150kDa oligomer. First, the C-strand forms an antiparallel β -sheet as the one in the tetramer (Figure 4.13), which serves as a hydrophobic core in the membrane mimicking environment. Then, the N-strands adopt β -hairpin conformation at the end of C-strand β -sheet. When the membrane mimicking reagent is removed, the C-strand β -sheets assemble as the hydrophobic center and the free N-strands come together to form parallel β -sheet and domain swapping strands (Figure 4.16). It is worth noting that the formation of large oligomer (150 kDa oligomer) does not rely on monomer addition but is based on the gathering of small oligomers, which agrees with our previous discussion about size limitations.

With the proposed aggregation pathway, we can easily block it with different strategies to avoid the formation of 150kDa oligomer. For example, we can use the synthesized tetramer to produce antibodies that specifically recognize the C-strand antiparallel β -sheet. When the antibodies bind to the tetramers, the further aggregation is completely blocked. In addition, the antibodies also help to clear the tetramers in patient's brain. Thus, a direct targeting of the aggregating intermediate (the tetramers) can efficiently prevent the entire aggregation pathway. This is why we want to further investigate the unstable species in the aggregating process.

CHAPTER 5

NMR-CONSTRAINED MOLECULAR MODELING OF AMYLOID FIBRIL FORMED BY P1 PEPTIDE DERIVED FROM THE GLAUCOMA-ASSOCIATED MYOCILIN

Portions of this chapter have been adapted and reproduced from Y. Gao, E. G. Saccuzzo, S. E. Hill, D. J. E. Huard, A. S. Robang, R. L. Lieberman, and A. K. Paravastu, “Structural Arrangement within a Peptide Fibril Derived from the Glaucoma-Associated Myocilin Olfactomedin Domain,” *J. Phys. Chem. B*, vol. 125, no. 11, pp. 2886–2897, 2021 [302]. Copyright 2021 American Chemical Society (See Appendix A for the reprint license agreement). Additional supporting materials is included in Appendix E.

5.1 Project Overview

The misfolding and amyloid formation of myocilin has been shown to cause glaucoma, the second leading cause of blindness in the world. Some glaucoma-associated mutations of the myocilin olfactomedin domain (mOLF) result in protein aggregation, suggesting that this 257-residue domain plays an important role in the amyloid formation. Here, we analyze the 12-residue peptide P1 (GAVVYSGSLYFQ), corresponding to residues 326–337 of mOLF, previously shown to form amyloid fibrils *in vitro* and *in silico*. We applied solid-state NMR structural measurements to test the hypothesis that P1 fibrils adopt one of three predicted structures: i) a U-shaped in-register parallel β -sheet; ii) an S-shaped in-register parallel β -sheet; iii) a β -sheet formed by native-like β -hairpins. NMR spectra are consistent with a U-shaped fibril arrangement for P1, which is related to the U-shape predicted previously *in silico*. Our data are also consistent with an antiparallel fibril arrangement, likely arising from terminal electrostatics. Finally, we proposed a structural model with multi-

ple U-shaped antiparallel β -sheets stacked for the P1 amyloid fibril. Overall, our results strengthen the connection between mOLF fibrils and the broader amyloids and contribute to our understanding of the fundamental molecular interactions governing fibril architecture and stability.

5.2 Introduction

Mutations in the mOLF (Figure 5.1A) domain comprise the strongest genetic link to early onset open angle glaucoma [14, 128], and disease-causing myocilin variants are associated with toxic misfolding [133, 135, 303–306]. Dr. Lieberman’s lab has already demonstrated amyloid formation by full-length myocilin variants in cells and by the isolated mOLF domain *in vitro* [136, 137]. They also found that the wild-type mOLF could assemble into two different fibril morphologies, long straight fibrils and more unusual lassoed oligomers. These morphologies are also observed in aggregates of glaucoma-associated variants, A427T and D380A, respectively [137], indicating these amyloid fibrils are closely connected with the disease.

Analysis of the mOLF sequence by amyloid prediction softwares, including Waltz [307], PASTA [308], AmylPred [309], and TANGO [310], identified three peptides within mOLF with high amyloid-forming propensity: G₃₂₆AVVYSGSLYFQ₃₃₇ (P1, the residues will be mentioned as G1 to Q12 in P1 for convenience), G₃₈₇LWVIYSTDEAK GAIVLSK₄₀₅ (P2), and V₄₂₆ANAFIICGTLTYTVSSY₄₄₂ (P3). In the experiments, two of these peptides, P1 and P3, formed thioflavin-T (ThT)-positive aggregates whereas P2 remained soluble [137]. Moreover, atomic force microscopy (AFM) images show that the fibril morphologies of P1 and P3 recapitulate morphologies seen for the full mOLF protein domain [137], in which the P1 amyloid adopts the long straight fibril shape (Figure 5.1B). These observations suggest that P1 and P3 are in the amyloid-forming cores responsible for the amyloidogenesis of the full mOLF.

Dr. Hall’s lab performed discontinuous molecular dynamics (DMD) simulations com-

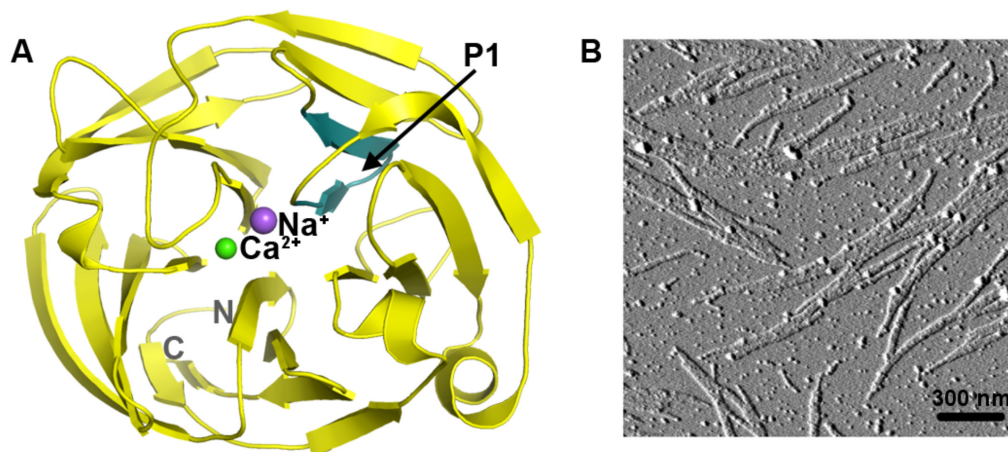


Figure 5.1 Crystal structure of mOLF and fibrils formed by P1 peptide. A) The β -hairpins formed by residues in the P1 peptide are highlighted in teal within the context of the mOLF propeller fold. The green and purple spheres are calcium and sodium ions, respectively. B) AFM image of P1 fibrils [137] prepared under conditions as those for the NMR experiments presented in this manuscript.

binned with the PRIME20 force field [311–313] to predict molecular structures in P1 and P3 aggregations. Their conclusion is that that P1 and P3 are both aggregation-prone; P1 consistently forms fibrillar aggregates with parallel in-register β -sheets, whereas P3 forms β -sheet-containing aggregates without distinct order. Our preliminary NMR data of natural abundance ^{13}C samples are consistent with their prediction – the 1D CP-MAS spectrum of P1 amyloid shows sharp linewidths, while the spectrum of P3 amyloid has broad cross-peaks (Figure 5.2) [314]. Thus, we decide to focus on characterizing the molecular structure within the P1 amyloid because it is more compatible with future ssNMR studies.

The structure of P1 peptide amyloid fibrils is also interesting for understanding what molecular structures are possible in amyloid formation and how the structure could be predicted. Similar to how P1 was discovered through analysis of the mOLF protein, fragment peptides of similar size to P1 have been identified within larger amyloid-forming proteins. Examples include residues 16–22 of Alzheimer’s amyloid- β ($\text{A}\beta(1\text{--}40)$ and $\text{A}\beta(1\text{--}42)$) [198, 315], residues 20–41 of β_2 -microglobulin (K3) [316], and residues 105–115 of transthyretin (TTR) [317, 318]. $\text{A}\beta(16\text{--}22)$ adopts a linear β -strand conformation within the $\text{A}\beta$

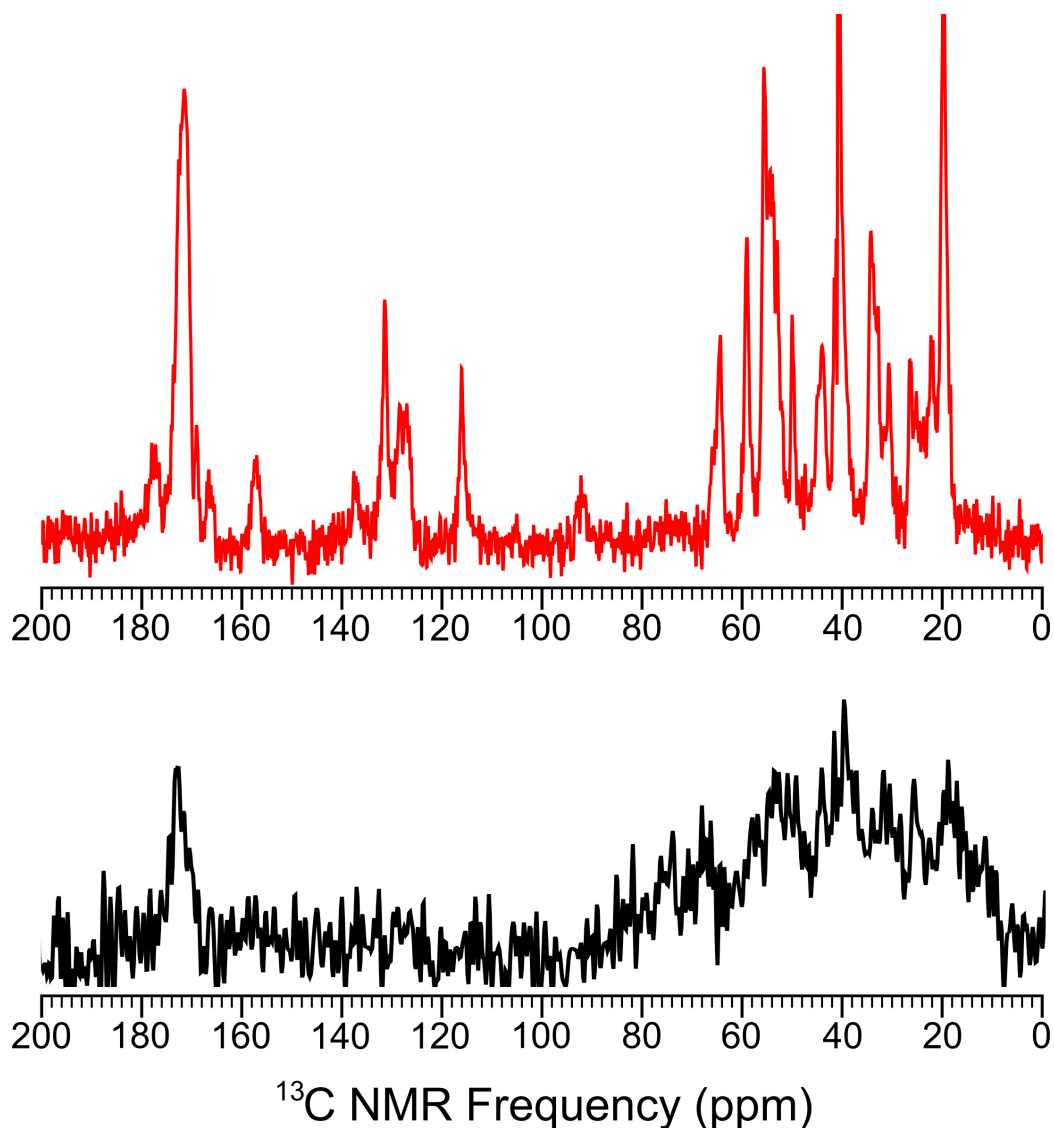


Figure 5.2 CPMAS ^{13}C spectrum of P1 and P3 aggregates with no ^{13}C enrichment. Red: the spectrum of P1 aggregates. Black: the spectrum of P3 aggregates.

amyloid fibril structure, and K3 and TTR(105–115) both adopt linear β -strands in natively-folded β_2 -microglobulin and transthyretin, respectively. These precedents support the interpretation that fragment peptides derived from β -strand regions of larger aggregates or folded proteins are prone to adopt β -strand conformations when they self-assemble on their own. However, the P1 peptide is different from these examples in that residues 326–337 do not adopt a linear β -strand conformation within mOLF. The P1 segment instead forms a β -hairpin within a well-folded β -propeller (Figure 5.1A) with a β -turn at residues S331

and G332. Although β -hairpin configurations (Figure 5.3A) are compatible with amyloid formation, as has been demonstrated for the MAX1 family of designer peptides [319, 320] and proposed for A β protofibrils (prefibrillar aggregates) [298], P1 would be, to our knowledge, the smallest peptide shown to form this structure. DMD simulations of P1 assembly predicted that the P1 peptide could assemble into amyloid fibrils without adopting linear β -strand or β -hairpin conformations. Simulations predicted U-shaped (Figure 5.3B) or S-shaped (Figure 5.3C) molecular conformations organize into in-register parallel β -sheet in the amyloid fibrils [314]. Our study of P1 amyloid structure was motivated by the desire to test these structural predictions.

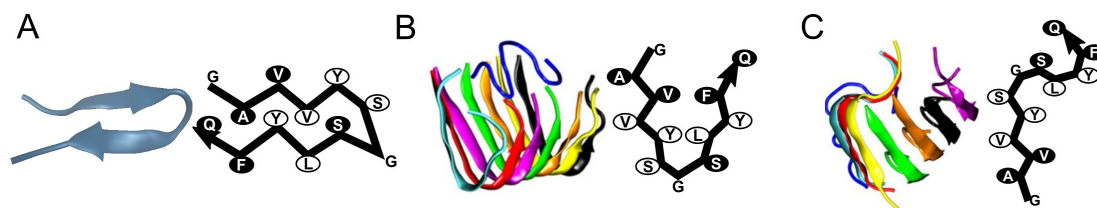


Figure 5.3 Hypothesized structures for P1 peptide amyloids. A) Native β -hairpin conformation adopted by the P1 residues within the mOLF folded protein. B) and C) U-Shaped and S-shaped parallel β -sheet models predicted by DMD simulations of Wang *et al* [314]. Each model is represented with ribbons rendered from all-atom (panel A) or course-grained (panels B and C) models (left side of each panel) and a schematic (right part in each panel). The ovals in the schematics represent side chains of indicated amino acids. Black ovals with white letters correspond to residues that were isotopically labeled for 2D NMR experiments.

We gain insight into the molecular structure of P1 amyloid by testing hypothesized structures using ssNMR. The data presented herein are most consistent with the DMD-predicted U-shaped molecular conformation, but with molecules arranged into antiparallel rather than parallel β -sheets. Electrostatic attraction between the termini likely drives this antiparallel arrangement. Our results strengthen the connection between mOLF fibrils and the broader amyloids, and also contribute to our understanding of the fundamental molecular interactions determining fibril architecture and stability.

5.3 Materials and Methods

5.3.1 Peptide Fibrillization Experiments

Isotope-labeled and unlabeled P1 peptides (>95% final purity) were synthesized by CPC Scientific (Sunnyvale, CA). The amyloid sample was prepared as previously reported [137, 314]. Briefly, P1 peptide was first stored at room temperature as 5 mg/mL solution in DMSO. To generate amyloid fibrils, 500 μ M peptide was dissolved into 10 mM Na₂HPO₄/KH₂PO₄ buffer at pH 7.2, which contained 200 mM NaCl plus 10 μ M ThT, and the solution was incubated at 36 °C for 24 to 48 h. The products of three 4 mL reactions were combined for NMR experiments. Insoluble aggregates were directly packed into 3.2 mm ssNMR rotors through ultracentrifugation (280,000 x g, 30 min at 4 °C). For isotope-diluted experiments, 30% labeled and 70% unlabeled peptides were mixed in DMSO solution and then subjected to the same aggregation procedure.

5.3.2 Solid-State NMR

All of the ssNMR experiments were performed on a Bruker narrow-bore 11.7 T magnet (¹H frequency of 500 MHz), equipped with a 3.2 mm HCN MAS probe. The 2D fpRFDR (Section 2.3.2.4), 2D DARR (Section 2.3.2.5), and 2D CHHC (Section 2.3.2.6) experiments use different mechanisms to reintroduce the dipolar coupling between ¹³C atoms and thus provide different structural information. For 2D fpRFDR experiments, the power of the π pulse on the ¹³C channel was adjusted to 33 kHz to match the duration (15.2 μ s) of one-third of the rotor period at 22 kHz MAS. For the 2D DARR experiments, continuous irradiation with power corresponding to 11 kHz nutation frequencies (same as the MAS spinning rate) in the ¹H channel was applied during the exchange periods, which were set to 500 ms to detect inter-residue contacts. In the 2D CHHC experiments, 150 μ s ¹³C-¹H and ¹H-¹³C cross-polarization periods and a 182 μ s ¹H-¹H spin diffusion period (2 rotor cycles in 11 kHz MAS spinning) was used. Proton decoupling with two-pulse-phase modulation [214]

and a ^1H radiofrequency field of 100 kHz was used in all of the 2D experiments. The signal averaging of 2D fpRFDR, 2D DARR, and 2D CHHC required 36 to 48 h to produce decent signal-to-noise ratio, and it was increased to 72 h for the 2D DARR experiment on the isotope-diluted sample.

After obtaining the 2D spectra, nonlinear fitting with a 3D Gaussian function was performed for every distinguished crosspeak to determine the chemical shifts, the line widths, and the peak heights. The intensities of peaks were calculated by integrating the 3D Gaussian functions of the crosspeaks or the diagonal peaks. For the weakest crosspeaks (V3 C α /F11 C α , V3 C α /F11 C δ , A2 C β /F11 C ϵ , and V3 C γ /S8 C β) in the isotope-diluted 2D DARR spectrum, their signals are too weak to be distinguished from the noise. For these crosspeaks, we estimated the peak intensities using the corresponding linewidths we measured in the nondiluted spectrum and assumed that the peak heights that were half the height of the noise in the isotope-diluted spectrum. This estimation is not accurate but it provides semi-quantitative values of peak intensities in our analysis.

To quantify the effects of isotopic dilution on 2D DARR NMR crosspeaks (dilution ratios), the relative crosspeak intensity for pairs of ^{13}C atoms was measured in the spectrum of Sample 5.A (listed in Table 5.1). The intensity of each crosspeak was scaled to corresponding diagonal peaks using $(I_{AB} + I_{BA})/(I_{AA} + I_{BB})$. I_{AB} and I_{BA} are the intensities of crosspeaks on different sides of the diagonal, and I_{AA} and I_{BB} are intensities of the corresponding diagonal peaks. Finally, the relative crosspeak intensities from the 2D DARR spectra of Sample 5.A and 5.B were compared to calculate the dilution ratios.

PITHIRDS-CT (Section 2.3.2.2) and R 2 W (Section 2.3.2.3) experiments measured the distances between specific ^{13}C atoms in the amyloid sample. PITHIRDS-CT experiments were performed with a MAS spinning rate of 12.5 kHz. The dipolar recoupling time was adjusted by the number of blocks of pulses (k_1 , k_2 , and k_3 defined by Tycko [206]), and it was fixed to be between 0 and 61.4 ms in our measurements. Proton decoupling with 100 kHz ^1H radiofrequency field using continuous wave was applied during PIRHIRDS

recoupling and acquisition. PITHIRDS curves required data acquisition for about 24 h. R²W experiments were performed according to Costa et al [224]. We set a fixed evolution time of 50 ms and variable MAS spinning rates (ω_{MAS}), which vary from on-resonance to ± 0.4 kHz off-resonance for the frequency difference between the two ¹³C-labeled sites ($\omega_{MAS} = \Delta\omega(^{13}C) \pm 0.4\text{kHz}$). The spectra with 0 ms evolution time at each spinning rate were also collected as reference. Each 1D spectrum in R²W required about 2 h signal averaging.

5.3.3 NMR-Related Spin Simulations

Spin simulations were performed using SPINEVOLUTION [204] with the same conditions as in the experiments. The chemical shift anisotropy parameters of Phe11 CO and Ala2 C β were measured in static CP 1D spectra (set $\omega_{MAS} = 0$) and were used in all of the simulations. For Phe11 CO, the δ_{aniso} is -75 ppm, and η_Q is 0.75. For Ala2 C β , the δ_{aniso} is -18 ppm, and η_Q is 0.89. In the PITHIRDS-CT simulations, a linear eight-spin system was used to mimic the atom coordinates in the in-register parallel β -sheet structure, which is a linear array of eight ¹³C spins separated by constant distance. For the R²W simulations, a two-spin system was chosen to better describe the relative atom positions in the antiparallel β -sheet model. R²W simulations with different combinations of $T_{2,zq}$ and distances were performed, and the results are compared with experimental data to find the best fit.

5.3.4 Molecular Dynamics Modeling

The all-atom models of P1 amyloid were built by constraining β -strands with NAMD scripts [240]. First, a single P1 peptide was generated using standard β -strand backbone torsion angles (antiparallel β -sheets, $\phi = -139^\circ$, $\psi = 135^\circ$; parallel β -sheets, $\phi = -119^\circ$, $\psi = 113^\circ$). Second, the torsion angles of the turn region (S6, G7, S8) were manually adjusted to make the desirable conformation. The SGS region for the U-shaped model was similar to previous DMD simulations [314], while the SGS for the β -hairpin model was similar to 3-residue β -

turns [321]. Third, the U-shaped P1 peptides were placed in antiparallel alignment to form β -sheets for the U-shaped antiparallel model, and the β -hairpin P1 peptides were placed into *syn* alignment to form β -sheet layers for the non-native β -hairpin model. These β -sheet layers were optimized in NAMD to get the energy-minimized conformation. Finally, the U-shaped antiparallel layers (or the *syn* β -hairpin layers) were brought to close positions parallel to the fibril axes, and the intermolecular side chain constraints (Val3-Ser8) were used to guide their stacking. The multi-layer structural models were generated from the molecular dynamic simulation in NAMD.

To calculate the expected dilution ratio for atom pairs, we counted the corresponding ^{13}C atom contacts (*i.e.*, a pair of atoms within 0.6 nm distance) in the structural model. We counted the fraction of intramolecular contacts in total contacts for every atom pair, and then we calculated the expected signal attenuation in the isotope-diluted sample (dilution ratio). For example, there are 52 V3 C α -F11 C α contacts in our final β -hairpin model with four layers of β -sheets. Intramolecular contacts are 50% of the total number of contacts. Thus, half of the V3 C α -F11 C α contacts are intramolecular, which do not cause signal attenuation, and the other half are intermolecular contacts, whose contribution to NMR signal reduces with a decreasing contact chance in isotope dilution. With the 30% diluted concentration of ^{13}C -labeled materials, the expected dilute ratio can be calculated as $0.5 + 0.5 \times 0.3 = 0.65$ if we assume that all contacts equally contribute to the crosspeak intensity.

5.4 Experimental Results

5.4.1 Isotope Labeling Strategy

The tested amyloid samples with ^{13}C , ^{15}N labels on specific residues are summarized in Table 5.1.

To differentiate between the hypothesized structures in Figure 5.3, five residues with uniform ^{13}C labeling were placed into Sample 5.A. They are two residues near the N-terminus (Ala2 and Val3), one at the center of the amino acid sequence (Ser8), and two

Table 5.1 Isotope-labeling scheme for P1 amyloid samples.

| Sample | Isotope labeling | Experiments |
|--------|---|---|
| 5.A | uniform ^{13}C , ^{15}N labels on residues A2, V3, S8, F11 and Q12 | 2D fpRFDR, 500 ms mixing 2D DARR, 2D CHHC |
| 5.B | 70% unlabeled peptide and 30% with uniform ^{13}C , ^{15}N labels on residues A2, V3, S8, F11 and Q12 | 500 ms mixing 2D DARR, 2D CHHC |
| 5.C | ^{13}C label on A2 C β and F11 CO | PITHIRDS-CT, R 2 W |

on the C-terminus (Phe11 and Gln12). The positions of these labeled sites in different conformations are illustrated by black ovals in Figure 5.3. We planned to employ a 2D DARR experiment to probe inter-residue proximities in the assembled amyloid structure, and to compare the NMR results with the model-predicted contact charts (see Section 2.4.2). Figure 5.4 shows the predicted patterns of inter-residue contacts based on the three hypothesized structural models. More specifically, the native β -hairpin structure (Figure 5.3A and 5.4A) predicts contacts Ala2/Phe11 and Val3/Ser8, the U-shaped parallel β -sheet (Figure 5.3B and 5.4B) predicts a contact Val3/Phe11, and the S-shaped parallel β -sheet (Figure 5.3C and 5.4C) predicts a contact Ser8/Gln12. There might be unexpected inter-residue contacts if the structural models correspond to subunits (protofilaments) that associate into thicker fibrils, a common phenomenon in known amyloid structures [38, 89]. An isotope-diluted sample (Table 5.1, Sample 5.B) was created through fibrilization of P1 mixture solution of 30% peptide labeled as Sample 5.A and 70% unlabeled peptide. It was designed to reveal the NMR signal attenuation in isotope dilution, which could be further interpreted in terms of model-dependent intra- and intermolecular ^{13}C nuclei contacts. Although the isotope-dilution effect had been quantitatively analyzed to help determine structures in some literature [88, 322], we, at first, did not expect Sample 5.B would play a critical role in our structural study.

In addition, another P1 amyloid sample (Table 5.1, Sample 5.C) was synthesized with ^{13}C labels on the carbonyl (CO) of Phe11 and the C β methyl of Ala2. It is compatible with

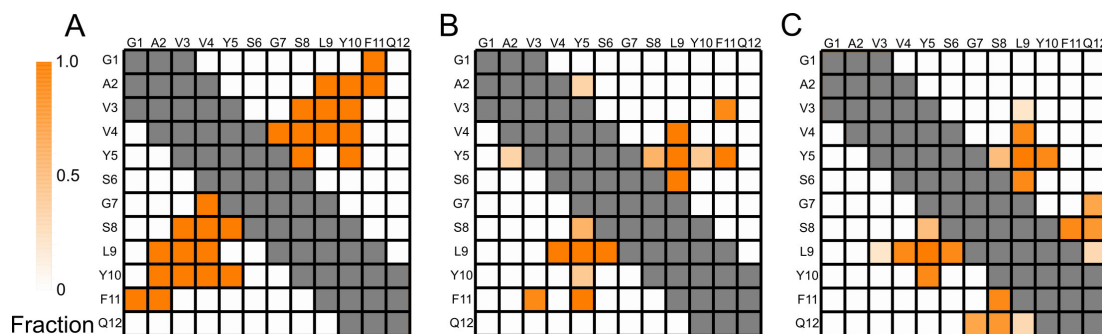


Figure 5.4 Panels A-C correspond to the models in parts A-C of Figure 5.3, respectively. The format of contact charts was discussed in Section 2.4.2. The orange color indicates that the structural model predicts NMR crosspeaks between the corresponding residues, provided that both residues are isotopically labeled with ^{13}C uniformly. As indicated on the left, the color scale (white to dark orange) indicates the fraction of peptide molecules predicted to contribute to inter-residue 2D NMR crosspeak intensity; the darkest orange squares correspond to the strongest expected crosspeaks. If all molecules in a sample have the same isotopic labels, contacts between residues that are 2 amino acids apart or less in the primary structure would not report on molecular conformation; these combinations of residues are indicated by gray squares.

^{13}C - ^{13}C dipolar recoupling experiments, namely PITHIRDS-CT and R^2W (Section 2.3.2.2 and 2.3.2.3), which could provide more accurate distance constraints on the organization of peptide backbones.

5.4.2 2D fpRFDR Experiments: Single Uniform Structure

The 2D fpRFDR spectral signatures in Figure 5.5 of Sample 5.A are consistent with an amyloid fibril, which also agree with prior biophysical data [137]. Notably, each directly bonded pair of ^{13}C nuclei exhibits only one crosspeak on the 2D fpRFDR spectrum, indicating a homogeneous amyloid structure that produces a single chemical environment per labeled nucleus. The crosspeaks have linewidths in 0.6 to 1.7 ppm range (Table 5.2), which match analyses of amyloid- β fibrils [38, 88, 323] but are mostly larger than linewidths of peptide microcrystals [324, 325]. The secondary chemical shifts for CO, $\text{C}\alpha$, and $\text{C}\beta$ were also calculated (Table 5.2) to verify the β -strand secondary structure. The negative secondary chemical shifts for $\text{C}\alpha$ and CO, and the positive shifts for $\text{C}\beta$ in all the labeled residue (ex-

cept Gln12 at C-terminus) suggest that most of the residues in P1 peptide adopt β -strand-like backbone conformation [229]. These experimental results are right as we expected for short peptide amyloid.

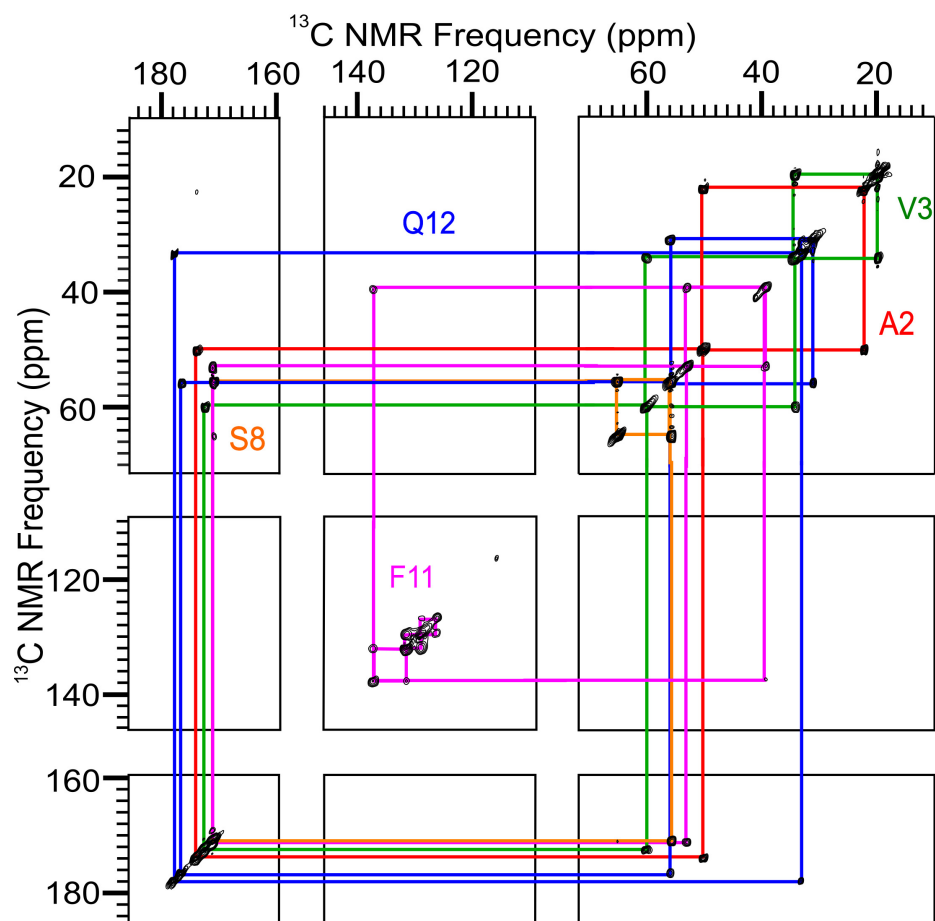


Figure 5.5 2D fpRFDR spectrum of amyloid fibrils formed by P1 peptide uniformly labeled with ^{13}C at A2, V3, S8, F11, and Q12 (Sample 5.A). Colored lines indicate residue-level spectral assignments based on crosspeaks between directly bonded ^{13}C atoms.

Table 5.2 Chemical shifts (ppm)/linewidths (full width at half-maximum, ppm) for ^{13}C -labeled sites in 2D fpRFDR spectrum of Sample A. The error is ± 0.1 ppm for both the chemical shift and linewidth based on nonlinear least-square fitting to Gaussian functions. Secondary chemical shifts for CO, C α , and C β are calculated by comparing the measured chemical shifts to the values from the same amino acid in random-coil model peptides [228].

| Residue | CO | C α | C β | C γ | other C |
|--------------------------|-----------|------------|-----------|------------|---|
| A2 | 173.7/1.0 | 50.1/1.0 | 22.1/0.7 | | |
| secondary chemical shift | -2.4 | -0.7 | +4.7 | | |
| V3 | 172.3/1.0 | 59.8/1.2 | 34.1/1.1 | 19.8/0.7 | |
| secondary chemical shift | -2.3 | -0.7 | +2.9 | | |
| S8 | 170.7/1.0 | 55.6/1.0 | 64.9/1.0 | | |
| secondary chemical shift | -2.2 | -1.0 | +2.8 | | |
| F11 | 170.9/1.0 | 52.8/1.2 | 39.2/1.4 | 137.1/1.4 | C δ : 131.5/1.4 C ϵ : 129.2/1.6 C ζ : 126.5/1.7 |
| secondary chemical shift | -3.2 | -3.2 | +1.3 | | |
| Q12 | 176.4/0.9 | 55.9/1.1 | 31.0/0.9 | 33.1/0.7 | C δ : 177.6/0.6 |
| secondary chemical shift | +2.1 | +1.9 | +3.3 | | |

5.4.3 2D DARR Experiments: Inter-residue Contacts Exclude the S-Shaped Model

2D DARR experiments with 500 ms mixing time (Section 2.3.2.5) were performed on Sample 5.A to interrogate ^{13}C - ^{13}C contacts between labeled residues. The inter-residue cross-peaks on the 2D DARR spectrum (Figure 5.6) can be identified based on chemical shift

values of labeled ^{13}C atoms. The identified inter-residue crosspeaks are all labeled in Figure 5.6 and listed in Table 5.3.

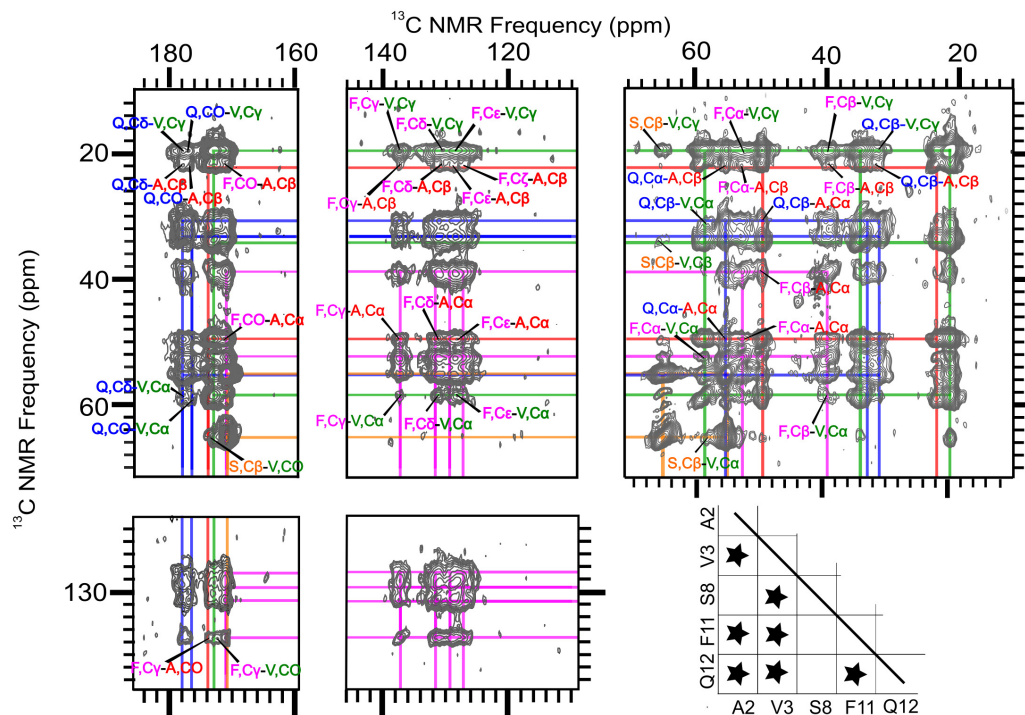


Figure 5.6 2D DARR spectrum taken on Sample 5.A with 500 ms mixing. Colored lines indicate intra-residue crosspeak patterns as in 2D fpRFDR spectrum (Figure 5.5). Bottom right panel: Table of detected contacts (stars) between isotopically labeled residues, interpreted based on the detected crosspeak patterns detailed in Table 5.3.

These results indicate that the N- and C-termini of the peptide are in proximity (A2/F11, A2/Q12, V3/F11, and V3/Q12 contacts in Figure 5.6) and that V3 is close to S8. These residue contacts, apparently, do not support the S-shaped peptide conformation, which predicts S8/F11 or S8/Q12 contact (Figure 5.3C and 5.4C) but does not expect the observed ones. As for the native β -hairpin and the U-shaped parallel β -sheet models, some of the model-predicted contacts corresponding to ^{13}C -labeled residues were observed. However, we noticed that, the contact chart in Figure 5.4A and 5.4B each predict fewer inter-residue contacts than those observed experimentally. Hence, more experiments and more modeling efforts were needed to resolve the amyloid structure.

Table 5.3 Crosspeaks detected in the 2D DARR spectrum of Sample 5.A (Figure 5.6). An asterisk means the crosspeak is not resolved from nearby NMR signals. A check mark indicates the crosspeak is well resolved and marked in the spectra (Figure 5.6 and 5.13). A dash indicates that the crosspeak is not detected.

| | A2, CO | A2, C α | A2, C β | V3, CO | V3, C α | V3, C β | V3, C γ 1 C γ 2 |
|-------------------|--------|----------------|---------------|--------|----------------|---------------|-------------------------------|
| S8, CO | - | - | - | * | * | * | * |
| S8, C α | - | - | - | * | * | * | * |
| S8, C β | - | - | - | √ | √ | √ | √ |
| F11, CO | * | √ | √ | * | * | * | * |
| F11, C α | * | √ | √ | * | √ | * | √ |
| F11, C β | * | √ | √ | * | √ | * | √ |
| F11, C γ | √ | √ | √ | √ | √ | * | √ |
| F11, C δ | * | √ | √ | * | √ | * | √ |
| F11, C ϵ | * | √ | √ | * | √ | * | √ |
| F11, C ζ | * | * | √ | * | * | * | * |
| Q12, CO | * | * | √ | * | √ | * | √ |
| Q12, C α | * | √ | √ | * | * | * | * |
| Q12, C β | * | √ | √ | * | √ | * | √ |
| Q12, C γ | * | * | * | * | * | * | * |
| Q12, C δ | * | * | √ | * | √ | * | √ |

5.4.4 Dipolar Recoupling NMR and 2D CHHC Experiments: Antiparallel β -Sheets

To define the inter-strand arrangement of P1 peptide backbones, PITHIRDS-CT (Section 2.3.2.2) and R²W (Section 2.3.2.3) were applied on Sample 5.C and the 2D CHHC experiment (Section 2.3.2.6) was performed on Sample 5.A.

The PITHIRDS-CT technique was widely used to verify whether the β -strands assemble into in-register parallel β -sheet [222, 326], also known as “parallel-in-register” (PIR) β -sheet. Previously, the U-shaped and S-shaped models (Figure 5.3B and C, respectively) both predicted such PIR β -sheet structure. If the PIR hypothesis were correct, the sim-

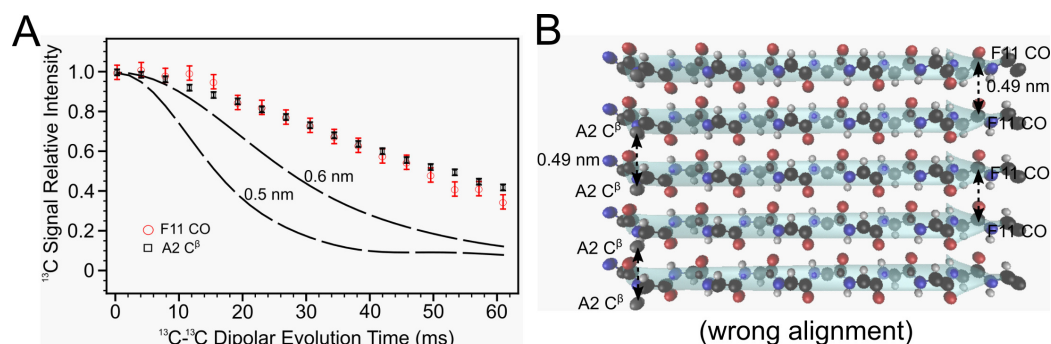


Figure 5.7 PITHIRDS-CT data indicates not an in-register parallel β -sheet. (A) PITHIRDS-CT applied to Sample 5.C measures the distance-dependent homonuclear intermolecular dipolar couplings between equivalent ^{13}C labeled sites through loss of NMR peak intensity as a function of dipolar recoupling time. Symbols represent the experimental data points, and the dashed lines are simulated curves based on equally-distributed linear spin system with variable inter-nucleus distances. (B) All-atom model for in-register parallel β -sheet formed by P1 peptide. The predicted homonuclear distances of labeled sites are marked by double headed arrows.

ulated dashed curves in Figure 5.7A would bracket the measured PITHIRDS-CT decays, as indicated by measurements on A β (1-42) fibrils [185, 275] (see Section 4). These two simulated curves are based on eight ^{13}C atoms positioned as predicted for an in-register parallel β -sheet: in linear arrangements with constant nearest-neighbor ^{13}C - ^{13}C distances of 0.5 or 0.6 nm (Figure 5.7B). The measured decays in Figure 5.7A, unexpectedly, show weaker ^{13}C - ^{13}C dipolar couplings between the equivalent labeled sites, hence the disagreement with in-register parallel β -sheet structure. To explain the non-negligible measured PITHIRDS-CT decays, more spin simulations of different spin systems with variable distance parameters are compared with the data set (Figure E.1). It seems that the measured decays of F11 CO or A2 C β are consistent with a ^{13}C - ^{13}C distance of approximately 0.7 nm in some geometry of ^{13}C atoms (see Figure E.1A and B). However, when the detected dipolar coupling between labeled sites are this weak, the apparent inter-atomic distance can be significantly affected by coupling to natural-abundance ^{13}C nucleus at nearby unlabeled carbon sites [222]. In Figure E.1C, we attempted to simulate the PITHIRDS-CT signal evolution caused by nearby natural-abundance ^{13}C and faraway labeled ^{13}C in a structural

model, and found the estimated signal decay is close to the observed data sets. This was our **first attempt** to simulate and explain the weak decay by introducing nearby natural-abundance ^{13}C nuclei. In addition, PITHIRDS-CT signal decays can also be affected by other factors, such as imperfect compensation of the pulse sequence for transverse spin relaxation [206]. Take together, we do not believe that weak PITHIRDS-CT decays in Figure 5.7A can be reliably interpreted in terms of specific structure features. They only suggest that the homonuclear distances between the labeled ^{13}C atoms are longer than 0.6 nm, and thus P1 amyloid does not consist of in-register parallel β -sheet.

We used R^2W technique to constrain the distance between the $\text{C}\beta$ atom of A2 and the CO atom of F11, the two ^{13}C -labeled sites in Sample 5.C. As explained in Section 2.3.2.3, it assesses the dephasing of ^{13}C NMR signal intensity when the MAS rate (ω_{MAS}) is near the difference of NMR peak frequency between the two labeled sites ($\omega_{\text{CO}} - \omega_{\text{C}\beta}$). Because two parameters of the spin system, namely the zero-quantum relaxation time and the inter-nuclear distance, affect the theoretical dependence of signal intensities on resonance mismatch ($\nu_{\text{mis}} = \omega_{\text{MAS}} - \omega_{\text{CO}} + \omega_{\text{C}\beta}$), a two-parameter optimization was conducted to find the best-fit spin simulation for the experimental data (Figure 5.8A). Finally, the best-fit MAS-frequency dependent NMR signal loss indicates a ^{13}CO - $^{13}\text{C}\beta$ of 0.57 ± 0.01 nm (Figure 5.8B). It supports the interpretation that P1 β -strands are organized into antiparallel β -sheet (Figure 5.8D).

To get detailed constraints on the antiparallel arrangement of β -strands within P1 amyloid, a 2D-CHHC experiment was performed on Sample 5.A. The 2D CHHC spectrum in Figure 5.8C was collected with $182 \mu\text{s}$ ^1H - ^1H dipolar coupling, and it detected a crosspeak between the $\text{C}\alpha$ of V3 and F11, indicating that the $\text{H}\alpha$ atoms on these two residues are separated by 0.3 nm or less. The structural feature, $\text{H}\alpha$ atoms from two residues get so close, confirms that P1 peptides are arranged into antiparallel β -sheet or β -hairpins (Figure 5.8D). However, the NMR result is not consistent with the native β -hairpin (Figure 5.3A and 5.9A). We tested different arrangements of the P1 native β -hairpins (Figure 5.9B and C), but none

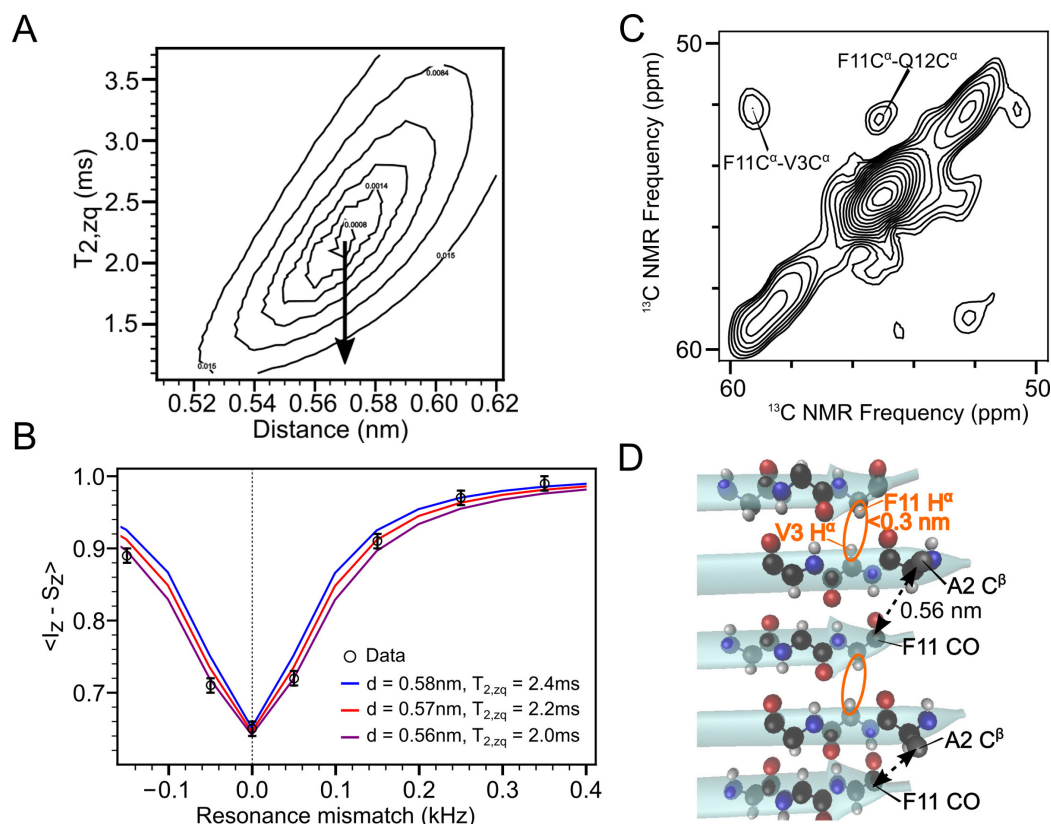


Figure 5.8 R²W and 2D CHHC measurements indicating an antiparallel β -sheet. (A) Sum squared residual between the R²W data from Sample 5.C and the spin simulation predictions with two parameters, the zero-quantum relaxation time $T_{2,zq}$ and the distance between the ^{13}C -labeled sites. The best fitted result is labeled by an arrow. (B) R²W applied to Sample 5.C measures the effect of dipolar coupling between ^{13}C -labeled A2 C $^\beta$ and F11 CO, through relative attenuation of NMR signal intensity (circles) as a function of MAS speed. The solid lines are simulated curves with the best fitted parameters in panel A. (C) 2D CHHC spectrum of Sample 5.A. (D) All-atom model of an antiparallel β -sheet, showing the expected distances between the ^{13}C -labeled sites and H α atoms.

of them rationalizes the 0.3 nm distance between V3 H α and F11 H α . In addition, we collected a CHHC spectrum on sample 5.B (Figure 5.10) to test the isotope-dilution effect on crosspeaks. It shows that the V3 C α /F11 C α crosspeak is attenuated with isotope-dilution, suggesting that the atoms that contribute to this crosspeak are on neighboring molecules. Inquiringly, a crosspeak between F11 C α and Q12 C α shows up on the 2D CHHC spectrum, although the corresponding H α atoms should be separated by around 0.4 nm distance in a β -strand. It indicates that the terminal Q12 backbone torsion angles may depart from

the typical values of β -strands. Alternatively, the unexpected sharpness and intensity of the Q12 $C\alpha$ signal could have made this crosspeak easier to be detected despite an F11 $H\alpha$ -Q12 $H\alpha$ distance longer than 0.3 nm. We did not detect a crosspeak between A2 $C\alpha$ and V3 $C\alpha$ in the 2D CHHC spectrum, though the two residues are also adjacent in the P1 peptide.

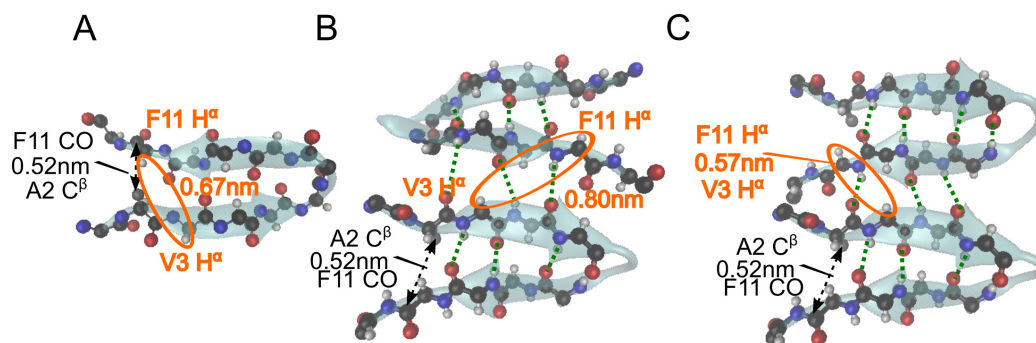


Figure 5.9 All-atom models of P1 native β -hairpin (see Figure 5.1) in different alignments. (A) single P1 peptide in the native β -hairpin conformation. (B) Two P1 peptide molecules with *anti* alignment of β -hairpins. (C) Two P1 peptide molecules with *syn* alignment of β -hairpins.

To summarize, we observed the following important constraints regarding the P1 amyloid fibril: (a) a single chemical environment for each ^{13}C -labeled site indicating a homogeneous fibril, (b) an antiparallel arrangement of β -strands within β -sheets, (c) close intermolecular proximity between V3 and F11 backbone atoms, and (d) intermolecular contact between sidechains of V3 and S8. Moreover, according to AFM characterization (Figure 5.1) [137], where the height of fibril was measured to be around 1 nm, while the widths of fibrils were much larger (varying between 10 and 20 nm), we infer that the proposed fibril structures would contain stacking of multiple layers to form mature fibrils. Although the constraints reveal inconsistencies with all three of the hypothesized models (Figure 5.3), two of the models can be modified for harmony with the data.

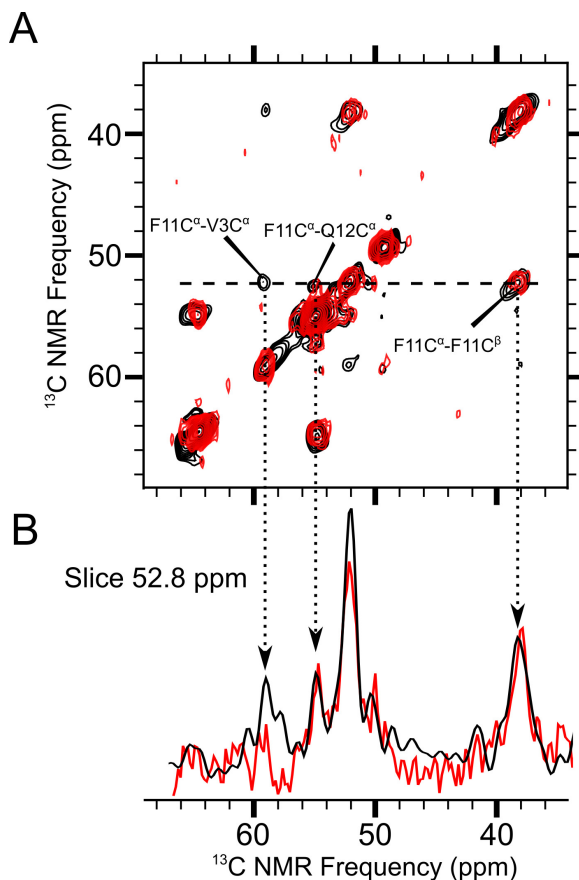


Figure 5.10 Isotope-dilution effect on the crosspeak between V3 C α and F11 C α in 2D CHHC spectra. A) Overlay of the regions near the C α signals of the 2D CHHC spectra for Samples 5.A (black contours) and 5.B (red contours). These samples are isotopically labeled at the same residues, but Sample 5.B was produced by co-assembly of 30% labeled peptide with 70% unlabeled peptide. B) Slices at 52.8 ppm from spectra in panel A.

5.4.5 Structural Modeling and Isotope-Dilution Effect: U-Shaped Antiparallel Model

The first modification is based on the U-shaped model predicted by DMD (Figure 5.3B). We designed an antiparallel β -sheet fibril that retains the U-shaped molecular conformation (Figure 5.11A). In this model, the V3 backbone forms C=O \cdots H-N hydrogen bonds with the F11 backbone, just as in Figure 5.8D. Also, the Val3 side chain is at the opening of the “U” and the Ser8 side chain is at the bottom turn of the “U”. To rationalize the intermolecular V3-S8 sidechain contact, we put the U-shaped β -sheets stacking top-to-bottom (Figure 5.11B). Analysis of the multilayer stacked structural model for predicted DARR contacts (Figure

5.11C) is consistent with our experimental 2D DARR results (Figure 5.6). Although we modeled only four U-shaped layers (Figure 5.11B), it should be noted that additional layers would be necessary for agreement with the fibril dimensions measured by AFM (10–20 nm).

The second model was based on a β -hairpin conformation of P1 peptide, one that partially preserves the native structure of P1 within the mOLF crystal structure (Figure 5.1A and 5.9A). The 2-residue β -turn (S6-G7) in the native β -hairpin was changed into a 3-residue β -turn (S6-G7-S8) (Figure 5.12A), with initial torsion angles from a similar 3-residue-turn structure (G28-I29-G30 turn in T4 lysozyme) [321, 327]. Thus, the two β -strands in the hairpin model are formed by V3-Y5 and L9-F11, and the β -strands are arranged into an antiparallel β -sheet by bringing V3 and F11 backbones within hydrogen-bonding distance (Figure 5.11D and 5.12A). Following the terminology of Leonard *et al.* [320] and Nagy-Smith *et al.* [319], which defines the terms “*syn*” and “*anti*” to describe whether turns of β -hairpins are oriented in the same or opposite directions, respectively, β -hairpins aligned in an *anti* configuration (Figure 5.12B) cannot be stabilized by sufficient intermolecular hydrogen bonds nor satisfy the short distance between V3 H α and F11 H α ; while the *syn* arrangement of the non-native β -hairpins (Figure 5.11D and 5.12C) can form an extended P1 β -sheet. Moreover, the non-native β -hairpin model resolves the intermolecular V3-S8 side chain contact through stacking of β -sheet with *anti* arrangement between adjacent β -sheets (Figure 5.11E). When we put the β -sheets formed by non-native β -hairpins in multiple stacked layers (Figure 5.11E), the V3 and S8 sidechain proximity happens between every layer. Like the U-shaped model, the stacked β -hairpin model predicts a DARR contact pattern that is consistent with the experimental data (Figure 5.11F). Again, additional layers would be required for agreement with the fibril dimensions detected by AFM.

To this point, the two proposed models (Figure 5.11B and E) both satisfy the experimental constraints in Figure 5.6 and 5.8, how can we differentiate between them using ssNMR techniques? We first realized the two models differ in their predictions of the relative ori-

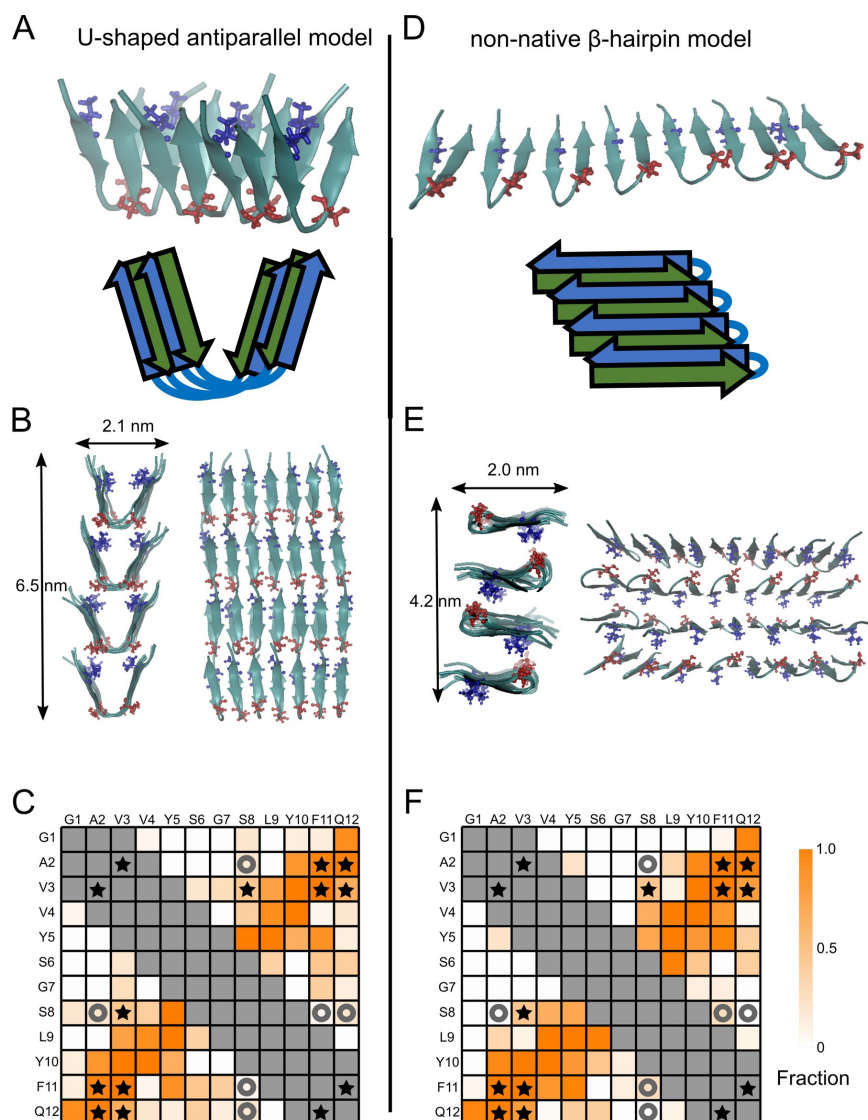


Figure 5.11 Two candidate models, namely U-shaped antiparallel model and non-native β -hairpin model, inspired by experimental constraints and their expected patterns of 2D DARR contacts. In the depictions of all-atom models, the backbones are drawn as ribbons and the V3 and S8 residues are shown in blue and red, respectively. In the 2D DARR contact charts, the orange and gray coloring is as defined in Figure 5.4, and the symbols indicate detected (stars) and undetected (circles) DARR contacts between the ^{13}C -labeled residues in the 2D DARR spectrum of Sample 5.A (Figure 5.6). (A) U-shaped P1 peptide molecules arranged into antiparallel β -sheets. (B) Stacked U-shaped antiparallel β -sheets in P1 amyloid structure. (C) Predicted pattern of 2D DARR contacts for the U-shaped antiparallel model. (D) P1 peptide molecules in the non-native β -hairpin conformation (described in Figure 5.12) arranged into a *syn* β -sheet. (E) Four β -sheets from panel D stacked into P1 amyloid fibril. (F) Predicted 2D DARR contact pattern for the non-native β -hairpin model.

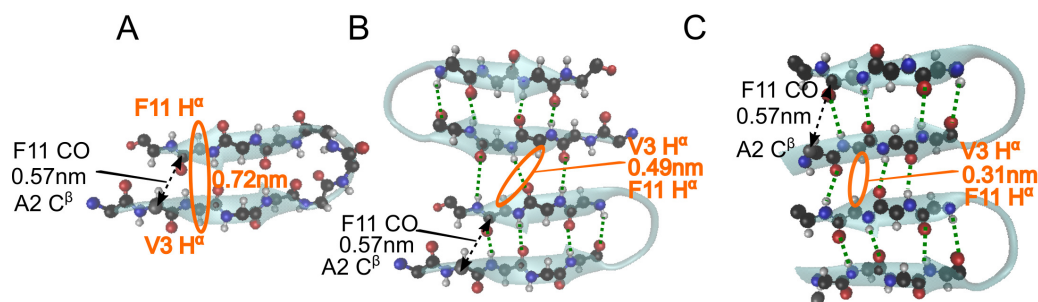


Figure 5.12 All-atom models of P1 peptide in non-native β -hairpin. (A) A P1 non-native β -hairpin with a three-residue β -turn. (B) A pair of P1 non-native β -hairpins with *anti* alignment. (C) A pair of P1 non-native β -hairpins with *syn* alignment.

entations and the relative positions of residues within the same or adjacent molecules. The inter- or intra-molecular ^{13}C - ^{13}C proximity may cause the change of signal intensities on the 2D NMR spectra collected on the isotope-diluted Sample 5.B. More specifically, intensities of crosspeaks in this isotope-diluted spectrum are attenuated relative to diagonal peaks when they correspond to atoms on different molecules, which is a widely-used strategy in ssNMR structural characterization [88, 322].

Panel A and B of Figure 5.13 illustrate model-dependent differences in the relative positions and orientations of the V3 and F11 residues. The U-shaped model (Figure 5.11A and B, Figure 5.13A) predicts that each V3 has two adjacent F11 residues on different molecules and one adjacent F11 residue on the same molecule. The β -hairpin model (Figure 5.11D and E, Figure 5.13B), standing on each V3 residue, predicts one intramolecular V3/F11 contact, one intermolecular V3/F11 contact, and no V3/F11 contacts between stacking layers. Thus, the models predict different degrees of crosspeak attenuation between the labeled ^{13}C nuclei on V3 and F11. Close examination of residue orientations in the U-shaped model motivates greater degrees of isotopic dilution for crosspeaks between V3 and F11 backbone atoms when compared to crosspeaks between V3 and F11 sidechain atoms (Figure 5.13A), fitting right into our observation of signals on the 2D DARR spectra (Figure 5.13C and E.2). Noting that 2D DARR crosspeaks are sensitive to ^{13}C - ^{13}C dipolar couplings corresponding to distances of up to 0.6 nm, the U-shaped model predicts that crosspeaks between backbone

atoms (*e.g.*, F11 C α -V3 C α , F11 CO-V3 C α , F11 C α -V3 CO) would be exclusively between atoms on different molecules, whereas F11/V3 sidechain crosspeaks (V3 C γ 1/C γ 2-F11 C γ , V3 C γ 1/C γ 2-F11 C δ 1/C δ 2, V3 C γ 1/C γ 2-F11 C ϵ 1/C ϵ 2) would include contributions from both inter- and intramolecular dipolar couplings. In contrast, the β -hairpin model would predict uniform isotopic dilution effects for all crosspeaks between ^{13}C atoms on V3 and those on F11. Thus, we compared the predicted dilution ratios from the two models (see Section 5.3.4) and the calculated ratios based on experimental data (see Section 5.3.2). The calculation was based on the spectra of Sample 5.A and 5.B (Figure 5.13C) and their peak integrals tabulated in Table E.1. The final dilution ratios are listed in Table 5.4 and plotted in Figure 5.14, which apparently favor the U-shaped antiparallel β -sheet model. Taken together, although the U-shaped amyloid model and the β -hairpin model both largely satisfy the available data, the U-shaped antiparallel fibril model is favored because of consistency with the measured isotope-dilution effect.

5.5 Discussion

In this study, we characterized an unanticipated amyloid structure of a recently identified peptide fibril, that of the 12-residue P1 from the mOLF 5-blade β -propeller (Figure 5.1A), whose misfolding is associated with glaucoma. Prior to solving the mOLF amyloid structure, amyloid prediction servers (Waltz, AmylPred, and TANGO) [307, 310, 328] converged on three peptide sequences, P1, P2, and P3 within mOLF with high propensity to form amyloid. Consistent with predictions, fibril formation by P1 and P3 were confirmed experimentally [137]. Unlike P3, which forms heterogeneous fibrils [314], incubation of dissolved P1 peptide at 37 °C and pH 7.2, without seeding, reliably produces fibrils with consistent morphology and ThT aggregation kinetic curves. Most important, the P1 fibril morphology was akin to that observed for full-length mOLF aggregated under similar conditions [137]. While computational tools exist that enabled discovery of P1 within the mOLF sequence, amyloid structure predictions are still lacking. Despite having three seemingly reasonable

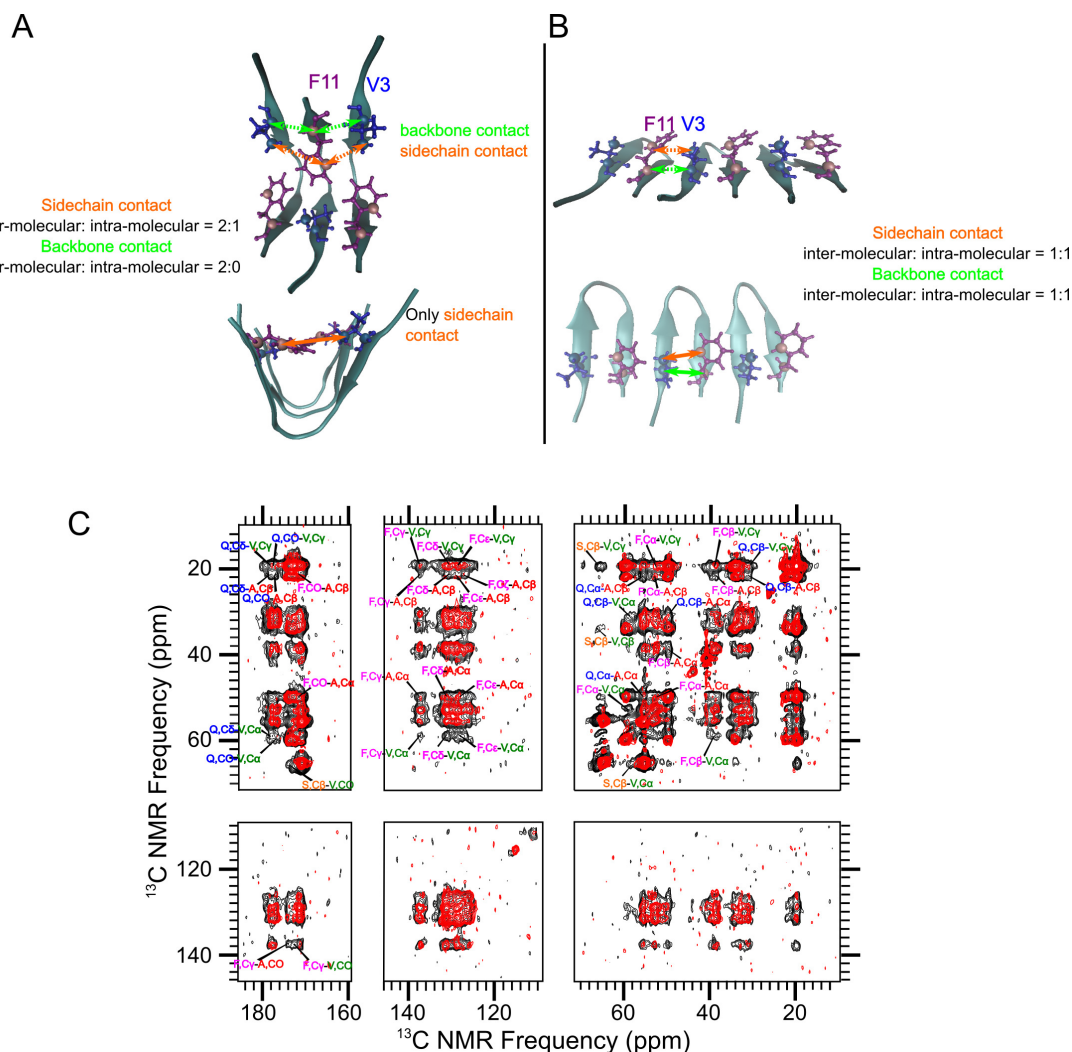


Figure 5.13 Effects of isotopic dilution on the 2D DARR spectrum. (A) Two views of the U-shaped antiparallel structural model, with backbones drawn as ribbons and V3 and F11 drawn with ball-and-stick representations (blue and purple, respectively). Double-headed arrows indicate selected pairs of ^{13}C atoms that would correspond to 2D NMR crosspeaks between V3 and F11. The green arrows indicate NMR-detectable crosspeaks between V3 and F11 backbone atoms (CO, C α), and orange arrows indicate crosspeaks between sidechain atoms. Solid lines indicate that the pair of atoms is from the same peptide molecule, while dashed indicates that the arrowheads point to atoms on different molecules. (B) Similar diagrams to those shown in panel A, but for the non-native β -hairpin model. (C) Overlaid 2D DARR spectra from sample 5.A (black contours) and 5.B (red contours). The samples were isotopically labeled at the same residues, but sample 5.B was isotopically diluted by coassembly of labeled peptide (30%) with unlabeled peptide (70%). The measured effects of isotopic dilution are tabulated in Table 5.4.

Table 5.4 Dilution ratios of well-distinguished crosspeaks in the 2D DARR spectra. Measured ratios corresponding to intra-residue crosspeaks and adjacent residue crosspeaks (solely intra-molecular dipolar couplings) are first scaled to an average of 1 (gray rows). The other measured ratios are scaled by the same factor. The expected dilution ratios for these crosspeaks are estimated based on the all-atom models (see Section 5.3.4).

| Crosspeaks | Dilution ratio | Expected dilution ratio in U-shape model | Expected dilution ratio in β -hairpin model |
|----------------------------|-----------------|---|--|
| A2 – A2 $\alpha - \beta$ | 1.08 \pm 0.05 | 1.0 | 1.0 |
| V3 – V3 $\alpha - \gamma$ | 1.04 \pm 0.06 | 1.0 | 1.0 |
| F11 – F11 $\alpha - \beta$ | 0.95 \pm 0.10 | 1.0 | 1.0 |
| $\beta - \gamma$ | 0.96 \pm 0.10 | 1.0 | 1.0 |
| $\alpha - \gamma$ | 0.93 \pm 0.10 | 1.0 | 1.0 |
| A2 – V3 $\alpha - \alpha$ | 0.97 \pm 0.06 | 1.0 | 1.0 |
| $\beta - \alpha$ | 1.05 \pm 0.09 | 1.0 | 1.0 |
| F11 – Q12 $\gamma - \beta$ | 0.97 \pm 0.12 | 1.0 | 1.0 |
| $\delta - \beta$ | 0.99 \pm 0.10 | 1.0 | 1.0 |
| $\varepsilon - \beta$ | 1.06 \pm 0.13 | 1.0 | 1.0 |
| A2 – F11 $\alpha - \alpha$ | 0.35 \pm 0.05 | 0.30 | 0.65 |
| $\alpha - \beta$ | 0.28 \pm 0.05 | 0.30 | 0.65 |
| $\alpha - \gamma$ | 0.36 \pm 0.05 | 0.30 | 0.65 |
| $\alpha - \delta$ | 0.37 \pm 0.05 | 0.30 | 0.65 |
| $\alpha - \varepsilon$ | 0.30 \pm 0.04 | 0.30 | 0.65 |
| $\beta - \delta$ | 0.18 \pm 0.03 | 0.30 | 0.65 |
| $\beta - \varepsilon$ | 0.31 \pm 0.06 | 0.30 | 0.65 |
| V3 – F11 $\alpha - \alpha$ | 0.29 \pm 0.06 | 0.30 | 0.65 |
| $\alpha - \delta$ | 0.35 \pm 0.08 | 0.30 | 0.65 |
| $\gamma - \gamma$ | 0.50 \pm 0.06 | 0.53 | 0.65 |
| $\gamma - \delta$ | 0.56 \pm 0.04 | 0.53 | 0.65 |
| $\gamma - \varepsilon$ | 0.49 \pm 0.04 | 0.53 | 0.65 |
| V3 – S8 $\gamma - \beta$ | 0.35 \pm 0.06 | 0.30 | 0.30 |

structural predictions to guide our experiments, the NMR data in this paper describe a surprising and unique amyloid molecular structure.

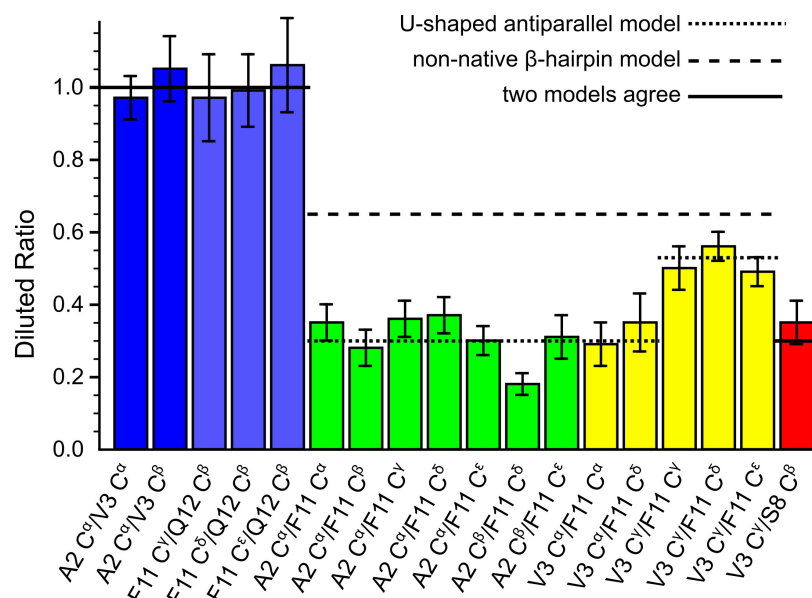


Figure 5.14 Comparison of measured dilution ratios with the expected values from the U-shaped antiparallel and the non-native β -hairpin models. The solid horizontal lines indicate where the models both predict the same amount of isotopic dilution. The dashed and dotted lines indicate where the models predict different degrees of isotopic dilution.

5.5.1 Stability of U-Shaped Antiparallel Amyloid Model

Our data are most consistent with stacked U-shaped antiparallel P1 protofibrils (Figure 5.11A-B and 5.15). Although the structure does not contain the canonical steric zipper with interdigitated side chains forming a dry core, it maximizes H-bonding interactions like other peptide amyloid structures [89, 167, 172] and also has a buried hydrophobic region within each proto fibril, hence a stable arrangement. Specifically, the opportunities for intermolecular backbone H-bonding span the residues within each peptide of the protofibril, including the S-G-S turn (Figure 5.16A). Despite no constraints for the H-bonding in turn region during our modeling process, the hydrogen bonds automatically form in molecular dynamic simulations. In forming the U shape conformation, each peptide shields hydrophobic residues V3 and L9 creating a hydrophobic pocket, which is then topped with π -stacked Y5 and F11 to form a hydrophobic patch on each protofibril (Figure 5.15A and Figure 5.16B). The protofibril surface containing the hydrophobic patch then nestles with a

neighboring protofibril wherein the two Ser residues of the S-G-S turn form polar contacts with the peptide termini from the neighboring protofibril (Figure 5.16C).

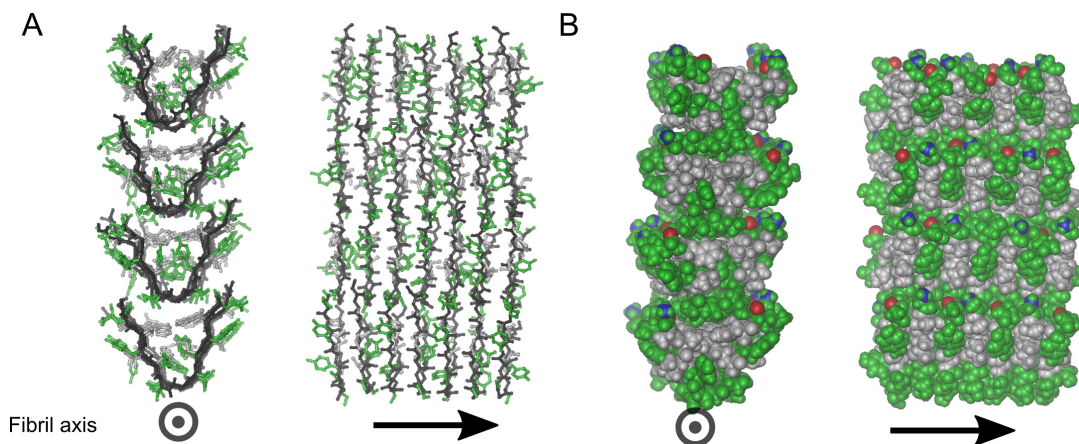


Figure 5.15 U-Shaped antiparallel model of the P1 amyloid fibril, which agrees best with the data. (A) Two views of a ball-and-stick representation including all non-hydrogen atoms in the model. The backbone of each peptide is colored black. The hydrophilic side chains are drawn in green, and the hydrophobic side chains are drawn in gray. (B) Models drawn with each atom depicted as a sphere with its van der Waals radius. The hydrophobic residues are colored gray, and the hydrophilic residues are drawn in green. The positively charged N-termini are drawn in blue, and the negatively charged C-termini are red.

Conversely, the non-native β -hairpin arrangement would seem less thermodynamically stable even though this model predicts stacking in a direction perpendicular to the β -strand backbone (see Figure 5.11E) commonly seen in amyloid structures [88, 329]. First, it has fewer options for H-bonding: the S-G-S turn within each β -hairpin is not in proximity of S-G-S turns in other peptides. Second, the hydrophobic residues are on the surface where they stabilize interactions among the protofibril layers and may be less effective at protecting the hydrophobic core from water.

5.5.2 Comparison of P1 Model with Other Amyloid Structures

One reason for studying new amyloid-forming peptides is to explore the diversity of sequences capable of forming amyloid and their structural arrangements. It is usually a very

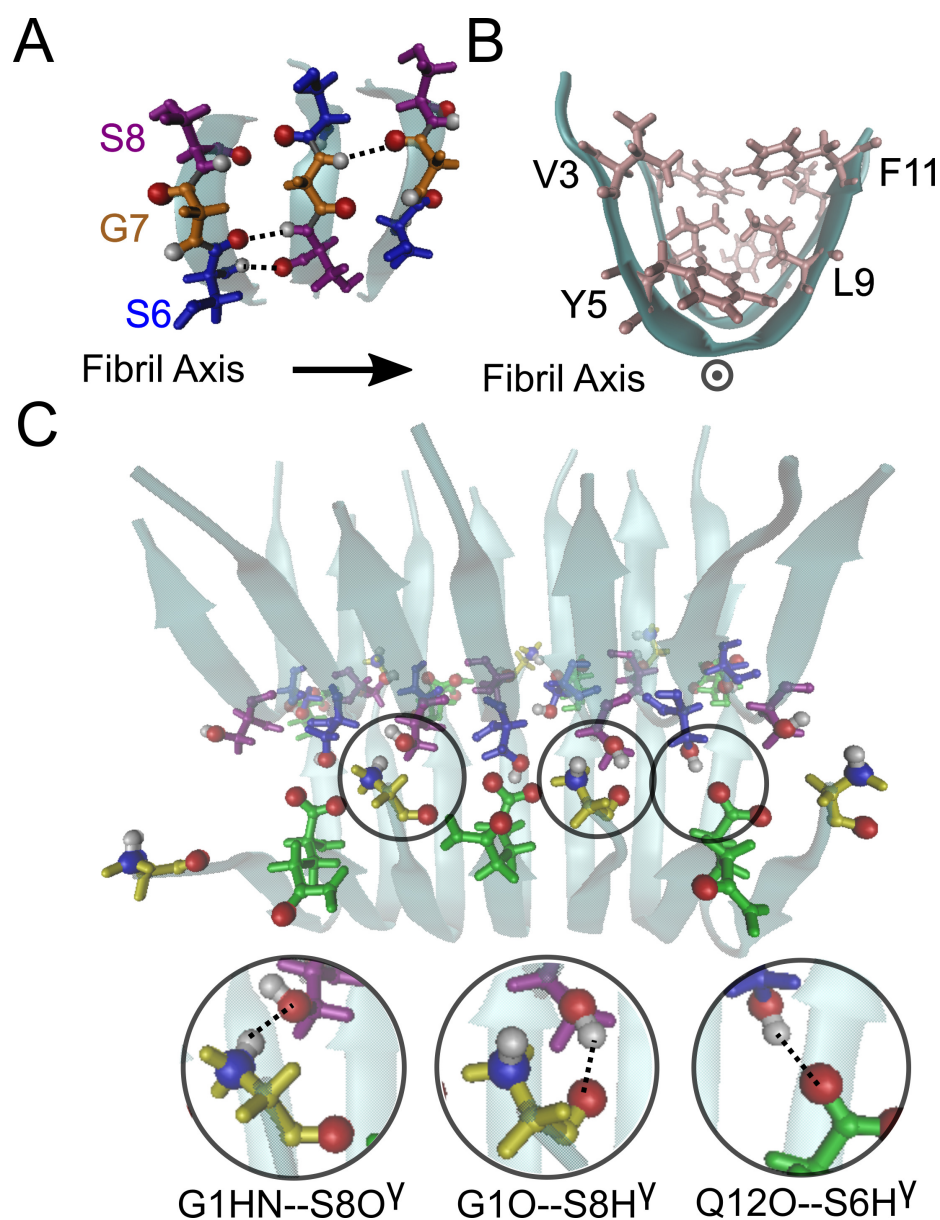


Figure 5.16 Representations of the U-shaped antiparallel structural model showing hydrogen bonds and hydrophobic core. A) Intermolecular backbone hydrogen bonding (dashed lines) between the S6-G7-S8 turns. B) Hydrophobic core formed by the sidechains of V3, Y5, L9, and F11 residues. C) The hydrogen bonding between the termini of P1 peptides and the S6/S8 from the neighboring protofibril. As for the color scheme for residues, G1, S6, G7, S8, and Q12 are drawn in yellow, blue, orange, purple, and green, respectively. Hydrophobic residues V3, Y5, L9, and F11 are drawn in pink in panel B. Dashed lines indicate hydrogen bonds involving O atoms, N atoms, and H atoms drawn as red, blue, and white spheres, respectively.

complicated problem: amyloid assembly can produce a variety of possible structures within a single sequence, and amyloid structures are not uniquely determined by amino acid sequence [38, 330]. Thus, the observation of new structural motifs for any peptide reveals structures that may be accessible to other peptides of similar size.

The U-shaped antiparallel amyloid structure of P1 has not been observed previously, even if assemblies of other larger peptides are considered. To our knowledge, all other amyloid-forming peptides of this small length, *e.g.*, the 11-mer peptide of TTR [318, 331], have been reported to form extended β -strands when they assemble. Our P1 amyloid model is reminiscent of a model reported by Qiang *et al.* for an amyloid of the Iowa mutant (D23N) of the A β (1–40) peptide [284]. However, in this structure, the C-terminal 25 residues form a U shape wherein 14 residues form two antiparallel β -sheets associated along a sidechain interdigitated steric zipper, and the remaining residues form a connecting loop. Unlike our P1 model, the model of Iowa mutant A β amyloid predicts that the turn regions of A β alternate in orientation along the long axis of the β -sheet. Since the P1 peptide has only 12 residues, which means each β -strand consists of only 4 or 5 residues, the loop is shorter, and the extent of sidechain interdigitation is less between β -sheets. These features result in a widened U shape that invites other U-shaped protofibrils to bind and satisfy the solvent-exposed hydrophobic surface formed by the Val3 and Phe11 sidechains (Figure 5.15A). The observation of proximity between V3 and S8 further supports this stacking model.

Even though the β -hairpin models we considered in this study were not favored by data on the isotopically diluted sample, we could formulate a β -hairpin model with side chain proximities that almost matched those for the final U-shaped antiparallel model (Figure 5.11C and F). A similar β -hairpin model has been reported for the 20-amino acid designed peptide MAX1 [319], which forms β -hairpins by taking advantage of a Pro-^DPro hinge, suggesting that the β -hairpin structure may be more accessible for larger peptides and also require some special β -turn conformation.

Previously, we predicted a parallel U-shaped fibril arrangement, using coarse-grained

molecular dynamic (cgMD) simulations (Figure 5.3B) [314]. These simulations did not consider the charges on the peptide termini [313], which would favor antiparallel over parallel β -sheets. Indeed, in the antiparallel model presented here, the electrostatic compatibility of adjacent termini adds stability to the antiparallel arrangement, forming H-bonding interactions with polar residues (see Figure 5.15B and 5.16C). As suggested by Qiang *et al.* [332], who also observed both antiparallel and parallel β -sheet structures for D23N-A β (1–40) fibrils, a parallel fibril arrangement might be more thermodynamically stable. Even though our *de novo*-formed P1 fibrils are antiparallel β -sheets, future studies could test whether this β -strand alignment persists upon seeding P1 fibrils. More importantly, even though short peptide fragments derived from amyloidogenic proteins (*e.g.*, A β (16–22)) [198] often adopt antiparallel β -sheets, experimental results from numerous larger peptide and full-length protein fibrils (A β (1–40) [38, 88, 167], A β (1–42) [39, 89, 172], α -syn [267], amylin [333], HET-s [196, 334], β_2 m [335], Ure2p [336], SUP35 [337], and PrP [338]) always indicate hinged in-register parallel fibril structures. It is plausible that our cgMD simulations are relevant to the arrangement of full-length mOLF fibrils where terminal charges would be remote from the core fibril-forming segment. Furthermore, the full-length mOLF fibril core could possibly include discontinuous segments, for example, from P3 region. In general, as mOLF is a member of the large protein family named olfactomedin, the propeller domain may serve as a rich new source of amyloid-forming proteins and peptides, which would be helpful to investigate novel amyloid structures, to develop new peptide-based nanomaterials, and to test amyloid properties associated with human disease.

CHAPTER 6

CONCLUSIONS AND FUTURE WORK

6.1 Conclusions and Next Steps

We successfully characterize three different forms of protein aggregates—the thermally aggregate of FGF-1, the oligomers of A β , and the amyloid formed by P1 peptide—using ssNMR. The flexibility and diversity of ssNMR technique can reveal the structural information on different scales, from strand alignment to atom proximity. Thus, we performed different ssNMR experiments on each sample and applied variable analyzing strategies to reveal different structural information. Although we do not resolve any structures directly related to the pathological mechanisms, the experimental results help us expand our knowledge of aggregate structures, understand protein assembly pathways, and optimize research strategies.

In chapter 3, we performed 2D NMR measurements to demonstrate the well-structured region in the FGF-1 aggregate is consistent with the native-like folding nucleus region. Furthermore, the aggregating intermediate and the folding intermediate are connected because both of them contain the native-like folded folding nucleus region. The current ssNMR data, however, only provided preliminary evidence about the native-like folding structure in the aggregate sample. We can use state-of-art isotope-labeling techniques and ssNMR experiments to accurately identify whether the native-like β -strand alignments are in the FGF-1 aggregate. First, for the uniformly ^{13}C , ^{15}N -labeled FGF-1 sample, we can run 3D NCACX, CONCA and NCOCX experiments in high magnetic field to assign the well-ordered β -strand backbone regions in the primary sequence [183]. Second, the selectively isotope-labeling techniques can introduce ^{13}C and ^{15}N labels at selected types of amino acids. We can use the selectively-labeled samples to verify specific inter-strand residue

contacts [262] and to locate the native-like regions in the FGF-1 aggregate. With these tests, we can reveal the details of β -strand arrangements in the aggregated state, which may further validate the native-like folding nucleus in the aggregating intermediate.

From the structural studies of 150kDa A β oligomer samples, we successfully characterized the two β -strand regions and their relative alignments in the oligomer structure. The NMR data and the cryo-EM class average finally led to a four-subunit structural model of the oligomer. The structural model agrees with most experimental data and provides reasonable explanations for the pore-induced cytotoxicity and the size limitation. Additionally, we deduced an aggregation mechanism for the oligomeric assembly pathway, which may play a critical role in AD pathology (Figure 1.1 and 4.1). The next steps should focus on linking the oligomer structural model to the molecular mechanism initiating AD. First, we will perform some MD simulations to validate the interaction between the oligomer model and the membrane molecules. Meanwhile, the oligomer samples need to be characterized in the membrane-mimicking environment to check its structural integrity and pore-forming behavior. If we could get the interface structures between the oligomer and the membrane, small molecules may be designed to block the insertion of the oligomers, hence the removal of cytotoxicity. Second, we want to verify and optimize the oligomer structural model. There are some structural features proposed by our model that can be quickly verified. For example, ^{13}C -label on A42 and ^{15}N -label on K16 can easily test the salt bridge through fsREDOR experiments. Furthermore, we need to apply the new sample-packing tool to the old samples to review the results in a higher spectrum resolution. Hopefully, the previous broadening peaks may split into multiple small peaks representing multiple conformations, which leads to an oligomer structure with more atomic-level details.

The ssNMR measurements and molecular modeling works in Chapter 5 discovered a special amyloid structure of short peptide–antiparallel U-shaped amyloid, which only partially agrees with the DMD predictions. Although the P1 peptide was derived from glaucoma-associated mOLF and the P1 sequence may locate in the amyloid core of full

mOLF, the short peptide amyloid can provide little insight into the mOLF amyloid structures. This structural study mainly demonstrates that we are ready to investigate the large protein amyloids. Thus, the next step is to look into the mOLF amyloid structures. First, the same as other amyloid studies [171, 183], the uniformly ^{13}C , ^{15}N -labeled mOLF amyloid should be prepared and measured to make chemical shift assignments of the well-structured region. The requested NMR experiments are the multidimensional backbone-walking measurements, *e.g.*, 3D NCACX and 3D NCOCX. Second, inspired by the FGF-1 study, we may use conventional techniques to characterize mOLF folding process. For example, we can locate the folding nucleus region of mOLF by phi-value analysis [245]. Third, we may test two possible structures in the amyloid—the in-register parallel cross- β architecture or the native-like structure. These hypotheses can be examined by ssNMR with different isotope-labeling schemes [262, 339]. Finally, given the size of mOLF protein, we may seek help from cryo-EM to fully determine the mOLF amyloid structure.

With all these works, we demonstrated that modern ssNMR is capable of resolving complicated protein aggregate structures, including oligomeric assemblies and amyloid fibrils. ssNMR, with necessary support from other techniques, has the potential to resolve important structures in pathological pathways. However, ssNMR usually requires a large amount of stable aggregate samples. The limitation makes it impossible for conventional ssNMR to detect transient and heterogeneous intermediate species in the aggregation pathways. The new techniques and strategies to confront this challenge are discussed in the next section. I hope our lab will implement these new techniques to solve the underlying mechanisms of protein aggregation.

6.2 Emerging Techniques and New Challenges

6.2.1 New Solid-State NMR Techniques

The development of ssNMR techniques focuses on two limitations: the low signal-to-noise ratio and the broad linewidth of NMR signals. On the one hand, higher signal-to-noise

ratio facilitate the test of rare samples, such as the aggregates from patients brain or the intermediate species. On the other hand, sharp linewidth of NMR signals improves the spectrum resolution, which enables getting more structural constraints from fewer NMR tests. The high resolution experiments are extremely practical for the uniformly isotope-labeled samples.

The most recent milestone in ssNMR is the development of dynamic nuclear polarization (DNP) techniques [340]. It is a method that permits NMR signal intensities of solids and liquids to be enhanced significantly, and is therefore potentially an important tool in structural and mechanistic studies of biologically relevant molecules. During a DNP experiment, the large polarization of an exogeneous or endogeneous unpaired electron is transferred to the nuclei of interest by microwave irradiation of the sample. Nevertheless, it requires special treatment of the sample and novel instrument to perform the experiments, so we need to wait a long time before DNP can be fully commercial use. There are some examples of studying the transient conformation during aggregation [341, 342].

The sharpness of NMR peaks depends on many efforts. One of them is NMR sample synthesis and rotor packing, *e.g.* the ultracentrifugation of A β oligomers (see Section 4.3.2). Currently, many labs used bio-synthesized peptide or protein (with selective or uniform isotope labels [343]), and they found the bio-synthesized peptides produced more uniform structures [89]. Another effort is the implement of high magnetic field, which will significantly increase the spectral resolution, especially for those insensitive nuclei (*e.g.*, ^{15}N). The latest reported strongest practical NMR is under 1.5 GHz magnet (35.2 Tesla) [344]. The new commercial instruments with 800 MHz meet most of requirements for bio-structural studies. Also, enormous effort has been put into developing the ^1H detection method in ssNMR to generating a similar resolution to solution-state NMR. The ultra-fast MAS technique enables some preliminary attempts in this field [345, 346].

In addition, applying state-of-art NMR pulse sequences is also very important to achieve efficient structural determination. Different pulsed experiments extract different structural

information from a single sample. For example, 2D fpRFDR is usually used for assigning chemical shifts, while 2D DARR can obtain the distance constraints up to 0.6 nm (see Section 2.3.2). We should always look at new pulse sequence for more informative test. A new technique, 3D $C\alpha(N)COC\alpha$, utilizing band-selective homonuclear cross polarization (BSH-CP) [347] to collecting multidimensional NMR spectra based on backbone carbon connections, which provides better NMR signals by avoiding ^{15}N measurement. Another example for measuring long-distance internuclear contacts is a pulse program called Proton-Enhanced Rotor-echo Short-Pulse IRradiATION Cross-Polarization (PERSPIRATION-CP) [348], which has higher sensitivity for characterizing weak ^{15}N - ^{13}C correlations. Finally, with these advanced multidimensional NMR measurements and the improved spectral resolution, we will be able to establish a structural model from the uniformly-labeled samples.

6.2.2 Help from Other Techniques

Some problems cannot be resolved by ssNMR alone, but many other tools can help. One common concern is the distance scale that can be revealed in ssNMR. The scale is range from 0.1 to 0.9 nm for most ssNMR test, which is pretty useful in the characterization of secondary structures, especially β -sheets. However, ssNMR itself is hard to observe the quaternary structure—the assembly of subunits in proteins. Another concern is that normal ssNMR methods cannot directly measure the unstable or transient assemblies of proteins, such as the oligomeric intermediates, because of the time-consuming experiments.

In latest studies, labs used AFM, TEM, and STEM measurements to fulfill the information of the dimension and symmetry of amyloid structure. For example, Connelly *et al.* used AFM to observe the pore-like structure of $A\beta$ oligomers [57]. Colvin *et al.* applied MPL measurement to reveal the two-fold symmetry in the cross-section of $A\beta$ amyloid fibrils [89]. The missing information of subunits may mislead structure determination. Xiao *et al.* proposed a very similar $A\beta(1-42)$ conformation in 2015 as Colvin *et al.* published in 2016, but they thought the cross-section of amyloid fibrils only contains one peptide molecule

[39].

The emerging cryo-EM technique is a good complement to observe the overall arrangement and even the detailed conformation in protein aggregates [176, 177, 349]. The low resolution cryo-EM class average is relatively easy to perform: it does not require strict sample optimization and complex image analysis [350]. It can provide valuable information about subunit assembly and symmetry (see Section 4.4) and assist building the whole aggregate structure. The comprehensive high resolution cryo-EM analyses (< 0.4 nm), had already been applied in aggregate structural studies [174]. The achievable high resolution enables single particle observation, so the cryo-EM could deal with heterogeneous peptide assemblies, like A β oligomers [351]. Although cryo-EM itself is very powerful in structural studies, ssNMR is still helpful in validating the structural model [176] or characterizing some structural region with limited resolution [177].

To directly investigate the intermediates during assembly process, a novel technique, called freeze trapping, was invented to separate the intermediate species [352, 353]. In short, they used a rapid mixing and freeze-quenching apparatus to initiate the structural conversion process and trap transient states with a minimum evolution time of 1–2 ms, and then used DNP ssNMR experiments to disclose the structure. It could be a revolutionary technique to study the assembly pathway.

Last, MD simulation is usually a necessary part in ssNMR works to build a reasonable structural model [354]. Just like in our structural studies, the MD modeling not only provides structure hypothesis, but also guides the analysis of ssNMR data (see Section 5.4.5). For the novel modeling methods, it is getting faster and more efficient to simulate multi-molecule assembly process [76], making it possible to study complicated oligomeric/intermediate aggregates.

6.2.3 New Challenges

An important question is still to look into the molecular mechanisms underlying the assembly pathways. Current structural studies are mainly characterizing the stable or meta-stable states in the pathways. However, the transient intermediate structures seem to be more critical in revealing the assembly process. We need to find new methods (like freeze-trapping) to shed light on the unstable intermediate species. Another idea is to borrow some tools from conventional protein folding studies (such as phi-analysis for locating the folding nucleus), given the similar dimension of the aggregating intermediates and the well-folded proteins.



Another emerging field is the standardization and automation of ssNMR structural studies. Because ssNMR has many different techniques and they provide dataset with various format, it is very difficult to implement a general methodology in ssNMR research. A designed ssNMR experiment may be good for several amyloid samples, but may fail on another oligomer sample. The processing of ssNMR data is also, unfortunately, not straightforward and requires extensive experience [188]. In addition, NMR-constrained structural modeling works are done by different softwares in different research groups without a unique standard. Thus, the next step in NMR field is to develop standard tools to standardize ssNMR studies. With an standardized workflow, the automated ssNMR structural studies, probably using AI or deep learning, can be expected.


Appendices


APPENDIX A


REPRINT LICENSE AGREEMENT


A.1 Reprint License Agreement for Chapter 3



 Home

 Help

 Email Support

 Yuan Gao ▾



Folding nucleus structure persists in thermally-aggregated FGF-1

Author: Michael Blaber, Anant K. Paravastu, Gan Wang, et al

Publication: Protein Science

Publisher: John Wiley and Sons

Date: Nov 21, 2017

© 2017 The Protein Society

Order Completed

Thank you for your order.

This Agreement between Mr. Yuan Gao ("You") and John Wiley and Sons ("John Wiley and Sons") consists of your license details and the terms and conditions provided by John Wiley and Sons and Copyright Clearance Center.

Your confirmation email will contain your order number for future reference.

License Number5035020356203

[Printable Details](#)

License dateMar 23, 2021

|  Licensed Content |  Order Details |
|--|---|
| Licensed Content PublisherJohn Wiley and Sons | Type of useDissertation/Thesis |
| Licensed Content PublicationProtein Science | Requestor typeAuthor of this Wiley article |
| Licensed Content TitleFolding nucleus structure persists in thermally-aggregated FGF-1 | FormatPrint and electronic |
| Licensed Content AuthorMichael Blaber, Anant K. Paravastu, Gan Wang, et al | PortionFull article |
| Licensed Content DateNov 21, 2017 | Will you be translating?No |
| Licensed Content Volume27 | |
| Licensed Content Issue2 | |
| Licensed Content Pages10 | |

 About Your Work

 Additional Data


TitleUse solid-state NMR to study the molecular structures of disease-associated peptide aggregations


Institution nameGeorgia Institute of Technology


Expected presentation dateApr 2021


| Requestor Location | Tax Details |
|---|---------------------------------|
| Mr. Yuan Gao 251 10th St. NW | Publisher Tax ID EU826007151 |
| Requestor Location ATLANTA, GA 30318 United States Attn: Mr. Yuan Gao | |
| \$ Price | |
| Total | 0.00 USD |
| <p>Would you like to purchase the full text of this article? If so, please continue on to the content ordering system located here: Purchase PDF If you click on the buttons below or close this window, you will not be able to return to the content ordering system.</p> | |
| Total: 0.00 USD | |
| CLOSE WINDOW | ORDER MORE |


A.2 Reprint License Agreement for Chapter 4




 Home

 Help ▾

 Email Support

 Yuan Gao ▾



Out-of-Register Parallel β -Sheets and Antiparallel β -Sheets Coexist in 150-kDa Oligomers Formed by Amyloid- β (1-42)

Author:
Yuan Gao, Cong Guo, Jens O. Watzlawik, Peter S. Randolph, Elizabeth J. Lee, Danting Huang, Scott M. Stagg, Huan-Xiang Zhou, Terrone L. Rosenberry, Anant K. Paravastu

Publication: Journal of Molecular Biology

Publisher: Elsevier

Date: 24 July 2020

© 2020 Elsevier Ltd. All rights reserved.

Journal Author Rights



Please note that, as the author of this Elsevier article, you retain the right to include it in a thesis or dissertation, provided it is not published commercially. Permission is not required, but please ensure that you reference the journal as the original source. For more information on this and on your other retained rights, please visit: <https://www.elsevier.com/about/our-business/policies/copyright#Author-rights>


BACKCLOSE WINDOW


© 2022 Copyright - All Rights Reserved | Copyright Clearance Center, Inc. | Privacy statement | Terms and Conditions


Comments? We would like to hear from you. E-mail us at customer-care@copyright.com


A.3 Reprint License Agreement for Chapter 5




 Home

 Help

 Email Support

 Yuan Gao ▾



ACS Publications
Most Trusted. Most Cited. Most Read.

Structural Arrangement within a Peptide Fibril Derived from the Glaucoma-Associated Myocilin Olfactomedin Domain

Author: Yuan Gao, Emily G. Saccuzzo, Shannon E. Hill, et al
Publication: The Journal of Physical Chemistry B
Publisher: American Chemical Society
Date: Mar 1, 2021

Copyright © 2021, American Chemical Society

PERMISSION/LICENSE IS GRANTED FOR YOUR ORDER AT NO CHARGE

This type of permission/license, instead of the standard Terms & Conditions, is sent to you because no fee is being charged for your order. Please note the following:

- Permission is granted for your request in both print and electronic formats, and translations.
- If figures and/or tables were requested, they may be adapted or used in part.
- Please print this page for your records and send a copy of it to your publisher/graduate school.
- Appropriate credit for the requested material should be given as follows: "Reprinted (adapted) with permission from (COMPLETE REFERENCE CITATION). Copyright (YEAR) American Chemical Society." Insert appropriate information in place of the capitalized words.
- One-time permission is granted only for the use specified in your request. No additional uses are granted (such as derivative works or other editions). For any other uses, please submit a new request.

BACKCLOSE WINDOW

© 2021 Copyright - All Rights Reserved | [Copyright Clearance Center, Inc.](#) | [Privacy statement](#) | [Terms and Conditions](#)
Comments? We would like to hear from you. E-mail us at customer@copyright.com

APPENDIX B

SUPPLEMENTARY MATERIALS FOR CHAPTER 2

B.1 Pulse Program Code of R²W Experiment

This section include the pulse program for running R²W experiment in Bruker TopSpin. The program code was developed based on Ramachandran's work [225] with some modification of phase cycles. To get one data point in R²W (see Figure 2.9), four 1D spectra with identical MAS frequency should be measured: the ¹³C difference spectra with 0 ms and 50 ms mixing respectively, generating $I_{dif} = I_{1z} - I_{2z}$, and the ¹³C reference spectra with 0 ms and 50 ms mixing respectively, producing $I_{ref} = I_{1z,ref} + I_{2z,ref}$. The final signal attenuation can be calculated as $\frac{I_{dif,50ms}/I_{ref,50ms}}{I_{dif,0ms}/I_{ref,0ms}}$. For further practical guide of the experiment, see reference [355].

```
;GY_1dRR_dif (TopSpin 3.5)
;based on Ramachandran, R., et al. J.A.C.S. 125, -156239
;phase cycle was modified to make 1D measurement work
;This experiment measures the difference spectra of
;two 13C nuclei, which produces I_dif = I_1z - I_2z

;Avance II+ version
;parameters:
;p3 : proton 90 at power level pl12
;p15 : contact time at plw1 (f1) and spw0 (f2)
;p11 : X power level during contact
;sp0 : proton power level during contact
;p12 : =120dB, not used
;p112 : decoupling power level (if not pl13)
;p113 : special decoupling power level
;d1 : recycle delay
;cnst21 : on resonance, usually = 0
;cnst31 : spin rate (Hz)
;cnst32 : delta-sigma (Hz) (difference in nuclear frequency)
;d5 : total decoupling time (s) (used in CT version of RR)
;pcpd2 : pulse length in decoupling sequence
;cpdprg2 : cw, tppm (at pl12), or lgs, cwlg, cwlg (LG-decoupling)
;spnam0 : use e.g. ramp.100 for variable amplitude CP
;zgoptns : -Dfslg, -Dlacq, or blank
;l1 : control mixing time
;postacq: not used in this version
;cnst11 : to adjust t=0 for acquisition, if digmod = baseopt
```

```

"acqt0=1u*cnst11"

;use l1 to control the mixing time (evolution time)
define delay mixing
"mixing=1s*l1/cnst31"
;inverse delay
define delay inverse
"inverse=0.5s/cnst32"

;used only in CT version of RR
define delay postacq
"postacq=d5-mixing"

1 ze
2 d1 do:f2 ;recycle delay, decoupler off in go-loop

; test p15 and aq length for safety
#include <p15_prot.incl>
#ifdef lacq
#include <aq_prot.incl>
#endif

1u fq=cnst21:f2
(p3 pl12 ph1):f2 ;90 on 1H
(p15 pl1 ph2):f1 (p15:sp0 ph10):f2 ;cp
(1u cpds2):f2 (inverse) ;Turn on dec. Use inverse delay to make I1z
    ↪ and I2z have opposite signs
(p13 pl13 ph3):f1 ;13C flip back
mixing ;mixing time (choose 50 or 60 ms for dephasing)
(p13 pl13 ph4):f1 ;13C read
go=2 ph31 ;data acquisition
1m do:f2
wr #0
HaltAcqu, 1m
exit

;phase cycle
ph1 = 1 3;H90
ph2 = 0 0 2 2 1 1 3 3;cpX
ph3 = 0 0 2 2 1 1 3 3;X90-1
ph4 = {0 2}*4 {1 3}*4 {2 0}*4 {3 1}*4;X90-2
ph10 = 0 ;cpH
ph31 = {3}*8 {0}*8 {1}*8 {2}*8

;GY_1dRR_ref pulse sequence
;This experiment measures the reference spectra
;(with the same mixing time) of
;two 13C nuclei, which produces I_ref = I_1z + I_2z
;Modify two places in GY_1dRR_dif
;
;1. remove inverse delay or set inverse delay to 0
;
;2. adjust ph3 to:
; ph3 = 3 3 1 1 0 0 2 2

```

B.2 An example of SPINEVOLUTION input and output

This is a PITHIRDS-CT simulation for a linear array of eight ^{13}C spins (Figure 2.7). The contents of input file, atom coordinate file, pulse sequence file, and the output file are shown below.

```
***** Input file: input *****
** The Spin System **
** define the magnetic field **
spectrometer(MHz) 500
** define the spin rate **
spinning_freq(kHz) 12.5
** NMR channels in experiment**
channels C13
** define atoms **
nuclei C13 C13 C13 C13 C13 C13 C13 C13
** atom positions **
atomic_coords linear8spin5A.cor
** CSA parameters **
cs_isotropic *
csa_parameters 1 -75 0.75 0 0 0 ppm
csa_parameters 2 -75 0.75 0 0 0 ppm
csa_parameters 3 -75 0.75 0 0 0 ppm
csa_parameters 4 -75 0.75 0 0 0 ppm
csa_parameters 5 -75 0.75 0 0 0 ppm
csa_parameters 6 -75 0.75 0 0 0 ppm
csa_parameters 7 -75 0.75 0 0 0 ppm
csa_parameters 8 -75 0.75 0 0 0 ppm
j_coupling *
quadrupole *
dip_switchboard *
csa_switchboard *
exchange_nuclei *
bond_len_nuclei *
bond_ang_nuclei *
tors_ang_nuclei *
groups_nuclei *
**Pulse Sequence **
CHN 1
timing(usec) (ABCBlock12p5KHzMAS-4A-xy16.pp)17 (BBBBlock12p5KHzMAS-12B
    ↪ -xy16.pp)-17
power(kHz) * *
phase(deg) * *
freq_offs(kHz) * *
**Variables **
** Options **
rho0 F1x
observables I1p+I2p+I3p+I4p+I5p+I6p+I7p+I8p
**powder averaging**
EulerAngles rep376
n_gamma 36
line_broaden(Hz) *
zerofill *
FFT_dimensions *
```

```

options -dw2
***** End of input file: input *****

***** Atom Coordinate File: linear8spin5A.cor *****
** a linear array of eight 13C spins **
** x y z (unit:A) **
0 0 0
0 0 5
0 0 10
0 0 15
0 0 20
0 0 25
0 0 30
0 0 35
***** End of File: linear8spin5A.cor *****

***** Pulse Sequence File: ABCBlock12p5KHzMAS-4A-xy16.pp *****
** timing(usec) power(kHz) phase(deg) freq_offs(kHz) **
26.67 18.75 0.00 0.00
53.33 0.00 0.00 0.00
26.67 18.75 90.00 0.00
53.33 0.00 0.00 0.00
26.67 18.75 0.00 0.00
53.33 0.00 0.00 0.00
26.67 18.75 90.00 0.00
53.33 0.00 0.00 0.00
.....
.....
.....
** some lines are omitted **
***** End of File: ABCBlock12p5KHzMAS-4A-xy16.pp *****

***** Pulse Sequence File: BBBBlock12p5KHzMAS-12B-xy16.pp *****
not shown
*****

***** Output File: output_re.dat *****
** time(ms) signal intensity **
61.44000 1.031510
57.60000 1.054142
53.76000 1.061191
49.92000 1.065767
46.08000 1.088962
42.24000 1.154260
38.40000 1.281116
34.56000 1.482303
30.72000 1.766748
26.88000 2.144433
23.04000 2.626500
19.20000 3.215750
15.36000 3.889910
11.52000 4.587819
7.680000 5.210742

```

```
3.840000 5.644614  
-2.486900e-14 5.796860  
***** End of File: output_re.dat *****
```

APPENDIX C
SUPPLEMENTARY MATERIALS FOR CHAPTER 3

Table C.1 Chemical shifts (ppm)/linewidths (full width half maximum, ppm) for distinguishable ^{13}C -NMR peaks in the 2D fpRFDR spectrum of hydrated FGF-1 aggregated sample. Some cells contain two frequencies and two linewidths because two distinct NMR cross-peaks are observed for these ^{13}C sites, which may correspond to different residues of the same type within FGF-1. For residues other than Pro and Gly in β -strands, CO and C α peak frequencies are expected to be at least 0.5 ppm under corresponding random-coil values (measured from random-coil model peptides) [228], and C β peak frequencies are expected to be at least 0.5 ppm above corresponding random-coil values. Chemical shifts marked with * are estimated from two-bond cross-peaks on 2D fpRFDR or from 2D DARR spectra. Unless otherwise specified, the error is ± 0.1 ppm for both the chemical shift and linewidth from fitting.

| Residue | CO | C α | C β | C γ | other C |
|---------------|--------|---|--------------------------------|---|-----------------------|
| A | | 49.2/1.8 | 21.1/1.8 18.4/1.6 ± 0.2 | | |
| A random coil | 176.1 | 50.8 | 17.4 | | |
| T | 171.7* | 59.1/2.6 60.7 ± 0.2 / 4.4 ± 0.3 | 70.2/1.7 67.8/2.5 | 19.8/1.3 | |
| T random coil | 173 | 60.1 | 68.1 | 19.8 | |
| S | 171.7* | 55.1/1.9 57.2/3.8 ± 0.2 | 64.1/2.2 61.8/2.3 ± 0.2 | | |
| S random coil | 172.9 | 56.6 | 62.1 | | |
| I | 172.6* | 57.8/1.8 | 40.4/2.4 37.8/3.3 ± 0.2 | C γ 1: 25.9/1.4, C γ 2: 15.6/1.8 | C δ : 12.2/2.3 |
| I random coil | 174.7 | 59.4 | 37.1 | C γ 1: 25.5, C γ 2: 15.7 | C δ : 11.2 |

Table C.1 (continued)

| Residue | CO | C α | C β | C γ | other C |
|---------------|-----------|------------|--------------------------------|---|---|
| K | | | 34.1/3.4 \pm 0.2 | 23.2/1.9 \pm 0.2 | |
| K random coil | 174.9 | 54.5 | 31.4 | 23 | C δ : 27.3 C ϵ : 40.2 |
| P | | 60.6/2.6 | 30.2/2.3 | 25.5/1.6 | C δ : 48.3/2.2 |
| P random coil | 175.6 | 61.6 | 30.4 | 25.5 | C δ : 48.1 |
| Y | 172.3* | 53.5* | 39.9/3.3 | 127.6/2.9 | C δ : 131.3/3.9 C ϵ : 116.0/2.4 C ζ : 155.8/2.1 |
| Y random coil | 174.2 | 56.2 | 37.1 | 128.9 | C δ : 131.6 C ϵ : 116.5 C ζ : 155.6 |
| F | 172.4* | 53.8* | 41.2/2.5 \pm 0.2 | 136.6/2.4 \pm 0.2 | |
| F random coil | 174.1 | 56 | 37.9 | 137.2 | C δ : 130.2 C ϵ : 129.8 C ζ : 128.2 |
| V | | 58.8/2.1 | 33.7/1.7 31.5/3.4 \pm 0.3 | 19.4/2.1 19.0/1.6 | |
| V random coil | 174.6 | 60.5 | 31.2 | C γ 1: 19.4, C γ 2: 18.6 | |
| E | 172.9* | 52.9* | | 34.8/1.7 | C δ : 181.1/1.7 |
| E random coil | 174.9 | 54.9 | 28.2 | 33.9 | C δ : 181.7 |
| G | 170.1/2.4 | 43.4/2.6 | | | |
| G random coil | 173.2 | 43.4 | | | |
| R | 172.6* | 52.5* | 31.8* | 25.1* | C δ : 41.8* C ζ : 157.6/1.4 |
| R random coil | 174.6 | 54.3 | 29.2 | 25.4 | C δ : 41.6 C ζ : 157.8 |
| Q | | 52.5* | | 32.5/2.0 | C δ : 177.6/2.0 |
| Q random coil | 174.3 | 54.0 | 27.7 | 32.0 | C δ : 178.8 |

Table C.1 (continued)

| Residue | CO | C α | C β | C γ | other C |
|---------------|-------|------------|-----------|------------|---|
| L | | 51.9* | 43.8* | 25.5* | |
| L random coil | 175.9 | 53.4 | 40.7 | 25.2 | C δ 1: 21.6, C δ 2: 23.2 |

Table C.2 Chemical shifts (ppm)/linewidths (full width half maximum, ppm) for distinguishable ^{13}C -labeled sites in 2D fpRFDR spectrum of dehydrated FGF-1 aggregated sample. The errors are ± 0.1 ppm for both the chemical shift and linewidth.

| Residue | CO | C α | C β | C γ | other C |
|---------------|-------|------------|-----------|---|---|
| A | | 48.8/3.0 | 21.3/5.8 | | |
| A random coil | 176.1 | 50.8 | 17.4 | | |
| T | | 59.7/6.4 | 68.1/5.1 | 20.1/1.2 | |
| T random coil | 173 | 60.1 | 68.1 | 19.8 | |
| S | | 55.8/4.6 | 62.7/5.0 | | |
| S random coil | 172.9 | 56.6 | 62.1 | | |
| I | | | 38.7/2.5 | C γ 1: 25.7/2.4, C γ 2: 15.6/2.9 | C δ : 12.0/3.1 |
| I random coil | 174.7 | 59.4 | 37.1 | C γ 1: 25.5, C γ 2: 15.7 | C δ : 11.2 |
| P | | 60.3/4.4 | 30.2/3.4 | 25.4/2.7 | C δ : 48.1/2.8 |
| P random coil | 175.6 | 61.6 | 30.4 | 25.5 | C δ : 48.1 |
| Y | | | | | C δ : 130.9/4.7, C ϵ : 116.1/3.5, C ζ : 156.2/2.6 |
| Y random coil | 174.2 | 56.2 | 37.1 | 128.9 | C δ : 131.6, C ϵ : 116.5, C ζ : 155.6 |
| F | | | | 136.4/4.7 | C ϵ : 129.2/4.2 |
| F random coil | 174.1 | 56 | 37.9 | 137.2 | C δ : 130.2, C ϵ : 129.8, C ζ : 128.2 |

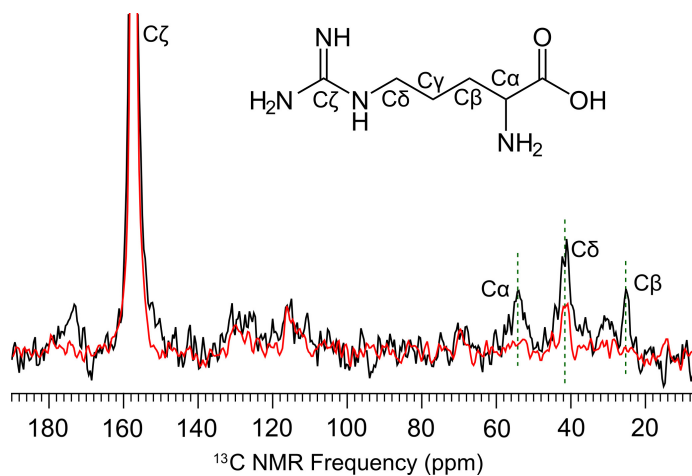


Figure C.1 Comparison of DARR spectra slices with different mixing times for Arg in FGF-1. DARR spectra slices from 50 ms (red) and 100 ms (black) mixing. The slices are taken from 157.6 ppm, corresponding to the C ζ of Arg. The crosspeaks corresponding to C α -C ζ , C β -C ζ , and C δ -C ζ interactions become more intense with longer mixing times.

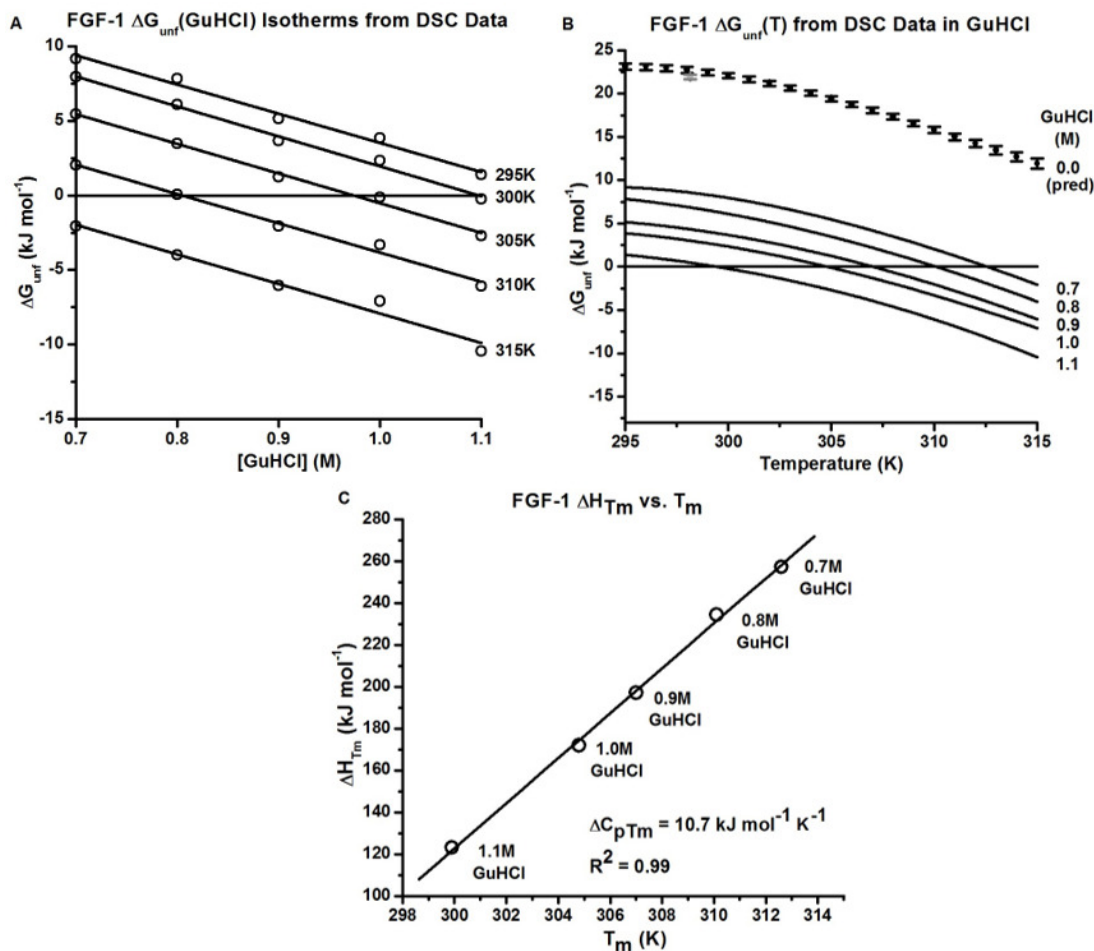


Figure C.2 Isothermal extrapolation of FGF-1 DSC data. (A) Unfolding isotherms at 295, 300, 305, 310, and 315 K were plotted from DSC data collected in 0.7, 0.8, 0.9, 1.0, and 1.1 M GuHCl in ADA buffer. Thermal denaturation under these conditions is two-state and reversible, thereby enabling orthogonal isotherms to be derived. (B) $\Delta G_{\text{unf}}(T)$ functions for FGF-1 generated from DSC data collected in 0.7–1.1 M GuHCl are plotted over 295–315 K. This temperature range spans the DSC T_m for each buffer condition (the region where the $\Delta G_{\text{unf}}(T)$ function is most accurately determined). Also shown are predicted $\Delta G_{\text{unf}}(T)$ data points (small circles) from the linear extrapolation of the corresponding endotherms at each temperature (shown with their associated confidence intervals to the linear fit). These data predict the $\Delta G_{\text{unf}}(T)$ function between 295–315 K for FGF-1 under non-aggregating conditions in ADA buffer (0 M GuHCl). Also shown in gray at 298.15 K is the $\Delta G_{\text{unf}}(T)$ (0 M GuHCl) value ($21.9 \pm 0.3 \text{ kJ} \cdot \text{mol}^{-1}$) reported for FGF-1 from IED studies monitored by fluorescence [255]. (C) The ΔH_{Tm} and associated T_m values for FGF-1 were derived from the reported DSC data collected in the presence of the indicated concentrations of GuHCl (conditions under which the thermal unfolding was reversible and two-state) [255]. The slope yields a ΔC_{pTm} of $10.7 \text{ kJ} \cdot \text{mol}^{-1} \cdot \text{K}^{-1}$ with a coefficient of correlation $R^2 = 0.99$ for the linear fit.

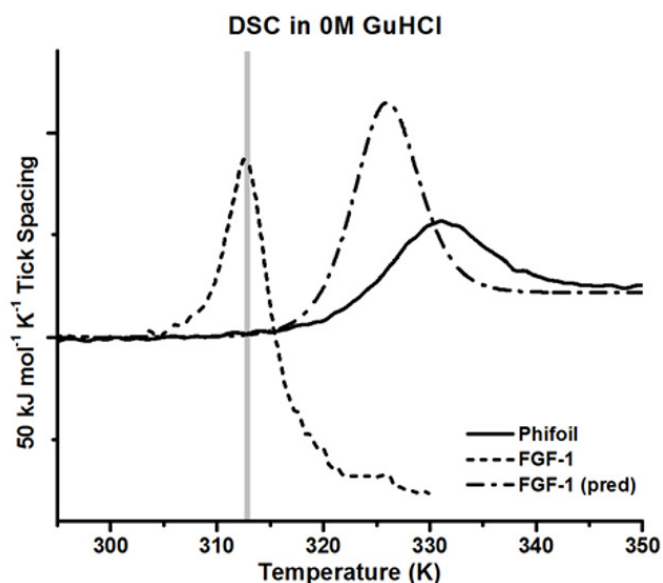


Figure C.3 Predicted non-aggregating FGF-1 DSC endotherm. The experimental DSC endotherm for Phifoil in ADA buffer is indicated by the solid line. Under these conditions the thermal denaturation is two-state reversible. The predicted DSC endotherm for FGF-1 in ADA buffer under the two-state reversible condition is indicated by the dash-dot line. The experimental DSC endotherm for FGF-1 (38 μ M) in ADA buffer (i.e., aggregating condition) is indicated by the dashed line. The actual FGF-1 unfolding is perturbed by irreversible aggregation, leading to a substantially lowered T_m and post-transition exotherm/noise.

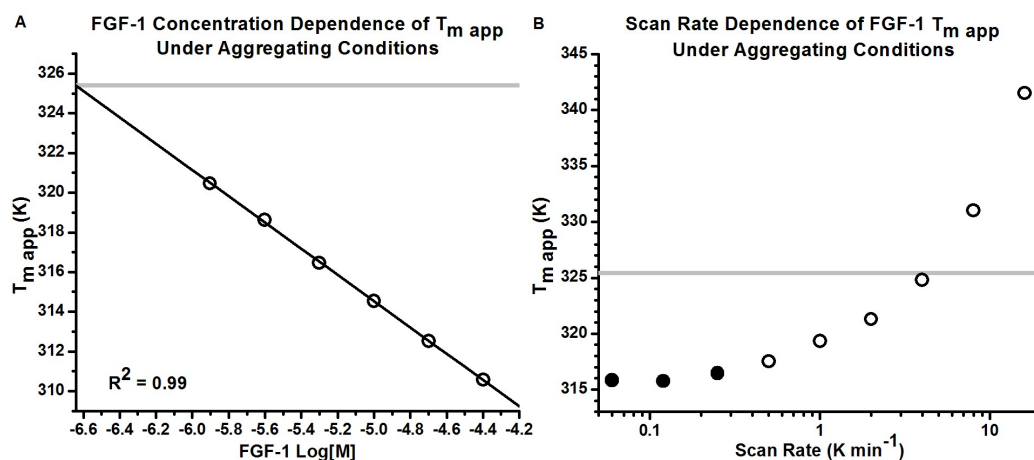


Figure C.4 Concentration and scan rate dependence of FGF-1 apparent T_m . (A) Decreasing the protein concentration decreases aggregation and increases the T_m of FGF-1 under conditions of 0 M GuHCl (ADA buffer). The gray line indicates the predicted T_m of FGF-1 in ADA buffer under conditions of two-state reversible denaturation. The intersection of the two lines predicts that the critical concentration of FGF-1 that avoids aggregation is 0.22 μM . (B) The T_m of FGF-1 (5 μM) under aggregating conditions (ADA buffer; 0 M GuHCl) is proportional to the scan rate when the scan rate is faster (open circles) than the rate (0.25 $K\cdot\text{min}^{-1}$) required for thermal equilibrium of FGF-1 unfolding (filled circles). The gray line indicates the predicted T_m of FGF-1 under non-aggregating conditions in ADA buffer.

APPENDIX D

SUPPLEMENTARY MATERIALS FOR CHAPTER 4

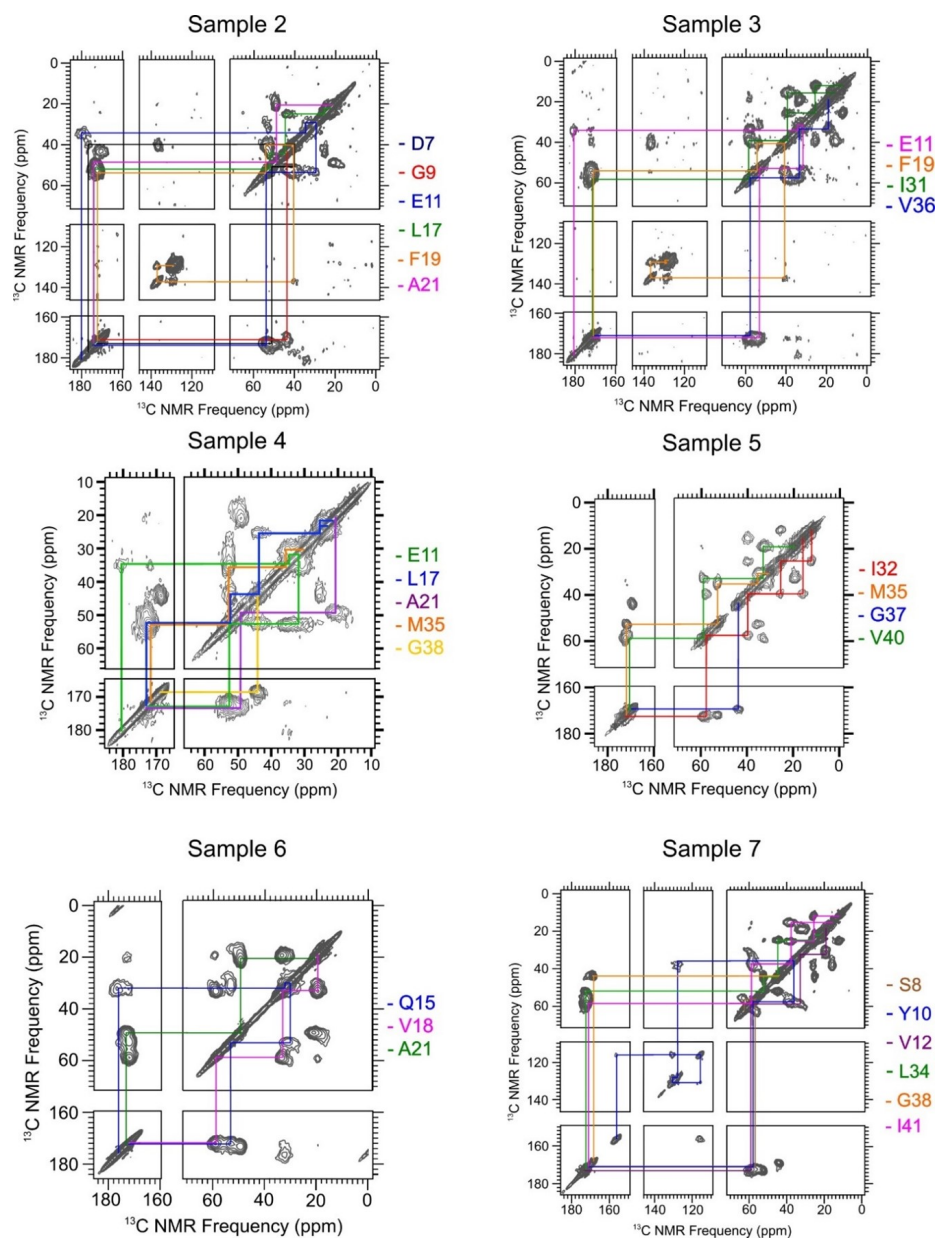


Figure D.1 The fpRFDR spectra of the isotope-labeled Aβ(1-42) 150kDa oligomers from Samples 4.2 to 4.7 in Table 4.1.

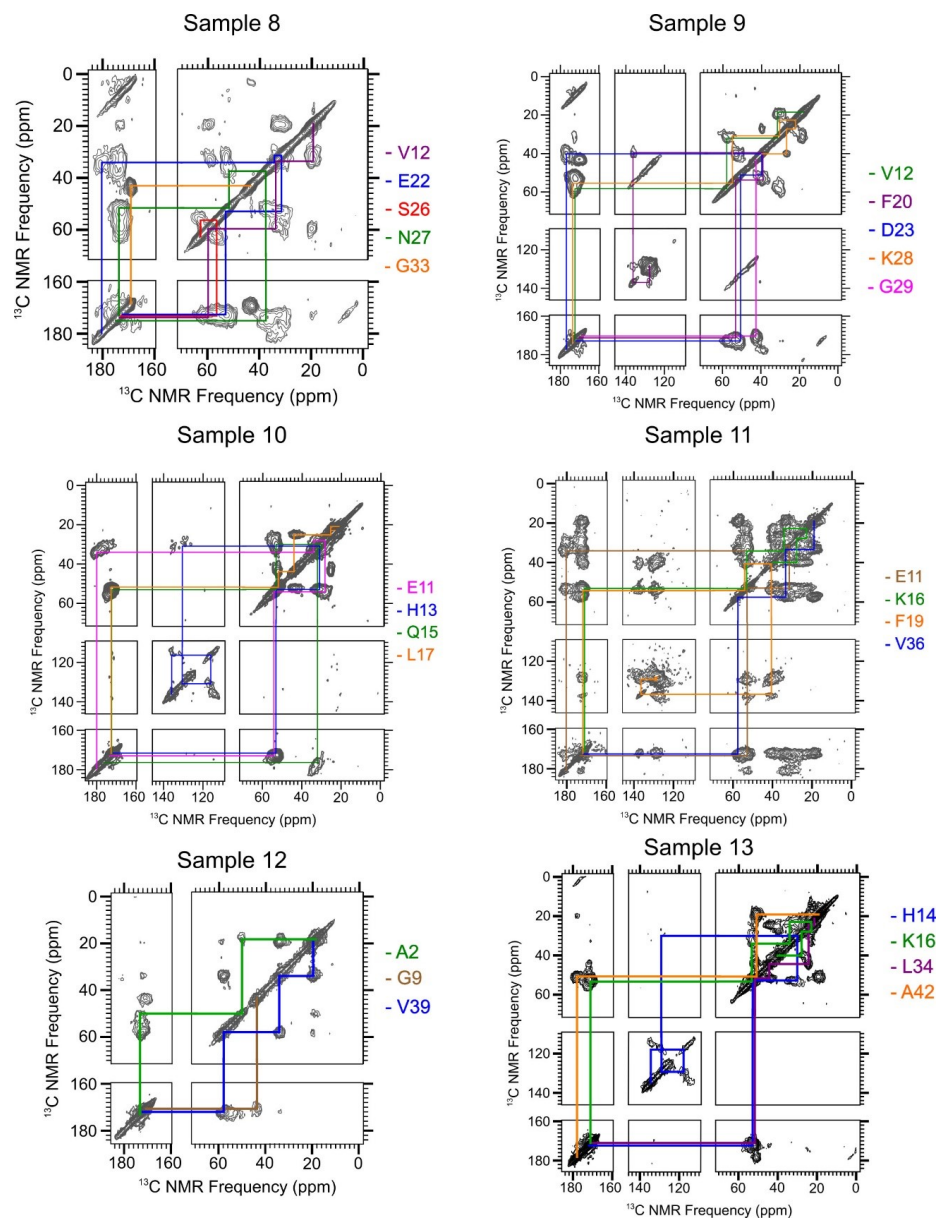


Figure D.2 The fpRFDR spectra of the isotope-labeled A β (1-42) 150kDa oligomers from Samples 4.8 to 4.13 in Table 4.1.

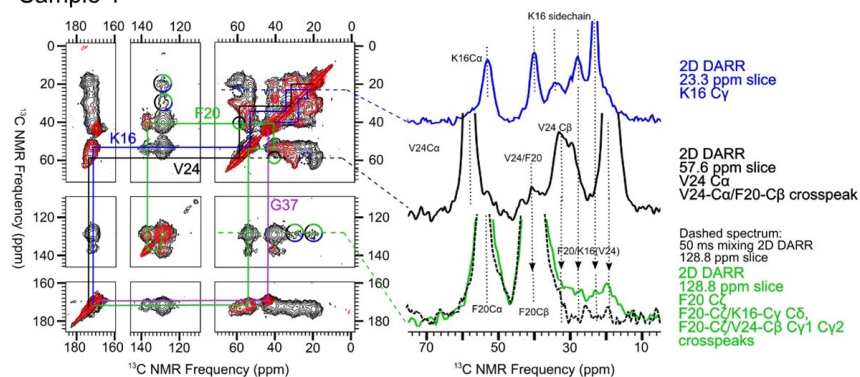
Table D.1 Chemical shifts (ppm)/linewidths (full width at half-maximum, ppm) for ^{13}C -labeled sites in 2D fpRFDR spectrum of A β (1-42) 150 kDa oligomers. The carbons in each amino acid are labeled as they are in the Biological Magnetic Resonance Data Bank [356]. Estimated error, based on nonlinear least-square fitting to Gaussian functions, is ± 0.1 ppm for both the chemical shift and line width unless specified otherwise.

| Residue | CO | C α | C β | C γ | other C |
|---------|-----------|------------|--------------------|------------|---|
| D7 | 172.7/2.8 | 51.1/2.3 | 40.0/4.8 | 176.9/3.8 | |
| S8 | 171.6/3.3 | 56.5/4.6 | 62.3/5.2 | | |
| G9 | 170.8/4.7 | 43.5/3.2 | | | |
| Y10 | 171.9/2.7 | 57.7/3.8 | 35.7/5.1 | 127.9/2.4 | C δ :130.6/3.2 C ϵ :116.0/3.6 C ζ : 156.3/3.1 |
| E11 | 173.8/4.5 | 53.0/3.1 | 31.7/8.1 | 34.4/3.8 | C δ :180.2/3.1 |
| V12 | 174.1/3.2 | 58.8/4.0 | 32.7/2.9 | 19.3/3.3 | |
| H13 | 171.8/1.9 | 52.5/2.3 | 31.1/2.6 | 128.8/5.3 | C δ 2:114.7/4.4 C ϵ 1:135.9/2.8 |
| H14 | 172.4/5.7 | 52.7/4.8 | 30.2/7.1 \pm 0.2 | 129.3/4.9 | C δ 2:118.2/4.7 C ϵ 1:134.6/4.4 |
| Q15 | 172.4/3.1 | 52.9/3.3 | 30.2/4.2 | 32.1/5.3 | C δ :176.3/5.1 |
| K16 | 171.3/3.7 | 53.2/2.6 | 34.4/5.2 | 23.9/2.2 | C δ :28.0/3.0 C ϵ :40.1/2.2 |
| L17 | 172.4/2.4 | 51.9/2.9 | 44.0/4.7 | 25.1/2.1 | C δ 1:22.4/2.7 C δ 2:20.6/1.8 |
| V18 | 172.0/3.4 | 58.6/3.5 | 33.0/3.8 | 19.5/3.5 | |
| F19 | 172.1/2.7 | 54.2/3.9 | 40.8/2.2 | 136.6/3.2 | C δ :129.0/2.6 |
| F20 | 172.1/5.0 | 54.2/3.9 | 40.1/5.5 | 137.2/3.1 | C δ :128.7/4.2 |
| A21 | 174.3/3.4 | 48.7/3.1 | 20.9/5.1 | | |
| E22 | 172.4/3.1 | 52.9/3.1 | 31.5/6.4 | 34.2/7.5 | C δ :180.5/5.0 |
| D23 | 173.6/4.2 | 51.6/3.2 | 40.7/8.2 | 177.8/4.4 | |
| V24 | 172.1/2.3 | 57.6/3.0 | 33.1/2.6 | 19.2/3.7 | |
| G25 | 171.0/4.7 | 43.4/3.7 | | | |
| S26 | 172.9/4.4 | 56.3/5.3 | 62.5/4.6 | | |
| N27 | 173.9/5.3 | 51.6/4.8 | 37.5/7.5 | 174.8/4.2 | |

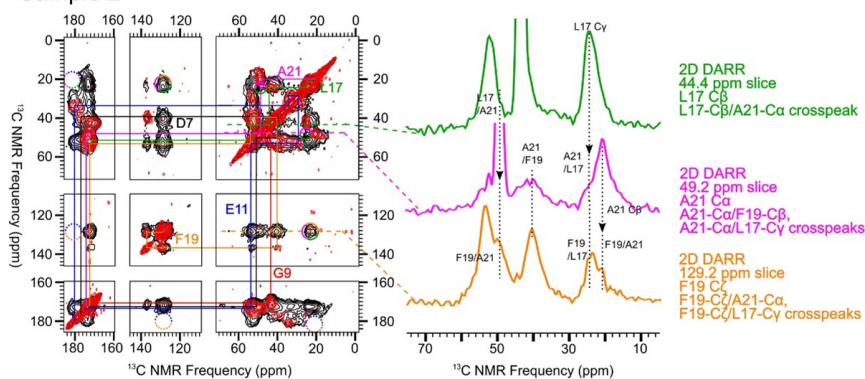
Table D.1 (continued)

| Residue | CO | C α | C β | C γ | other C |
|---------|-----------|--------------------|-----------|--|---|
| K28 | 174.7/6.6 | 55.3 \pm 0.2/5.9 | 34.0/5.1 | 23.3/4.6 | C δ :27.9/3.2 C ϵ :40.7/2.6 |
| G29 | 171.0/5.0 | 43.6/3.9 | | | |
| A30 | 173.1/2.0 | 48.8/2.8 | 19.9/3.8 | | |
| I31 | 172.1/2.3 | 58.3/2.9 | 39.3/1.2 | C γ 1:25.3/2.5 C γ 2:15.0/3.6 | C δ 1:12.0/2.1 |
| I32 | 170.6/2.1 | 57.5/2.9 | 39.7/3.1 | C γ 1:25.6/2.8 C γ 2:15.9/3.7 | C δ 1:12.3/2.4 |
| G33 | 169.3/2.1 | 43.1/2.8 | | | |
| L34 | 171.1/3.7 | 51.6/2.3 | 44.4/2.8 | 24.5/2.5 | C δ 1, C δ 2: 21.6 \pm 0.4/1.8 \pm 0.3 |
| M35 | 171.8/2.1 | 52.7/2.4 | 35.4/3.5 | 30.4/1.6 | C ϵ :15.6/2.3 |
| V36 | 172.4/3.0 | 57.6/3.1 | 33.6/2.9 | 19.3/2.9 | |
| G37 | 169.3/1.9 | 43.8/2.7 | | | |
| G38 | 168.5/1.8 | 44.0/2.2 | | | |
| V39 | 171.9/3.1 | 57.8/2.7 | 34.0/2.5 | 19.5/2.7 | |
| V40 | 172.5/2.5 | 58.8/3.2 | 33.1/3.0 | 19.4/2.9 | |
| I41 | 171.3/3.3 | 58.6/2.9 | 37.6/4.5 | C γ 1:25.5/2.2 C γ 2: 15.7/3.0 | C δ 1:12.2/2.5 |
| A42 | 178.0/3.8 | 50.7/3.5 | 19.4/3.8 | | |

Sample 1



Sample 2



Sample 3

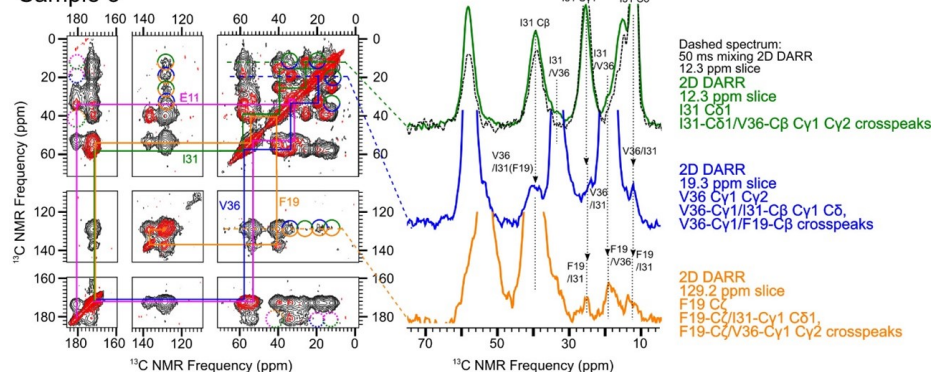


Figure D.3 2D 500ms DARR spectra from sample 4.1, 4.2, and 4.3. Black contours: 500ms mixing time 2D DARR spectra. Red contours: 2D fpRFDR or short mixing time 2D DARR spectra to show the intra-residue ^{13}C - ^{13}C cross-peaks.

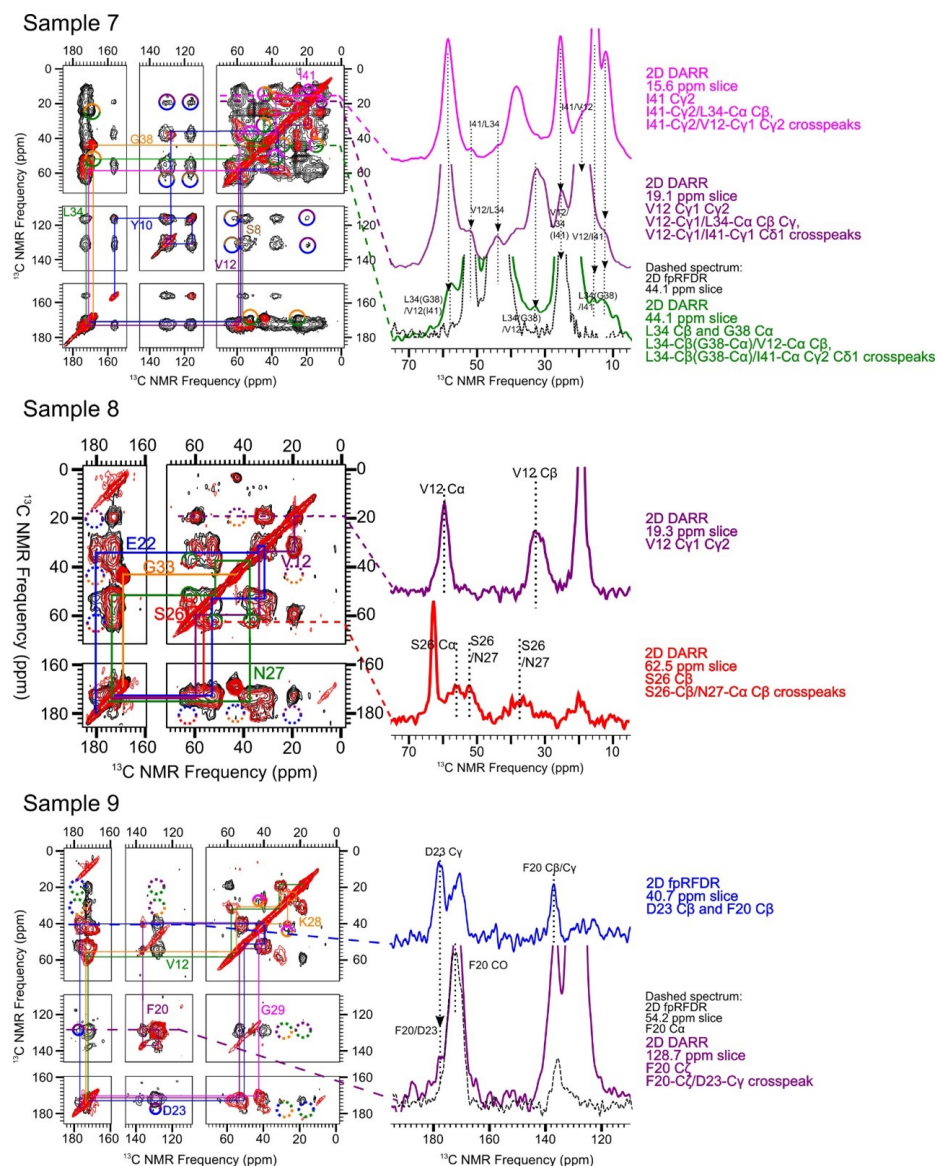


Figure D.5 2D 500ms DARR spectra from sample 4.7, 4.8, and 4.9. Black contours: 500ms mixing time 2D DARR spectra. Red contours: 2D fpRFDR or short mixing time 2D DARR spectra to show the intra-residue ^{13}C - ^{13}C cross-peaks.

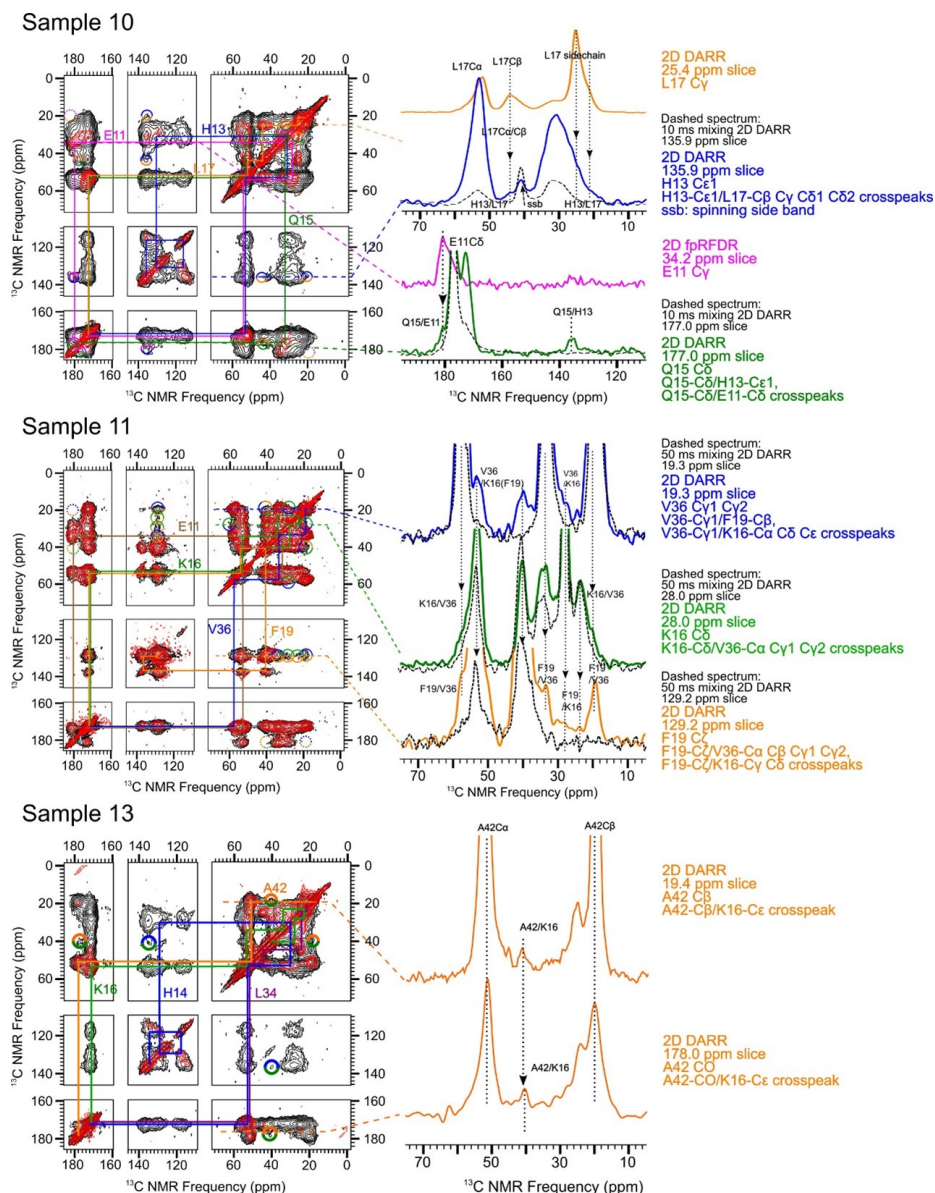


Figure D.6 2D 500ms DARR spectra from sample 4.10, 4.11, and 4.13. Black contours: 500ms mixing time 2D DARR spectra. Red contours: 2D fpRFDR or short mixing time 2D DARR spectra to show the intra-residue ^{13}C - ^{13}C cross-peaks. (Due to the low intensity of signals from A2, E3, and F4 in sample 4.12, the 2D DARR spectrum of it was not collected.)

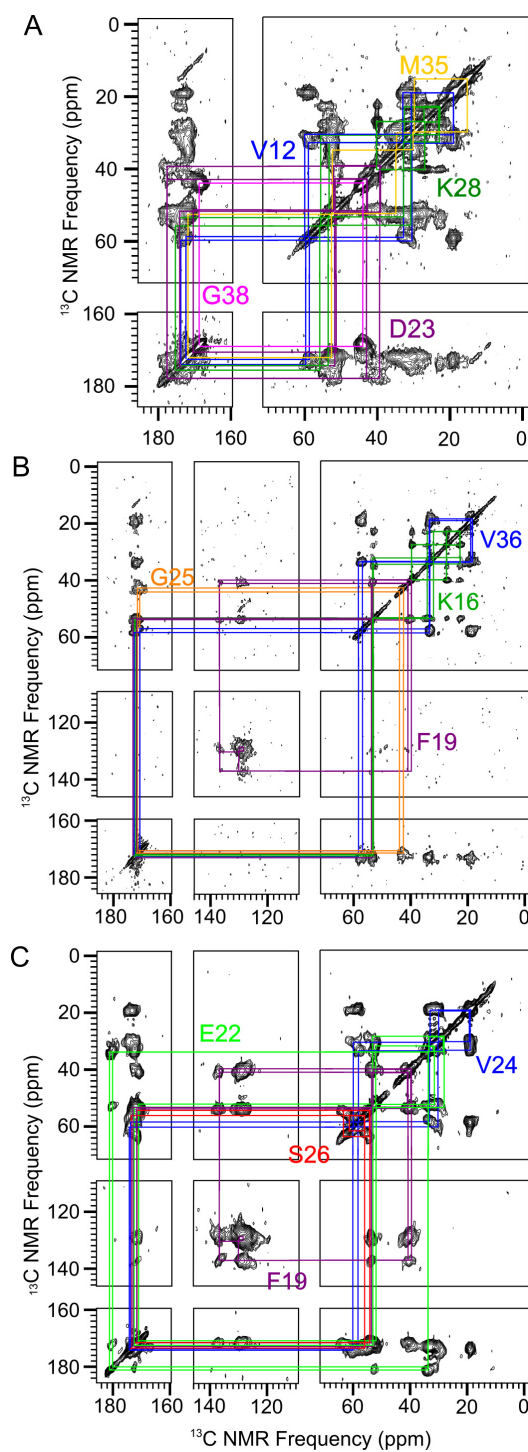


Figure D.7 2D 50ms DARR spectra from ultracentrifuged samples 4.15 (A), 4.16 (B), and 4.17 (C). Colored lines indicate spectral assignments based on crosspeaks between directly bonded ^{13}C atoms.

Table D.2 Chemical shifts (ppm)/linewidths (full width at half-maximum, ppm) of ^{13}C -labeled sites in the ultracentrifuged A β 150kDa oligomer sampels. The carbons in each amino acid are labeled as they are in the Biological Magnetic Resonance Data Bank [356]. Estimated error, based on nonlinear least-square fitting to Gaussian functions, is ± 0.1 ppm for both the chemical shift and line width unless specified otherwise. Secondary chemical shifts for CO, C α , and C β are listed right under the chemical shift values and are calculated by comparing the measured chemical shifts to the values from the same amino acid in random-coil model peptides [228]. The purple rows are the chemical shift/linewidth values from the same labeled residues in the previous lyophilized samples (Table D.1). The estimated conformations are labeled next to the residue name—“ β ” represents β -strand-like conformation and “c” represents random-coil.

| Residue | CO | C α | C β | C γ | other C |
|------------------|---------------------|------------|------------------------|--------------------|---|
| V12 (β 1) | 172.6/2.4 | 58.7/2.1 | 32.9/2.6 | 19.2/2.1 | |
| | -2.0 | -1.8 | +1.7 | | |
| V12 (c2) | 174.0/2.4 | 59.7/2.5 | 30.6/2.0 | 19.1/1.8 | |
| | -0.6 | -0.8 | -0.6 | | |
| V12 | 174.1/3.2 | 58.8/4.0 | 32.7/2.9 | 19.3/3.3 | |
| | -0.5 | -1.7 | +1.5 | | |
| K16 (β 1) | 172.6/1.8 | 53.2/1.7 | 34.5/2.9 | 23.1/1.9 | C δ : 27.8/1.6, C ϵ : 39.9/1.3 |
| | -2.3 | -1.3 | +3.1 | | |
| K16 (β 2) | 172.1/1.8 | 53.5/1.8 | 32.3/ 1.5 \pm 0.3 | 23.1/1.9 | C δ : 27.8/1.6, C ϵ : 39.9/1.3 |
| | -2.8 | -1.0 | +0.9 | | |
| K16 | 171.3/3.7 | 53.2/2.6 | 34.4/5.2 | 23.9/2.2 | C δ : 28.0/3.0, C ϵ : 40.1/2.2 |
| | -3.6 | -1.3 | +3.0 | | |
| F19 (β 1) | 172.8/1.6 | 53.4/2.3 | 40.0/ 2.2 \pm 0.2 | 136.9/3.5 | C δ : 130.3/1.6 \pm 0.2, C ϵ : 130.0/1.6 \pm 0.2, C ζ : 128.7/1.4 \pm 0.2 |
| | -1.3 | -2.6 | +2.1 | | |
| F19 (β 2) | 171.5/2.0 | 53.9/1.8 | 41.2/1.6 | 136.9/3.5 | C δ : 130.3/1.6 \pm 0.2, C ϵ : 130.0/1.6 \pm 0.2, C ζ : 128.7/1.4 \pm 0.2 |
| | -2.6 | -2.1 | +3.3 | | |
| F19 | 172.1/2.7 | 54.2/3.9 | 40.8/2.2 | 136.6/3.2 | C δ : 129.0/2.6 |
| | -2.0 | -1.8 | +2.9 | | |
| E22 (β 1) | 171.1/2.6 \pm 0.3 | 52.3/2.0 | 32.0/3.5 | 33.9/4.9 \pm 0.3 | C δ : 179.9/2.6 |
| | -3.8 | -2.6 | +3.8 | | |
| E22 (c2) | 172.7/2.5 | 53.4/2.1 | 28.6/2.3 | 33.9/4.9 | C δ : 181.0/1.4 |
| | -2.2 | -1.5 | +0.4 | | |
| E22 | 172.4/3.1 | 52.9/3.1 | 31.5/6.4 | 34.2/7.5 | C δ : 180.5/5.0 |
| | -2.5 | -2.0 | +3.3 | | |

Table D.2 (continued)

| Residue | CO | Ca | Cβ | Cγ | other C |
|----------|-------------------|----------------------|----------|-------------------|------------------------------|
| D23 (β1) | 170.6/4.6 | 51.4/2.1 | 42.8/3.7 | 177.6/ 3.3±0.2 | |
| | -4.0 | -1.1 | +3.4 | | |
| D23 (c2) | 174.3/5.1 | 51.8/3.9 | 39.2/3.4 | 177.6/ 2.8±0.2 | |
| | -0.3 | -0.7 | -0.2 | | |
| D23 | 173.6/4.2 | 51.6/3.2 | 40.7/8.2 | 177.8/4.4 | |
| | -1.0 | -0.9 | +1.3 | | |
| V24 (β1) | 173.6/3.0 | 58.5/2.2 | 33.5/2.6 | 19.2/2.6 | |
| | -1.0 | -2.0 | +2.3 | | |
| V24 (c2) | 174.1/4.2±0.4 | 60.3±0.2/ 4.8±0.3 | 30.5/3.1 | 19.5/1.9 | |
| | -0.5 | -0.2 | -0.7 | | |
| V24 | 172.1/2.3 | 57.6/3.0 | 33.1/2.6 | 19.2/3.7 | |
| | -2.5 | -2.9 | +1.9 | | |
| G25 (c1) | 171.6/4.0 ±0.2 | 42.7/2.8 | | | |
| | -1.6 | -0.7 | | | |
| G25 (c2) | 170.8/1.2 | 44.1/1.1 | | | |
| | -2.4 | +0.7 | | | |
| G25 | 171.0/4.7 | 43.4/3.7 | | | |
| | -2.2 | 0.0 | | | |
| S26 (c1) | 173.7/3.5 | 56.3/2.5 | 61.7/2.1 | | |
| | +0.8 | -0.3 | -0.4 | | |
| S26 (c2) | 171.7/2.3 | 54.5/2.2 | 63.7/3.1 | | |
| | -1.2 | -2.1 | +1.6 | | |
| S26 | 172.9/4.4 | 56.3/5.3 | 62.5/4.6 | | |
| | 0.0 | -0.3 | +0.4 | | |
| K28 (c1) | 175.3/1.2 | 55.6/1.8 | 30.7/1.8 | 23.1/2.8 | Cδ: 27.1/1.9 Cε: 40.1/1.3 |
| | +0.4 | +1.1 | -0.7 | | |
| K28 (β2) | 174.0/2.9 | 53.3/2.7 | 32.7/3.5 | 22.9/2.4 | Cδ: 27.1/1.9 Cε: 40.1/1.3 |
| | -0.9 | -1.2 | +1.3 | | |
| K28 | 174.7/6.6 | 55.3±0.2/ 5.9 | 34.0/5.1 | 23.3/4.6 | Cδ: 27.9/3.2 Cε: 40.7/2.6 |
| | -0.2 | +0.8 | +2.6 | | |
| M35(β1) | 171.8/2.3 | 52.4/2.3 | 34.8/3.6 | 30.1/2.8 | Cε: 15.5/2.7 |
| | -2.8 | -1.3 | +3.6 | | |
| M35 | 171.8/2.1 | 52.7/2.4 | 35.4/3.5 | 30.4/1.6 | Cε: 15.6/2.3 |
| | -2.8 | -1.0 | +4.2 | | |

Table D.2 (continued)

| Residue | CO | C α | C β | C γ | other C |
|------------------|-----------|------------|-----------|------------------------|---------|
| V36 (β 1) | 172.4/2.4 | 58.4/1.7 | 33.8/1.9 | 19.4/2.4 | |
| | -2.2 | -2.1 | +2.6 | | |
| V36 (β 2) | 170.4/1.2 | 57.0/1.9 | 33.6/2.1 | 18.8/ 3.8 \pm 0.2 | |
| | -4.2 | -3.5 | +2.4 | | |
| V36 | 172.4/3.0 | 57.6/3.1 | 33.6/2.9 | 19.3/2.9 | |
| | -2.2 | -2.9 | +2.4 | | |
| G38 (β 1) | 168.7/2.1 | 43.8/2.3 | | | |
| | -4.5 | +0.4 | | | |
| G38 | 168.5/1.8 | 44.0/2.2 | | | |
| | -4.7 | +0.6 | | | |

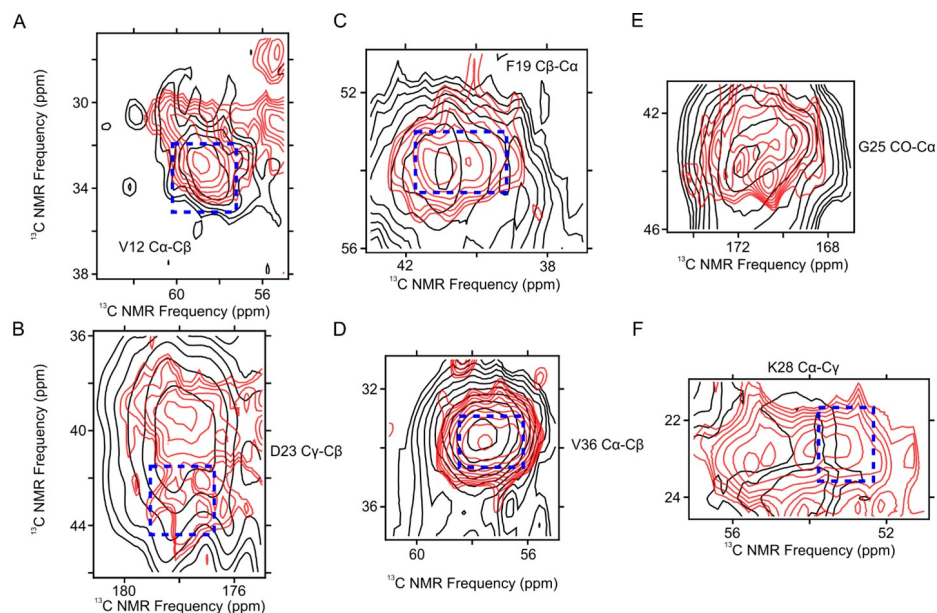


Figure D.8 Comparing intra-residue crosspeaks between lyophilized and ultracentrifuged A β (1-42) oligomer samples. (A - F) Comparison of intra-residue crosspeaks of V12 $\text{C}\alpha$ - $\text{C}\beta$, D23 $\text{C}\beta$ - $\text{C}\gamma$, F19 $\text{C}\alpha$ - $\text{C}\beta$, V36 $\text{C}\alpha$ - $\text{C}\beta$, G25 CO - $\text{C}\alpha$, and K28 CO - $\text{C}\alpha$. Red contours: ultracentrifuge samples; black contours: lyophilized samples; Dashed blue boxes: the region matching secondary chemical shifts of β -strand.

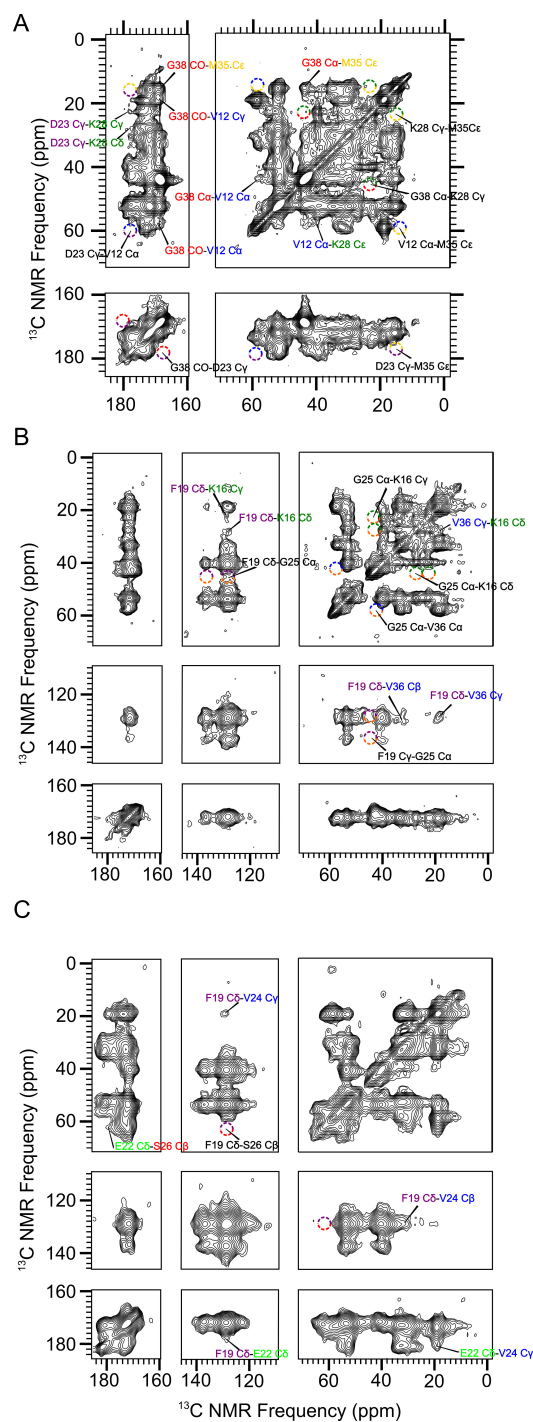


Figure D.9 2D 1000 ms DARR spectra from ultracentrifuged samples 4.15 (A), 4.16 (B), and 4.17 (C).

APPENDIX E

SUPPLEMENTARY MATERIALS FOR CHAPTER 5

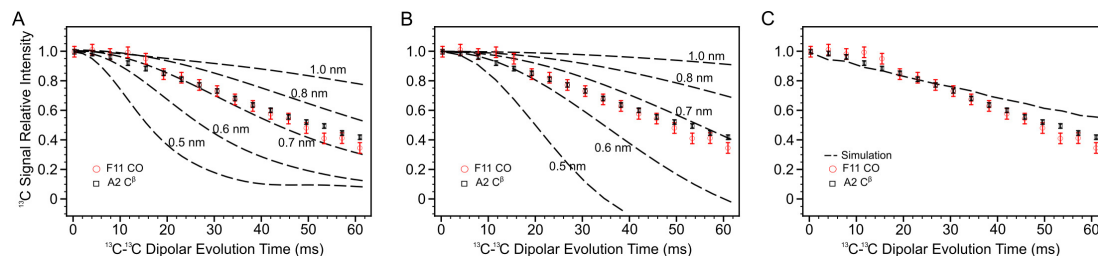


Figure E.1 The PITHIRDS-CT experimental data of Sample 5.C and different spin simulation curves. (A) Simulations of PITHIRDS-CT signal of eight ^{13}CO spins placed in a linear array with constant inter-spin distance. (B) Simulations of PITHIRDS-CT signal of two ^{13}CO spins separated by different distances. (C) Simulation of PITHIRDS-CT signal of F11 ^{13}CO spins in the U-shaped antiparallel model (Figure 5.11A), showing that while the model predicts distances of 1.0 nm between nearest-neighbor F11 ^{13}CO sites and 0.9 nm between nearest-neighbor A2 $^{13}\text{C}\beta$ sites, coupling to nearby natural-abundance ^{13}C atoms can still account for the measured decay. The dashed curve was a weighted sum of a four-spin simulation and a series of five-spin simulations. All the simulations included two nearest-neighbor F11 ^{13}CO atoms and two nearest A2 $^{13}\text{C}\beta$ atoms. For each five-spin simulation, the fifth ^{13}C atom represented a natural-abundance ^{13}C at an unlabeled carbon position near an F11 ^{13}CO . We performed a simulation with the fifth spin at each carbon site within 0.6 nm from a F11 ^{13}CO . The weighting employed in the co-addition of simulated curves was based on the 1.1% probability of a ^{13}C atom occurring at each unlabeled carbon site.

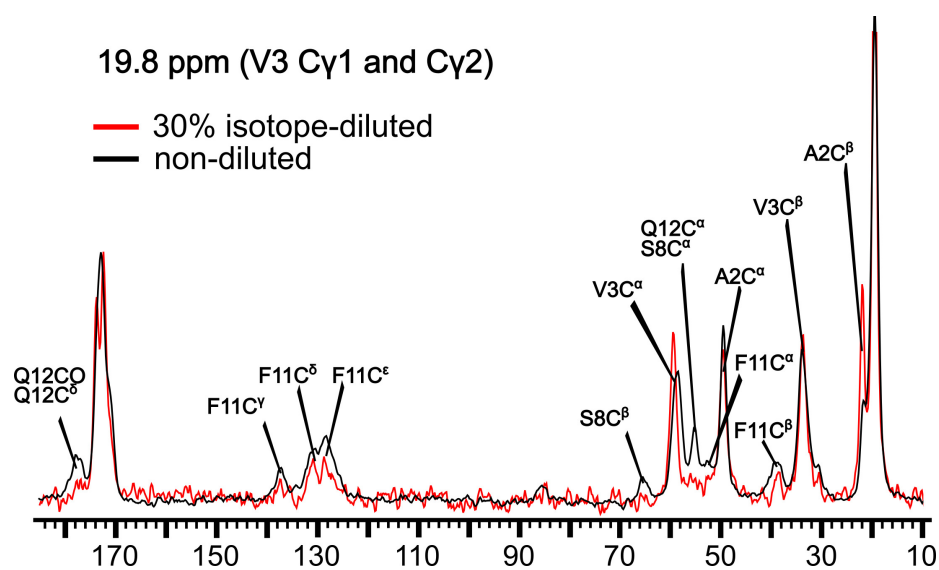


Figure E.2 Comparison between the slices from 500ms 2D DARR spectra of non-diluted (Sample 5.A) and isotope-diluted (Sample 5.B) samples of P1 amyloid. Crosspeaks that exhibited isotopic dilution effects are labeled.

Table E.1 Measured relative intensities of 2D DARR crosspeaks on isotope-diluted and non-diluted spectra. The cross-peak intensities are calculated using $(I_{AB} + I_{BA})/(I_{AA} + I_{BB})$. I_{AB} and I_{BA} are the intensities of crosspeaks on different sides of the diagonal, and I_{AA} and I_{BB} are intensities of the corresponding diagonal peaks.

| Cross-peaks | | Crosspeaks from non-diluted sample | Crosspeaks from 30% diluted sample |
|-------------|------------------------|---------------------------------------|---------------------------------------|
| A2 – A2 | $\alpha - \beta$ | 0.79±0.03 | 0.66±0.02 |
| V3 – V3 | $\alpha - \gamma$ | 0.67±0.03 | 0.55±0.02 |
| F11 – F11 | $\alpha - \beta$ | 1.02±0.09 | 0.77±0.04 |
| | $\beta - \gamma$ | 0.95±0.08 | 0.71±0.04 |
| | $\alpha - \gamma$ | 0.64±0.06 | 0.47±0.03 |
| A2 – V3 | $\alpha - \alpha$ | 0.98±0.06 | 0.74±0.02 |
| | $\alpha - \beta$ | 0.53±0.04 | 0.43±0.02 |
| F11 - Q12 | $\gamma - \beta$ | 0.66±0.06 | 0.51±0.07 |
| | $\delta - \beta$ | 0.74±0.05 | 0.57±0.04 |
| | $\varepsilon - \beta$ | 0.66±0.06 | 0.55±0.05 |
| A2 – F11 | $\alpha - \alpha$ | 0.35±0.03 | 0.10±0.01 |
| | $\alpha - \beta$ | 0.57±0.04 | 0.12±0.02 |
| | $\alpha - \gamma$ | 0.35±0.02 | 0.10±0.01 |
| | $\alpha - \delta$ | 0.33±0.02 | 0.10±0.01 |
| | $\alpha - \varepsilon$ | 0.34±0.03 | 0.08±0.01 |
| | $\beta - \delta$ | 0.23±0.04 | 0.032±0.003 |
| | $\beta - \varepsilon$ | 0.21±0.02 | 0.05±0.01 |
| V3 – F11 | $\alpha - \alpha$ | 0.33±0.04 | 0.08±0.01 |
| | $\alpha - \delta$ | 0.18±0.02 | 0.047±0.009 |
| | $\gamma - \gamma$ | 0.13±0.01 | 0.050±0.006 |
| | $\gamma - \delta$ | 0.28±0.02 | 0.124±0.005 |
| | $\gamma - \varepsilon$ | 0.29±0.02 | 0.113±0.005 |
| V3 – S8 | $\gamma - \beta$ | 0.069±0.003 | 0.019±0.003 |

REFERENCES

- [1] F. Chiti and C. M. Dobson, “Protein Misfolding, Functional Amyloid, and Human Disease,” *Annu. Rev. Biochem.*, vol. 75, no. 1, pp. 333–366, 2006.
- [2] C. M. Dobson, “The Amyloid Phenomenon and Its Links with Human Disease,” *Cold Spring Harb. Perspect. Biol.*, vol. 9, no. 6, a023648, 2017.
- [3] A. Alzheimer, “Über eine eigenartige Erkrankung der Hirnrinde,” *Allg. Zschr. Psychiat.*, vol. 64, pp. 146–8, 1907.
- [4] H.-J. Möller and M. B. Graeber, “The case described by Alois Alzheimer in 1911,” *Eur. Arch. Psychiatry Clin. Neurosci.*, vol. 248, no. 3, pp. 111–122, 1998.
- [5] B. Mroczko, M. Groblewska, A. Litman-Zawadzka, J. Kornhuber, and P. Lewczuk, “Amyloid β oligomers (A β Os) in Alzheimer’s disease,” *J. Neural Transm.*, vol. 125, no. 2, pp. 177–191, 2018.
- [6] M. D. Kirkitadze, G. Bitan, and D. B. Teplow, “Paradigm shifts in Alzheimer’s disease and other neurodegenerative disorders: The emerging role of oligomeric assemblies,” *J. Neurosci. Res.*, vol. 69, no. 5, pp. 567–577, 2002.
- [7] E. N. Cline, M. A. Bicca, K. L. Viola, and W. L. Klein, “The Amyloid- β Oligomer Hypothesis: Beginning of the Third Decade,” *J. Alzheimers Dis.*, vol. 64, no. s1, S567–S610, 2018.
- [8] L. Stefanis, “A-Synuclein in Parkinson’s Disease,” *Cold Spring Harb. Perspect. Med.*, vol. 2, no. 2, a009399–a009399, 2012.
- [9] C. W. Olanow and P. Brundin, “Parkinson’s Disease and Alpha Synuclein: Is Parkinson’s Disease a Prion-Like Disorder?” *Mov. Disord.*, vol. 28, no. 1, pp. 31–40, 2013.
- [10] K. Pillay and P. Govender, “Amylin Uncovered: A Review on the Polypeptide Responsible for Type II Diabetes,” *Biomed Res. Int.*, vol. 2013, pp. 1–17, 2013.
- [11] S. Asthana, B. Mallick, A. T. Alexandrescu, and S. Jha, “IAPP in type II diabetes: Basic research on structure, molecular interactions, and disease mechanisms suggests potential intervention strategies,” *Biochim. Biophys. Acta, Biomembr.*, Protein Aggregation and Misfolding at the Cell Membrane Interface, vol. 1860, no. 9, pp. 1765–1782, 2018.

- [12] H. Wille and J. R. Requena, “The Structure of PrP^{Sc} Prions,” *Pathogens*, vol. 7, no. 1, p. 20, 2018.
- [13] Y. H. Kwon, J. H. Fingert, M. H. Kuehn, and W. L. Alward, “Primary Open-Angle Glaucoma,” *N. Engl. J. Med.*, vol. 360, no. 11, pp. 1113–1124, 2009.
- [14] J. L. Wiggs and L. R. Pasquale, “Genetics of glaucoma,” *Hum. Mol. Genet.*, vol. 26, no. R1, R21–R27, 2017.
- [15] A. Ramon, M. Señorale, and M. Marin, “Inclusion bodies: Not that bad...,” *Front. Microbiol.*, vol. 5, 2014.
- [16] N. Hirota-Nakaoka, K. Hasegawa, H. Naiki, and Y. Goto, “Dissolution of β 2-Microglobulin Amyloid Fibrils by Dimethylsulfoxide,” *J. Biochem.*, vol. 134, no. 1, pp. 159–164, 2003.
- [17] C. M. Dobson, R. J. Ellis, A. R. Fersht, and C. M. Dobson, “The structural basis of protein folding and its links with human disease,” *Philos. Trans. R. Soc. Lond. B. Biol. Sci.*, vol. 356, no. 1406, pp. 133–145, 2001.
- [18] M. Biancalana and S. Koide, “Molecular mechanism of Thioflavin-T binding to amyloid fibrils,” *Biochim. Biophys. Acta, Proteins Proteomics*, vol. 1804, no. 7, pp. 1405–1412, 2010.
- [19] E. I. Yakupova, L. G. Bobyleva, I. M. Vikhlyantsev, and A. G. Bobylev, “Congo Red and amyloids: History and relationship,” *Biosci. Rep.*, vol. 39, no. 1, 2019.
- [20] C. Xue, T. Y. Lin, D. Chang, and Z. Guo, “Thioflavin T as an amyloid dye: Fibril quantification, optimal concentration and effect on aggregation,” *R. Soc. Open Sci.*, vol. 4, no. 1, 2017.
- [21] T. P. Knowles, A. W. Fitzpatrick, S. Meehan, H. R. Mott, M. Vendruscolo, C. M. Dobson, and M. E. Welland, “Role of Intermolecular Forces in Defining Material Properties of Protein Nanofibrils,” *Science*, vol. 318, no. 5858, pp. 1900–1903, 2007.
- [22] E. D. Eanes and G. G. Glenner, “X-ray diffraction studies on amyloid filaments,” *J. Histochem. Cytochem.*, vol. 16, no. 11, pp. 673–677, 1968.
- [23] L. Haataja, T. Gurlo, C. J. Huang, and P. C. Butler, “Islet Amyloid in Type 2 Diabetes, and the Toxic Oligomer Hypothesis,” *Endocr. Rev.*, vol. 29, no. 3, pp. 303–316, 2008.

- [24] M. L. Choi and S. Gandhi, "Crucial role of protein oligomerization in the pathogenesis of Alzheimer's and Parkinson's diseases," *FEBS J.*, vol. 285, no. 19, pp. 3631–3644, 2018.
- [25] K. Blennow, M. J. de Leon, and H. Zetterberg, "Alzheimer's disease," *Lancet*, vol. 368, no. 9533, pp. 387–403, 2006.
- [26] J. Hardy, "A Hundred Years of Alzheimer's Disease Research," *Neuron*, vol. 52, no. 1, pp. 3–13, 2006.
- [27] J. A. Hardy and G. A. Higgins, "Alzheimer's disease: The amyloid cascade hypothesis," *Science*, vol. 256, no. 5054, pp. 184–185, 1992.
- [28] D. J. Selkoe and J. Hardy, "The amyloid hypothesis of Alzheimer's disease at 25 years," *EMBO Mol. Med.*, vol. 8, no. 6, pp. 595–608, 2016.
- [29] E. Karran and B. De Strooper, "The amyloid cascade hypothesis: Are we poised for success or failure?" *J. Neurochem.*, vol. 139, no. S2, pp. 237–252, 2016.
- [30] O. Fischer, "Die presbyophrene demenz, deren anatomische grundlage und klinische Abgrenzung," *Z. Ges. Neurol. Psychiat.*, vol. 3, no. 1, pp. 371–471, 1910.
- [31] J. Götz, F. Chen, J. van Dorpe, and R. M. Nitsch, "Formation of Neurofibrillary Tangles in P301L Tau Transgenic Mice Induced by A β 42 Fibrils," *Science*, vol. 293, no. 5534, pp. 1491–1495, 2001.
- [32] R. J. Bateman, C. Xiong, T. L. Benzinger, A. M. Fagan, A. Goate, N. C. Fox, D. S. Marcus, N. J. Cairns, X. Xie, T. M. Blazey, D. M. Holtzman, A. Santacruz, V. Buckles, A. Oliver, K. Moulder, P. S. Aisen, B. Ghetti, W. E. Klunk, E. McDade, R. N. Martins, C. L. Masters, R. Mayeux, J. M. Ringman, M. N. Rossor, P. R. Schofield, R. A. Sperling, S. Salloway, and J. C. Morris, "Clinical and Biomarker Changes in Dominantly Inherited Alzheimer's Disease," *N. Engl. J. Med.*, vol. 367, no. 9, pp. 795–804, 2012.
- [33] G. S. Bloom, "Amyloid- β and Tau: The Trigger and Bullet in Alzheimer Disease Pathogenesis," *JAMA Neurol.*, vol. 71, no. 4, pp. 505–508, 2014.
- [34] C. J. Pike, D. Burdick, A. J. Walencewicz, C. G. Glabe, and C. W. Cotman, "Neurodegeneration induced by beta-amyloid peptides in vitro: The role of peptide assembly state," *J. Neurosci.*, vol. 13, no. 4, pp. 1676–1687, 1993.
- [35] A. Lorenzo and B. A. Yankner, "Beta-amyloid neurotoxicity requires fibril formation and is inhibited by congo red," *Proc. Natl. Acad. Sci. U.S.A.*, vol. 91, no. 25, pp. 12 243–12 247, 1994.

- [36] S. Estus, H. M. Tucker, C. van Rooyen, S. Wright, E. F. Brigham, M. Wogulis, and R. E. Rydel, "Aggregated Amyloid- β Protein Induces Cortical Neuronal Apoptosis and Concomitant "Apoptotic" Pattern of Gene Induction," *J. Neurosci.*, vol. 17, no. 20, pp. 7736–7745, 1997.
- [37] Y. Morishima, Y. Gotoh, J. Zieg, T. Barrett, H. Takano, R. Flavell, R. J. Davis, Y. Shirasaki, and M. E. Greenberg, "B-Amyloid Induces Neuronal Apoptosis Via a Mechanism that Involves the c-Jun N-Terminal Kinase Pathway and the Induction of Fas Ligand," *J. Neurosci.*, vol. 21, no. 19, pp. 7551–7560, 2001.
- [38] A. K. Paravastu, R. D. Leapman, W.-M. Yau, and R. Tycko, "Molecular structural basis for polymorphism in Alzheimer's β -amyloid fibrils," *Proc. Natl. Acad. Sci. U.S.A.*, vol. 105, no. 47, pp. 18 349–18 354, 2008.
- [39] Y. Xiao, B. Ma, D. McElheny, S. Parthasarathy, F. Long, M. Hoshi, R. Nussinov, and Y. Ishii, "A β (1–42) fibril structure illuminates self-recognition and replication of amyloid in Alzheimer's," *Nat. Struct. Mol. Biol.*, vol. 22, no. 6, pp. 499–505, 2015.
- [40] W. Qiang, W.-M. Yau, J.-X. Lu, J. Collinge, and R. Tycko, "Structural variation in amyloid- β fibrils from Alzheimer's disease clinical subtypes," *Nature*, vol. 541, no. 7636, pp. 217–221, 2017.
- [41] A. Aguzzi and J. Falsig, "Prion propagation, toxicity and degradation," *Nat. Neurosci.*, vol. 15, no. 7, pp. 936–939, 2012.
- [42] J. C. Watts and S. B. Prusiner, "B-Amyloid Prions and the Pathobiology of Alzheimer's Disease," *Cold Spring Harb. Perspect. Med.*, vol. 8, no. 5, a023507, 2018.
- [43] C. A. McLean, R. A. Cherny, F. W. Fraser, S. J. Fuller, M. J. Smith, K. Vbeyreuther, A. I. Bush, and C. L. Masters, "Soluble pool of A β amyloid as a determinant of severity of neurodegeneration in Alzheimer's disease," *Ann. Neurol.*, vol. 46, no. 6, pp. 860–866, 1999.
- [44] B. DaRocha-Souto, T. C. Scotton, M. Coma, A. Serrano-Pozo, T. Hashimoto, L. Serenó, M. Rodríguez, B. Sánchez, B. T. Hyman, and T. Gómez-Isla, "Brain Oligomeric β -Amyloid but Not Total Amyloid Plaque Burden Correlates With Neuronal Loss and Astrocyte Inflammatory Response in Amyloid Precursor Protein/Tau Transgenic Mice," *J. Neuropathol. Exp. Neurol.*, vol. 70, no. 5, pp. 360–376, 2011.
- [45] P. T. Nelson, I. Alafuzoff, E. H. Bigio, C. Bouras, H. Braak, N. J. Cairns, R. J. Castellani, B. J. Crain, P. Davies, K. D. Tredici, C. Duyckaerts, M. P. Frosch, V. Haroutunian, P. R. Hof, C. M. Hulette, B. T. Hyman, T. Iwatsubo, K. A. Jellinger, G. A. Jicha, E. Kövari, W. A. Kukull, J. B. Leverenz, S. Love, I. R. Mackenzie, D. M. Mann, E. Masliah, A. C. McKee, T. J. Montine, J. C. Morris, J. A. Schneider, J. A.

- Sonnen, D. R. Thal, J. Q. Trojanowski, J. C. Troncoso, T. Wisniewski, R. L. Woltjer, and T. G. Beach, "Correlation of Alzheimer Disease Neuropathologic Changes With Cognitive Status: A Review of the Literature," *J. Neuropathol. Exp. Neurol.*, vol. 71, no. 5, pp. 362–381, 2012.
- [46] T. J. Esparza, H. Zhao, J. R. Cirrito, N. J. Cairns, R. J. Bateman, D. M. Holtzman, and D. L. Brody, "Amyloid-beta Oligomerization in Alzheimer Dementia vs. High Pathology Controls," *Ann. Neurol.*, vol. 73, no. 1, pp. 104–119, 2013.
- [47] R. Cappai and K. J. Barnham, "Delineating the Mechanism of Alzheimer's Disease A β Peptide Neurotoxicity," *Neurochem. Res.*, vol. 33, no. 3, pp. 526–532, 2008.
- [48] M. P. Lambert, P. T. Velasco, L. Chang, K. L. Viola, S. Fernandez, P. N. Lacor, D. Khuon, Y. Gong, E. H. Bigio, P. Shaw, F. G. De Felice, G. A. Krafft, and W. L. Klein, "Monoclonal antibodies that target pathological assemblies of A β ," *J. Neurochem.*, vol. 100, no. 1, pp. 23–35, 2007.
- [49] A. Zameer, S. Kasturirangan, S. Emadi, S. V. Nimmagadda, and M. R. Sierks, "Anti-oligomeric A β Single-chain Variable Domain Antibody Blocks A β -induced Toxicity Against Human Neuroblastoma Cells," *J. Mol. Biol.*, vol. 384, no. 4, pp. 917–928, 2008.
- [50] M. Zhao, S.-w. Wang, Y.-j. Wang, R. Zhang, Y.-n. Li, Y.-j. Su, W.-w. Zhou, X.-l. Yu, and R.-t. Liu, "Pan-Amyloid Oligomer Specific scFv Antibody Attenuates Memory Deficits and Brain Amyloid Burden in Mice with Alzheimer's Disease," *Curr. Alzheimer Res.*, vol. 11, no. 1, pp. 69–78, 2014.
- [51] A. Sebollela, E. N. Cline, I. Popova, K. Luo, X. Sun, J. Ahn, M. A. Barcelos, V. N. Bezerra, N. M. Lyra e Silva, J. Patel, N. R. Pinheiro, L. A. Qin, J. M. Kamel, A. Weng, N. DiNunno, A. M. Bebenek, P. T. Velasco, K. L. Viola, P. N. Lacor, S. T. Ferreira, and W. L. Klein, "A human scFv antibody that targets and neutralizes high molecular weight pathogenic amyloid- β oligomers," *J. Neurochem.*, vol. 142, no. 6, pp. 934–947, 2017.
- [52] D. M. Walsh, I. Klyubin, J. V. Fadeeva, W. K. Cullen, R. Anwyl, M. S. Wolfe, M. J. Rowan, and D. J. Selkoe, "Naturally secreted oligomers of amyloid β protein potently inhibit hippocampal long-term potentiation in vivo," *Nature*, vol. 416, no. 6880, pp. 535–539, 2002.
- [53] G. M. Shankar, S. Li, T. H. Mehta, A. Garcia-Munoz, N. E. Shepardson, I. Smith, F. M. Brett, M. A. Farrell, M. J. Rowan, C. A. Lemere, C. M. Regan, D. M. Walsh, B. L. Sabatini, and D. J. Selkoe, "Amyloid- β protein dimers isolated directly from Alzheimer's brains impair synaptic plasticity and memory," *Nat. Med.*, vol. 14, no. 8, pp. 837–842, 2008.

- [54] J. Brito-Moreira, M. V. Lourenco, M. M. Oliveira, F. C. Ribeiro, J. H. Ledo, L. P. Diniz, J. F. S. Vital, M. H. Magdesian, H. M. Melo, F. Barros-Aragão, J. M. de Souza, S. V. Alves-Leon, F. C. A. Gomes, J. R. Clarke, C. P. Figueiredo, F. G. D. Felice, and S. T. Ferreira, "Interaction of amyloid- β (A β) oligomers with neurexin 2 α and neuroligin 1 mediates synapse damage and memory loss in mice," *J. Biol. Chem.*, vol. 292, no. 18, pp. 7327–7337, 2017.
- [55] C. A. H. Petersen, N. Alikhani, H. Behbahani, B. Wiehager, P. F. Pavlov, I. Alafuzoff, V. Leinonen, A. Ito, B. Winblad, E. Glaser, and M. Ankarcrona, "The amyloid β -peptide is imported into mitochondria via the TOM import machinery and localized to mitochondrial cristae," *Proc. Natl. Acad. Sci. U.S.A.*, vol. 105, no. 35, pp. 13 145–13 150, 2008.
- [56] H. Du and S. S. Yan, "Mitochondrial permeability transition pore in Alzheimer's disease: Cyclophilin D and amyloid beta," *Biochim. Biophys. Acta, Mol. Basis Dis., Mitochondrial Dysfunction*, vol. 1802, no. 1, pp. 198–204, 2010.
- [57] L. Connelly, H. Jang, F. Teran Arce, R. Capone, S. A. Kotler, S. Ramachandran, B. L. Kagan, R. Nussinov, and R. Lal, "Atomic Force Microscopy and MD Simulations Reveal Pore-Like Structures of All-d-Enantiomer of Alzheimer's β -Amyloid Peptide: Relevance to the Ion Channel Mechanism of AD Pathology," *J. Phys. Chem. B*, vol. 116, no. 5, pp. 1728–1735, 2012.
- [58] E. J. Fernandez-Perez, C. Peters, and L. G. Aguayo, "Membrane Damage Induced by Amyloid Beta and a Potential Link with Neuroinflammation," *Curr. Pharm. Des.*, vol. 22, no. 10, pp. 1295–1304, 2016.
- [59] D. C. Bode, M. D. Baker, and J. H. Viles, "Ion Channel Formation by Amyloid- β 42 Oligomers but Not Amyloid- β 40 in Cellular Membranes," *J. Biol. Chem.*, vol. 292, no. 4, pp. 1404–1413, 2017.
- [60] M. Mezler, S. Barghorn, H. Schoemaker, G. Gross, and V. Nimmrich, "A β -amyloid oligomer directly modulates P/Q-type calcium currents in *Xenopus* oocytes: A β oligomers modulate P/Q-type calcium currents," *Br. J. Pharmacol.*, vol. 165, no. 5, pp. 1572–1583, 2012.
- [61] D. Hermann, M. Mezler, M. K. Müller, K. Wicke, G. Gross, A. Draguhn, C. Bruehl, and V. Nimmrich, "Synthetic A β oligomers (A β 1–42 globulomer) modulate presynaptic calcium currents: Prevention of A β -induced synaptic deficits by calcium channel blockers," *Eur. J. Pharmacol.*, vol. 702, no. 1-3, pp. 44–55, 2013.
- [62] A. Pannaccione, I. Piccialli, A. Secondo, R. Ciccone, P. Molinaro, F. Boscia, and L. Annunziato, "The Na⁺/Ca²⁺ exchanger in Alzheimer's disease," *Cell Calcium*, p. 102 190, 2020.

- [63] E. Sturchler, A. Galichet, M. Weibel, E. Leclerc, and C. W. Heizmann, "Site-Specific Blockade of RAGE-Vd Prevents Amyloid- β Oligomer Neurotoxicity," *J. Neurosci.*, vol. 28, no. 20, pp. 5149–5158, 2008.
- [64] M. Guglielmotto, D. Monteleone, A. Piras, V. Valsecchi, M. Tropiano, S. Ariano, M. Fornaro, A. Vercelli, J. Puyal, O. Arancio, M. Tabaton, and E. Tamagno, "A β 1-42 monomers or oligomers have different effects on autophagy and apoptosis," *Autophagy*, vol. 10, no. 10, pp. 1827–1843, 2014.
- [65] B. Zott, M. M. Simon, W. Hong, F. Unger, H.-J. Chen-Engerer, M. P. Frosch, B. Sakmann, D. M. Walsh, and A. Konnerth, "A vicious cycle of β amyloid-dependent neuronal hyperactivation," *Science*, vol. 365, no. 6453, pp. 559–565, 2019.
- [66] J. Sevigny, P. Chiao, T. Bussière, P. H. Weinreb, L. Williams, M. Maier, R. Dunstan, S. Salloway, T. Chen, Y. Ling, J. O’Gorman, F. Qian, M. Arastu, M. Li, S. Chollate, M. S. Brennan, O. Quintero-Monzon, R. H. Scannevin, H. M. Arnold, T. Engber, K. Rhodes, J. Ferrero, Y. Hang, A. Mikulskis, J. Grimm, C. Hock, R. M. Nitsch, and A. Sandrock, "The antibody aducanumab reduces A β plaques in Alzheimer’s disease," *Nature*, vol. 537, no. 7618, pp. 50–56, 2016.
- [67] E. R. Siemers, K. L. Sundell, C. Carlson, M. Case, G. Sethuraman, H. Liu-Seifert, S. A. Dowsett, M. J. Pontecorvo, R. A. Dean, and R. Demattos, "Phase 3 solanezumab trials: Secondary outcomes in mild Alzheimer’s disease patients," *Alzheimers. Dement.*, vol. 12, no. 2, pp. 110–120, 2016.
- [68] A. J. Doig, M. P. del Castillo-Frias, O. Berthoumieu, B. Tarus, J. Nasica-Labouze, F. Sterpone, P. H. Nguyen, N. M. Hooper, P. Faller, and P. Derreumaux, "Why Is Research on Amyloid- β Failing to Give New Drugs for Alzheimer’s Disease?" *ACS Chem. Neurosci.*, vol. 8, no. 7, pp. 1435–1437, 2017.
- [69] C. Piller, "Blots on a field?" *Science*, vol. 377, no. 6604, pp. 358–363, 2022.
- [70] X. Du, X. Wang, and M. Geng, "Alzheimer’s disease hypothesis and related therapies," *Transl. Neurodegener.*, vol. 7, 2018.
- [71] J. Cummings, G. Lee, P. Nahed, M. E. Z. N. Kambar, K. Zhong, J. Fonseca, and K. Taghva, "Alzheimer’s disease drug development pipeline: 2022," *Alzheimer’s Dement.: Transl. Res. Clin. Interv.*, vol. 8, no. 1, e12295, 2022.
- [72] K. Iqbal, F. Liu, C.-X. Gong, and I. Grundke-Iqbal, "Tau in Alzheimer Disease and Related Tauopathies," *Curr. Alzheimer Res.*, vol. 7, no. 8, pp. 656–664, 2010.
- [73] A. F. T. Arnsten, D. Datta, K. D. Tredici, and H. Braak, "Hypothesis: Tau pathology is an initiating factor in sporadic Alzheimer’s disease," *Alzheimers. Dement.*, vol. 17, no. 1, pp. 115–124, 2021.

- [74] B. Readhead, J.-V. Haure-Mirande, C. C. Funk, M. A. Richards, P. Shannon, V. Haroutunian, M. Sano, W. S. Liang, N. D. Beckmann, N. D. Price, E. M. Reiman, E. E. Schadt, M. E. Ehrlich, S. Gandy, and J. T. Dudley, “Multiscale Analysis of Independent Alzheimer’s Cohorts Finds Disruption of Molecular, Genetic, and Clinical Networks by Human Herpesvirus,” *Neuron*, vol. 99, no. 1, 64–82.e7, 2018.
- [75] G.-f. Chen, T.-h. Xu, Y. Yan, Y.-r. Zhou, Y. Jiang, K. Melcher, and H. E. Xu, “Amyloid beta: Structure, biology and structure-based therapeutic development,” *Acta Pharmacol. Sin.*, vol. 38, no. 9, pp. 1205–1235, 2017.
- [76] P. H. Nguyen, A. Ramamoorthy, B. R. Sahoo, J. Zheng, P. Faller, J. E. Straub, L. Dominguez, J.-E. Shea, N. V. Dokholyan, A. De Simone, B. Ma, R. Nussinov, S. Najafi, S. T. Ngo, A. Loquet, M. Chiricotto, P. Ganguly, J. McCarty, M. S. Li, C. Hall, Y. Wang, Y. Miller, S. Melchionna, B. Habenstein, S. Timr, J. Chen, B. Hnath, B. Strodel, R. Kayed, S. Lesné, G. Wei, F. Sterpone, A. J. Doig, and P. Derreumaux, “Amyloid Oligomers: A Joint Experimental/Computational Perspective on Alzheimer’s Disease, Parkinson’s Disease, Type II Diabetes, and Amyotrophic Lateral Sclerosis,” *Chem. Rev.*, vol. 121, no. 4, pp. 2545–2647, 2021.
- [77] A. K. Dunker, M. M. Babu, E. Barbar, M. Blackledge, S. E. Bondos, Z. Dosztányi, H. J. Dyson, J. Forman-Kay, M. Fuxreiter, J. Gsponer, K.-H. Han, D. T. Jones, S. Longhi, S. J. Metallo, K. Nishikawa, R. Nussinov, Z. Obradovic, R. V. Pappu, B. Rost, P. Selenko, V. Subramaniam, J. L. Sussman, P. Tompa, and V. N. Uversky, “What’s in a name? Why these proteins are intrinsically disordered,” *Intrinsically Disord. Proteins*, vol. 1, no. 1, e24157, 2013.
- [78] P. R. Turner, K. O’Connor, W. P. Tate, and W. C. Abraham, “Roles of amyloid precursor protein and its fragments in regulating neural activity, plasticity and memory,” *Prog. Neurobiol.*, vol. 70, no. 1, pp. 1–32, 2003.
- [79] R. J. O’Brien and P. C. Wong, “Amyloid Precursor Protein Processing and Alzheimer’s Disease,” *Annu. Rev. Neurosci.*, vol. 34, no. 1, pp. 185–204, 2011.
- [80] E. Winkler, A. Julius, H. Steiner, and D. Langosch, “Homodimerization Protects the Amyloid Precursor Protein C99 Fragment from Cleavage by γ -Secretase,” *Biochemistry*, vol. 54, no. 40, pp. 6149–6152, 2015.
- [81] W. Yu, K. Zou, J.-S. Gong, M. Ko, K. Yanagisawa, and M. Michikawa, “Oligomerization of amyloid β -protein occurs during the isolation of lipid rafts,” *J. Neurosci. Res.*, vol. 80, no. 1, pp. 114–119, 2005.
- [82] E. Winkler, F. Kamp, J. Scheuring, A. Ebke, A. Fukumori, and H. Steiner, “Generation of Alzheimer Disease-associated Amyloid β 42/43 Peptide by γ -Secretase Can Be Inhibited Directly by Modulation of Membrane Thickness*,” *J. Biol. Chem.*, vol. 287, no. 25, pp. 21 326–21 334, 2012.

- [83] J. Zhao, X. Liu, W. Xia, Y. Zhang, and C. Wang, “Targeting Amyloidogenic Processing of APP in Alzheimer’s Disease,” *Front. Mol. Neurosci.*, vol. 13, 2020.
- [84] G. Bitan, M. D. Kirkitadze, A. Lomakin, S. S. Vollers, G. B. Benedek, and D. B. Teplow, “Amyloid β -protein ($A\beta$) assembly: $A\beta$ 40 and $A\beta$ 42 oligomerize through distinct pathways,” *Proc. Natl. Acad. Sci. U.S.A.*, vol. 100, no. 1, pp. 330–335, 2003.
- [85] G. Bellomo, S. Bologna, L. Gonnelli, E. Ravera, M. Fragai, M. Lelli, and C. Luchinat, “Aggregation kinetics of the $A\beta$ 1–40 peptide monitored by NMR,” *Chem. Commun.*, vol. 54, no. 55, pp. 7601–7604, 2018.
- [86] T. C. T. Michaels, A. Šarić, S. Curk, K. Bernfur, P. Arosio, G. Meisl, A. J. Dear, S. I. A. Cohen, C. M. Dobson, M. Vendruscolo, S. Linse, and T. P. J. Knowles, “Dynamics of oligomer populations formed during the aggregation of Alzheimer’s $A\beta$ 42 peptide,” *Nat. Chem.*, vol. 12, no. 5, pp. 445–451, 2020.
- [87] A. J. Dear, T. C. T. Michaels, G. Meisl, D. Klenerman, S. Wu, S. Perrett, S. Linse, C. M. Dobson, and T. P. J. Knowles, “Kinetic diversity of amyloid oligomers,” *Proc. Natl. Acad. Sci. U.S.A.*, vol. 117, no. 22, pp. 12 087–12 094, 2020.
- [88] A. T. Petkova, W.-M. Yau, and R. Tycko, “Experimental Constraints on Quaternary Structure in Alzheimer’s β -Amyloid Fibrils,” *Biochemistry*, vol. 45, no. 2, pp. 498–512, 2006.
- [89] M. T. Colvin, R. Silvers, Q. Z. Ni, T. V. Can, I. Sergeyev, M. Rosay, K. J. Donovan, B. Michael, J. Wall, S. Linse, and R. G. Griffin, “Atomic resolution structure of monomorphic $A\beta$ 42 amyloid fibrils,” *J. Am. Chem. Soc.*, vol. 138, no. 30, pp. 9663–9674, 2016.
- [90] T. Iwatsubo, A. Odaka, N. Suzuki, H. Mizusawa, N. Nukina, and Y. Ihara, “Visualization of $A\beta$ 42(43) and $A\beta$ 40 in senile plaques with end-specific $A\beta$ monoclonals: Evidence that an initially deposited species is $A\beta$ 42(43),” *Neuron*, vol. 13, no. 1, pp. 45–53, 1994.
- [91] S. A. Gravina, L. Ho, C. B. Eckman, K. E. Long, L. Otvos, L. H. Younkin, N. Suzuki, and S. G. Younkin, “Amyloid beta protein (A beta) in Alzheimer’s disease brain. Biochemical and immunocytochemical analysis with antibodies specific for forms ending at A beta 40 or A beta 42(43),” *J. Biol. Chem.*, vol. 270, no. 13, pp. 7013–7016, 1995.
- [92] L. Gu and Z. Guo, “Alzheimer’s $A\beta$ 42 and $A\beta$ 40 form mixed oligomers with direct molecular interactions,” *Biochem. Biophys. Res. Commun.*, 2020.
- [93] L. Cerofolini, E. Ravera, S. Bologna, T. Wiglenda, A. Böddrich, B. Purfürst, I. Benilova, M. Korsak, G. Gallo, D. Rizzo, L. Gonnelli, M. Fragai, B. D. Strooper,

- E. E. Wanker, and C. Luchinat, "Mixing A β (1–40) and A β (1–42) peptides generates unique amyloid fibrils," *Chem. Commun.*, 2020.
- [94] C. J. Barrow, A. Yasuda, P. T. M. Kenny, and M. G. Zagorski, "Solution conformations and aggregational properties of synthetic amyloid β -peptides of Alzheimer's disease: Analysis of circular dichroism spectra," *J. Mol. Biol.*, vol. 225, no. 4, pp. 1075–1093, 1992.
- [95] S. Zhang, K. Iwata, M. J. Lachenmann, J. W. Peng, S. Li, E. R. Stimson, Y. -a. Lu, A. M. Felix, J. E. Maggio, and J. P. Lee, "The Alzheimer's Peptide A β Adopts a Collapsed Coil Structure in Water," *J. Struct. Biol.*, vol. 130, no. 2, pp. 130–141, 2000.
- [96] H. Shao, S.-c. Jao, K. Ma, and M. G. Zagorski, "Solution structures of micelle-bound amyloid β -(1-40) and β -(1-42) peptides of Alzheimer's disease," *J. Mol. Biol.*, vol. 285, no. 2, pp. 755–773, 1999.
- [97] Y. Xu, J. Shen, X. Luo, W. Zhu, K. Chen, J. Ma, and H. Jiang, "Conformational transition of amyloid β -peptide," *Proc. Natl. Acad. Sci. U.S.A.*, vol. 102, no. 15, pp. 5403–5407, 2005.
- [98] Y.-M. Kuo, M. R. Emmerling, C. Vigo-Pelfrey, T. C. Kasunic, J. B. Kirkpatrick, G. H. Murdoch, M. J. Ball, and A. E. Roher, "Water-soluble A β (N-40, N-42) Oligomers in Normal and Alzheimer Disease Brains," *J. Biol. Chem.*, vol. 271, no. 8, pp. 4077–4081, 1996.
- [99] M. Sakono and T. Zako, "Amyloid oligo-mers: Formation and toxicity of A β oligomers," *FEBS J.*, vol. 277, no. 6, pp. 1348–1358, 2010.
- [100] M. Hoshi, M. Sato, S. Matsumoto, A. Noguchi, K. Yasutake, N. Yoshida, and K. Sato, "Spherical aggregates of β -amyloid (amylospheroid) show high neurotoxicity and activate tau protein kinase I/glycogen synthase kinase-3 β ," *Proc. Natl. Acad. Sci. U.S.A.*, vol. 100, no. 11, pp. 6370–6375, 2003.
- [101] M. Ahmed, J. Davis, D. Aucoin, T. Sato, S. Ahuja, S. Aimoto, J. I. Elliott, W. E. Van Nostrand, and S. O. Smith, "Structural conversion of neurotoxic amyloid- β _{1–42} oligomers to fibrils," *Nat. Struct. Mol. Biol.*, vol. 17, no. 5, pp. 561–567, 2010.
- [102] P. N. Lacor, M. C. Buniel, L. Chang, S. J. Fernandez, Y. Gong, K. L. Viola, M. P. Lambert, P. T. Velasco, E. H. Bigio, C. E. Finch, G. A. Krafft, and W. L. Klein, "Synaptic Targeting by Alzheimer's-Related Amyloid β Oligomers," *J. Neurosci.*, vol. 24, no. 45, pp. 10 191–10 200, 2004.
- [103] P. N. Lacor, M. C. Buniel, P. W. Furlow, A. S. Clemente, P. T. Velasco, M. Wood, K. L. Viola, and W. L. Klein, "A β Oligomer-Induced Aberrations in Synapse Com-

position, Shape, and Density Provide a Molecular Basis for Loss of Connectivity in Alzheimer's Disease," *J. Neurosci.*, vol. 27, no. 4, pp. 796–807, 2007.

- [104] P. T. Velasco, M. C. Heffern, A. Sebollela, I. A. Popova, P. N. Lacor, K. B. Lee, X. Sun, B. N. Tiano, K. L. Viola, A. L. Eckermann, T. J. Meade, and W. L. Klein, "Synapse-Binding Subpopulations of A β Oligomers Sensitive to Peptide Assembly Blockers and scFv Antibodies," *ACS Chem. Neurosci.*, vol. 3, no. 11, pp. 972–981, 2012.
- [105] C. P. Figueiredo, J. R. Clarke, J. H. Ledo, F. C. Ribeiro, C. V. Costa, H. M. Melo, A. P. Mota-Sales, L. M. Saraiva, W. L. Klein, A. Sebollela, F. G. D. Felice, and S. T. Ferreira, "Memantine Rescues Transient Cognitive Impairment Caused by High-Molecular-Weight A β Oligomers But Not the Persistent Impairment Induced by Low-Molecular-Weight Oligomers," *J. Neurosci.*, vol. 33, no. 23, pp. 9626–9634, 2013.
- [106] S. T. Ferreira, M. V. Lourenco, M. M. Oliveira, and F. G. De Felice, "Soluble amyloid- β oligomers as synaptotoxins leading to cognitive impairment in Alzheimer's disease," *Front. Cell. Neurosci.*, vol. 9, 2015.
- [107] S. Matsumura, K. Shinoda, M. Yamada, S. Yokojima, M. Inoue, T. Ohnishi, T. Shimada, K. Kikuchi, D. Masui, S. Hashimoto, M. Sato, A. Ito, M. Akioka, S. Takagi, Y. Nakamura, K. Nemoto, Y. Hasegawa, H. Takamoto, H. Inoue, S. Nakamura, Y.-i. Nabeshima, D. B. Teplow, M. Kinjo, and M. Hoshi, "Two distinct Amyloid β -protein (A β) assembly pathways leading to oligomers and fibrils identified by combined fluorescence correlation spectroscopy, morphology, and toxicity analyses," *J. Biol. Chem.*, vol. 286, no. 13, pp. 11 555–11 562, 2011.
- [108] L. Breydo, D. Kourouski, S. Rasool, S. Milton, J. W. Wu, V. N. Uversky, I. K. Lednev, and C. G. Glabe, "Structural differences between amyloid beta oligomers," *Biochem. Biophys. Res. Commun.*, vol. 477, no. 4, pp. 700–705, 2016.
- [109] T. Watanabe-Nakayama, K. Ono, M. Itami, R. Takahashi, D. B. Teplow, and M. Yamada, "High-speed atomic force microscopy reveals structural dynamics of amyloid β 1–42 aggregates," *Proc. Natl. Acad. Sci. U.S.A.*, vol. 113, no. 21, pp. 5835–5840, 2016.
- [110] B. Barz, Q. Liao, and B. Strodel, "Pathways of Amyloid- β Aggregation Depend on Oligomer Shape," *J. Am. Chem. Soc.*, vol. 140, no. 1, pp. 319–327, 2018.
- [111] K. Ono and M. Tsuji, "Protofibrils of Amyloid- β are Important Targets of a Disease-Modifying Approach for Alzheimer's Disease," *Int. J. Mol. Sci.*, vol. 21, no. 3, p. 952, 2020.

- [112] C. Goldsbury, P. Frey, V. Olivieri, U. Aebi, and S. A. Müller, “Multiple Assembly Pathways Underlie Amyloid- β Fibril Polymorphisms,” *J. Mol. Biol.*, vol. 352, no. 2, pp. 282–298, 2005.
- [113] R. Tycko, “Molecular Structure of Aggregated Amyloid- β : Insights from Solid-State Nuclear Magnetic Resonance,” *Cold Spring Harb. Perspect. Med.*, vol. 6, no. 8, a024083, 2016.
- [114] C. M. Dobson, T. P. J. Knowles, and M. Vendruscolo, “The Amyloid Phenomenon and Its Significance in Biology and Medicine,” *Cold Spring Harb. Perspect. Biol.*, a033878, 2019.
- [115] M. R. Sawaya, M. P. Hughes, J. A. Rodriguez, R. Riek, and D. S. Eisenberg, “The expanding amyloid family: Structure, stability, function, and pathogenesis,” *Cell*, vol. 184, no. 19, pp. 4857–4873, 2021.
- [116] Xue Christine, Tran Joyce, Wang Hongsu, Park Giovanna, Hsu Frederick, and Guo Zhefeng, “A β 42 fibril formation from predominantly oligomeric samples suggests a link between oligomer heterogeneity and fibril polymorphism,” *R. Soc. Open Sci.*, vol. 6, no. 7, p. 190 179, 2019.
- [117] A. J. Dear, G. Meisl, A. Šarić, T. C. T. Michaels, M. Kjaergaard, S. Linse, and T. P. J. Knowles, “Identification of on- and off-pathway oligomers in amyloid fibril formation,” *Chem. Sci.*, vol. 11, no. 24, pp. 6236–6247, 2020.
- [118] L. Yu, R. Edalji, J. E. Harlan, T. F. Holzman, A. P. Lopez, B. Labkovsky, H. Hillen, S. Barghorn, U. Ebert, P. L. Richardson, L. Miesbauer, L. Solomon, D. Bartley, K. Walter, R. W. Johnson, P. J. Hajduk, and E. T. Olejniczak, “Structural Characterization of a Soluble Amyloid β -Peptide Oligomer,” *Biochemistry*, vol. 48, no. 9, pp. 1870–1877, 2009.
- [119] C. Lendel, M. Bjerring, A. Dubnovitsky, R. T. Kelly, A. Filippov, O. N. Antzutkin, N. C. Nielsen, and T. Härd, “A Hexameric Peptide Barrel as Building Block of Amyloid- β Protofibrils,” *Angew. Chem. Int. Ed.*, vol. 53, no. 47, pp. 12 756–12 760, 2014.
- [120] S. Ciudad, E. Puig, T. Botzanowski, M. Meigooni, A. S. Arango, J. Do, M. Mayzel, M. Bayoumi, S. Chaignepain, G. Maglia, S. Cianferani, V. Orekhov, E. Tajkhorshid, B. Bardiaux, and N. Carulla, “A β (1-42) tetramer and octamer structures reveal edge conductivity pores as a mechanism for membrane damage,” *Nat. Commun.*, vol. 11, no. 1, p. 3014, 2020.
- [121] S. Barghorn, V. Nimmrich, A. Striebinger, C. Krantz, P. Keller, B. Janson, M. Bahr, M. Schmidt, R. S. Bitner, J. Harlan, E. Barlow, U. Ebert, and H. Hillen, “Globu-

- lar amyloid β -peptide1–42 oligomer – a homogenous and stable neuropathological protein in Alzheimer’s disease,” *J. Neurochem.*, vol. 95, no. 3, pp. 834–847, 2005.
- [122] V. Nimmrich, C. Grimm, A. Draguhn, S. Barghorn, A. Lehmann, H. Schoemaker, H. Hillen, G. Gross, U. Ebert, and C. Bruehl, “Amyloid β Oligomers (A β 1–42 Globulomer) Suppress Spontaneous Synaptic Activity by Inhibition of P/Q-Type Calcium Currents,” *J. Neurosci.*, vol. 28, no. 4, pp. 788–797, 2008.
 - [123] G. P. Gellermann, H. Byrnes, A. Striebinger, K. Ullrich, R. Mueller, H. Hillen, and S. Barghorn, “A β -globulomers are formed independently of the fibril pathway,” *Neurobiol. Dis.*, vol. 30, no. 2, pp. 212–220, 2008.
 - [124] S. Parthasarathy, M. Inoue, Y. Xiao, Y. Matsumura, Y.-i. Nabeshima, M. Hoshi, and Y. Ishii, “Structural Insight into an Alzheimer’s Brain-Derived Spherical Assembly of Amyloid β by Solid-State NMR,” *J. Am. Chem. Soc.*, vol. 137, no. 20, pp. 6480–6483, 2015.
 - [125] Y. Xiao, I. Matsuda, M. Inoue, T. Sasahara, M. Hoshi, and Y. Ishii, “NMR-based site-resolved profiling of β -amyloid misfolding reveals structural transitions from pathologically relevant spherical oligomer to fibril,” *J. Biol. Chem.*, vol. 295, no. 2, pp. 458–467, 2020.
 - [126] D. Shea, C.-C. Hsu, T. M. Bi, N. Paranjapye, M. C. Childers, J. Cochran, C. P. Tomberlin, L. Wang, D. Paris, J. Zonderman, G. Varani, C. D. Link, M. Mullan, and V. Daggett, “A-Sheet secondary structure in amyloid β -peptide drives aggregation and toxicity in Alzheimer’s disease,” *Proc. Natl. Acad. Sci. U.S.A.*, vol. 116, no. 18, pp. 8895–8900, 2019.
 - [127] L. Pauling and R. B. Corey, “Configurations of Polypeptide Chains With Favored Orientations Around Single Bonds: Two New Pleated Sheets,” *Proc. Natl. Acad. Sci. U.S.A.*, vol. 37, no. 11, pp. 729–740, 1951.
 - [128] Y. Liu and R. R. Allingham, “Major review: Molecular genetics of primary open-angle glaucoma,” *Exp. Eye Res.*, vol. 160, pp. 62–84, 2017.
 - [129] K. Zhang, L. Zhang, and R. N. Weinreb, “Ophthalmic drug discovery: Novel targets and mechanisms for retinal diseases and glaucoma,” *Nat. Rev. Drug Discov.*, vol. 11, no. 7, pp. 541–559, 2012.
 - [130] J. H. Fingert, E. Héon, J. M. Liebmann, T. Yamamoto, J. E. Craig, J. Rait, K. Kawase, S.-T. Hoh, Y. M. Buys, J. Dickinson, R. R. Hockey, D. Williams-Lyn, G. Trope, Y. Kitazawa, R. Ritch, D. A. Mackey, W. L. M. Alward, V. C. Sheffield, and E. M. Stoned, “Analysis of Myocilin Mutations in 1703 Glaucoma Patients From Five Different Populations,” *Hum. Mol. Genet.*, vol. 8, no. 5, pp. 899–905, 1999.

- [131] M. A. Aldred, L. Baumber, A. Hill, E. C. Schwalbe, K. Goh, W. Karwatowski, and R. C. Trembath, "Low prevalence of MYOC mutations in UK primary open-angle glaucoma patients limits the utility of genetic testing," *Hum. Genet.*, vol. 115, no. 5, pp. 428–431, 2004.
- [132] E. M. Stone, J. H. Fingert, W. L. M. Alward, T. D. Nguyen, J. R. Polansky, S. L. F. Sunden, D. Nishimura, A. F. Clark, A. Nystuen, B. E. Nichols, D. A. Mackey, R. Ritch, J. W. Kalenak, E. R. Craven, and V. C. Sheffield, "Identification of a Gene That Causes Primary Open Angle Glaucoma," *Science*, vol. 275, no. 5300, pp. 668–670, 1997.
- [133] M. K. Joe, S. Sohn, W. Hur, Y. Moon, Y. R. Choi, and C. Kee, "Accumulation of mutant myocilins in ER leads to ER stress and potential cytotoxicity in human trabecular meshwork cells," *Biochem. Biophys. Res. Commun.*, vol. 312, no. 3, pp. 592–600, 2003.
- [134] Y. Liu and D. Vollrath, "Reversal of mutant myocilin non-secretion and cell killing: Implications for glaucoma," *Hum. Mol. Genet.*, vol. 13, no. 11, pp. 1193–1204, 2004.
- [135] G. H.-F. Yam, K. Gaplovska-Kysela, C. Zuber, and J. Roth, "Aggregated myocilin induces russell bodies and causes apoptosis: Implications for the pathogenesis of myocilin-caused primary openangle glaucoma," *Am. J. Pathol.*, vol. 170, no. 1, pp. 100–109, 2007.
- [136] S. D. Orwig, C. W. Perry, L. Y. Kim, K. C. Turnage, R. Zhang, D. Vollrath, I. Schmidt-Krey, and R. L. Lieberman, "Amyloid fibril formation by the glaucoma-associated olfactomedin domain of myocilin," *J. Mol. Biol.*, vol. 421, no. 2-3, pp. 242–255, 2012.
- [137] S. E. Hill, R. K. Donegan, and R. L. Lieberman, "The glaucoma-associated olfactomedin domain of myocilin forms polymorphic fibrils that are constrained by partial unfolding and peptide sequence," *J. Mol. Biol.*, vol. 426, no. 4, pp. 921–935, 2014.
- [138] S. D. Orwig and R. L. Lieberman, "Biophysical Characterization of the Olfactomedin Domain of Myocilin, an Extracellular Matrix Protein Implicated in Inherited Forms of Glaucoma," *PLoS One*, vol. 6, no. 1, e16347, 2011.
- [139] R. K. Donegan, S. E. Hill, D. M. Freeman, E. Nguyen, S. D. Orwig, K. C. Turnage, and R. L. Lieberman, "Structural basis for misfolding in myocilin-associated glaucoma," *Hum. Mol. Genet.*, vol. 24, no. 8, pp. 2111–2124, 2015.

- [140] R. L. Lieberman and M. T. Ma, "Molecular Insights into Myocilin and Its Glaucoma-Causing Misfolded Olfactomedin Domain Variants," *Acc. Chem. Res.*, vol. 54, no. 9, pp. 2205–2215, 2021.
- [141] M. D. Martin, D. J. E. Huard, R. C. Guerrero-Ferreira, I. M. Desai, B. M. Barlow, and R. L. Lieberman, "Molecular architecture and modifications of full-length myocilin," *Exp. Eye Res.*, vol. 211, p. 108 729, 2021.
- [142] I. I. Rabi, J. R. Zacharias, S. Millman, and P. Kusch, "A New Method of Measuring Nuclear Magnetic Moment," *Phys. Rev.*, vol. 53, no. 4, pp. 318–318, 1938.
- [143] A. Filler, "The History, Development and Impact of Computed Imaging in Neurological Diagnosis and Neurosurgery: CT, MRI, and DTI," *Nat. Preced.*, pp. 1–1, 2009.
- [144] E. L. Hahn, "Spin Echoes," *Phys. Rev.*, vol. 80, no. 4, pp. 580–594, 1950.
- [145] B. A. Jung and M. Weigel, "Spin echo magnetic resonance imaging," *J. Magn. Reson. Imaging*, vol. 37, no. 4, pp. 805–817, 2013.
- [146] E. R. Andrew, A. Bradbury, and R. G. Eades, "Removal of Dipolar Broadening of Nuclear Magnetic Resonance Spectra of Solids by Specimen Rotation," *Nature*, vol. 183, no. 4678, p. 1802, 1959.
- [147] I. J. Lowe, "Free Induction Decays of Rotating Solids," *Phys. Rev. Lett.*, vol. 2, no. 7, pp. 285–287, 1959.
- [148] R. R. Ernst, "The Success Story of Fourier Transformation in NMR," in *eMagRes*, John Wiley & Sons, Ltd, 2007.
- [149] J. Jeener, B. H. Meier, P. Bachmann, and R. R. Ernst, "Investigation of exchange processes by two-dimensional NMR spectroscopy," *J. Chem. Phys.*, vol. 71, no. 11, pp. 4546–4553, 1979.
- [150] D. J. States, R. A. Haberkorn, and D. J. Ruben, "A two-dimensional nuclear overhauser experiment with pure absorption phase in four quadrants," *J. Magn. Reson.*, vol. 48, no. 2, pp. 286–292, 1982.
- [151] E. R. Johnston, M. J. Dellwo, and J. Hendrix, "Quantitative 2D exchange spectroscopy using time-proportional phase incrementation," *J. Magn. Reson.*, vol. 66, no. 3, pp. 399–409, 1986.
- [152] A. Pines, M. G. Gibby, and J. S. Waugh, "Proton-enhanced NMR of dilute spins in solids," *J. Chem. Phys.*, vol. 59, no. 2, pp. 569–590, 1973.

- [153] J. Schaefer and E. O. Stejskal, "Carbon-13 nuclear magnetic resonance of polymers spinning at the magic angle," *J. Am. Chem. Soc.*, vol. 98, no. 4, pp. 1031–1032, 1976.
- [154] T. Gullion and J. Schaefer, "Rotational-echo double-resonance NMR," *J. Magn. Reson.*, vol. 81, no. 1, pp. 196–200, 1989.
- [155] D. Raleigh, M. Levitt, and R. Griffin, "Rotational resonance in solid state NMR," *Chem. Phys. Lett.*, vol. 146, no. 1-2, pp. 71–76, 1988.
- [156] M. P. Williamson, T. F. Havel, and K. Wüthrich, "Solution conformation of proteinase inhibitor IIA from bull seminal plasma by ^1H nuclear magnetic resonance and distance geometry," *J. Mol. Biol.*, vol. 182, no. 2, pp. 295–315, 1985.
- [157] T. L. S. Benzinger, D. M. Gregory, T. S. Burkoth, H. Miller-Auer, D. G. Lynn, R. E. Botto, and S. C. Meredith, "Propagating structure of Alzheimer's β -amyloid(10–35) is parallel β -sheet with residues in exact register," *Proc. Natl. Acad. Sci. U.S.A.*, vol. 95, no. 23, pp. 13 407–13 412, 1998.
- [158] D. M. Gregory, T. L. S. Benzinger, T. S. Burkoth, H. Miller-Auer, D. G. Lynn, S. C. Meredith, and R. E. Botto, "Dipolar recoupling NMR of biomolecular self-assemblies: Determining inter- and intrastrand distances in fibrilized Alzheimer's β -amyloid peptide," *Solid State Nucl. Magn. Reson.*, vol. 13, no. 3, pp. 149–166, 1998.
- [159] C. Hilbich, B. Kisters-Woike, J. Reed, C. L. Masters, and K. Beyreuther, "Aggregation and secondary structure of synthetic amyloid βA4 peptides of Alzheimer's disease," *J. Mol. Biol.*, vol. 218, no. 1, pp. 149–163, 1991.
- [160] H. Fabian, D. Naumann, L. Otvos, C. Schultz, J. Backmann, G. I. Szendrei, U. Hahn, W. Saenger, and H. H. Mantsch, "Impact of point mutations and amino acid modifications on the structure and stability of peptides and proteins probed by FT-IR spectroscopy," *J. Mol. Struct.*, Molecular Spectroscopy and Molecular Structure 1994, vol. 348, pp. 5–8, 1995.
- [161] A. McDermott, T. Polenova, A. Bockmann, K. W. Zilm, E. K. Paulson, R. W. Martin, and G. T. Montelione, "Partial NMR assignments for uniformly (^{13}C , ^{15}N)-enriched BPTI in the solid state," *J. Biomol. NMR*, vol. 16, no. 3, pp. 209–219, 2000.
- [162] C. M. Rienstra, L. Tucker-Kellogg, C. P. Jaroniec, M. Hohwy, B. Reif, M. T. McMahon, B. Tidor, T. Lozano-Pérez, and R. G. Griffin, "De novo determination of peptide structure with solid-state magic-angle spinning NMR spectroscopy," *Proc. Natl. Acad. Sci. U.S.A.*, vol. 99, no. 16, pp. 10 260–10 265, 2002.

- [163] F. Castellani, B. van Rossum, A. Diehl, M. Schubert, K. Rehbein, and H. Oschkinat, "Structure of a protein determined by solid-state magic-angle-spinning NMR spectroscopy," *Nature*, vol. 420, no. 6911, pp. 99–102, 2002.
- [164] A. Lange, S. Becker, K. Seidel, K. Giller, O. Pongs, and M. Baldus, "A Concept for Rapid Protein-Structure Determination by Solid-State NMR Spectroscopy," *Angew. Chem. Int. Ed.*, vol. 44, no. 14, pp. 2089–2092, 2005.
- [165] S. G. Zech, A. J. Wand, and A. E. McDermott, "Protein Structure Determination by High-Resolution Solid-State NMR Spectroscopy: Application to Microcrystalline Ubiquitin," *J. Am. Chem. Soc.*, vol. 127, no. 24, pp. 8618–8626, 2005.
- [166] C. Schwieters, J. Kuszewski, and G. Mariusclore, "Using Xplor–NIH for NMR molecular structure determination," *Prog. Nucl. Magn. Reson. Spectrosc.*, vol. 48, no. 1, pp. 47–62, 2006.
- [167] A. T. Petkova, Y. Ishii, J. J. Balbach, O. N. Antzutkin, R. D. Leapman, F. Delaglio, and R. Tycko, "A structural model for Alzheimer's beta -amyloid fibrils based on experimental constraints from solid state NMR," *Proc. Natl. Acad. Sci. U.S.A.*, vol. 99, no. 26, pp. 16 742–16 747, 2002.
- [168] A. K. Paravastu, A. T. Petkova, and R. Tycko, "Polymorphic Fibril Formation by Residues 10–40 of the Alzheimer's β -Amyloid Peptide," *Biophys. J.*, vol. 90, no. 12, pp. 4618–4629, 2006.
- [169] R. Tycko, "Molecular structure of amyloid fibrils: Insights from solid-state NMR," *Q. Rev. Biophys.*, vol. 39, no. 1, pp. 1–55, 2006.
- [170] H. Van Melckebeke, C. Wasmer, A. Lange, E. AB, A. Loquet, A. Böckmann, and B. H. Meier, "Atomic-Resolution Three-Dimensional Structure of HET-s(218–289) Amyloid Fibrils by Solid-State NMR Spectroscopy," *J. Am. Chem. Soc.*, vol. 132, no. 39, pp. 13 765–13 775, 2010.
- [171] M. D. Tuttle, G. Comellas, A. J. Nieuwkoop, D. J. Covell, D. A. Berthold, K. D. Kloepper, J. M. Courtney, J. K. Kim, A. M. Barclay, A. Kendall, W. Wan, G. Stubbs, C. D. Schwieters, V. M. Y. Lee, J. M. George, and C. M. Rienstra, "Solid-state NMR structure of a pathogenic fibril of full-length human α -synuclein," *Nat. Struct. Mol. Biol.*, vol. 23, no. 5, pp. 409–415, 2016.
- [172] M. A. Wälti, F. Ravotti, H. Arai, C. G. Glabe, J. S. Wall, A. Böckmann, P. Güntert, B. H. Meier, and R. Riek, "Atomic-resolution structure of a disease-relevant A β (1–42) amyloid fibril," *Proc. Natl. Acad. Sci. U.S.A.*, vol. 113, no. 34, E4976–E4984, 2016.

- [173] A. W. P. Fitzpatrick, B. Falcon, S. He, A. G. Murzin, G. Murshudov, H. J. Garringer, R. A. Crowther, B. Ghetti, M. Goedert, and S. H. W. Scheres, “Cryo-EM structures of tau filaments from Alzheimer’s disease,” *Nature*, vol. 547, no. 7662, pp. 185–190, 2017.
- [174] A. W. Fitzpatrick and H. R. Saibil, “Cryo-EM of amyloid fibrils and cellular aggregates,” *Curr. Opin. Struct. Biol.*, Cryo Electron Microscopy • Biophysical and Computational Methods • Biophysical and Computational Methods - Part B, vol. 58, pp. 34–42, 2019.
- [175] C. Röder, T. Kupreichyk, L. Gremer, L. U. Schäfer, K. R. Pothula, R. B. G. Ravelli, D. Willbold, W. Hoyer, and G. F. Schröder, “Cryo-EM structure of islet amyloid polypeptide fibrils reveals similarities with amyloid- β fibrils,” *Nat. Struct. Mol. Biol.*, vol. 27, no. 7, pp. 660–667, 2020.
- [176] L. Gremer, D. Schölzel, C. Schenk, E. Reinartz, J. Labahn, R. B. G. Ravelli, M. Tusche, C. Lopez-Iglesias, W. Hoyer, H. Heise, D. Willbold, and G. F. Schröder, “Fibril structure of amyloid- β (1–42) by cryo-electron microscopy,” *Science*, vol. 358, no. 6359, pp. 116–119, 2017.
- [177] U. Ghosh, K. R. Thurber, W.-M. Yau, and R. Tycko, “Molecular structure of a prevalent amyloid- β fibril polymorph from Alzheimer’s disease brain tissue,” *Proc. Natl. Acad. Sci. U.S.A.*, vol. 118, no. 4, e2023089118, 2021.
- [178] A. Falsone and S. F. Falsone, “Legal but lethal: Functional protein aggregation at the verge of toxicity,” *Front. Cell. Neurosci.*, vol. 9, 2015.
- [179] W. Wang, S. Nema, and D. Teagarden, “Protein aggregation—Pathways and influencing factors,” *Int. J. Pharm.*, vol. 390, no. 2, pp. 89–99, 2010.
- [180] M. Batool, B. Ahmad, and S. Choi, “A Structure-Based Drug Discovery Paradigm,” *Int. J. Mol. Sci.*, vol. 20, no. 11, p. 2783, 2019.
- [181] M. I. F. J. Oerlemans, K. H. G. Rutten, M. C. Minnema, R. A. P. Raymakers, F. W. Asselbergs, and N. de Jonge, “Cardiac amyloidosis: The need for early diagnosis,” *Neth. Heart J.*, vol. 27, no. 11, pp. 525–536, 2019.
- [182] A. R. Cormier, X. Pang, M. I. Zimmerman, H.-X. Zhou, and A. K. Paravastu, “Molecular Structure of RADA16-I Designer Self-Assembling Peptide Nanofibers,” *ACS Nano*, vol. 7, no. 9, pp. 7562–7572, 2013.
- [183] M. T. Colvin, R. Silvers, B. Frohm, Y. Su, S. Linse, and R. G. Griffin, “High resolution structural characterization of A β 42 amyloid fibrils by Magic Angle Spinning NMR,” *J. Am. Chem. Soc.*, vol. 137, no. 23, pp. 7509–7518, 2015.

- [184] S. Jehle, B. van Rossum, J. R. Stout, S. M. Noguchi, K. Falber, K. Rehbein, H. Oschkinat, R. E. Klevit, and P. Rajagopal, “ α B-Crystallin: A Hybrid Solid-State/Solution-State NMR Investigation Reveals Structural Aspects of the Heterogeneous Oligomer,” *J. Mol. Biol.*, vol. 385, no. 5, pp. 1481–1497, 2009.
- [185] W. M. Tay, D. Huang, T. L. Rosenberry, and A. K. Paravastu, “The Alzheimer’s Amyloid- β (1–42) Peptide Forms Off-Pathway Oligomers and Fibrils That Are Distinguished Structurally by Intermolecular Organization,” *J. Mol. Biol.*, vol. 425, no. 14, pp. 2494–2508, 2013.
- [186] D. Huang, M. I. Zimmerman, P. K. Martin, A. Nix, T. L. Rosenberry, and A. K. Paravastu, “Antiparallel β -Sheet Structure within the C-Terminal Region of 42-Residue Alzheimer’s Amyloid- β Peptides When They Form 150-kDa Oligomers,” *J. Mol. Biol.*, vol. 427, no. 13, pp. 2319–2328, 2015.
- [187] T. Sugiki, N. Kobayashi, and T. Fujiwara, “Modern Technologies of Solution Nuclear Magnetic Resonance Spectroscopy for Three-dimensional Structure Determination of Proteins Open Avenues for Life Scientists,” *Comput. Struct. Biotechnol. J.*, vol. 15, pp. 328–339, 2017.
- [188] C. D. Schwieters, G. A. Bermejo, and G. M. Clore, “Xplor-NIH for molecular structure determination from NMR and other data sources,” *Protein Sci.*, vol. 27, no. 1, pp. 26–40, 2018.
- [189] R. W. Russell, M. P. Fritz, J. Kraus, C. M. Quinn, T. Polenova, and A. M. Gronenborn, “Accuracy and precision of protein structures determined by magic angle spinning NMR spectroscopy: For some ‘with a little help from a friend’,” *J. Biomol. NMR*, vol. 73, no. 6, pp. 333–346, 2019.
- [190] B. L. Bray, “Large-scale manufacture of peptide therapeutics by chemical synthesis,” *Nat. Rev. Drug Discov.*, vol. 2, no. 7, pp. 587–593, 2003.
- [191] M. Amblard, J.-A. Fehrentz, J. Martinez, and G. Subra, “Methods and protocols of modern solid phase Peptide synthesis,” *Mol. Biotechnol.*, vol. 33, no. 3, pp. 239–254, 2006.
- [192] I. Coin, M. Beyermann, and M. Bienert, “Solid-phase peptide synthesis: From standard procedures to the synthesis of difficult sequences,” *Nat. Protoc.*, vol. 2, no. 12, pp. 3247–3256, 2007.
- [193] J. K. Kasim, I. Kaviani, P. W. R. Harris, and M. A. Brimble, “Three Decades of Amyloid Beta Synthesis: Challenges and Advances,” *Front. Chem.*, vol. 7, 2019.

- [194] J. M. Collins, “Microwave-Enhanced Synthesis of Peptides, Proteins, and Peptidomimetics,” in *Microwaves in Organic Synthesis*, John Wiley & Sons, Ltd, 2013, pp. 897–959.
- [195] J. M. Collins, K. A. Porter, S. K. Singh, and G. S. Vanier, “High-Efficiency Solid Phase Peptide Synthesis (HE-SPPS),” *Org. Lett.*, vol. 16, no. 3, pp. 940–943, 2014.
- [196] C. Wasmer, A. Lange, H. V. Melckebeke, A. B. Siemer, R. Riek, and B. H. Meier, “Amyloid Fibrils of the HET-s(218–289) Prion Form a β Solenoid with a Triangular Hydrophobic Core,” *Science*, vol. 319, no. 5869, pp. 1523–1526, 2008.
- [197] A. T. Petkova, G. Buntkowsky, F. Dyda, R. D. Leapman, W. M. Yau, and R. Tycko, “Solid State NMR Reveals a pH-dependent Antiparallel β -Sheet Registry in Fibrils Formed by a β -Amyloid Peptide,” *J. Mol. Biol.*, vol. 335, no. 1, pp. 247–260, 2004.
- [198] A. K. Mehta, K. Lu, W. S. Childers, Y. Liang, S. N. Dublin, J. Dong, J. P. Snyder, S. V. Pingali, P. Thiyagarajan, and D. G. Lynn, “Facial Symmetry in Protein Self-Assembly,” *J. Am. Chem. Soc.*, vol. 130, no. 30, pp. 9829–9835, 2008.
- [199] A. Abelein, J. Jarvet, A. Barth, A. Gräslund, and J. Danielsson, “Ionic Strength Modulation of the Free Energy Landscape of A β 40 Peptide Fibril Formation,” *J. Am. Chem. Soc.*, vol. 138, no. 21, pp. 6893–6902, 2016.
- [200] K. P. Scherpelz, J.-X. Lu, R. Tycko, and S. C. Meredith, “Preparation of Amyloid Fibrils Seeded from Brain and Meninges,” in *Protein Amyloid Aggregation: Methods and Protocols*, ser. Methods in Molecular Biology, D. Eliezer, Ed., New York, NY: Springer, 2016, pp. 299–312.
- [201] B. S. Bhatnagar, R. H. Bogner, and M. J. Pikal, “Protein Stability During Freezing: Separation of Stresses and Mechanisms of Protein Stabilization,” *Pharm. Dev. Technol.*, vol. 12, no. 5, pp. 505–523, 2007.
- [202] A. Mandal, J. C. Boatz, T. B. Wheeler, and P. C. A. van der Wel, “On the use of ultracentrifugal devices for routine sample preparation in biomolecular magic-angle-spinning NMR,” *J. Biomol. NMR*, vol. 67, no. 3, pp. 165–178, 2017.
- [203] E. K. Roberts, K. M. Wong, E. J. Lee, M. M. Le, D. M. Patel, and A. K. Paravastu, “Post-assembly α -helix to β -sheet structural transformation within SAF-p1/p2a peptide nanofibers,” *Soft Matter*, vol. 14, no. 44, pp. 8986–8996, 2018.
- [204] M. Veshtort and R. G. Griffin, “SPINEVOLUTION: A powerful tool for the simulation of solid and liquid state NMR experiments,” *J. Magn. Reson.*, vol. 178, no. 2, pp. 248–282, 2006.

- [205] C. Bengs and M. H. Levitt, "SpinDynamica: Symbolic and numerical magnetic resonance in a Mathematica environment," *Magn. Reson. Chem.*, vol. 56, no. 6, pp. 374–414, 2018.
- [206] R. Tycko, "Symmetry-based constant-time homonuclear dipolar recoupling in solid state NMR," *J. Chem. Phys.*, vol. 126, no. 6, p. 064 506, 2007.
- [207] C. P. Jaroniec, B. A. Tounge, J. Herzfeld, and R. G. Griffin, "Frequency Selective Heteronuclear Dipolar Recoupling in Rotating Solids: Accurate ^{13}C – ^{15}N Distance Measurements in Uniformly ^{13}C , ^{15}N -labeled Peptides," *J. Am. Chem. Soc.*, vol. 123, no. 15, pp. 3507–3519, 2001.
- [208] Y. Ishii, " ^{13}C – ^{13}C dipolar recoupling under very fast magic angle spinning in solid-state nuclear magnetic resonance: Applications to distance measurements, spectral assignments, and high-throughput secondary-structure determination," *J. Chem. Phys.*, vol. 114, no. 19, pp. 8473–8483, 2001.
- [209] E. Crocker, A. B. Patel, M. Eilers, S. Jayaraman, E. Getmanova, P. J. Reeves, M. Ziliox, H. G. Khorana, M. Sheves, and S. O. Smith, "Dipolar assisted rotational resonance NMR of tryptophan and tyrosine in rhodopsin," *J. Biomol. NMR*, vol. 29, no. 1, pp. 11–20, 2004.
- [210] J. R. Lewandowski, G. De Paëpe, and R. G. Griffin, "Proton Assisted Insensitive Nuclei Cross Polarization," *J. Am. Chem. Soc.*, vol. 129, no. 4, pp. 728–729, 2007.
- [211] A. Lange, S. Luca, and M. Baldus, "Structural Constraints from Proton-Mediated Rare-Spin Correlation Spectroscopy in Rotating Solids," *J. Am. Chem. Soc.*, vol. 124, no. 33, pp. 9704–9705, 2002.
- [212] J. Pauli, M. Baldus, B. van Rossum, H. de Groot, and H. Oschkinat, "Backbone and Side-Chain ^{13}C and ^{15}N Signal Assignments of the α -Spectrin SH3 Domain by Magic Angle Spinning Solid-State NMR at 17.6 Tesla," *ChemBioChem*, vol. 2, no. 4, pp. 272–281, 2001.
- [213] D. Huang, B. C. Hudson, Y. Gao, E. K. Roberts, and A. K. Paravastu, "Solid-State NMR Structural Characterization of Self-Assembled Peptides with Selective ^{13}C and ^{15}N Isotopic Labels," in *Peptide Self-Assembly: Methods and Protocols*, ser. Methods in Molecular Biology, B. L. Nilsson and T. M. Doran, Eds., New York, NY: Springer, 2018, pp. 23–68.
- [214] A. E. Bennett, C. M. Rienstra, M. Auger, K. V. Lakshmi, and R. G. Griffin, "Heteronuclear decoupling in rotating solids," *J. Chem. Phys.*, vol. 103, no. 16, pp. 6951–6958, 1995.

- [215] C. S. Yannoni, "High-resolution NMR in solids: The CPMAS experiment," *Acc. Chem. Res.*, vol. 15, no. 7, pp. 201–208, 1982.
- [216] O. B. Peersen, X. L. Wu, and S. O. Smith, "Enhancement of CP-MAS Signals by Variable-Amplitude Cross Polarization. Compensation for Inhomogeneous B1 Fields," *J. Magn. Reson., Ser. A*, vol. 106, no. 1, pp. 127–131, 1994.
- [217] X. L. Wu and K. W. Zilm, "Cross Polarization with High-Speed Magic-Angle Spinning," *J. Magn. Reson., Ser. A*, vol. 104, no. 2, pp. 154–165, 1993.
- [218] J. Schaefer, T. A. Skokut, E. O. Stejskal, R. A. McKay, and J. E. Varner, "Asparagine amide metabolism in developing cotyledons of soybean," *Proc. Natl. Acad. Sci. U.S.A.*, vol. 78, no. 10, pp. 5978–5982, 1981.
- [219] G. Hou, F. Deng, S. Ding, R. Fu, J. Yang, and C. Ye, "Quantitative cross-polarization NMR spectroscopy in uniformly ^{13}C -labeled solids," *Chem. Phys. Lett.*, vol. 421, no. 4-6, pp. 356–360, 2006.
- [220] K. Takeda, Y. Noda, K. Takegoshi, O. Lafon, J. Trébosc, and J.-P. Amoureux, "Quantitative cross-polarization at magic-angle spinning frequency of about 20kHz," *J. Magn. Reson.*, vol. 214, pp. 340–345, 2012.
- [221] R. L. Johnson and K. Schmidt-Rohr, "Quantitative solid-state ^{13}C NMR with signal enhancement by multiple cross polarization," *J. Magn. Reson.*, vol. 239, pp. 44–49, 2014.
- [222] A. Gorkovskiy, K. R. Thurber, R. Tycko, and R. B. Wickner, "Locating folds of the in-register parallel β -sheet of the Sup35p prion domain infectious amyloid," *Proc. Natl. Acad. Sci. U.S.A.*, vol. 111, no. 43, E4615–E4622, 2014.
- [223] B. C. Hudson, A. Battigelli, M. D. Connolly, J. Edison, R. K. Spencer, S. Whitlam, R. N. Zuckermann, and A. K. Paravastu, "Evidence for cis Amide Bonds in Peptoid Nanosheets," *J. Phys. Chem. Lett.*, vol. 9, no. 10, pp. 2574–2578, 2018.
- [224] P. R. Costa, B. Sun, and R. G. Griffin, "Rotational resonance NMR: Separation of dipolar coupling and zero quantum relaxation," *J. Magn. Reson.*, vol. 164, no. 1, pp. 92–103, 2003.
- [225] R. Ramachandran, V. Ladizhansky, V. S. Bajaj, and R. G. Griffin, " ^{13}C – ^{13}C rotational resonance width distance measurements in uniformly ^{13}C -labeled peptides," *J. Am. Chem. Soc.*, vol. 125, no. 50, pp. 15 623–15 629, 2003.
- [226] M. H. Levitt, D. P. Raleigh, F. Creuzet, and R. G. Griffin, "Theory and simulations of homonuclear spin pair systems in rotating solids," *J. Chem. Phys.*, vol. 92, no. 11, pp. 6347–6364, 1990.

- [227] L. Petrakis, "Spectral line shapes: Gaussian and Lorentzian functions in magnetic resonance," *J. Chem. Educ.*, vol. 44, no. 8, p. 432, 1967.
- [228] D. S. Wishart, C. G. Bigam, A. Holm, R. S. Hodges, and B. D. Sykes, " ^1H , ^{13}C and ^{15}N random coil NMR chemical shifts of the common amino acids. I. Investigations of nearest-neighbor effects," *J. Biomol. NMR*, vol. 5, no. 1, pp. 67–81, 1995.
- [229] K. J. Fritzsche, Y. Yang, K. Schmidt-Rohr, and M. Hong, "Practical use of chemical shift databases for protein solid-state NMR: 2D chemical shift maps and amino-acid assignment with secondary-structure information," *J. Biomol. NMR*, vol. 56, no. 2, pp. 155–167, 2013.
- [230] Y. Shen, F. Delaglio, G. Cornilescu, and A. Bax, "TALOS+: A hybrid method for predicting protein backbone torsion angles from NMR chemical shifts," *J. Biomol. NMR*, vol. 44, no. 4, pp. 213–223, 2009.
- [231] Y. Shen and A. Bax, "Protein backbone and sidechain torsion angles predicted from NMR chemical shifts using artificial neural networks," *J. Biomol. NMR*, vol. 56, no. 3, pp. 227–241, 2013.
- [232] K. Takegoshi, S. Nakamura, and T. Terao, " ^{13}C - ^1H dipolar-assisted rotational resonance in magic-angle spinning NMR," *Chem. Phys. Lett.*, vol. 344, no. 5, pp. 631–637, 2001.
- [233] K. Takegoshi, S. Nakamura, and T. Terao, " ^{13}C - ^1H dipolar-driven ^{13}C - ^{13}C recoupling without ^{13}C rf irradiation in nuclear magnetic resonance of rotating solids," *J. Chem. Phys.*, vol. 118, no. 5, pp. 2325–2341, 2003.
- [234] L. M. Longo, Y. Gao, C. A. Tenorio, G. Wang, A. K. Paravastu, and M. Blaber, "The Folding Nucleus Structure Persists in Thermally-Aggregated FGF-1," *Protein Sci.*, vol. 27, no. 2, pp. 431–440, 2017.
- [235] A. Naito, K. Okushita, K. Nishimura, G. S. Boutis, A. Aoki, and T. Asakura, "Quantitative Analysis of Solid-State Homonuclear Correlation Spectra of Antiparallel β -Sheet Alanine Tetramers," *J. Phys. Chem. B*, vol. 122, no. 10, pp. 2715–2724, 2018.
- [236] A. Lange, K. Seidel, L. Verdier, S. Luca, and M. Baldus, "Analysis of Proton–Proton Transfer Dynamics in Rotating Solids and Their Use for 3D Structure Determination," *J. Am. Chem. Soc.*, vol. 125, no. 41, pp. 12 640–12 648, 2003.
- [237] R. Tycko and Y. Ishii, "Constraints on Supramolecular Structure in Amyloid Fibrils from Two-Dimensional Solid-State NMR Spectroscopy with Uniform Isotopic Labeling," *J. Am. Chem. Soc.*, vol. 125, no. 22, pp. 6606–6607, 2003.

- [238] W. Humphrey, A. Dalke, and K. Schulten, “VMD: Visual molecular dynamics,” *J. Mol. Graphics*, vol. 14, no. 1, pp. 33–38, 27–28, 1996.
- [239] L. Kalé, R. Skeel, M. Bhandarkar, R. Brunner, A. Gursoy, N. Krawetz, J. Phillips, A. Shinozaki, K. Varadarajan, and K. Schulten, “NAMD2: Greater Scalability for Parallel Molecular Dynamics,” *J. Comput. Phys.*, vol. 151, no. 1, pp. 283–312, 1999.
- [240] J. C. Phillips, R. Braun, W. Wang, J. Gumbart, E. Tajkhorshid, E. Villa, C. Chipot, R. D. Skeel, L. Kalé, and K. Schulten, “Scalable molecular dynamics with NAMD,” *J. Comput. Chem.*, vol. 26, no. 16, pp. 1781–1802, 2005.
- [241] F. Salemme, “Structural properties of protein β -sheets,” *Prog. Biophys. Mol. Biol.*, vol. 42, pp. 95–133, 1983.
- [242] Z. Bikadi, L. Demko, and E. Hazai, “Functional and structural characterization of a protein based on analysis of its hydrogen bonding network by hydrogen bonding plot,” *Arch. Biochem. Biophys.*, vol. 461, no. 2, pp. 225–234, 2007.
- [243] M. J. Pietal, J. M. Bujnicki, and L. P. Kozlowski, “GDFuzz3D: A method for protein 3D structure reconstruction from contact maps, based on a non-Euclidean distance function,” *Bioinformatics*, vol. 31, no. 21, pp. 3499–3505, 2015.
- [244] H.-M. Wang and C. Yu, “Investigating the refolding pathway of human acidic fibroblast growth factor (hFGF-1) from the residual structure(s) Obtained by denatured-state hydrogen/deuterium exchange,” *Biophys. J.*, vol. 100, no. 1, pp. 154–164, 2011.
- [245] L. Longo, J. Lee, and M. Blaber, “Experimental support for the foldability–function tradeoff hypothesis: Segregation of the folding nucleus and functional regions in fibroblast growth factor-1,” *Protein Sci.*, vol. 21, no. 12, pp. 1911–1920, 2012.
- [246] L. Longo, O. Kumru, C. R. Middaugh, and M. Blaber, “Evolution and design of protein structure by folding nucleus symmetric expansion,” *Structure*, vol. 22, no. 10, pp. 1377–1384, 2014.
- [247] P. Malhotra and J. B. Udgaonkar, “How cooperative are protein folding and unfolding transitions?” *Protein Sci.*, vol. 25, no. 11, pp. 1924–1941, 2016.
- [248] S. Abeln and D. Frenkel, “Disordered Flanks Prevent Peptide Aggregation,” *PLoS Comput. Biol.*, vol. 4, no. 12, e1000241, 2008.
- [249] F. Bemporad, A. De Simone, F. Chiti, and C. Dobson, “Characterizing Intermolecular Interactions That Initiate Native-Like Protein Aggregation,” *Biophys. J.*, vol. 102, no. 11, pp. 2595–2604, 2012.

- [250] G. Schreiber, A. M. Buckle, and A. R. Fersht, "Stability and function: Two constraints in the evolution of barstar and other proteins," *Structure*, vol. 2, no. 10, pp. 945–951, 1994.
- [251] B. K. Shoichet, W. A. Baase, R. Kuroki, and B. W. Matthews, "A relationship between protein stability and protein function.," *Proc. Natl. Acad. Sci. U.S.A.*, vol. 92, no. 2, pp. 452–456, 1995.
- [252] S. Gosavi, P. C. Whitford, P. A. Jennings, and J. N. Onuchic, "Extracting function from a β -trefoil folding motif," *Proc. Natl. Acad. Sci. U.S.A.*, vol. 105, no. 30, pp. 10 384–10 389, 2008.
- [253] A. G. Murzin, A. M. Lesk, and C. Chothia, "B-Trefoil fold: Patterns of structure and sequence in the Kunitz inhibitors interleukins-1 β and 1 α and fibroblast growth factors," *J. Mol. Biol.*, vol. 223, no. 2, pp. 531–543, 1992.
- [254] M. Blaber, J. DiSalvo, and K. A. Thomas, "X-ray Crystal Structure of Human Acidic Fibroblast Growth Factor," *Biochemistry*, vol. 35, no. 7, pp. 2086–2094, 1996.
- [255] S. I. Blaber, J. F. Culajay, A. Khurana, and M. Blaber, "Reversible Thermal Denaturation of Human FGF-1 Induced by Low Concentrations of Guanidine Hydrochloride," *Biophys. J.*, vol. 77, no. 1, pp. 470–477, 1999.
- [256] A. R. Fersht and S. Sato, " Φ -Value analysis and the nature of protein-folding transition states," *Proc. Natl. Acad. Sci. U.S.A.*, vol. 101, no. 21, pp. 7976–7981, 2004.
- [257] L. Pellegrini, D. F. Burke, F. von Delft, B. Mulloy, and T. L. Blundell, "Crystal structure of fibroblast growth factor receptor ectodomain bound to ligand and heparin," *Nature*, vol. 407, no. 6807, pp. 1029–1034, 2000.
- [258] J. Schlessinger, A. N. Plotnikov, O. A. Ibrahimi, A. V. Eliseenkova, B. K. Yeh, A. Yayon, R. J. Linhardt, and M. Mohammadi, "Crystal Structure of a Ternary FGF-FGFR-Heparin Complex Reveals a Dual Role for Heparin in FGFR Binding and Dimerization," *Mol. Cell*, vol. 6, no. 3, pp. 743–750, 2000.
- [259] S. van der Walt, S. C. Colbert, and G. Varoquaux, "The NumPy Array: A Structure for Efficient Numerical Computation," *Comput. Sci. Eng.*, vol. 13, no. 2, pp. 22–30, 2011.
- [260] B. G. Sasha, K. D. John, and B. Michael, "An Efficient, Flexible-Model Program For The Analysis Of Differential Scanning Calorimetry Protein Denaturation Data," *Protein Pept. Lett.*, vol. 8, no. 6, pp. 429–436, 2001.

- [261] D. Huster, “Solid-State NMR Investigations of the Hydration and Molecular Dynamics of Collagen in Biological Tissue,” in *Modern Magnetic Resonance*, G. A. Webb, Ed., Cham: Springer International Publishing, 2017, pp. 1–18.
- [262] K. H. Lim, A. K. R. Dasari, I. Hung, Z. Gan, J. W. Kelly, P. E. Wright, and D. E. Wemmer, “Solid-State NMR Studies Reveal Native-like β -Sheet Structures in Trans-thyretin Amyloid,” *Biochemistry*, vol. 55, no. 37, pp. 5272–5278, 2016.
- [263] J. R. Lepock, K. P. Ritchie, M. C. Kolios, A. M. Rodahl, K. A. Heinz, and J. Kruuv, “Influence of transition rates and scan rate on kinetic simulations of differential scanning calorimetry profiles of reversible and irreversible protein denaturation,” *Biochemistry*, vol. 31, no. 50, pp. 12 706–12 712, 1992.
- [264] A. L. Fink, “Protein aggregation: Folding aggregates, inclusion bodies and amyloid,” *Fold. Des.*, vol. 3, no. 1, R9–R23, 1998.
- [265] J. Lee and M. Blaber, “Increased Functional Half-life of Fibroblast Growth Factor-1 by Recovering a Vestigial Disulfide Bond,” *J. Prot. Proteom.*, vol. 1, pp. 37–42, 2010.
- [266] J. C. Stroud, C. Liu, P. K. Teng, and D. Eisenberg, “Toxic fibrillar oligomers of amyloid- β have cross- β structure,” *Proc. Natl. Acad. Sci. U.S.A.*, vol. 109, no. 20, pp. 7717–7722, 2012.
- [267] Y. Li, C. Zhao, F. Luo, Z. Liu, X. Gui, Z. Luo, X. Zhang, D. Li, C. Liu, and X. Li, “Amyloid fibril structure of α -synuclein determined by cryo-electron microscopy,” *Cell Res.*, vol. 28, no. 9, pp. 897–903, 2018.
- [268] J. Loeb, “The colloidal behavior of proteins,” *J. Gen. Physiol.*, vol. 3, no. 4, pp. 557–564, 1921.
- [269] M. S. Lawrence, K. J. Phillips, and D. R. Liu, “Supercharging Proteins Can Impart Unusual Resilience,” *J. Am. Chem. Soc.*, vol. 129, no. 33, pp. 10 110–10 112, 2007.
- [270] B. Mészáros, G. Erdős, and Z. Dosztányi, “IUPred2A: Context-dependent prediction of protein disorder as a function of redox state and protein binding,” *Nucleic Acids Res.*, vol. 46, no. W1, W329–W337, 2018.
- [271] E. Y. Chi, S. Krishnan, T. W. Randolph, and J. F. Carpenter, “Physical stability of proteins in aqueous solution: Mechanism and driving forces in nonnative protein aggregation,” *Pharm. Res.*, vol. 20, no. 9, pp. 1325–1336, 2003.
- [272] M. A. Alsenaidy, T. Wang, J. H. Kim, S. B. Joshi, J. Lee, M. Blaber, D. B. Volkin, and C. R. Middaugh, “An empirical phase diagram approach to investigate con-

- formational stability of “second-generation” functional mutants of acidic fibroblast growth factor-1,” *Protein Sci.*, vol. 21, no. 3, pp. 418–432, 2012.
- [273] S. J. Saupe and A. Daskalov, “The [Het-s] Prion, an Amyloid Fold as a Cell Death Activation Trigger,” *PLoS Pathog.*, vol. 8, no. 5, e1002687, 2012.
- [274] H. Innan and F. Kondrashov, “The evolution of gene duplications: Classifying and distinguishing between models,” *Nat. Rev. Genet.*, vol. 11, no. 2, pp. 97–108, 2010.
- [275] Y. Gao, C. Guo, J. O. Watzlawik, P. S. Randolph, E. J. Lee, D. Huang, S. M. Stagg, H.-X. Zhou, T. L. Rosenberry, and A. K. Paravastu, “Out-of-register parallel β -sheets and antiparallel β -sheets coexist in 150-kDa oligomers formed by amyloid- β (1–42),” *J. Mol. Biol.*, vol. 432, no. 16, pp. 4388–4407, 2020.
- [276] D. M. Walsh and D. J. Selkoe, “Deciphering the Molecular Basis of Memory Failure in Alzheimer’s Disease,” *Neuron*, vol. 44, no. 1, pp. 181–193, 2004.
- [277] J. L. Tomic, A. Pensalfini, E. Head, and C. G. Glabe, “Soluble fibrillar oligomer levels are elevated in Alzheimer’s disease brain and correlate with cognitive dysfunction,” *Neurobiol. Dis.*, vol. 35, no. 3, pp. 352–358, 2009.
- [278] M. L. Cohen, C. Kim, T. Haldiman, M. ElHag, P. Mehndiratta, T. Pichet, F. Lissimore, M. Shea, Y. Cohen, W. Chen, J. Blevins, B. S. Appleby, K. Surewicz, W. K. Surewicz, M. Sajatovic, C. Tatsuoka, S. Zhang, P. Mayo, M. Butkiewicz, J. L. Haines, A. J. Lerner, and J. G. Safar, “Rapidly progressive Alzheimer’s disease features distinct structures of amyloid- β ,” *Brain*, vol. 138, no. 4, pp. 1009–1022, 2015.
- [279] S. Epelbaum, I. Youssef, P. N. Lacor, P. Chaurand, E. Duplus, B. Brugg, C. Duyckaerts, and B. Delatour, “Acute amnesic encephalopathy in amyloid- β oligomer-injected mice is due to their widespread diffusion in vivo,” *Neurobiol. Aging*, vol. 36, no. 6, pp. 2043–2052, 2015.
- [280] T. Kawarabayashi, M. Shoji, L. H. Younkin, L. Wen-Lang, D. W. Dickson, T. Murakami, E. Matsubara, K. Abe, K. H. Ashe, and S. G. Younkin, “Dimeric Amyloid β Protein Rapidly Accumulates in Lipid Rafts followed by Apolipoprotein E and Phosphorylated Tau Accumulation in the Tg2576 Mouse Model of Alzheimer’s Disease,” *J. Neurosci.*, vol. 24, no. 15, pp. 3801–3809, 2004.
- [281] E. Y. Chi, S. L. Frey, A. Winans, K. L. H. Lam, K. Kjaer, J. Majewski, and K. Y. C. Lee, “Amyloid- β Fibrillogenesis Seeded by Interface-Induced Peptide Misfolding and Self-Assembly,” *Biophys. J.*, vol. 98, no. 10, pp. 2299–2308, 2010.

- [282] R. Aleksis, F. Oleskovs, K. Jaudzems, J. Pahnke, and H. Biverstål, “Structural studies of amyloid- β peptides: Unlocking the mechanism of aggregation and the associated toxicity,” *Biochimie*, vol. 140, pp. 176–192, 2017.
- [283] J. Adamcik and R. Mezzenga, “Amyloid Polymorphism in the Protein Folding and Aggregation Energy Landscape,” *Angew. Chem. Int. Ed.*, vol. 57, no. 28, pp. 8370–8382, 2018.
- [284] W. Qiang, W.-M. Yau, Y. Luo, M. P. Mattson, and R. Tycko, “Antiparallel β -sheet architecture in Iowa-mutant β -amyloid fibrils,” *Proc. Natl. Acad. Sci. U.S.A.*, vol. 109, no. 12, pp. 4443–4448, 2012.
- [285] V. Rangachari, B. D. Moore, D. K. Reed, L. K. Sonoda, A. W. Bridges, E. Conboy, D. Hartigan, and T. L. Rosenberry, “Amyloid- β (1–42) Rapidly Forms Protofibrils and Oligomers by Distinct Pathways in Low Concentrations of Sodium Dodecylsulfate,” *Biochemistry*, vol. 46, no. 43, pp. 12 451–12 462, 2007.
- [286] B. D. Moore, V. Rangachari, W. M. Tay, N. M. Milkovic, and T. L. Rosenberry, “Biophysical Analyses of Synthetic Amyloid- β (1–42) Aggregates before and after Covalent Cross-Linking. Implications for Deducing the Structure of Endogenous Amyloid- β Oligomers,” *Biochemistry*, vol. 48, no. 49, pp. 11 796–11 806, 2009.
- [287] M. Serra-Batiste, M. Ninot-Pedrosa, M. Bayoumi, M. Gairí, G. Maglia, and N. Carulla, “A β 42 assembles into specific β -barrel pore-forming oligomers in membrane-mimicking environments,” *Proc. Natl. Acad. Sci. U.S.A.*, vol. 113, no. 39, pp. 10 866–10 871, 2016.
- [288] J. Yang, A. J. Dear, T. C. T. Michaels, C. M. Dobson, T. P. J. Knowles, S. Wu, and S. Perrett, “Direct Observation of Oligomerization by Single Molecule Fluorescence Reveals a Multistep Aggregation Mechanism for the Yeast Prion Protein Ure2,” *J. Am. Chem. Soc.*, vol. 140, no. 7, pp. 2493–2503, 2018.
- [289] M. Bak and N. C. Nielsen, “REPULSION, A Novel Approach to Efficient Powder Averaging in Solid-State NMR,” *J. Magn. Reson.*, vol. 125, no. 1, pp. 132–139, 1997.
- [290] A. Punjani, J. L. Rubinstein, D. J. Fleet, and M. A. Brubaker, “cryoSPARC: Algorithms for rapid unsupervised cryo-EM structure determination,” *Nat. Methods*, vol. 14, no. 3, pp. 290–296, 2017.
- [291] R. Verel, I. T. Tomka, C. Bertozzi, R. Cadalbert, R. A. Kammerer, M. O. Steinmetz, and B. H. Meier, “Polymorphism in an Amyloid-Like Fibril-Forming Model Peptide,” *Angew. Chem. Int. Ed.*, vol. 47, no. 31, pp. 5842–5845, 2008.

- [292] E. Cerf, R. Sarroukh, S. Tamamizu-Kato, L. Breydo, S. Derclaye, Y. F. Dufrêne, V. Narayanaswami, E. Goormaghtigh, J.-M. Ruysschaert, and V. Raussens, “Antiparallel β -sheet: A signature structure of the oligomeric amyloid β -peptide,” *Biochem. J.*, vol. 421, no. 3, pp. 415–423, 2009.
- [293] C. Liu, M. Zhao, L. Jiang, P.-N. Cheng, J. Park, M. R. Sawaya, A. Pensalfini, D. Gou, A. J. Berk, C. G. Glabe, J. Nowick, and D. Eisenberg, “Out-of-register β -sheets suggest a pathway to toxic amyloid aggregates,” *Proc. Natl. Acad. Sci. U.S.A.*, vol. 109, no. 51, pp. 20 913–20 918, 2012.
- [294] H. A. Lashuel, D. Hartley, B. M. Petre, T. Walz, and P. T. Lansbury Jr, “Neurodegenerative disease: Amyloid pores from pathogenic mutations,” *Nature*, vol. 418, no. 6895, p. 291, 2002.
- [295] H. Jang, F. T. Arce, S. Ramachandran, B. L. Kagan, R. Lal, and R. Nussinov, “Disordered amyloidogenic peptides may insert into the membrane and assemble into common cyclic structural motifs,” *Chem. Soc. Rev.*, vol. 43, no. 19, pp. 6750–6764, 2014.
- [296] N. Arispe, E. Rojas, and H. B. Pollard, “Alzheimer disease amyloid beta protein forms calcium channels in bilayer membranes: Blockade by tromethamine and aluminum,” *Proc. Natl. Acad. Sci. U.S.A.*, vol. 90, no. 2, pp. 567–571, 1993.
- [297] C. F. Wright, S. A. Teichmann, J. Clarke, and C. M. Dobson, “The importance of sequence diversity in the aggregation and evolution of proteins,” *Nature*, vol. 438, no. 7069, pp. 878–881, 2005.
- [298] T. Doi, Y. Masuda, K. Irie, K.-i. Akagi, Y. Monobe, T. Imazawa, and K. Takegoshi, “Solid-state NMR analysis of the β -strand orientation of the protofibrils of amyloid β -protein,” *Biochem. Biophys. Res. Commun.*, vol. 428, no. 4, pp. 458–462, 2012.
- [299] A. Sandberg, L. M. Luheshi, S. Söllvander, T. P. de Barros, B. Macao, T. P. J. Knowles, H. Biverstål, C. Lendel, F. Ekholm-Petterson, A. Dubnovitsky, L. Lannfelt, C. M. Dobson, and T. Härd, “Stabilization of neurotoxic Alzheimer amyloid- β oligomers by protein engineering,” *Proc. Natl. Acad. Sci. U.S.A.*, vol. 107, no. 35, pp. 15 595–15 600, 2010.
- [300] A. Dubnovitsky, A. Sandberg, M. M. Rahman, I. Benilova, C. Lendel, and T. Härd, “Amyloid- β Protofibrils: Size, Morphology and Synaptotoxicity of an Engineered Mimic,” *PLoS One*, vol. 8, no. 7, e66101, 2013.
- [301] S. R. Collins, A. Douglass, R. D. Vale, and J. S. Weissman, “Mechanism of Prion Propagation: Amyloid Growth Occurs by Monomer Addition,” *PLoS Biol.*, vol. 2, no. 10, David Eisenberg, Ed., e321, 2004.

- [302] Y. Gao, E. G. Saccuzzo, S. E. Hill, D. J. E. Huard, A. S. Robang, R. L. Lieberman, and A. K. Paravastu, "Structural Arrangement within a Peptide Fibril Derived from the Glaucoma-Associated Myocilin Olfactomedin Domain," *J. Phys. Chem. B*, vol. 125, no. 11, pp. 2886–2897, 2021.
- [303] Z. Zhou and D. Vollrath, "A cellular assay distinguishes normal and mutant TIGR/myocilin protein," *Hum. Mol. Genet.*, vol. 8, no. 12, pp. 2221–2228, 1999.
- [304] S. Gobeil, M.-A. Rodrigue, S. Moisan, T. D. Nguyen, J. R. Polansky, J. Morissette, and V. Raymond, "Intracellular Sequestration of Hetero-oligomers Formed by Wild-Type and Glaucoma-Causing Myocilin Mutants," *Invest. Ophthalmol. Visual Sci.*, vol. 45, no. 10, pp. 3560–3567, 2004.
- [305] S. Gobeil, L. Letartre, and V. Raymond, "Functional analysis of the glaucoma-causing TIGR/myocilin protein: Integrity of amino-terminal coiled-coil regions and olfactomedin homology domain is essential for extracellular adhesion and secretion," *Exp. Eye Res.*, Special Issue in Honour of Jon R. Polansky, vol. 82, no. 6, pp. 1017–1029, 2006.
- [306] D. Vollrath and Y. Liu, "Temperature sensitive secretion of mutant myocilins," *Exp. Eye Res.*, Special Issue in Honour of Jon R. Polansky, vol. 82, no. 6, pp. 1030–1036, 2006.
- [307] M. Oliveberg, "Waltz, an exciting new move in amyloid prediction," *Nat. Methods*, vol. 7, no. 3, pp. 187–188, 2010.
- [308] I. Walsh, F. Seno, S. C. E. Tosatto, and A. Trovato, "PASTA 2.0: An improved server for protein aggregation prediction," *Nucleic Acids Res.*, vol. 42, no. W1, W301–W307, 2014.
- [309] A. C. Tsolis, N. C. Papandreou, V. A. Iconomidou, and S. J. Hamodrakas, "A consensus method for the prediction of 'aggregation-prone' peptides in globular proteins," *PLoS One*, vol. 8, no. 1, e54175, 2013.
- [310] A.-M. Fernandez-Escamilla, F. Rousseau, J. Schymkowitz, and L. Serrano, "Prediction of sequence-dependent and mutational effects on the aggregation of peptides and proteins," *Nat. Biotechnol.*, vol. 22, no. 10, pp. 1302–1306, 2004.
- [311] B. J. Alder and T. E. Wainwright, "Studies in Molecular Dynamics. I. General Method," *J. Chem. Phys.*, vol. 31, no. 2, pp. 459–466, 1959.
- [312] H. D. Nguyen and C. K. Hall, "Molecular dynamics simulations of spontaneous fibril formation by random-coil peptides," *Proc. Natl. Acad. Sci. U.S.A.*, vol. 101, no. 46, pp. 16 180–16 185, 2004.

- [313] M. Cheon, I. Chang, and C. K. Hall, "Extending the PRIME model for protein aggregation to all 20 amino acids," *Proteins: Struct., Funct., Bioinf.*, vol. 78, no. 14, pp. 2950–2960, 2010.
- [314] Y. Wang, Y. Gao, S. E. Hill, D. J. E. Huard, M. O. Tomlin, R. L. Lieberman, A. K. Paravastu, and C. K. Hall, "Simulations and Experiments Delineate Amyloid Fibrilization by Peptides Derived from Glaucoma-Associated Myocilin," *J. Phys. Chem. B*, vol. 122, no. 22, pp. 5845–5850, 2018.
- [315] J. J. Balbach, Y. Ishii, O. N. Antzutkin, R. D. Leapman, N. W. Rizzo, F. Dyda, J. Reed, and R. Tycko, "Amyloid Fibril Formation by A β 16-22, a Seven-Residue Fragment of the Alzheimer's β -Amyloid Peptide, and Structural Characterization by Solid State NMR," *Biochemistry*, vol. 39, no. 45, pp. 13 748–13 759, 2000.
- [316] K. Iwata, T. Fujiwara, Y. Matsuki, H. Akutsu, S. Takahashi, H. Naiki, and Y. Goto, "3D structure of amyloid protofilaments of β 2-microglobulin fragment probed by solid-state NMR," *Proc. Natl. Acad. Sci. U.S.A.*, vol. 103, no. 48, pp. 18 119–18 124, 2006.
- [317] C. P. Jaroniec, C. E. MacPhee, N. S. Astrof, C. M. Dobson, and R. G. Griffin, "Molecular conformation of a peptide fragment of transthyretin in an amyloid fibril," *Proc. Natl. Acad. Sci. U.S.A.*, vol. 99, no. 26, pp. 16 748–16 753, 2002.
- [318] C. P. Jaroniec, C. E. MacPhee, V. S. Bajaj, M. T. McMahon, C. M. Dobson, and R. G. Griffin, "High-resolution molecular structure of a peptide in an amyloid fibril determined by magic angle spinning NMR spectroscopy," *Proc. Natl. Acad. Sci. U.S.A.*, vol. 101, no. 3, pp. 711–716, 2004.
- [319] K. Nagy-Smith, E. Moore, J. Schneider, and R. Tycko, "Molecular structure of monomorphic peptide fibrils within a kinetically trapped hydrogel network," *Proc. Natl. Acad. Sci. U.S.A.*, vol. 112, no. 32, pp. 9816–9821, 2015.
- [320] S. Leonard, A. Cormier, X. Pang, M. Zimmerman, H.-X. Zhou, and A. Paravastu, "Solid-State NMR Evidence for β -Hairpin Structure within MAX8 Designer Peptide Nanofibers," *Biophys. J.*, vol. 105, no. 1, pp. 222–230, 2013.
- [321] B. L. Sibanda, T. L. Blundell, and J. M. Thornton, "Conformation of β -hairpins in protein structures: A systematic classification with applications to modelling by homology, electron density fitting and protein engineering," *J. Mol. Biol.*, vol. 206, no. 4, pp. 759–777, 1989.
- [322] M. Tang, A. J. Waring, and M. Hong, "Intermolecular Packing and Alignment in an Ordered β -Hairpin Antimicrobial Peptide Aggregate from 2D Solid-State NMR," *J. Am. Chem. Soc.*, vol. 127, no. 40, pp. 13 919–13 927, 2005.

- [323] A. T. Petkova, R. D. Leapman, Z. Guo, W.-M. Yau, M. P. Mattson, and R. Tycko, "Self-Propagating, Molecular-Level Polymorphism in Alzheimer's β -Amyloid Fibrils," *Science*, vol. 307, no. 5707, pp. 262–265, 2005.
- [324] P. C. A. van der Wel, J. R. Lewandowski, and R. G. Griffin, "Solid-State NMR Study of Amyloid Nanocrystals and Fibrils Formed by the Peptide GNNQQNY from Yeast Prion Protein Sup35p," *J. Am. Chem. Soc.*, vol. 129, no. 16, pp. 5117–5130, 2007.
- [325] P. C. A. van der Wel, J. R. Lewandowski, and R. G. Griffin, "Structural Characterization of GNNQQNY Amyloid Fibrils by Magic Angle Spinning NMR," *Biochemistry*, vol. 49, no. 44, pp. 9457–9469, 2010.
- [326] R. Tycko, K. L. Sciarretta, J. P. R. O. Orgel, and S. C. Meredith, "Evidence for novel β -Sheet structures in Iowa mutant β -Amyloid fibrils," *Biochemistry*, vol. 48, no. 26, pp. 6072–6084, 2009.
- [327] R. Liu, W. A. Baase, and B. W. Matthews, "The introduction of strain and its effects on the structure and stability of T4 lysozyme," *J. Mol. Biol.*, vol. 295, no. 1, pp. 127–145, 2000.
- [328] K. K. Frousios, V. A. Iconomidou, C.-M. Karletidi, and S. J. Hamodrakas, "Amyloidogenic determinants are usually not buried," *BMC Struct. Biol.*, vol. 9, no. 1, p. 44, 2009.
- [329] M. R. Sawaya, S. Sambashivan, R. Nelson, M. I. Ivanova, S. A. Sievers, M. I. Apostol, M. J. Thompson, M. Balbirnie, J. J. W. Wiltzius, H. T. McFarlane, A. Ø. Madsen, C. Riekel, and D. Eisenberg, "Atomic structures of amyloid cross- β spines reveal varied steric zippers," *Nature*, vol. 447, no. 7143, pp. 453–457, 2007.
- [330] M. Fändrich, S. Nyström, K. P. R. Nilsson, A. Böckmann, H. LeVine, and P. Hammarström, "Amyloid fibril polymorphism: A challenge for molecular imaging and therapy," *J. Intern. Med.*, vol. 283, no. 3, pp. 218–237, 2018.
- [331] A. W. P. Fitzpatrick, G. T. Debelouchina, M. J. Bayro, D. K. Clare, M. A. Caporini, V. S. Bajaj, C. P. Jaroniec, L. Wang, V. Ladizhansky, S. A. Müller, C. E. MacPhee, C. A. Waudby, H. R. Mott, A. De Simone, T. P. J. Knowles, H. R. Saibil, M. Vendruscolo, E. V. Orlova, R. G. Griffin, and C. M. Dobson, "Atomic structure and hierarchical assembly of a cross- β amyloid fibril," *Proc. Natl. Acad. Sci. U.S.A.*, vol. 110, no. 14, pp. 5468–5473, 2013.
- [332] W. Qiang, W.-M. Yau, and R. Tycko, "Structural Evolution of Iowa Mutant β -Amyloid Fibrils from Polymorphic to Homogeneous States under Repeated Seeded Growth," *J. Am. Chem. Soc.*, vol. 133, no. 11, pp. 4018–4029, 2011.

- [333] J. J. W. Wiltzius, S. A. Sievers, M. R. Sawaya, D. Cascio, D. Popov, C. Riek, and D. Eisenberg, "Atomic structure of the cross- β spine of islet amyloid polypeptide (amylin)," *Protein Sci.*, vol. 17, no. 9, pp. 1467–1474, 2008.
- [334] C. Wasmer, A. Schütz, A. Loquet, C. Buhtz, J. Greenwald, R. Riek, A. Böckmann, and B. H. Meier, "The Molecular Organization of the Fungal Prion HET-s in Its Amyloid Form," *J. Mol. Biol.*, vol. 394, no. 1, pp. 119–127, 2009.
- [335] M. G. Iadanza, M. P. Jackson, E. W. Hewitt, N. A. Ranson, and S. E. Radford, "A new era for understanding amyloid structures and disease," *Nat. Rev. Mol. Cell Biol.*, vol. 19, no. 12, pp. 755–773, 2018.
- [336] A. V. Kajava, U. Baxa, R. B. Wickner, and A. C. Steven, "A model for Ure2p prion filaments and other amyloids: The parallel superpleated β -structure," *Proc. Natl. Acad. Sci. U.S.A.*, vol. 101, no. 21, pp. 7885–7890, 2004.
- [337] F. Shewmaker, D. Kryndushkin, B. Chen, R. Tycko, and R. B. Wickner, "Two Prion Variants of Sup35p Have In-Register Parallel β -Sheet Structures, Independent of Hydration," *Biochemistry*, vol. 48, no. 23, pp. 5074–5082, 2009.
- [338] N. J. Cobb, F. D. Sönnichsen, H. Mchaourab, and W. K. Surewicz, "Molecular architecture of human prion protein amyloid: A parallel, in-register β -structure," *Proc. Natl. Acad. Sci. U.S.A.*, vol. 104, no. 48, pp. 18 946–18 951, 2007.
- [339] R. B. Wickner, F. Dyda, and R. Tycko, "Amyloid of Rnq1p, the basis of the [PIN+] prion, has a parallel in-register β -sheet structure," *Proc. Natl. Acad. Sci. U.S.A.*, vol. 105, no. 7, pp. 2403–2408, 2008.
- [340] T. Maly, G. T. Debelouchina, V. S. Bajaj, K.-N. Hu, C.-G. Joo, M. L. Mak-Jurkauskas, J. R. Sirigiri, P. C. A. van der Wel, J. Herzfeld, R. J. Temkin, and R. G. Griffin, "Dynamic nuclear polarization at high magnetic fields," *J. Chem. Phys.*, vol. 128, no. 5, p. 052 211, 2008.
- [341] A. Potapov, W.-M. Yau, R. Ghirlando, K. R. Thurber, and R. Tycko, "Successive Stages of Amyloid- β Self-Assembly Characterized by Solid-State Nuclear Magnetic Resonance with Dynamic Nuclear Polarization," *J. Am. Chem. Soc.*, vol. 137, no. 25, pp. 8294–8307, 2015.
- [342] B. Uluca, T. Viennet, D. Petrović, H. Shaykhalishahi, F. Weirich, A. Gönülalan, B. Strodel, M. Etzkorn, W. Hoyer, and H. Heise, "DNP-Enhanced MAS NMR: A Tool to Snapshot Conformational Ensembles of α -Synuclein in Different States," *Biophys. J.*, vol. 114, no. 7, pp. 1614–1623, 2018.
- [343] R. Verardi, N. J. Traaseth, L. R. Masterson, V. V. Vostrikov, and G. Veglia, "Isotope Labeling for Solution and Solid-State NMR Spectroscopy of Membrane Proteins,"

in *Isotope Labeling in Biomolecular NMR*, ser. Advances in Experimental Medicine and Biology, H. S. Atreya, Ed., Dordrecht: Springer Netherlands, 2012, pp. 35–62.

- [344] Z. Gan, I. Hung, X. Wang, J. Paulino, G. Wu, I. M. Litvak, P. L. Gor'kov, W. W. Brey, P. Lendi, J. L. Schiano, M. D. Bird, I. R. Dixon, J. Toth, G. S. Boebinger, and T. A. Cross, "NMR spectroscopy up to 35.2T using a series-connected hybrid magnet," *J. Magn. Reson.*, vol. 284, pp. 125–136, 2017.
- [345] F. M. Paruzzo, B. J. Walder, and L. Emsley, "Line narrowing in ^1H NMR of powdered organic solids with TOP-CT-MAS experiments at ultra-fast MAS," *J. Magn. Reson.*, vol. 305, pp. 131–137, 2019.
- [346] M. Schledorn, A. A. Malär, A. Torosyan, S. Penzel, D. Klose, A. Oss, M.-L. Org, S. Wang, L. Lecoq, R. Cadalbert, A. Samoson, A. Böckmann, and B. H. Meier, "Protein NMR Spectroscopy at 150 kHz Magic-Angle Spinning Continues To Improve Resolution and Mass Sensitivity," *ChemBioChem*, vol. 21, no. 17, pp. 2540–2548, 2020.
- [347] J. Hoffmann, J. Ruta, C. Shi, K. Hendriks, V. Chevelkov, W. T. Franks, H. Oschkinat, K. Giller, S. Becker, and A. Lange, "Protein resonance assignment by BSH-CP-based 3D solid-state NMR experiments: A practical guide," *Magn. Reson. Chem.*, vol. 58, no. 5, pp. 445–465, 2020.
- [348] M. D. Gelenter and M. Hong, "Efficient ^{15}N – ^{13}C Polarization Transfer by Third-Spin-Assisted Pulsed Cross-Polarization Magic-Angle-Spinning NMR for Protein Structure Determination," *J. Phys. Chem. B*, vol. 122, no. 35, pp. 8367–8379, 2018.
- [349] M. Kollmer, W. Close, L. Funk, J. Rasmussen, A. Bsoul, A. Schierhorn, M. Schmidt, C. J. Sigurdson, M. Jucker, and M. Fändrich, "Cryo-EM structure and polymorphism of A β amyloid fibrils purified from Alzheimer's brain tissue," *Nat. Commun.*, vol. 10, no. 1, pp. 1–8, 2019.
- [350] E. Nogales, "The development of cryo-EM into a mainstream structural biology technique," *Nat. Methods*, vol. 13, pp. 24–27, 2015.
- [351] R. D. Righetto, N. Biyani, J. Kowal, M. Chami, and H. Stahlberg, "Retrieving high-resolution information from disordered 2D crystals by single-particle cryo-EM," *Nat. Commun.*, vol. 10, no. 1, p. 1722, 2019.
- [352] J. Jeon, K. R. Thurber, R. Ghirlando, W.-M. Yau, and R. Tycko, "Application of millisecond time-resolved solid state NMR to the kinetics and mechanism of melittin self-assembly," *Proc. Natl. Acad. Sci. U.S.A.*, vol. 116, no. 34, pp. 16 717–16 722, 2019.

- [353] J. Jeon, W.-M. Yau, and R. Tycko, “Millisecond time-resolved solid-state NMR reveals a two-stage molecular mechanism for formation of complexes between calmodulin and a target peptide from Myosin light chain kinase,” *J. Am. Chem. Soc.*, vol. 142, no. 50, pp. 21 220–21 232, 2020.
- [354] J. Nasica-Labouze, P. H. Nguyen, F. Sterpone, O. Berthoumieu, N.-V. Buchete, S. Coté, A. De Simone, A. J. Doig, P. Faller, A. Garcia, A. Laio, M. S. Li, S. Melchionna, N. Mousseau, Y. Mu, A. Paravastu, S. Pasquali, D. J. Rosenman, B. Strodel, B. Tarus, J. H. Viles, T. Zhang, C. Wang, and P. Derreumaux, “Amyloid β Protein and Alzheimer’s Disease: When Computer Simulations Complement Experimental Studies,” *Chem. Rev.*, vol. 115, no. 9, pp. 3518–3563, 2015.
- [355] F. A. Kovacs, D. J. Fowler, G. J. Gallagher, and L. K. Thompson, “A practical guide for solid-state NMR distance measurements in proteins,” *Concepts Magn. Reson. Part A*, vol. 30A, no. 1, pp. 21–39, 2007.
- [356] E. L. Ulrich, H. Akutsu, J. F. Doreleijers, Y. Harano, Y. E. Ioannidis, J. Lin, M. Livny, S. Mading, D. Maziuk, Z. Miller, E. Nakatani, C. F. Schulte, D. E. Tolmie, R. Kent Wenger, H. Yao, and J. L. Markley, “BioMagResBank,” *Nucleic Acids Res.*, vol. 36, pp. D402–D408, 2008.

VITA

Yuan Gao was born in Maanshan, China. He earned his Bachelor of Science degree in Chemical Biology from the College of Chemistry and Molecular Engineering at Peking University (Beijing, China) in 2013 summer. To pursue higher education, Yuan applied to Florida State University (Tallahassee, Florida, USA) and started in Biomedical Engineering program in the fall of 2014. Then, he transferred to the School of Chemical and Biomolecular Engineering at Georgia Institute of Technology (Atlanta, Georgia, USA) at the beginning of 2015 fall. He continued to finish up his Ph.D. study in 2022 summer. The research topic in Yuan's graduate study is mainly focused on using solid-state NMR to characterize the atomic structures of some disease-associated proteins. He hopes to enter the chemical engineering industry after graduation.